



HAL
open science

Constraints on primordial gravitational waves from the large scales CMB data

Sylvain Vanneste

► **To cite this version:**

Sylvain Vanneste. Constraints on primordial gravitational waves from the large scales CMB data. Cosmology and Extra-Galactic Astrophysics [astro-ph.CO]. Université Paris Saclay (COMUE), 2019. English. NNT : 2019SACLS314 . tel-02426412

HAL Id: tel-02426412

<https://theses.hal.science/tel-02426412>

Submitted on 2 Jan 2020

HAL is a multi-disciplinary open access archive for the deposit and dissemination of scientific research documents, whether they are published or not. The documents may come from teaching and research institutions in France or abroad, or from public or private research centers.

L'archive ouverte pluridisciplinaire **HAL**, est destinée au dépôt et à la diffusion de documents scientifiques de niveau recherche, publiés ou non, émanant des établissements d'enseignement et de recherche français ou étrangers, des laboratoires publics ou privés.

NNT : 2019SACL314

n°LAL : 19-013

Thèse de doctorat

Constraints on primordial gravitational waves from large scales CMB data

Thèse de doctorat de l'Université Paris-Saclay
préparée à l'Université Paris-Sud au sein du Laboratoire de l'Accélérateur
Linéaire

École doctorale n°576 Particles, Hadrons, Energy, Nuclei, Instrumentation,
Imaging, Cosmos et Simulation (PHENIICS)
Spécialité de doctorat : Astroparticules et Cosmologie

Thèse présentée et soutenue à Orsay, le 20/09/2019, par

SYLVAIN VANNESTE

Composition du Jury :

Fabien Cavalier Directeur, LAL - Orsay	Président
Stéphanie Escoffier CPPM - Marseille	Rapporteur
Juan-Francisco Macias-Perez LPSC - Grenoble	Rapporteur
Anthony Banday IRAP - Toulouse	Examineur
Carlo Baccigaluppi SISSA - Trieste	Examineur
Julien Grain IAS - Orsay	Examineur
Matthieu Tristram LAL - Orsay	Directeur de thèse
Sophie Henrot-Versillé LAL - Orsay	Co-directeur de thèse

Contents

1	Introduction to modern Cosmology	6
1	The Big-Bang Cosmological Standard Model	6
1.1	Pillars of the Big-Bang model	6
1.2	General relativity and dynamic of the Universe	7
1.3	Thermal history of the Universe	11
1.4	The Cosmic Microwave Background	15
1.5	A puzzling model	17
2	Inflation	19
2.1	Motivation	19
2.2	Inflaton field	20
3	Inhomogeneous Universe	24
3.1	Perturbed FLRW Universe	24
3.2	Perturbations generated during inflation	25
3.3	Matter and radiation inhomogeneities	28
4	The Cosmic Microwave Background radiation	29
4.1	Temperature power spectrum	29
4.2	Temperature anisotropies	31
4.3	Polarization anisotropies	32
4.4	Polarization power spectra	36
4.5	Polarization secondary anisotropies	38
4.6	Parameters measurements	39
4.7	Λ CDM parametrization	41
5	Main CMB experiments	42
5.1	Space-based missions legacy	42
5.2	Recent ground-based experiments	43
5.3	Future measurements	43
6	Summary	46
2	Astrophysical foreground removal	48
1	Astrophysical foregrounds	49
1.1	Galactic sources	49
1.2	Extra galactic sources	52
2	Sky modelling and simulations	53
2.1	CMB signal	53
2.2	Foregrounds modelling	53
2.3	The Python Sky Model	54
2.4	The Planck sky model	54
2.5	Foreground models comparison	56

2.6	Noise	56
2.7	Dataset signals	58
3	Foregrounds removal methods	61
3.1	CMB cleaning methods	61
3.2	Component separation methods	62
4	Single frequency channel cleaning	63
4.1	Datasets	63
4.2	Polarization rotation	64
4.3	Clean CMB estimate	64
4.4	Outline	65
5	Foreground residuals	66
5.1	Contamination of the CMB map estimate	66
5.2	Forecast on foreground residuals	66
5.3	From global to patches	67
6	Linear regression estimators	72
6.1	Ordinary linear Regression	72
6.2	Normalised-model linear regression	73
6.3	Bias removal	74
6.4	Methods results and comparison	77
6.5	Summary and conclusion	79
7	Maximum likelihood estimator	80
7.1	One foreground model	80
7.2	Linearisation and Newton-Raphson algorithm	81
7.3	Two foregrounds model	81
7.4	Noise and algorithm convergence	82
7.5	Results	83
7.6	Conclusion and summary	83
8	Internal Linear Combination	84
8.1	Formalism	84
8.2	Optimal coefficients	84
8.3	Weights parametrisations	85
8.4	Foregrounds cleaning ILC	86
8.5	Relation to the linear regression	87
9	Polarization rotation	88
10	Patches cleaning	90
10.1	Dust-synchrotron correlation	90
10.2	Cosmic variance	90
10.3	Beyond cosmic variance	91
11	Residual covariance matrix	93
12	Summary and method comparison	95
12.1	Summary	95
12.2	Method comparison	95
3	Spectrum estimators	98
1	Context	98
1.1	Power spectrum estimator methods	98
1.2	Polarization leakage	99
2	Power spectrum definitions and notations	100
2.1	Spherical Fourier transform	100
2.2	Power spectrum	100
2.3	Spectrum variance	101
3	Simulations	102

3.1	Reionization survey	103
3.2	Recombination survey	103
4	Pure pseudo spectra	104
4.1	Formalism	104
4.2	Window function apodization	106
4.3	Results	108
4.4	Summary	114
5	Cross Quadratic maximum likelihood estimator	115
5.1	Formalism	115
5.2	Relation with the maximum likelihood estimator	119
5.3	Implementation	120
5.4	Power spectra reconstruction	125
5.5	Modes mixing and leakage	127
5.6	Summary	131
6	Methods comparison	132
6.1	B-modes	132
6.2	E-B correlation spectrum	133
6.3	Tensor-to-scalar ratio	133
6.4	Summary & conclusion	134
4	Planck data analysis	136
1	Planck legacy	137
1.1	Datasets	137
1.2	FFP10 noise simulations	137
1.3	White noise simulations	138
2	Foregrounds cleaning	139
2.1	Pre-smoothing and resolution degradation	139
2.2	Cleaning methods	139
2.3	Masks	140
2.4	Monte-Carlo simulations	140
2.5	Results on <i>Planck</i> data	142
3	Constraints on foreground spectral indices	147
3.1	From foreground coefficients to spectral indices	147
3.2	Methodology	147
3.3	Results	147
3.4	Conclusion	150
4	Cleaned polarisation maps	152
4.1	Cleaned datasets	152
4.2	Simulations	152
4.3	<i>Planck</i> data	153
5	Polarisation power spectra	161
5.1	Pixel covariance matrices	161
5.2	Full mission simulations	161
5.3	Planck data	162
6	Cosmological parameters likelihood	168
6.1	Large angular scale Likelihood	168
6.2	Results on individual cross-spectrum	170
6.3	Combined cross-spectra	178
6.4	Conclusion	179
7	Summary	183
A	Pixel signal covariance matrix	188

1	Introduction	194
2	Introduction à la Cosmologie moderne	196
2.1	Modèle du Big-bang	196
2.2	Inflation et Univers inhomogène	196
2.3	CMB et modes B	197
2.4	Plan	197
3	Nettoyage des contaminations d'avants-plan	198
3.1	Modélisation du signal	198
4	Estimateur de spectres	200
4.1	Estimateur maximum de vraisemblance quadratique	200
4.2	Comparaison avec d'autres méthodes	200
5	Analyse des données de <i>Planck</i>	201
5.1	Les données <i>Planck</i>	201
5.2	Résultats	201
	Bibliography	204

Remerciements

Cette thèse, c'est évidemment bien plus que l'aboutissement de trois années de travail. Aussi loin que mes souvenirs remontent, j'ai toujours eu une fascination ainsi qu'une forme d'incompréhension face au monde. Deux sentiments qui ont naturellement été comblés en découvrant les sciences, et plus particulièrement la physique.

Avant tout, je remercie mes parents, qui m'ont toujours offert la possibilité d'explorer et d'assouvir cette voie. Mam's, j'ai hérité de ta curiosité, et les nombreuses soirées passées à regarder la lune avec toi ne sont certainement pas innocentes face au chemin que j'ai pu emprunter plus tard. Pap's, je dirai qu'on partage cette claire-voyance face aux événements qui nous entourent. Cette forme de raison m'a toujours permis de me recentrer, et finalement d'évoluer dans une direction qui m'a toujours comblé. Quant à Félix et Louise, votre maturité et vos expériences m'ont toujours apporté un précieux troisième point de vu. J'ai pu comprendre tellement de choses grâce à vous.

Ce terreau a ensuite pu être nourri par des figures inspirantes, pour la plupart des enseignants et professeurs, et qui m'ont, chacun à leur manière, convaincu que le savoir et les connaissances faisaient parti des biens les plus enrichissants. Merci à Fifoune, Pino, Micheline, Dominique Latteur, Marc Devos, Philippe Janssens, Christophe Ringeval, Vincent Lemaitre, Jan Govaerts, et enfin Jean-Marc Gérard, qui restera à jamais mon exemple du physicien chercheur par excellence. Atteindre votre niveau à vous tous a toujours été, et restera, un de mes buts les plus chers.

C'est un peu la hasard qui m'a fait atterrir au LAL. J'ai dû réapprendre bien des choses face à cet esprit parfois trop rapide et efficace qu'est celui de Matthieu. Merci à toi pour la rigueur que tu m'as apprise. Merci aussi pour la patience face à mon esprit plus distrait, voir quelque peu nonchalant. Je repars avec un bagage qui me restera précieux toute ma vie, j'en suis certain. Merci aussi à Sophie pour les nombreux conseils et relectures. Et merci évidemment à Thibaut, tu m'as littéralement sauvé plus d'une fois. T'es vraiment trop fort, à tout point de vue.

Pour le reste, je remercie la cosmo-team et ses *satellites*, avec ces nombreuses soirées et festivals : Tguy, notre maître à tous, compagnon fidèle de festoches ; Toto, le bandit par excellence ; Maegon Smitchzs, l'insatiable Martien ; Axel, la bonne humeur venue du sud ; Remy et Smeg, deux belles rencontres collatérales ; ...

Il y a aussi ces chouettes amitiés tissées dans cet univers parallèle qu'est la ciup : Nils, Zeynep, Jilmar, Bassem, ... et bien-évidemment, le roi des branleurs, Jonathanne Lago Lago. Je nous prédis une belle carrière de chômeurs.

Merci aussi à ceux (plus ou moins) restés en Belgique : Guillaume, Chichi, Pablo, Vince', Antoine, Alan, Thom le grimpeur, Dorian le nounours, Denis compagnons de FF et plus, l'oasis, avec la (pas si) grosse Clacla, Marie, Suzon, et Leila l'activiste effrénée. Une chaleureuse pensée pour toi Nathan, j'en aurai encore beaucoup d'autres à ton égard mon ami. Et évidemment, Docteur Mahillonnaise, l'une des plus belle rencontre de ma vie, plus besoin d'expliquer pourquoi. Merci aussi à ceux venus d'ailleurs, ma Fourchette adoré, mon Anouki, et la Pantoufle des catacombes.

Et enfin, la surprise qui s'est rapidement transformée en évidence : Cló. Je suis si heureux que nos chemins se soient croisés. Avec toi, j'ai déjà vécu plus que je n'en aurai espéré, et la suite promets d'être toujours plus délirante. Puisse les cabanes et les boules magiques continuer à nous inspirer sur la petite route qu'on se trace à deux, à coup de calmez-vous maître bien sûr. Je t'aime tellement.

Introduction

The evolution of the world can be compared to a display of fireworks that has just ended: some few red wisps, ashes and smoke. Standing on a cooled cinder, we see the slow fading of the suns, and we try to recall the vanishing brilliance of the origin of the worlds.

(Georges Lemaître, 1931)

By the dawn of the 20th century the revolution in physics brought by quantum mechanics and general relativity led to further insights on studying the Universe as a whole. As the works from Albert Einstein, Willem de Sitter, and Alexandre Friedmann, laid the ground for the cosmological solutions of general relativity equations, the origin and evolution of the Universe became a subject of research, and contemporary Cosmology was born.

With the improvement of astrophysical observation techniques came the first evidences, from Edwin Hubble, that many observed nebulae were actually extra-galactic objects, known as galaxies (E. P. Hubble 1926). Their radial velocity measured by Vesto Slipher indicated an apparent recession from us which manifests itself as a redshift of the observed spectrum. The linear relation between the distance and the apparent velocity of the galaxies was first deduced by Georges Lemaître in 1927 (G. Lemaître 1927), and later on by Edwin Hubble in 1929 (E. Hubble 1929). Lemaître provided the first interpretation that the cosmological redshift is caused by the expansion of the Universe that is sourced by a cosmological constant, and not by the motion of the galaxies (see Luminet 2013). He also introduced for the first time a description of the primordial Universe as being much denser and hotter, emerging from the so-called ‘primordial atom’ (Georges Lemaître 1950). This idea, first jokingly referred to as the ‘Big-Bang’, later revealed to be revolutionary. The discovery of the Cosmic Microwave Background (CMB) and the observational evidences confirming the Big-Bang Nucleosynthesis theory developed by Gamow and its collaborators (Gamow 1948) paved the ground toward the standard model of cosmology.

The concept of a radiative remnant echo of the Big-Bang emanating from the first instants of a hot Universe was first studied by Alpher and Hermann (Ralph A. Alpher et al. 1948). They predicted that the CMB should follow a black-body radiation law, characterised by a temperature which dropped to a few Kelvin only since its emission. The CMB photons carry both the information about their cosmic journey and the imprint of the physics of the primordial Universe, which involves energy scales way beyond the reach of current particle accelerators. Therefore, the study of the CMB provides a unique cosmological lever arm to understand the history of the Universe, to test general relativity, to constrain particle physics, and to constrain the nature of dark energy as well as dark matter.

The first evidence of the CMB was provided in 1964 by Penzias and Wilson. Since then, numerous ground-based telescopes, satellites, and balloon-born experiments have made it possible to drastically improve its measurements. The first validation of the black-body spectrum nature of the CMB was achieved by the COBE satellite. Followed detailed mappings of the CMB anisotropies on the sky by the satellites WMAP and *Planck* in the 21st, bringing constraints of the cosmological standard model parameters up to the percent level, and marking the beginning of the precision cosmology era.

However, several pieces of the cosmological puzzle are still missing. The nature of the dark energy and dark matter is still unknown. The absence of anti-matter in the observable Universe is unexplained. Why does our Universe appear geometrically flat? And how did it become homogeneous on scales *a priori* not causally connected? What sourced the primordial fluctuations which seeded the CMB anisotropies and the cosmological large-scale structures observed today?

Corresponding to a short and early period during which the Universe would have grown exponentially, the inflation is the leading and probably the most elegant paradigm which provides a solution to three of the cosmological puzzles : the flatness and the horizon problems, as well as the origin of the primordial fluctuations.

The rapid expansion of the Universe at the epoch of inflation should have enlarge quantum fluctuations to macroscopic scales, producing a stochastic background of primordial gravitational waves. Those should have left an imprint on the CMB photons polarisation, the so-called *B-modes* patterns. The precise measurements of the B-modes, still undetected to this day, represents the most promising probe to inflationary physics as well as the first insight into the quantum nature of gravity. However, the expected amplitude of the signal is at least one thousand times smaller than that of the CMB temperature, and can be seriously impeded by foreground contaminations from Galactic emissions. Future B-mode detections thus require expertise in instrumental, physical, and computational sciences.

This thesis focuses on the development of analysis tools to study the primordial B modes of the Cosmic Microwave Background. Our goal is to extract the amplitude of the primordial gravitational waves produced during the inflationary period.

Specifically, we are interested in the large angular scales, for which the primary B modes signal is expected to be dominant. Since these scales are particularly contaminated by polarised galactic emissions, we have studied and developed approaches to reduce those contaminations and to characterise their residuals. Those methods are applicable to products from satellite missions such as *Planck* or LiteBIRD.

In order to estimate the B modes amplitude, we developed and characterised a CMB anisotropies power spectrum estimator. The algorithm is pixels-based and allows to cross-correlate maps measured by different detectors. The method is optimal and minimises the so-called E-to-B variance leakage.

We applied the cleaning and spectrum estimation approaches to the polarisation data and simulation maps publicly provided by *Planck*. The constraints that we deduce are in agreement with past analysis. Ultimately, we derive an upper limit on the primordial gravitational waves amplitude as well as the reionization parameter.

Introduction to modern Cosmology

1 The Big-Bang Cosmological Standard Model

As we will see, the Universe is highly dynamic. Its geometry and its constituents evolve with time, this evolution can be calculated. We review some of the key physical paradigms to study the Universe, as well as the important events filling its history.

1.1 Pillars of the Big-Bang model

Cosmology is based on the Big-Bang model for which its key stages are highlighted in Fig. 1.1. The so-called three pillars of the Big-Bang model can be summarised as follow :

- The Universe is expanding, and its expansion is characterised by a growing time-dependent scale factor $a(t)$ equals to unity today, $a_0 = 1$.
- The ‘baryonic’ matter, including electrons, was formed in the early Universe, when it was much denser and hotter than today. The Universe was smoothly filled with a plasma of elementary particles in thermal equilibrium, such as quarks, electrons, neutrino, and photons. The first nuclei (protons and neutrons) formed during a phase known as the Big-Bang Nucleosynthesis (BBN). Since temperature was still high, electrons and photons were tightly coupled by Coulomb scattering, and no atom bound states were allowed to form.
- As the Universe expanded, its temperature dropped low enough so that electrons started to combine efficiently with the nuclei to form the first atoms, mainly Hydrogen and Helium. As a consequence, photons decoupled from the primordial plasma, and were allowed to free-stream through space. They formed a background of radiation, known as the Cosmic Microwave Background, which still permeates the Universe today.

In addition, the Big-Bang model is based on two main properties of our Universe: it is both highly homogeneous and isotropic on large scales. This means that the Universe should present the same characteristics everywhere, and in all directions that we wish to observe.

The evolution across time of both the constituents and the geometry of the Universe is described by the Einstein equations of General Relativity (GR). The Big-Bang model is embedded in the Standard Model of cosmology, referred to as the Λ CDM model. It is characterised by an acceleration of the Universe expansion, encoded by a Cosmological constant, Λ , in the Einstein equations. The source of the expansion acceleration is assigned to an exotic, and yet not understood, type of energy filling the Universe, and contributing up to 70% of its total energy density, known as the Dark Energy (DE). Another constituent, the Cold Dark Matter (CDM), is responsible for most of the non-relativistic matter budget of the Universe. It does seems to

interact only through gravity, and it contributes up to 25% of the total energy density of the Universe. The remaining 5% come from Baryonic matter, that constitutes us among other.

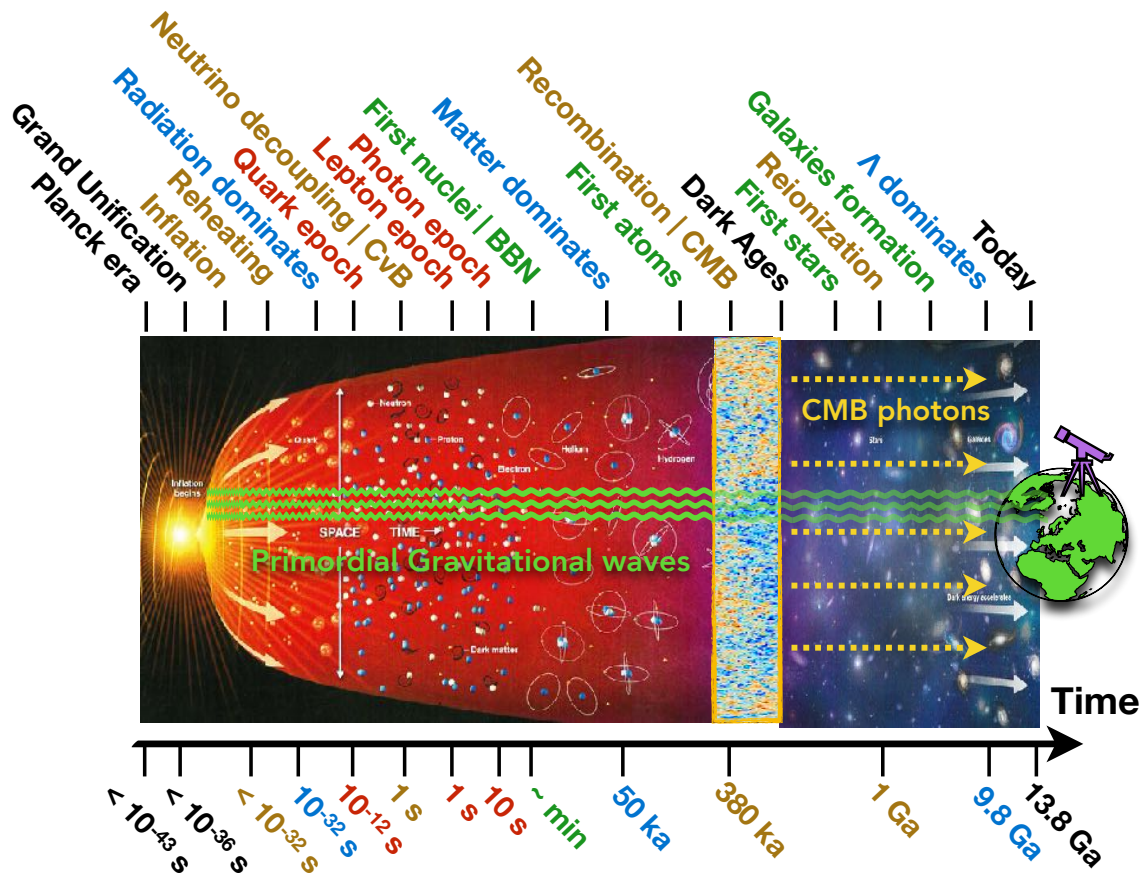


Figure 1.1: Chronology of the Universe. Vertical axis is space distances, horizontal axis is for time coordinates. During its evolution, the Universe expansion rate is driven by different constituents : first radiation, then matter, and up until quite recently, some dark-energy in the form of a cosmological constant Λ . The first light nuclei formed during the first 3 minutes and stayed ionized during 300000 years, until they captured electrons, forming neutral atoms. The CMB was emitted around 13 billions years ago. Adapted from National Geographic Society, April 2014.

1.2 General relativity and dynamic of the Universe

In GR, the apparent gravitational force is the result of the geometrical warping of space-time. GR is based on the equivalence principle (EP), which states that gravitational and inertial masses are equivalent (weak EP). In addition, gravity is seen as an apparent force which can be cancelled by choosing an appropriate new system of coordinates (Einstein EP), i.e. a coordinate system attached to the particle.

In the framework of GR, space-time and matter are related via the Einstein equation. As famously resumed by John Wheeler,

Space tells matter how to move, matter tells space how to curve.

Therefore, providing an appropriate description of the Universe's space-time properties, the evolution of both its geometry and its constituents can be calculated.

Metric

The local space-time geometry is described by the so-called metric, a two-indices tensor $g_{\mu\nu}$. The indices evolve in a four-dimensional coordinate system, $\mu, \nu = \{0, 1, 2, 3\}$, with 0 the time-like coordinate, and 1, 2, 3 the space coordinates x , y and z . The metric accounts for the relative change of (space and time) distances when changing of reference system. Physical invariants can be determined from it, such as the well-known distance interval, or line element, $ds^2 \equiv g_{\mu\nu} dx^\mu dx^\nu$. In the absence of gravitation, the special relativity is described by the (flat) Minkowski metric $g_{\mu\nu} = \eta_{\mu\nu}$, with $\eta_{\mu\nu} \equiv \text{diag}(-1, 1, 1, 1)$.

One key advantage of using the metric is that it easily accounts for the change in coordinates when describing the motion of a particle. Indeed, a free falling particle follows the Geodesic equation,

$$\frac{d^2 x^\mu}{d\lambda^2} = -\Gamma_{\alpha\beta}^\mu \frac{dx^\alpha}{d\lambda} \frac{dx^\beta}{d\lambda}. \quad (1.1)$$

The motion of the particle is described by the left hand-side of the equation, while the change of coordinates is accounted for in the right hand side. The latter involved the so-called Christoffel symbols, which depend on the metric,

$$\Gamma_{\sigma\mu}^\alpha \equiv \frac{1}{2} g^{\alpha\nu} [g_{\mu\nu,\sigma} + g_{\sigma\nu,\mu} - g_{\mu\sigma,\nu}]. \quad (1.2)$$

From the equivalence principle, we can always find a metric such that the Christoffel symbols vanish. In that case, we recover Newton first law conservation of motion.

A homogeneous and isotropic Universe is described by the space-independent Friedmann–Lemaître–Robertson–Walker (FLRW) metric $g_{\mu\nu} = \text{diag}(-c^2, a^2(t), a^2(t), a^2(t))$. The generic line element invariant is therefore

$$ds^2 = -c^2 dt^2 + a^2(t) dl^2, \quad dl^2 \equiv \frac{1}{1 - Kr^2} dr^2 + r^2 (d\theta^2 + \sin^2 \theta d\varphi). \quad (1.3)$$

The spatial metric dl^2 encodes the global spatial curvature parametrised by K . In a flat Euclidean Universe, K would vanish and $dl^2 = dx^2 + dy^2 + dz^2$, while for a closed (open) Universe, the curvature parameter is positive (negative).

Evolutions parameters and distances

In Eq. (1.3) we refer to x , y , and z as the comoving coordinates, as they do not evolve with time. While the physical coordinates are noted $a(t)x$, $a(t)y$, and $a(t)z$, and stretch proportionally to $a(t)$ as the Universe undergoes expansion. Defining χ as the comoving distance between two observers, the physical distance therefore reads $D = a(t)\chi$, and evolves following the Hubble–Lemaître law,

$$\dot{D} = HD, \quad (1.4)$$

with the upper dot indicates the time derivative, and $H \equiv \dot{a}/a$ the Hubble parameter, expressed in units of inverse-time, and whose current measurements reads $H_0 \simeq 67.74 \pm 0.46$ km/s/Mpc ([Planck 2015 Results. XIII](#)). This law reflects an important aspect : cosmological objects seem to go away from an observer with a velocity proportional to their relative distance.

Writing $d\chi = dD/a = c dt/a$, and taking $c = 1$, the comoving distance can therefore be computed as

$$\chi(a) = \int_{t(a)}^{t_0} \frac{dt'}{a(t')} \quad (1.5)$$

$$= \int_a^{a_0} \frac{da'}{a'^2 H(a')}. \quad (1.6)$$

An important evolution parameter is the comoving horizon, or conformal time (in contrast to cosmic time t).

$$\eta \equiv \chi(a = 0) \quad (1.7)$$

$$= \int_0^{t_0} \frac{dt'}{a(t')}, \quad (1.8)$$

measures the comoving distance travelled by a photons emitted at $t' = 0$, up until now, at $t' = t_0$.

As distant sources are moving away from us, the spectra of their image undergo a spectral shift. We define the (photon) redshift, $z(t)$, as the absolute difference between the wavelength of observation at time t , and the wavelength of emission,

$$z(t) \equiv \frac{\lambda_{\text{obs}}(t) - \lambda_{\text{emit}}}{\lambda_{\text{emit}}}. \quad (1.9)$$

Since photons pursue light geodesics $ds^2 = 0$, it follows from Eq. (1.3) that $dl/dt = a(t)^{-1}$. As the Universe expands, the wavelength of photons emitted by distant sources stretches proportionally to the scale factor, $\lambda_{\text{obs}}(t) \propto a(t)$. As a consequence, their energy, $E \propto \lambda^{-1}$, decreases, and from Eq. (1.9), we can write $1 + z = a(t)^{-1}$. It means that objects with higher redshifts belong to younger epochs of the Universe. Thus, in addition to η , both the scale factor $a(t)$ and the redshift $z(t)$ can be used as cosmological evolution parameters.

Einstein equations

The Einstein equation,

$$G_{\mu\nu} + \Lambda g_{\mu\nu} = \frac{8\pi G}{c^4} T_{\mu\nu}, \quad (1.10)$$

connects the space-time geometry (left side) with its energy content (right side), encoded in the stress-energy tensor $T_{\mu\nu}$. The factor on the right-hand side term can also be expressed in natural units, $8\pi G = M_{\text{pl}}^{-2}$, with $c = 1$, and $M_{\text{pl}} \simeq 2.5 \times 10^{18}$ GeV the reduced Planck mass. The Einstein tensor,

$$G_{\mu\nu} \equiv R_{\mu\nu} - \frac{1}{2} g_{\mu\nu} R, \quad (1.11)$$

is composed of the Ricci scalar $R \equiv R_{\mu\nu} g^{\mu\nu}$, and the Ricci tensor $R_{\mu\nu} \equiv R_{\mu\alpha\nu}^{\alpha}$. Both are contractions of the Riemann tensor¹ $R_{\beta\mu\nu}^{\alpha} \equiv \Gamma_{\beta\nu;\mu}^{\alpha} - \Gamma_{\beta\mu;\nu}^{\alpha} + \Gamma_{\sigma\mu}^{\alpha} \Gamma_{\beta\nu}^{\sigma} - \Gamma_{\sigma\nu}^{\alpha} \Gamma_{\beta\mu}^{\sigma}$ which characterises the space-time curvature, and can be computed from Eq. (1.2), thus from the metric as well as its first and second derivatives. The relations between the matter and the Universe geometry can therefore be found by solving the Einstein equations. The solutions for an expanding Universe were independently developed by Alexander Friedmann and Georges Lemaître.

Friedmann-Lemaître equations

The Universe can be idealized as filled with perfect fluids with density $\rho(t)$ and pressure $p(t)$. Therefore $T_{00} = \rho(t)$ and $T_{ij} = p(t)\delta_{ij}$, with i, j the spatial coordinates only.

Solving the Einstein equations respectively for the time component ($\mu = \nu = 0$) and spatial components ($\mu, \nu = i, j$) leads to the Friedmann-Lemaître (FL) equations,

$$H^2 = \frac{8\pi G}{3} \rho - \frac{K}{a^2} + \frac{\Lambda}{3}, \quad (1.12)$$

$$\frac{\ddot{a}}{a} = -\frac{8\pi G}{6} (\rho + 3p) + \frac{\Lambda}{3}. \quad (1.13)$$

¹The semi-column ; is the covariant derivative defined on a curved manifold

Those are cornerstone equations of modern cosmology. They relate the expansion evolution of the Universe to the different fluids that populate it. From the Bianchi identities, one can show that $G_{\mu\nu;\mu} = 0$, and we recover the energy-momentum conservation, $T_{\mu\nu;\mu} = 0$. Since spatial homogeneity is assumed, only the time component of the latter formulae leads to one non-trivial solution, the continuity equation,

$$\dot{\rho} = -3H(p + \rho). \quad (1.14)$$

This equation can also be found by combining both FL Eqs. (1.12) and (1.13).

Evolution of the Universe

Since we have only two independent equations for three unknowns (a , ρ , p), an equation of state relating the pressure with density is conveniently added,

$$p = w\rho. \quad (1.15)$$

Hence, integrating Eq. (1.14), we find an expression for the evolution of the densities,

$$\rho = \rho_0 a^{-3(1+w)}, \quad (1.16)$$

with ρ_0 the density today. The parameter w depends on the nature of the fluid:

- The non-relativistic matter is pressure-less and includes baryons (b) and cold dark matter (c), hence we write $w_m = 0$, and $\rho_m \propto a^{-3}$, with $m = b, c$.
- For radiation, which includes relativistic matter such as photons (γ) or early-time neutrinos (ν), we write $w_r = 1/3$ and $\rho_r \propto a^{-4}$, with $r = \gamma, \nu$.
- The cosmological constant can be considered as a fluid, with constant density and negative pressure, hence $w_\Lambda = -1$ and $\rho_\Lambda = \text{cst}$.

The matter conservation Eq. (1.16) simply reflects that matter and radiations energy densities dilute as the Universe expands. The rates however differ. Matter density decreases as the cube of the inverse scale factor, a^{-3} . Because the expansion stretches the photon wavelengths, the radiation density rate has an extra factor, hence scaling as a^{-4} . Considering only one fluid, with a density parametrised as in Eq. (1.16), the first FL Eq. (1.12) becomes

$$H(a) = H_0 a^{-3(1+w)/2}, \quad \text{and} \quad a \propto t^{2/(w+1)}. \quad (1.17)$$

In practice, the Universe is populated with multiple fluids. To quantify which terms dominate in the FL equations, we conveniently express them in term of dimensionless energy densities,

$$\Omega_\Lambda \equiv \frac{\Lambda}{3H^2} = \frac{\rho_\Lambda}{\rho_{\text{cr}}}, \quad \Omega_K \equiv -\frac{K}{a^2 H^2}, \quad \Omega_x \equiv \frac{8\pi G \rho_x}{3H^2} = \frac{\rho_x}{\rho_{\text{cr}}}, \quad x = \{m, r\}, \quad (1.18)$$

with $\rho_\Lambda \equiv \Lambda/8\pi G$, and $\rho_{\text{cr}} \equiv 3H_0^2/8\pi G$ the critical energy density which corresponds to the total density in a flat Λ -free Universe. Using this parametrisation, the first FL Eq. (1.12) and the conservation Eq. (1.14) can be re-expressed as

$$1 = \Omega_r + \Omega_m + \Omega_\Lambda + \Omega_K, \quad (1.19)$$

$$\Omega_x = \Omega_{x0} \left(\frac{a}{a_0} \right)^{-3(1-w_x)}. \quad (1.20)$$

Ultimately, from the FL equations, the evolution of the Hubble parameter is provided by

$$\left(\frac{H}{H_0} \right)^2 \equiv \Omega_{m0} a^{-3} + \Omega_{r0} a^{-4} + \Omega_{K0} a^{-2} + \Omega_{\Lambda 0}. \quad (1.21)$$

As it expands, the Universe is therefore dominated by different natures of energy densities. Current measurements (see Sec. 4.6) indicate that we live in a flat Universe, $|\Omega_{K0}| = 0.0008^{+0.0040}_{-0.0039}$ (Planck 2015 Results. XIII.). The remaining densities are radiation, matter, and dark energy (Peter et al. 2009) :

- Today, the Universe is dominated by a cosmological constant, $\Omega_{\Lambda 0} = 0.685 \pm 0.013$, and is composed of significant amount of matter $\Omega_{m0} = 0.315 \pm 0.013$, while radiation density is almost negligible $\Omega_{r0} \simeq 8.47 \times 10^{-5}$.
- In the past, the Universe has gone through two phases :
 - a radiation era, dominated by Ω_r ,
 - followed by a matter era, dominated by Ω_m . The transition between both phases is referred to as the matter-radiation equality, when $\Omega_m = \Omega_r$, therefore occurring at redshift $z_{\text{eq}} \simeq 3200$.
- In the future, Ω_{Λ} will continue to grow, and the Universe expansion will be driven by a cosmological constant only.

We define the Hubble time, or Hubble horizon, as the reciprocal of the Hubble parameter, $t_H \equiv 1/H$. For a monotone Universe expansion $a(t) = Ct$, $C = \text{cst}$, the Hubble time is nothing but the age of the Universe, $t_H = t$. In reality, the Universe does not expand linearly, so this relation is not exact. To obtain the age of the Universe, one must remember that $H = da/adt$ and integrate Eq. (1.21) between $a = 0$ and $a = 1$ (or between $z = 0$ and $z = \infty$). This roughly provides $t \simeq 14$ billions years.

1.3 Thermal history of the Universe

If we go back far enough in the past, the Universe was much denser and hotter than today. Though the earliest phases of the Big-Bang are uncertain, we generally assume that the early Universe ($\lesssim 1$ s) was filled with a hot plasma consisting of relativistic elementary particles in thermodynamic equilibrium. Those are mainly quarks, electrons, positrons, (anti-) neutrinos, and photons. The origin of such a plasma will be discussed in Sec. 2, when introducing the motivation and origin of the inflationary theory.

As the Universe expands, the pressure as well as the temperature decrease. The latter can therefore be used as a cosmic evolution parameter. We generally refer to the photons temperature either in kelvin or in electron-volt, since $T [\text{K}] = E/k_B [\text{K}]$, with $k_B = 8.6 \times 10^{-5} \text{ eV/K}$ the Boltzmann constant.

As the Universe cools down, processes droved by thermodynamic can occur, producing or annihilating particles, allowing bound states to form, or particles to decouple from the primordial thermal bath. Such processes are described by thermodynamic laws applied to an Universe in expansion. We will go through some of the key phases of the thermal history of the Universe. Those are highlighted in Table. 1.1.

Interaction rate and decoupling

At some point, because temperature was high as well as the rate of interaction between particles, the matter was forming a smooth homogeneous plasma, whose constituents maintained thermal equilibrium by multiple scattering. The rate of interaction, defined as $\Gamma = \langle n\sigma \rangle v$, depends on the cross-sections σ , the relative velocity v between the reacting particles, hence the effective temperature of the primordial plasma, and finally on the number density n of the particles. As the Universe expands, the temperature grew cooler, and the interaction rate decreases. At some point, when the interaction rate falls below the expansion (Hubble) rate H , the mean free path

Time	Temperature [k_B K]	Events
10^{-43} sec.	10^{19} GeV	• Planck Era, eventual quantum theory of gravity.
10^{-38} sec.	10^{16} GeV	• Eventual GUT transition.
?	?	• Cosmic inflation, and reheating.
10^{-30} sec.	10^{12} GeV	• Eventual Peccei-Quinn phase transition.
10^{-11} sec.	10^2 GeV	• Electroweak phase-transition.
?	?	• Baryogenesis, baryon asymmetry, neutron and protons production.
?	?	• Eventual dark matter freeze-out.
10^{-4} sec.	100 MeV	• $\mu^+ \mu^- \rightarrow \gamma\gamma$ annihilation.
\sim sec.	\sim MeV	• ν decoupling.
10 sec.	0.5 MeV	• $e^+ e^- \rightarrow \gamma\gamma$ annihilation
\sim sec. - min.	0.1 MeV	• Big-Bang Nucleosynthesis (BBN), formation of D, T, ^4He , ^3He , and ^7Li nuclei.
10^5 sec.	\sim keV	• Photons fall out of chemical equilibrium.
$10^{-(4-5)}$ yr	3 eV	• Matter-radiation equality. Start of matter domination.
400 000 yr	\sim eV	• Recombination $e + p \rightarrow \text{H} + \gamma$.
400 000 yr	\sim eV	• Decoupling of CMB photons from the primordial plasma.
10^6 yr	$10^{-(1-2)}$ eV	• End of baryon drag.
10^8 yr	10^{-3} eV	• Dark ages, then reionization.
10^9 yr	10^{-3} eV	• First stars and galaxies.
10^{10} yr	10^{-4} eV	• Galaxy clustering. Dark Energy - matter equality.
1.4×10^{10} yr	$< 10^{-4}$ eV	• Today, Dark Energy domination.

Table 1.1: Thermal history of the Universe. Most quantities are approximative, and serve as a rule of thumb.

of the particles becomes too long for reactions and thermalisation to occur. The interactions freeze, and the constituents decouple from the plasma. In the following we enumerate some key decoupling events.

Photon temperature

For any species, the energy density can be expressed as (Dodelson 2003)

$$\rho_i = g_i \int \frac{d^3p}{(2\pi)^3} f_i(\vec{x}, \vec{p}) E(p). \quad (1.22)$$

with \vec{x} and \vec{p} respectively the position and impulsion of the particles. The energy is $E = \sqrt{p^2 + m^2}$, and g_i accounts for the degeneracy of the species. The particles follow either Bose-Einstein (for bosons) or Fermi-Dirac (for fermions) distributions,

$$f_{\text{BE/FD}} = \frac{1}{e^{(E-\mu)/T(t)} \mp 1}. \quad (1.23)$$

At the temperatures of the early Universe, the chemical potential μ can generally be neglected in Eq. (1.23). For photons, integrating Eq. (1.22) with $g_\gamma = 2$ gives $\rho_\gamma = \pi^2 T^4/15$. At the early Universe, we are well into the radiation-dominated era. From Eq. (1.16), the energy density therefore scales as $\rho_r \propto a^{-4}$. The number density for radiation scales as $\rho_r \propto T^4$, thus the photons temperature scales as the inverse scale factor, $T \propto a^{-1}$.

Baryogenesis

The Universe is observed to be populated by matter (as opposed to anti-matter). However, one might expect the Big-Bang to produce particles and antiparticles in equal numbers. Our matter-dominated Universe can be explained by introducing a slight difference between the number of baryon and anti-baryon produced during the early Universe ($< 10^{-4}$ sec.). This yet unsolved riddle is referred to as the Baryogenesis. Several models in particle physics attempt to explain such baryon asymmetry, although none are decisively solving the issue. Two main theories exist, one describing the Baryogenesis during the Grand Unified Theory (GUT) epoch, and the other describing the Baryogenesis occurring during the electroweak epoch. Anyway, a set of three necessary conditions under which baryon asymmetry can be explained is generally attributed to Andrei Sakharov (1967) : the baryon number B should (obviously) be violated; \mathcal{C} and \mathcal{CP} symmetries should be broken; finally, it should take place out of thermal equilibrium such that the inverse process cannot occur (Cline 2006).

The baryon asymmetry is often quantified by the baryon/photons ratio (Planck 2015 Results. XIII.),

$$\eta_{b/\gamma} \equiv (n_B - n_{\bar{B}})/n_\gamma \simeq (6 \pm 0.25) \times 10^{-10}, \quad (1.24)$$

with n_B and $n_{\bar{B}}$ the respective baryons and anti-baryon number densities.

Neutrino decoupling

At temperatures a little above 1 MeV, neutrinos (ν) are efficiently coupled to the electrons (e^-) and positrons (e^+) of the plasma via weak interactions of the form $e^+e^- \leftrightarrow \nu\bar{\nu}$ and $e\nu_e \leftrightarrow e\nu_e$. The reactions involve the exchange of virtual Z bosons, as well as W^\pm for the electronic neutrinos.

We can roughly calculate the interaction rate of such process (Bernstein et al. 1989). For matter, the number density scales as the inverse cube of the scale factor, $n_m \propto a^{-3} \propto T^3$. Since particles are highly relativistic, the product between the relative velocity and the cross-section

is approximated by $\langle v\sigma \rangle \sim G_F^2 T^2$, with $G_F \simeq 10^{-5} \text{ GeV}^{-2}$ the Fermi constant. Hence, the reaction rate goes as $\Gamma \sim G_F^2 T^5$. Since the Universe is radiation dominated, from the first FL Eq. (1.12) we have $H = \sqrt{8\pi G\rho_r/3} \sim T^2/M_{\text{pl}}$.

Therefore, neutrinos decouple from the plasma when $\Gamma \sim H$, that is to say, when $T \sim (M_{\text{pl}}G_F^2)^{-1/3} \sim 1 \text{ MeV}$. They form the so-called Cosmic Neutrino Background (CνB).

Particle annihilation

When temperatures are much higher than the mass of the electrons, $m_e \simeq 0.5 \text{ MeV}$, the photons (γ), electrons, and positrons, are kept in relatively same abundance via the electromagnetic interaction $e^+e^- \leftrightarrow \gamma\gamma$. However, as soon as the temperature drops under $m_e \sim 0.5 \text{ MeV}$, the production of e^+e^- is no more effective, and they start to annihilate, transferring their entropy to the photons, hence slowing the decrease of the plasma temperature. The annihilation is stopped by a slight baryon asymmetry, as electrons have no more positrons to annihilate with. The same process occurred earlier for the muons and anti-muons μ^\pm , at a energy scale of $m_\mu \simeq 100 \text{ MeV}$.

Nucleosynthesis

Solving the Boltzmann equations in an expanding Universe allows us to deduce the relative quantities of bound states formed by protons and neutrons. Those computations especially follow from the ground-breaking work of Gamow, Alpher and Herman (R. A. Alpher et al. 1948; Gamow 1948). We enumerate four groups of process (Coc et al. 2017) :

- Neutron - protons equilibrium : at first, neutron and proton numbers are kept in equilibrium through the processes $p + e^- \leftrightarrow n + \nu$ and $n \leftrightarrow p + e^- + \bar{\nu}$. About 1 sec. after the ‘Big-Bang’, when the temperature becomes less than the neutron-proton mass difference, the reactions favour protons production (as their mass is slightly lower than that of neutrons), and the number ratio between both freezes out at about 1 neutron for every 6 protons.
- Neutrons decay : when the above weak interactions stop to be effective, neutron decay, $n \rightarrow p + e^- + \bar{\nu}$ begins, bringing down the nuclei ratio to 1 neutron for every 7 protons.
- Deuteron formation : between 1 to 3 minutes, at $T \sim 0.1 \text{ MeV}$, the temperature of photons is low enough to allow the protons and neutrons to fuse into deuteron, $p + n \leftrightarrow d + \gamma$.
- Helium nuclei formation : finally, further reactions proceed to make helium nuclei, which net effect can be written $d + d \rightarrow \text{He} + \gamma$. Almost each neutron ultimately finds itself in a Helium nucleus.

The number of resulting nuclei mainly depends on one parameter, the baryon/photons ratio $\eta_{b/\gamma}$, defined in Eq. (1.24). The larger $\eta_{b/\gamma}$ is, the more efficiently deuterium will be transformed into Helium. No heavier nuclei are formed above Helium (except for a small amount of Lithium and Beryllium). Indeed, temperatures become too small for the formation of stable nuclei with higher atomic number to be effective. All other elements that we observe today are produced much later, mainly during stellar nucleosynthesis (stars evolution and death).

From the predicted neutron-proton ratio 1 : 7, a quick calculation allows to roughly predict a mass fraction of Helium at about 25% that of the total mass of produced nuclei, which is in extremely good agreement with current observations. The evolution of all species with temperatures can be computed numerically, as shown on the top panel of Fig. 1.2.

A powerful probe consists in measuring the relative abundances of light elements in interstellar medium, other galaxies, or via Ly- α absorption in the spectra of quasars emissions. Those can be confronted with $\eta_{b/\gamma}$, which is proportional to Ω_b and measured independently on the

CMB, as shown on the bottom panel of Fig. 1.3. Both measurements are in excellent agreement. The Big Bang Nucleosynthesis (BBN) is considered as a triumph for Big-Bang cosmology, as it successfully describes the early Universe and production of the relative number of light elements such as Hydrogen and Helium (Burles et al. 1999).

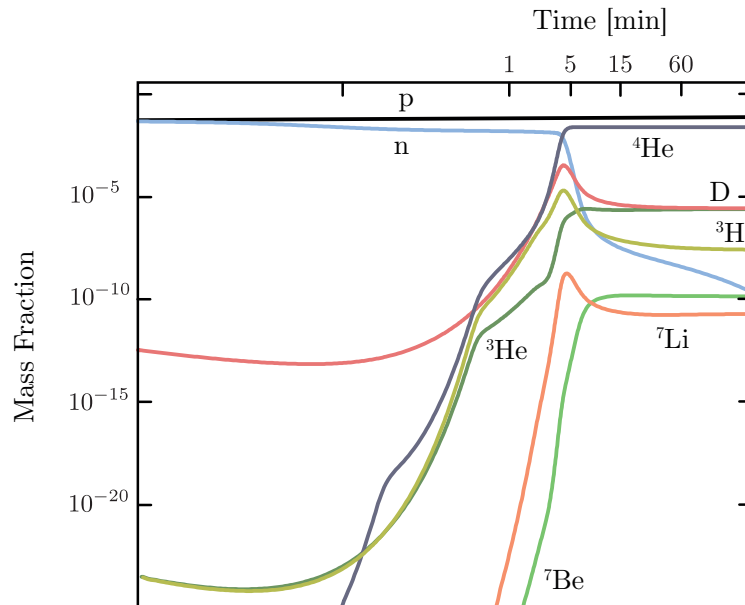


Figure 1.2: Predicted species abundance evolution during the Big-Bang Nucleosynthesis. From Daniel Baumann Lectures.

Recombination and photon decoupling

After BBN, the photons are still coupled to the thermal bath via Thomson scattering, $e^- \gamma \leftrightarrow e^- \gamma$. The Universe had to wait for the temperature to be low enough, around $\sim 1\text{eV}$, for electrons to form neutral bound state atoms with free nuclei produced during the BBN. As the number of free electrons exponentially decreases, photons decouple from the plasma and free-stream through the Universe, forming a Cosmic Microwave Background (CMB). The time of recombination can be roughly estimate by solving the so-called Saha equation, which gives $\sim 380\,000$ years, and $T \sim 3700\text{K}$. The photons decoupling can be considered as almost instantaneous. The CMB can therefore be pictured as a surface, the photons last scattering surface (LSS), whose redshift is around $z^* \simeq 1100$.

1.4 The Cosmic Microwave Background

As they travel through the expanding Universe, the CMB photons undergo a redshift and lose energy. Since most of them come from the primordial thermal bath, the CMB radiative spectrum is expected to follow a Black-Body (BB) emission law,

$$I_\nu = \frac{4\pi\hbar\nu^3}{c^2} \frac{1}{e^{2\pi\hbar\nu/k_B T_{CMB}} - 1}, \quad (1.25)$$

with ν the frequency of the electromagnetic radiation. The spectrum observed by the FIRAS instrument on board of the COBE satellite verified successfully this prediction, measuring

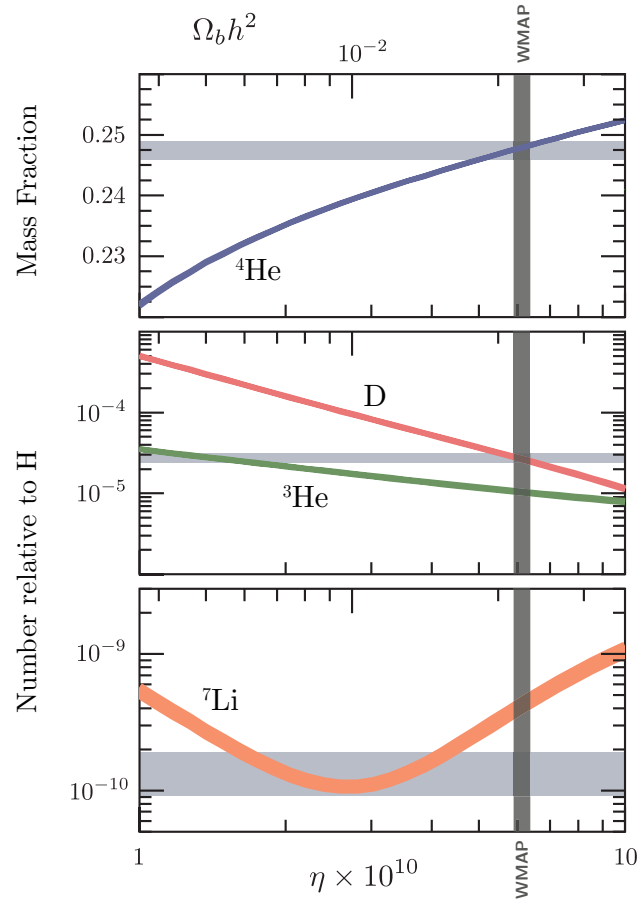


Figure 1.3: Theoretical prediction of number of light elements relative to Helium abundance. Horizontal boxes indicate current astrophysical observations, while the vertical grey band corresponds to the baryon/photons ratio measured on the CMB by the WMAP satellite experiment. Here, the photon-baryon ratio is defined as $\eta_{b/\gamma} = \eta$ inferred from CMB measurements of the by the WMAP satellite, not to be confused with the comoving distance. From Daniel Baumann Lectures.

$T_{\text{CMB}} = 2.725 \pm 0.001 \text{ K}$ (Mather et al. 1994), as shown in Fig. 1.4. This value is surprisingly close to the prediction first provided by Halper and Herman, with $T_{\text{CMB}} \approx T_*/z_* \simeq 5 \text{ K}$ (Ralph A. Alpher et al. 1948).

When mapping the CMB temperature, a dipole δT is also found, which originates from the combined movement of the solar system and the Milky Way relative to the CMB, hence inducing a Doppler shift on the CMB temperature map,

$$\delta T(\theta) = (3.346 \pm 0.017) \times 10^{-3} \text{ K} \cos \theta, \quad (1.26)$$

with θ the angle between the dipole and the observation direction. Residual CMB temperature fluctuations are observed with relative small amplitudes, $\delta T/T \simeq 10^{-5}$ (e.g. WMAP or *Planck* satellite experiments). Those anisotropies are the order of a few tenth of μK , and reveal the presence of matter density fluctuations at the epoch of photons decoupling. After decoupling, the inhomogeneities of matter density will continue to grow under gravitational effect, and will form the large scale structures such as galaxies and clusters of galaxies that we see today. CMB photons reveal to be valuable Cosmological probes, for they keep the imprint of their cosmic

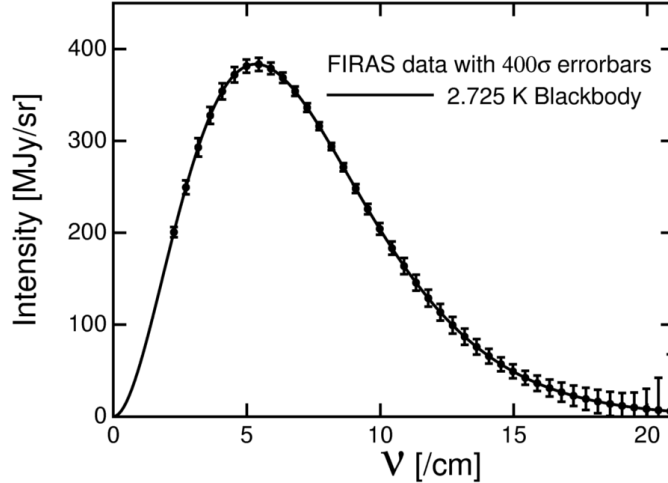


Figure 1.4: CMB black body spectrum measured by FIRAS instrument of the COBE satellite. Notice that error bars indicate 400σ . From *Ned Wright's Cosmology Tutorial - Part 1 2019*

journey all the way back to the time at which they decoupled. Details on the CMB physics is discussed in Sec. 4.

1.5 A puzzling model

The Big-Bang cosmological model as presented up until now suffers from several puzzling questions. Three of them prevail : the problem of horizon, the flatness problem, and the origin of primordial fluctuations.

The horizon problem

Using Eqs. (1.6) and (1.17), assuming a Universe dominated by a fluid characterised by a given w , we can compute the comoving distance between a distant object at redshift z and an observer, O , positioned at a much smaller redshift $z_O \ll z$,

$$\chi = \frac{2}{(3w+1)H_0} \left[(1+z_O)^{-(3w+1)/2} - (1+z)^{-(3w+1)/2} \right]. \quad (1.27)$$

Notice that for matter or radiation ($w \geq 0$) the comoving distance receives a contribution mostly from the z_O term.

From Eq. (1.27), assuming a matter-dominated Universe, $w = 0$, we can fairly estimate the comoving distance between us ($z_O = 0$) and the CMB photons LSS ($z = z_* \sim 1100$), hence $\chi_{\text{CMB}} \simeq 2/H_0$.

At time of decoupling, the Universe is already well into the matter-dominated era. At this time, the comoving horizon at time of decoupling was approximatively $\eta_* \simeq 2/H_0\sqrt{1100}$ (taking $z_O = z_*$ and $z = \infty$).

Therefore, the regions for which particles were in causal contact at the time of decoupling subtend an angle $\theta \simeq \eta_*/\chi_{\text{CMB}} \simeq$ few degrees on the CMB surface that we observe today. It means that the CMB can be divided into $\sim 40\,000$ patches that were not causally connected at the time of decoupling, but sharing the same temperature, with a difference of $\delta T/T \simeq 10^{-5}$ (Trodden et al. 2004). Understanding how the early Universe got thermalised and so much homogeneous over larger-than-causal distances is known as the horizon problem.

The flatness problem

Looking back to the metric defined in Eq. (1.3), the geometry of the Universe is allowed to adopt a global curvature, characterised by the parameter K . However, current measurement from the CMB indicates that we live in a flat Universe, with $|\Omega_{K0}| \lesssim 10^2$. This reveals to be quite problematic. Indeed, we can neglect the relatively recent contribution from dark energy, such that the second FL Eq. (1.13) can be rearranged as

$$\frac{\dot{H}}{H^2} + 1 = -\frac{(1+3w)}{2}\Omega, \quad (1.28)$$

or, combined with $\Omega \equiv \Omega_m + \Omega_r = 1 - \Omega_K$, into the form

$$\frac{d\Omega_K}{dN} = (3w+1)(1-\Omega_K)\Omega_K, \quad (1.29)$$

where $N \equiv \ln(a)$ the number of e-folds. Integrating this equation, supposing w constant, provides

$$\frac{\Omega_K(z)}{\Omega(z)} = \frac{\Omega_{K0}}{\Omega_0}(1+z)^{-(1+3w)}. \quad (1.30)$$

This equation shows that a Universe with non-zero curvature is very unstable. As it expands, any initial departure from $\Omega_K = 0$ will induce growth of the curvature density for a fluid characterised by $w > -1/3$, which is the case during matter and radiation epochs. Hence, a curvature density observed today at $|\Omega_{K0}/\Omega_0| \lesssim 10^{-2}$ requires that $|\Omega_K/\Omega|_{z_{\text{eq}}} \lesssim 10^{-5}$ at the epoch of matter-radiation equality, and $|\Omega_K/\Omega|_{z_{\text{pl}}} \lesssim 10^{-60}$ at Planck time (Trodden et al. 2004). This puzzling observation where the early Universe seems extremely fine tuned is the so-called flatness problem.

Origin of structures

The Universe that we observe today at small scales is characterised by highly inhomogeneous structures such as clusters of galaxies or cosmic voids. When matter era began, small inhomogeneities could start to grow, forming the large scale structures of today. The origin of those anisotropies of densities can be found on the CMB, reflected by the fact that photons temperature distribution shows slight inhomogeneities on the sky. However, the origin of those fluctuations is not explained by the standard FLRW model.

The cosmic inflation, a paradigm which emerged in the early 1980s, proposes to solve in an elegant way the three Big-Bang problems simultaneously. In the next section, we propose to review the main aspects of the inflationary theory.

2 Inflation

In this section, we explore the general formalism of the inflationary theory. It was motivated by the seemingly fine-tunings of the FLRW Universe introduced in Sec. 1.5.

2.1 Motivation

An accelerating expansion

One way to justify the high homogeneity between the different patches observed on the CMB is to assumed that a past causal connection existed between those regions. In other words, it amounts to demand that the comoving horizon η_* at time of photon decoupling was much larger. From Eq. (1.27), for a matter or radiation dominated Universe ($w \geq 0$), we see that most of the contribution to the comoving horizon η_* comes from late times (small redshift). Therefore, for η_* to receive contributions from early times, at some point during the early Universe, we should have had $w < -1/3$. Indeed, in that case, the factor $(3w + 1)$ in Eq. (1.27) is negative, and the z term (early time, high redshift) becomes dominant compared to the z_0 term (late time, observer redshift).

The need for a state equation with $w < -1/3$ at early times also shows up when attempting to solve the flatness problem. Indeed, from Eq. (1.30), the Universe content evolution becomes unstable only for $w > -1/3$, again, when assuming only a radiation-dominated early epochs.

Instead, if one assumes that another component, aside matter or radiation, drove the expansion rate before radiation-dominated epoch, the horizon problem can be solved. Such component should be characterised by a negative pressure, with $w < -1/3$. This is the case for a cosmological constant fluid, but Dark Energy only became dominant recently². The second Friedmann Eq. (1.13) dominated by a fluid with $w < -1/3$ requires that $\ddot{a} > 0$, that is to say, the early Universe must have underwent an accelerating expansion. Such phase is known as the cosmological inflation (Guth 1981; Linde 1982; Albrecht et al. 1982).

The sphere of causal contact at any time is defined as the comoving Hubble radius $(aH)^{-1}$. Therefore, From the Hubble-Lemaître law of Eq. (1.4), an object positioned at a distance equal to one comoving Hubble radius is receding from us at the speed of light. Requiring $\ddot{a} > 0$ is equivalent to

$$\frac{d(aH)^{-1}}{dt} = -\frac{1}{a} \left[\frac{\dot{H}}{H^2} + 1 \right] < 0. \quad (1.31)$$

Inflation e-folds

We define t_i and t_e the time at which inflation respectively started and ended. Most inflationary models assume H nearly constant during inflation, therefore $|\Omega_K(t_e)/\Omega_K(t_i)| \simeq (a_e/a_i)^{-2} = e^{-2N}$, with

$$N \equiv \int_{t_i}^{t_e} H dt = \int_{a_i}^{a_e} d \ln a \quad (1.32)$$

$$= \ln \left(\frac{a_e}{a_i} \right), \quad (1.33)$$

the number of e-folds during the inflation phase.

²Moreover, once a Universe becomes dominated by Λ , it stays dominated by a cosmological constant. Therefore, DE is not a viable solution to the Big-Bang problems.

From Sec. 1.5, the minimal length of the inflationary period that solves the flatness problem must provide $|\Omega_K(t_e)| \lesssim 10^{-60}$ at the time inflation ends, thus requiring $N \gtrsim 70$ (Peter et al. 2009).

Similarly, for inflation to solve the horizon problem, we demand that at least the largest scales observed today $\approx 1/H_0$ should be within the horizon before inflation started, $1/a_0 H_0 < 1/a_i H_i$. Equivalently,

$$\frac{H_i a_e}{H_0 a_0} \lesssim \frac{a_i}{a_e}. \quad (1.34)$$

Since, after inflation, the temperature goes as $T \propto a^{-1}$, we have $a_e/a_0 = T_0/T_e$. Therefore, replacing $a_i/a_e = e^{-N}$, we obtain

$$N \gtrsim \ln\left(\frac{T_0}{H_0}\right) + \ln\left(\frac{H_i}{T_e}\right) \simeq 67 + \ln\left(\frac{H_i}{T_e}\right). \quad (1.35)$$

The last term depends on the temperature at the end of inflation, and the Hubble parameter at the beginning of inflation. Those vary depending on the inflationary models considered. Typically, $N \gtrsim 40$. (Peter et al. 2009; Kamionkowski et al. 2016).

Horizons

Conventionally, conformal time during inflation is negative, and it is thus redefined as $\eta \rightarrow \eta - \eta_e$. Figure 1.5 provides the evolution of the Hubble radius during and after inflation era. It is observed to shrink during inflation, then starts to grow again as the Universe is dominated by radiation then by matter. Only recently, the Hubble radius began to reduce again, as Dark Energy dominates. If considering only the upper half of the diagram (no inflation), the horizon problem appears quite blatantly, as our past light cone seems to intersect opposite regions of the CMB separated by distances much larger than the Hubble radius at those times. Those regions appear never to have been in causal contact before reheating, since their respective light-cone do not overlap. The introduction of the inflationary phase solves this problem, and two distant patches observed on the CMB are allowed to have been in causal contact before the beginning of the inflation era.

2.2 Inflaton field

Action

The most popular and simplest mechanism to explain the inflation phase consists in considering a scalar field, the ‘inflaton’, whose vacuum energy produces negative pressure. The action of a scalar field ϕ evolving in a potential $V(\phi)$ is given by

$$S_\phi = \int d^4x \mathcal{L} \sqrt{-g}, \quad \mathcal{L} = \left(-\frac{1}{2} \partial^\mu \phi \partial_\mu \phi - V(\phi) \right), \quad (1.36)$$

with g the determinant of the metric. The stress-energy tensor is obtained when varying the action with respect to the metric,

$$T_{\mu\nu} = \frac{2}{\sqrt{-g}} \frac{\delta(\sqrt{-g} \mathcal{L})}{\delta g_{\mu\nu}} \quad (1.37)$$

$$= \partial_\mu \phi \partial_\nu \phi - g_{\mu\nu} \left(\frac{1}{2} \partial_\alpha \phi \partial^\alpha \phi + V(\phi) \right). \quad (1.38)$$

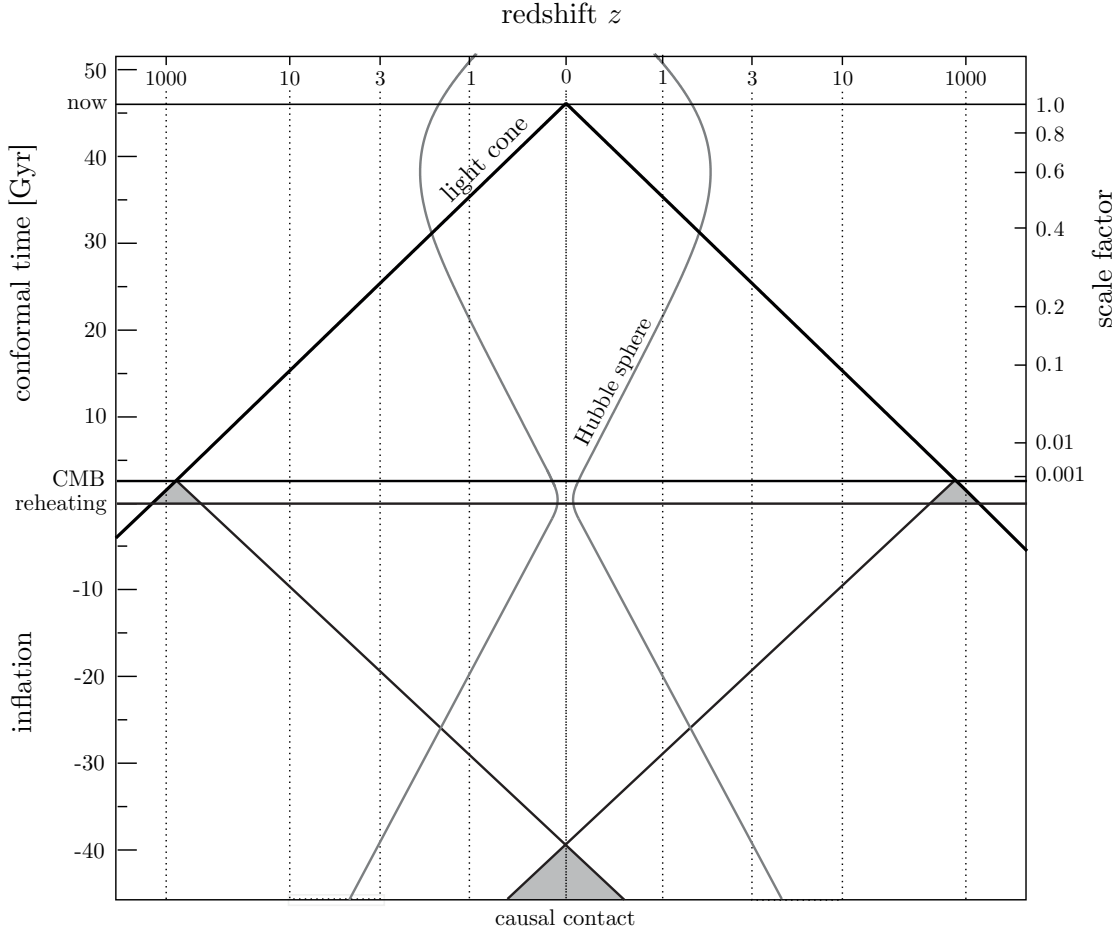


Figure 1.5: Horizons evolution during and after inflation. Vertical axis accounts for the conformal time η (left) or the scale factor a (right), while the horizontal axis is for space distances from us (in redshift z today). Our light cone represents all the sources from which we are receiving light now. The CMB surface (horizontal line) is seen at redshift $z \approx 1100$. Note that, by definition, the CMB surface should stop when intersecting our light cone. Opposite regions of the CMB on the sky have respective light cones intersecting in the past, allowing a causal contact, at the beginning of inflation. In the future, our light cone and the Hubble radius will converge to the same size, as an effect of dark matter domination. From Baumann et al. 2014.

Assuming the field is mostly spatially homogeneous, $\phi = \phi(t)$, the density and pressure of the field are respectively given by the time and the spatial components of the stress-energy tensor,

$$\rho_\phi = \frac{\dot{\phi}^2}{2} + V(\phi), \quad p_\phi = \frac{\dot{\phi}^2}{2} - V(\phi), \quad (1.39)$$

with $\dot{\phi} \equiv \partial_t \phi$. A negative pressure, i.e. the condition for inflation to occur, $w = p/\rho < -1/3$, translates to $\dot{\phi}^2 < V(\phi)$. The field must therefore have higher potential than kinetic energy.

For the inflaton, the matter conservation Eq. (1.16) translates into the Klein–Gordon equation³

$$\ddot{\phi} + 3H\dot{\phi} + \frac{dV(\phi)}{d\phi} = 0. \quad (1.40)$$

³Using $\dot{V} = V_{,\phi}\dot{\phi}$.

Slow-roll inflation

If $\dot{\phi}^2 \ll V(\phi)$, the inflaton has a nearly constant energy density, and is said to be in the slow-roll regime. In that case, the pressure is proportional to the field density and to the inflaton potential, $p \approx -\rho \approx -V(\phi)$, therefore $w = -1$. From the first FL Eq. (1.12), the Hubble parameter is therefore nearly constant. Since $da/a = Hdt$, the expansion is quasi-exponential, with $a(t) = a_e e^{H(t-t_e)}$. We also see that the conformal time from Eq. (1.8) is equal to the Hubble radius, $\eta \simeq -(aH)^{-1}$.

Today, slow-roll single-field inflation has becoming the most popular among minimal inflationary models. Other models consider various potential shapes, or even multiple coupled scalar fields (Martin et al. 2013). A simple example is shown in Fig. 1.6. At the end of inflation, the energy of the inflaton gets transferred into Standard Model particles⁴, a period known as reheating.

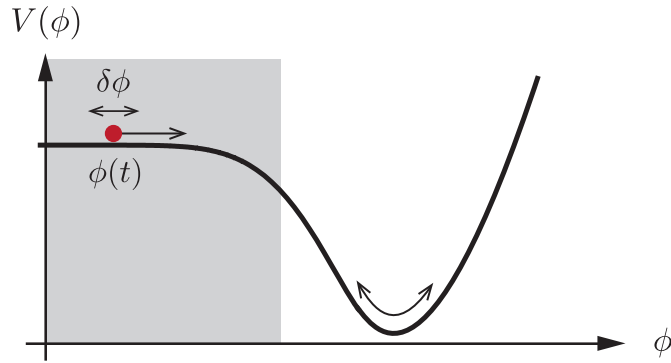


Figure 1.6: Example of slow-roll inflaton potential. The shaded region indicates where the condition for the field $\phi(t)$ to roll slowly is met. At the same time, the inflaton experiences spatial fluctuations $\delta\phi(x, t)$. From Baumann et al. 2014.

Parameters

We generally define the slow-roll parameters,

$$\epsilon_V \equiv -\frac{\dot{H}}{H^2} < 1, \quad (1.41)$$

$$\eta_V \equiv -\frac{1}{H} \frac{\ddot{\phi}}{\dot{\phi}} < 1, \quad (1.42)$$

which follows from the condition for inflation to occur, defined in Eq. (1.31).

In the slow-roll regime, $\epsilon_V \ll 1$ and $\eta_V \ll 1$. In that case, from the Friedman and Klein–Gordon Eqs. (1.12) and (1.40), we have

$$\epsilon_V = \frac{\dot{\phi}^2}{2M_{\text{pl}}^2 H^2} \quad (1.43)$$

$$= \frac{M_{\text{pl}}^2}{2} \left(\frac{V_{,\phi}(\phi)}{V(\phi)} \right)^2, \quad (1.44)$$

⁴... and possibility beyond the SM.

with $V_{,\phi}(\phi) \equiv \partial_\phi V(\phi) \equiv V'(\phi)$. And

$$\eta_V = M_{\text{pl}}^2 \left(\frac{V_{,\phi\phi}(\phi)}{V(\phi)} \right). \quad (1.45)$$

with $V_{,\phi\phi}(\phi) \equiv \partial_\phi^2 V(\phi) \equiv V''(\phi)$. The slow-roll parameters therefore characterise the shape of the scalar field potential. The smaller the parameters, the less the potential shows variations.

3 Inhomogeneous Universe

Understanding the origin of the primordial matter density fluctuations can be quite technical. We highlight the main ingredients to understand their nature. To achieve this, we consider that the Universe is not strictly homogeneous and isotropic. Such deviation from homogeneity and isotropy is understood by modelling a perturbed FLRW Universe.

3.1 Perturbed FLRW Universe

Perturbed quantities

To understand how inhomogeneities evolve in a perturbed FLRW Universe, we have to consider perturbations of the metric, the inflaton field, the stress-energy tensor of the cosmological fluids, and to the distribution functions of those fluids.

- A generic metric perturbation reads, $g^{\mu\nu} = \bar{g}^{\mu\nu} + \delta g^{\mu\nu}$, with $\delta g^{\mu\nu}$ characterising small first order perturbations around the FLRW background metric $\bar{g}^{\mu\nu}$. During inflation, the scale of the perturbations to the metric grow from quantum to macroscopic scales.
- Similarly, the perturbed energy-impulsion tensor reads $T^{\mu\nu} = \bar{T}^{\mu\nu} + \delta T^{\mu\nu}$. Solving the Einstein equations helps to describe how the perturbations to the fluids (inflaton, matter, or radiation) couple to the metric perturbations.
- The quantum spatial perturbations of the inflaton field are assumed to be Gaussian, and read $\phi(\vec{x}, t) = \bar{\phi}(t) + \delta\phi(\vec{x}, t)$, with $\bar{\phi}(t)$ the spatially homogeneous background inflaton field described in Sec. 2.2. Since part of the inflaton and metric fluctuations are coupled, the inflaton era allows us to characterise the initial conditions of primordial gravitational fluctuations of the Universe.
- Finally, the perturbations of the fluid distributions $f_{\text{BE/FD}}$ defined in Eq. (1.23) are accounted by expanding at first order the temperature field $T = \bar{T}(t) + \delta T(t, \vec{x}, \hat{n})$, with \vec{x} accounting for spatial inhomogeneous distributions of the photons temperature, and \hat{n} the photons direction of propagation accounting for their anisotropic distribution. A systematic approach to describe the fluid evolution is to solve the Boltzmann equation,

$$\frac{df}{dt} = C[f], \quad (1.46)$$

which quantifies how the phase space density of the fluids evolves with time, depending on all particle collision terms encapsulated in the $C[f]$ function.

Characterising the perturbations to the fluid distributions allows us to understand how inhomogeneities in the primordial plasma evolve and interact. It also connects the temperature anisotropies observed on the CMB to the primordial plasma density fluctuations. More generally, it helps to constrain the parameters of the standard cosmological model of the Universe as it will be described in Sec. 4.6.

Perturbation decomposition

From Helmholtz's theorem, a vector field can be decomposed into the sum of an irrotational part (written as the divergence of a scalar field) and rotational part. Similar decomposition holds for rank-two tensors. Therefore, the perturbations can be decomposed into three types : scalar, vector, and tensor perturbations. This reveals to be very useful, as at first order, those types of perturbation are decoupled from each other, allowing to study them separately. One must then solve the Einstein-Boltzmann equation in order to characterise the perturbations in the matter

field. It is generally simplest to proceed in Fourier space, where any function $g(\vec{x}, \eta)$ transforms as

$$g(\vec{x}, \eta) = \int \frac{d^3k}{(2\pi)^3} e^{i\vec{k}\cdot\vec{x}} g(\vec{k}, \eta), \quad (1.47)$$

with η the conformal time defined in Eq. (1.8), and \vec{k} the comoving wavenumber, which is the conjugate of the spatial coordinates \vec{x} , and which can be related to the physical wavenumber as $k_i = ak_i^{\text{phys}}$. In that case, the spatial derivative transforms as $\partial/\partial x^i \rightarrow k_i$. Because perturbations are assumed to be small, each Fourier mode can be considered to evolve independently.

3.2 Perturbations generated during inflation

The evolution of the metric and inflaton field set up the primordial fluctuations which will source the anisotropies of matter and radiation latter observed on the CMB. Those are statistically described by the variance of the fluctuations at each scale k (Dodelson 2003). We will discuss only scalar and tensor perturbations, since vector (vorticity) modes production is negligible, for they decay with the Universe expansion.

Tensor perturbations

The tensor perturbations to the background FLRW metric can be characterised as,

$$\delta g^{ij} = a^2 \begin{pmatrix} h_+ & h_\times & 0 \\ h_\times & h_+ & 0 \\ 0 & 0 & 0 \end{pmatrix}, \quad (1.48)$$

also known as gravitational waves. The perturbation functions h_+ and h_\times are assumed to be small, and represent the two polarization states of the wave. Indeed, solving the Einstein equation for the tensor part of the perturbed metric translates into the wave equation for both functions,

$$\frac{d^2 h_\alpha}{d\eta^2} + 2\frac{1}{a} \frac{da}{d\eta} \frac{dh_\alpha}{d\eta} + k^2 h_\alpha = 0, \quad (1.49)$$

with $\alpha = +, \times$. The magnitude of the wave-vector is defined as $k \equiv \sqrt{k^i k^i}$. Defining the field $\tilde{h}_\alpha \equiv ah_\alpha M_{\text{pl}}/\sqrt{2}$ which has the dimension of mass, the Eq. (1.49) becomes

$$\frac{1}{a} \left[\frac{d^2 \tilde{h}_\alpha}{d\eta^2} + \left(k^2 - \frac{1}{a} \frac{d^2 a}{d\eta^2} \right) \tilde{h}_\alpha \right] = 0. \quad (1.50)$$

The solution for this wave equation is simply that of a harmonic oscillator. The perturbation functions can be quantum-quantised, and seen as fields,

$$\hat{h}(\vec{k}, \eta) = v(k, \eta) \hat{a}_{\vec{k}} + v^*(k, \eta) \hat{a}_{\vec{k}}^\dagger, \quad (1.51)$$

with \hat{a} the creation operator, and the annihilation operator \hat{a}^\dagger its complex conjugate. The operators coefficients therefore satisfy the equation

$$\frac{d^2 v}{d\eta^2} + \left(k^2 - \frac{1}{a} \frac{d^2 a}{d\eta^2} \right) v = 0, \quad (1.52)$$

whose solution reads⁵

$$v(\vec{k}, \eta) = \frac{1}{\sqrt{2k}} e^{-ik\eta} \left(1 - \frac{i}{k\eta} \right). \quad (1.53)$$

The variance of the perturbation fields of the metric h_α reads⁶

$$\langle \hat{h}^\dagger(\vec{k}, \eta) \hat{h}(\vec{k}', \eta) \rangle \equiv \frac{(2\pi)^3}{k^3} P_h(k) \delta^3(\vec{k} - \vec{k}'), \quad (1.54)$$

where we defined the power spectrum

$$P_h(k) \equiv \frac{2k^3}{a^2 M_{\text{pl}}^2} |v(k, \eta)|^2, \quad (1.55)$$

as proportional to the variance of the field fluctuations for each wavenumber k . The so-called tensor power spectrum corresponds to the sum of power spectrum from both polarisation states of the wave,

$$P_k^{\mathcal{T}} \equiv P_{h_+}(k) + P_{h_\times}(k), \quad (1.56)$$

$$= \frac{2k^2 H^2 \eta^2}{M_{\text{pl}}^2} \left(1 + \frac{1}{k^2 \eta^2} \right). \quad (1.57)$$

From Eqs. (1.53) and (1.57),

- for scales smaller than the horizon, $k^{-1} \ll |\eta| \simeq (Ha)^{-1}$, the tensor power spectrum reads

$$P_k^{\mathcal{T}} = \frac{2k^2 H^2 \eta^2}{M_{\text{pl}}^2}. \quad (1.58)$$

- for scales larger the horizon, $k^{-1} \gg |\eta| \simeq (Ha)^{-1}$, the oscillations freeze and the tensor power spectrum is said to be scale-invariant as it does not depend on k ,

$$P_k^{\mathcal{T}} = \frac{2H^2}{M_{\text{pl}}^2}. \quad (1.59)$$

Therefore, at the end of inflation, since the horizon scale $|\eta|$ is small, most modes are outside the horizon, and most tensor fluctuations follow distribution from this power-spectrum.

Scalar perturbations

Similarly, one can work out the perturbations for the inflaton scalar field ϕ (Dodelson 2003).

- When the wavelength of the perturbations are smaller than the horizon scale, one can show that we can neglect scalar perturbations to the metric, and thus consider a (smooth) FLRW metric. In that case, solving for the energy-momentum conservation $T_{\nu;\mu}^\mu$ defined in Eq. (1.38) provides the following wave equation,

$$\delta\ddot{\phi} + 2aH\dot{\delta\phi} + k^2\delta\phi, \quad (1.60)$$

which is of same form as Eq. (1.49) for the tensor perturbation discussed in Sec. 3.2. The power spectrum of the scalar field perturbation is therefore similar (modulo the factor 2 for the two wave polarization states),

$$P_k^{\delta\phi} = \frac{k^2 H^2 \eta^2}{2} \left(1 + \frac{1}{k^2 \eta^2} \right). \quad (1.61)$$

⁵Since during inflation, H is supposed to be constant, we have $\eta \equiv \int_{a_e}^a da/Ha^2 \simeq -(aH)^{-1}$, hence, $\ddot{a}/a \simeq 2\eta^2$ in Eq. (1.52)

⁶Using the operators properties $[\hat{a}_{\vec{k}}, \hat{a}_{\vec{k}'}^\dagger] = \delta_{\vec{k}\vec{k}'}$, and $[\hat{a}_{\vec{k}}, \hat{a}_{\vec{k}}] = 0$.

- On the other hand, when the modes are larger than the horizon scale, the perturbations to the scalar field couple to the scalar perturbations of the metric. We define⁷ the latter as $\delta g_{00} = -2\Psi(\vec{x}, t)$ and $\delta g_{ij} = 2\Phi(\vec{x}, t)$, with Ψ and Φ the gravitational potentials. For⁸ $\Phi = -\Psi$, when modes are crossing the horizon, $k^{-1} = \eta$, one can show that the gravitational potentials are related to the inflaton perturbations after inflation ends,

$$\Psi|_{k^{-1} \geq |\eta|} = \frac{2}{3} aH \frac{\delta\phi}{\dot{\phi}} \Big|_{k^{-1} = \eta}. \quad (1.62)$$

The power spectrum of the gravitational potentials, the scalar power spectrum, becomes

$$P_k^{\mathcal{S}} = \frac{4}{9} \left(\frac{H}{\dot{\phi}} \right)^2 P_k^{\delta\phi} \Big|_{k^{-1} = \eta} \quad (1.63)$$

$$= \frac{2}{9} \frac{H^2}{\epsilon_V M_{\text{pl}}^2}, \quad (1.64)$$

where the second equality holds from the relation of Eq. (1.44).

Power spectra and inflation energy

Since $\epsilon_V \ll 1$ in the slow-roll regime, comparing Eqs. (1.59) and (1.64), the scalar modes are expected to be larger than the tensor modes.

When inflation ends, the wavelength of the quantum fluctuations of the inflaton field have been stretched to macroscopic scales. Because most of the modes are outside the horizon, we expect the power-spectra to be almost frozen. The scale dependence of the spectrum can be parametrised by the so-called scalar and tensor spectral indices n_s and n_t ,

$$P_k^{\mathcal{S}} = A_S k^{n_s - 1}, \quad \text{and} \quad P_k^{\mathcal{T}} = A_T k^{n_t}, \quad (1.65)$$

with A_S and A_T the amplitudes of the scalar and tensor power spectra. Their respective spectral index equal 1 and 0 for scale-invariant spectrum. We also define the running of the spectral indexes $dn/d \ln k$.

We define the tensor-to-scalar ratio parameter as the ratio of the power spectrum amplitudes,

$$r_{k_*} \equiv \frac{P_{k_*}^{\mathcal{T}}}{P_{k_*}^{\mathcal{S}}} \sim \epsilon_V. \quad (1.66)$$

where k_* is defined as the pivot scale (in $[\text{Mpc}^{-1}]$). The value of the ratio depends on the slow-roll parameter ϵ_V , therefore on the energy scale at which inflation occurred, $V^{1/4} \sim (r/0.01)^{1/4} \times 10^{16} \text{GeV}$. Therefore, for a tensor-t-scalar ratio of the order of $r \sim 10^{-2}$, the study of inflation physics allows us to probe energy scales way beyond levels of current particles accelerators.

We can write

$$\frac{d \ln P_k^{\mathcal{S}}}{d \ln k} = n_s - 1, \quad \frac{d \ln P_k^{\mathcal{T}}}{d \ln k} = n_t. \quad (1.67)$$

From Eqs. (1.59) and (1.64), at horizon crossing $k^{-1} = \eta$, we have $n_t = -2\epsilon_V$ and $n_s - 1 = 4\epsilon_V - 2\eta_V$. Notice that one can always define additional inflation parameters based on higher

⁷We use the so-called conformal Newtonian Gauge

⁸Neglecting neutrinos contribution.

order derivatives of the potential which contribute for example to the running of the spectral indexes $dn/d \ln k$.

Measuring the tensor-to-scalar ratio r would therefore allow us to constrain the potentials shape of the inflaton field. More generally, it would permit to discriminate among the many inflationary models currently on the market. One important prediction is that the scalar index should be less than unity, which has been confirmed by the *Planck* satellite measurement, yielding $n_s = 0.9667 \pm 0.0040$ ([Planck 2015 Results. XIII.](#)).

3.3 Matter and radiation inhomogeneities

The scalar and tensor power spectra computed in Sec. 3.2 allow us to describe the initial perturbations at the end of inflation. Because the inflation field is slightly spatially inhomogeneous, the time at which inflation ends will vary between each location. As a result, regions for which the inflation period ends early will undergo a slightly longer expansion phase after inflation, which then translates into lower density of matter. Those density anisotropies then eventually grow into larger structures under the influence of gravity.

After the epoch of reheating, the hot Big-Bang starts. In the tight coupling limit, photons and baryons act as a fluid, for the Coulomb and Compton interactions keep the photons, electrons, and protons coupled. The photons provide pressure to the fluid, while baryons provide inertia. The latter tend to fall into gravitational potentials, which are mainly driven by the Dark Matter densities. This balance between the outward pressure and the gravitational collapse translates into acoustic oscillations in the primordial plasma. As soon as modes re-enter into the causal horizon, such baryon-photons oscillation can start.

One strong prediction from inflation is the production of Gaussian primordial fluctuations which are adiabatic (as opposed to isocurvature). It means that energy densities were initially uniquely generated by inflation, and therefore spatially in phase. CMB measurements showed that fluctuations are both adiabatic and Gaussian, thus favouring the inflationary scenario ([Planck 2015 Results. XIII.](#)).

Knowing the initial conditions of the perturbations, we can compute their post-inflation evolution with time. The evolution of the power-spectra is propagated using the so-called transfer function, which depends on the evolution and energy content of the Universe. At the time of decoupling, the oscillations stop as photons are depleted. The photons therefore carry the imprint of those oscillations, as if their phase were frozen in time. Those are observed as anisotropies of temperatures on the CMB. In the next section, we describe qualitatively the main ingredients which characterise them.

4 The Cosmic Microwave Background radiation

We first describe how the anisotropies on the CMB can be related to the primordial fluctuations set-up during inflation, using the so-called CMB power spectrum. The different physical processes that shape the CMB power spectrum are described qualitatively. We then focus on the CMB photons polarization, and how their study could help us to constrain inflationary physics.

4.1 Temperature power spectrum

The statistical distribution of the CMB anisotropies in temperature and polarisation depend on the physical processes that sourced them. In order to study those anisotropies in a statistical manner, as a first step, the temperature inhomogeneity field is conveniently Fourier-decomposed into spherical harmonics,

$$\frac{\delta T(t, \vec{x}, \hat{n})}{\bar{T}(t)} = \sum_{\ell=1}^{\infty} \sum_{m=-\ell}^{m=\ell} a_{\ell m}(t, \vec{x}, \hat{n}) Y_{\ell m}(\hat{n}), \quad (1.68)$$

with $Y_{\ell m}(\hat{n})$ the set of spherical harmonics functions. The multipole ℓ is proportional to the inverse of the angular scale $\ell \propto \theta^{-1}$. For each ℓ , there is $2\ell + 1$ indices m , accounting for the multiple spatial orientations of the spherical modes. We can drop the spatial and time dependency, setting $\vec{x} = \vec{x}_0$ and $t = t_0$, our coordinates today, such that temperature anisotropies only depend on the direction of observation,⁹ \hat{n} . We draw some of the first spherical harmonic functions and their 2D mollview projections in Figure 1.7.

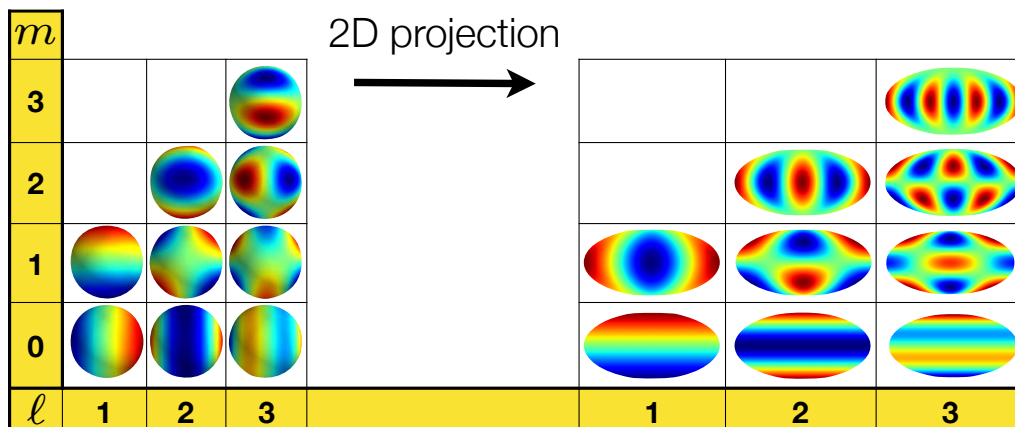


Figure 1.7: Some spherical harmonic functions $Y_{\ell m}$ on the sphere (left), and their 2D mollview projection (right) for $\ell = 1, 2, 3$ and $m = 0, 1, 2, 3$.

The harmonic coefficients $a_{\ell m}$ are simply another way to measure the CMB temperature anisotropies. Indeed, from the orthogonality property of the spherical harmonics,

$$\int d\Omega Y_{\ell m}(\hat{n}) Y_{\ell' m'}^*(\hat{n}) = \delta_{\ell\ell'} \delta_{mm'}, \quad (1.69)$$

⁹This assumption is justified, for the time and distance required to travel in order to observe variations of the CMB field are respectively of the order of the Hubble time and the Hubble distance, both much larger than our scale.

we have

$$a_{\ell m} = \int d\Omega Y_{\ell m}^*(\hat{n}) \frac{\delta T(\hat{n})}{\bar{T}}. \quad (1.70)$$

Cosmology models do not predict the position but rather the statistical distribution of the anisotropy. Hence, we define the variance of the harmonic coefficients as the temperature power spectrum,

$$\langle a_{\ell m} a_{\ell' m'}^* \rangle \equiv C_\ell \delta_{\ell\ell'} \delta_{mm'}. \quad (1.71)$$

The latter quantifies the amplitude of the anisotropies, and it can be related to the power spectra set up during inflation in Sec. 3.2. We define the scalar and tensor contributions to the temperature spectrum,

$$C_\ell^S = \int dk P_k^S |\Delta_\ell^S(k, \eta_0)|^2, \quad (1.72a)$$

$$C_\ell^T = \int dk P_k^T |\Delta_\ell^T(k, \eta_0)|^2. \quad (1.72b)$$

The transfer functions, $\Delta_\ell(k, \eta)$, encode the physical evolution of the temperature inhomogeneities, and they geometrically project the Fourier wavenumber k on the spherical modes ℓ . Fig. 1.8 is a representation of how a plane-wave perturbation with wavenumber k can source the anisotropies seen on the CMB surface. As pointed out in Sec. 3.2, because tensor perturbations do not couple to gravitational perturbations, we expect $P_k^T \ll P_k^S$, and therefore $C_\ell^T \ll C_\ell^S$.

Public Boltzmann codes are available to compute the CMB power spectra, such as CMBFAST (Seljak et al. 1996), CAMB (Lewis et al. 2000), or CLASS (Blas et al. 2011).

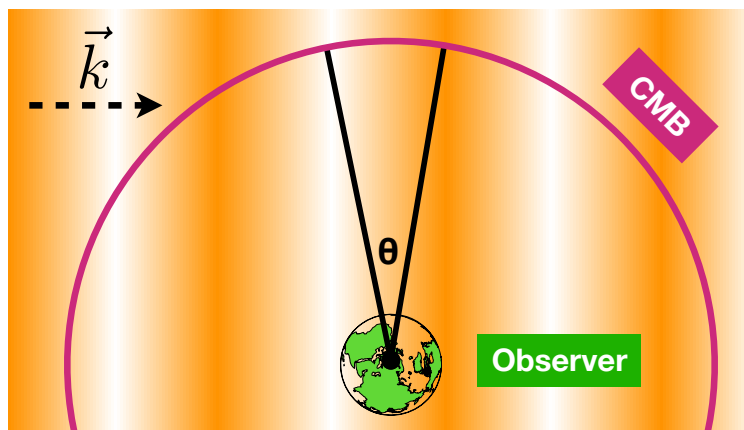


Figure 1.8: Visualization of a plane-wave density perturbation with wavenumber k propagating horizontally, and the CMB surface as seen from a central observer. White regions represent cold spots on the CMB, while deeper regions represent hot spots.

4.2 Temperature anisotropies

Several effects driving the shape of the CMB temperature spectrum can be identified, depending on the scale and time at which we consider the photons interactions.

Primary anisotropies

We identify four main contributions to the CMB temperature power spectrum occurring at the time of decoupling or before. Those are shown in Fig. 1.9 (Challinor et al. 2009).

- Acoustic perturbations : when photons decouple, they carry with them the imprint of the baryon acoustic oscillations. Those translate into harmonic series of peaks on the CMB temperature power spectrum. The first peak corresponds to the mode that just entered into the horizon, completed a quarter of a period, and reached maximal compression. The associated multipole, $\ell \approx 100$, therefore corresponds to the horizon scale at the time of decoupling, $\theta \approx 1^\circ$. The remaining odd (even) peak correspond to modes that reached maximal (minimal) compression at the time of decoupling. Because baryon inertia tends to decrease the oscillations rebound, the even peak amplitude are observed to be smaller than odd ones.
- Silk damping : the photons decoupling do not occur instantaneously. As a result, the LSS has a thickness. Because of the photons random walk, the multiple interactions tend to erase the information that they carry, which results in a damping of the acoustic peak for scales smaller than the LSS thickness.
- Doppler effect : due to the bulk velocity of the electrons in the primordial plasma, the scattered CMB photons experience a Doppler shift which manifests itself as oscillations that are out of phase with the acoustic oscillations. The Doppler shift is minimal when the plasma compressions or depletions reach their extrema. For scales smaller than the LSS width, this effect tends to cancel, because photons undergo the inverse Doppler shift when they enter into densities than when they come out of the perturbation.
- Sachs-Wolfe (SW) effect : The perturbations with scales larger than the causal horizon ($\ell \leq 100$) are only sourced by gravitational potentials arising from the initial conditions set-up during inflation. Photons coming from over-dense regions in the plasma are hotter, but must climb up a gravitational well which makes them lose energy, hence ultimately appearing colder to us. The converse is also true for under-dense regions. Because the scalar power spectrum is nearly scale-invariant for those modes, the corresponding $\ell(\ell + 1)C_\ell$ is almost a plateau.

Secondary anisotropies

We describe the main physical effects occurring after photons decoupling.

- Integrated Sachs-Wolfe (ISW) effect : similar to the SW effect, the integrated SW describes late-time red or blue shifting underwent by photons as they pass through gravitational potentials undergoing temporal variations. Those potentials decay are caused by recent structures formations. The ISW effect affects the temperature spectrum at large scales.

The recent dominance of the Dark Energy at low redshift produces this effect as it makes the gravitational potentials to evolve (which is not the case for a matter-dominated Universe). This contribution at linear order to the power-spectrum is referred to as late-time integrated Sachs-Wolfe effect.

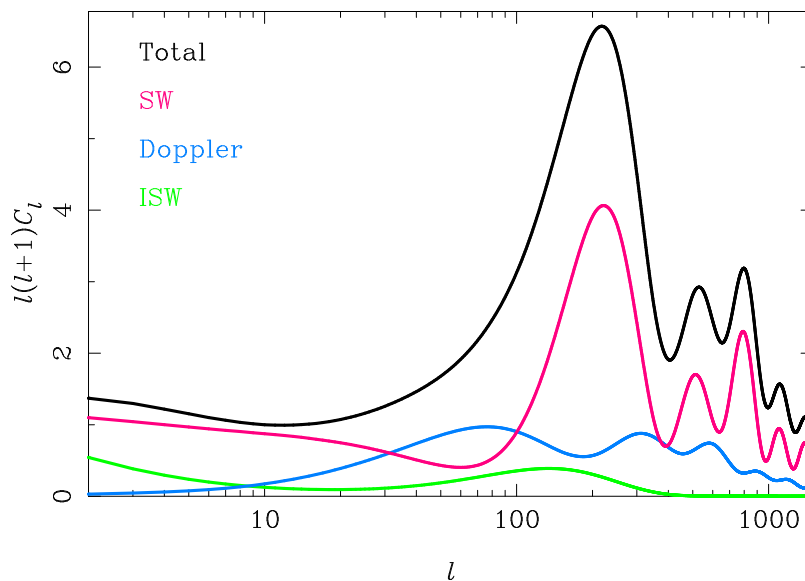


Figure 1.9: Dominant physical effects that contribute to the CMB temperature power spectrum : Sachs-Wolfe, and Doppler effects. From Challinor et al. 2009.

- Rees-Sciama (RS) effect: the Integrated Sachs-Wolfe effect at non-linear order is referred to as the Rees-Sciama effect. It accounts for the collapse of structures such as clusters, and the growth of voids, in an expanding Universe. It therefore mainly affects smaller scales of the spectrum than the ISW.
- Lensing : weak-gravitational lensing arises from the cumulative effect of large-scale structures as photons travel from the LSS to us. It distorts the image of the CMB, smooths the acoustic peaks of the CMB power spectrum, transfers large-scale power to small scales, and introduces non-Gaussian signatures to the CMB anisotropies.
- Sunyaev-Zel'dovich (SZ) : the CMB photons can be up-scattered from inverse Compton diffusion with electrons from hot and ionized gas present in galaxy clusters and filaments, and it is referred to as the thermal Sunyaev-Zel'dovich (tSZ). When clusters are moving with respect to the CMB frame, the photons can experience an additional Doppler shift, identified as kinetic SZ (kSZ) (Sunyaev et al. 1969; Sunyaev et al. 1980a; Sunyaev et al. 1980b).
- Reionization : during their journey, photons can scatter with free electrons produced during the reionization era. This results in a suppression of the power spectrum, by a factor of $e^{-\tau_{\text{re}}}$, where τ_{re} is the optical depth through reionization. Other effects occurring during or after the reionization can affect the CMB photons. For example, those can be a Doppler shift coming from free electrons if the reionization does not occur homogeneously.

4.3 Polarization anisotropies

The photons from the primordial thermal bath are not expected to have any polarization. However, Compton scattering can produce a net polarization, which can be observed on the CMB photons. We distinguish two primary anisotropies sources to the CMB polarization field : scalar and tensor.

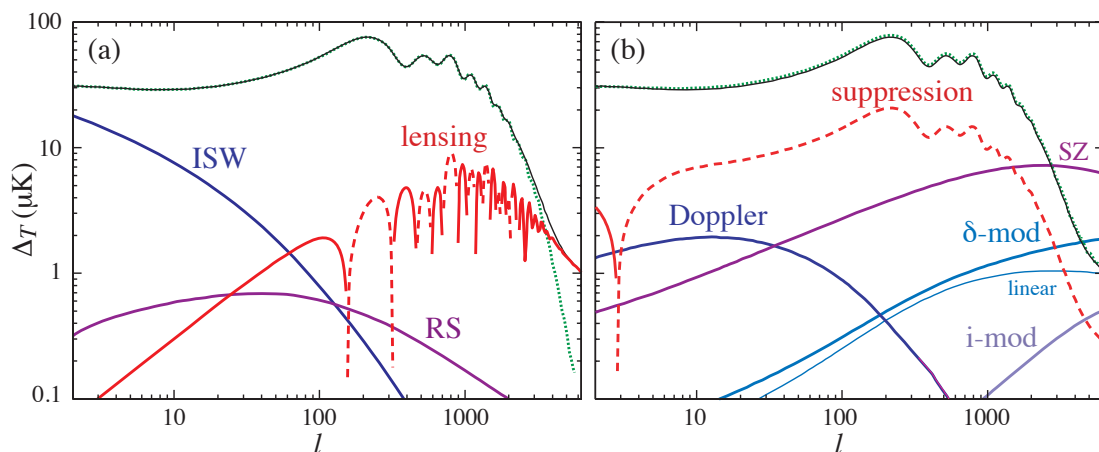


Figure 1.10: Secondary anisotropies from gravitational (left), and scattering effects (right). The total contribution (black) is compared to the primary anisotropies (green). Dashed curves show negative contributions. (b) Reionization suppression is in red. Doppler effect with linear densities is in thin cyan. Doppler effect including non-linearities is in thick cyan. The Doppler effect modulated by the patchiness of reionization (i-mod) is in purple. From Challinor et al. 2009.

Thomson induced polarization

The Thomson scattering cross-section depends on the polarization of the photons,

$$\frac{d\sigma}{d\Omega} \propto |\epsilon' \cdot \epsilon|^2, \quad (1.73)$$

with ϵ' the polarization direction of the incoming photons, and ϵ that of the scattered photons. If we consider an unpolarized beam of incoming photons perpendicular to the outgoing beam, in that case, the scattered beam will have a net linear polarization. When an electron sees a monopole or a dipole of temperature, the resulting polarization of the scattered photons coming from all directions will average to zero. However, if the electron sees a quadrupole, as pictured in Fig. 1.11, the outgoing average polarization will indeed be linear.

A quadrupole can be produced either from scalar or tensor perturbations in the baryon-photon plasma.

Scalar induced polarization

Consider Fig. 1.12, where a cold spot observed on the CMB surface corresponds to an overdensity of matter in the plasma. Electrons closer (farther) to the density will fall faster (slower) into the gravitational potential well. Similarly, electrons on an iso-latitude annulus of the density will tend to get closer and closer as they fall. If we now consider one electron, it will locally witness a quadrupole anisotropy of temperature as a result of a Doppler effect as in Fig. 1.11 : electrons going away from it will appear colder, while those getting closer will appear hotter. This results in a polarization of the CMB photons. The quadrupole pattern can be associated to the $\ell = 2, m = 0$ spherical harmonic (refer to Fig. 1.7).

We see that the mean polarization orientations (dark blue lines) from all scattered photons around the overdensity will be parallel to the gradient of the gravitational potential. Conversely, Compton scatterings occurring at the neighbourhood of a hot spot (underdensity) will produce mean polarization orientations perpendicular to the gradient of the gravitational potential.

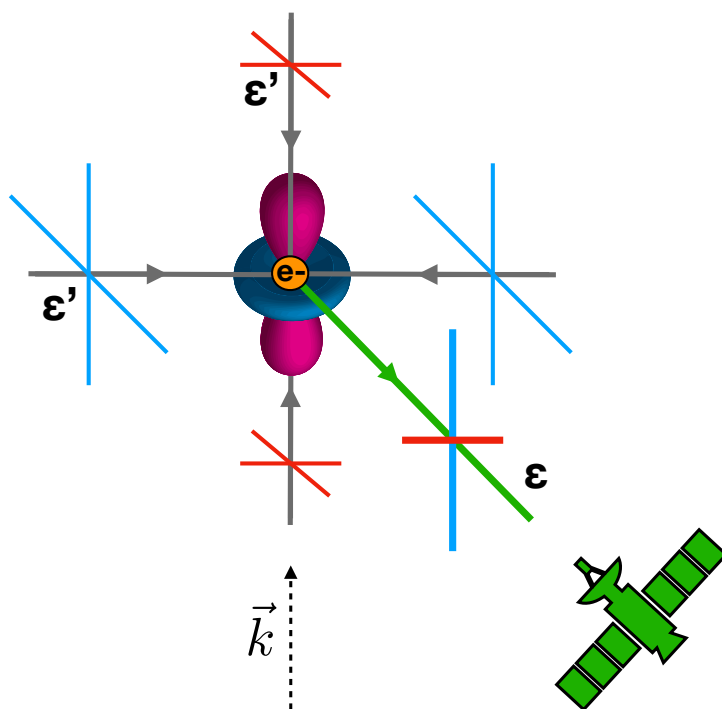


Figure 1.11: Thomson scattering for an electron seeing a temperature quadrupole produced by scalar perturbation propagating along \vec{k} . The mean polarization of the scattered photons is linear. The quadrupole pattern can be associated to the $\ell = 2, m = 0$ spherical harmonic, visualized by the lobe diagram at the centre.

Tensor induced polarization

An other source of CMB polarization can come from tensor perturbations, also described as gravitational waves (GWs). Those induce a temperature quadrupole when passing in the neighbourhood of an electron, as picture in Fig. 1.13 for one wave polarization h_+ . As it propagates, the wave distorts space in the plane perpendicular to the propagation of the perturbation \vec{k} , stretching a circle of test particles at rest into an ellipse. This induces a Doppler effect, and a temperature quadrupole is witnessed by an electron positioned at the centre. The quadrupole pattern can be associated to the $\ell = 2, m = +2$ spherical harmonic (refer to Fig. 1.7). The associated quadrupole with the h_\times polarization of the GW would be associated to $\ell = 2, m = -2$, and corresponds to a 45° rotation of the system about the direction \vec{k} .

Polarization field decomposition

The pictures for scalar and tensor perturbations inducing CMB polarization as presented above is quite simplified, for they do not account for all photons incident directions. Moreover, in order to make statistical predictions of the polarization observed on the CMB, one must also include all perturbations modes. In practice, we solve the Boltzmann equation for the polarisation field, similarly to what was presented for the temperature field in Sec. 4.1.

In practice, the measurement of the CMB polarization consists in mapping the Q and U Stokes parameters on the sky. For E_x and E_y the components of the wave electric field of a monochromatic electromagnetic wave propagating in the \hat{z} direction, the Stokes parameters are defined as (e.g. Zaldarriaga 1998; Kosowsky 1995; Kamionkowski et al. 1997; Ng et al. 1999)

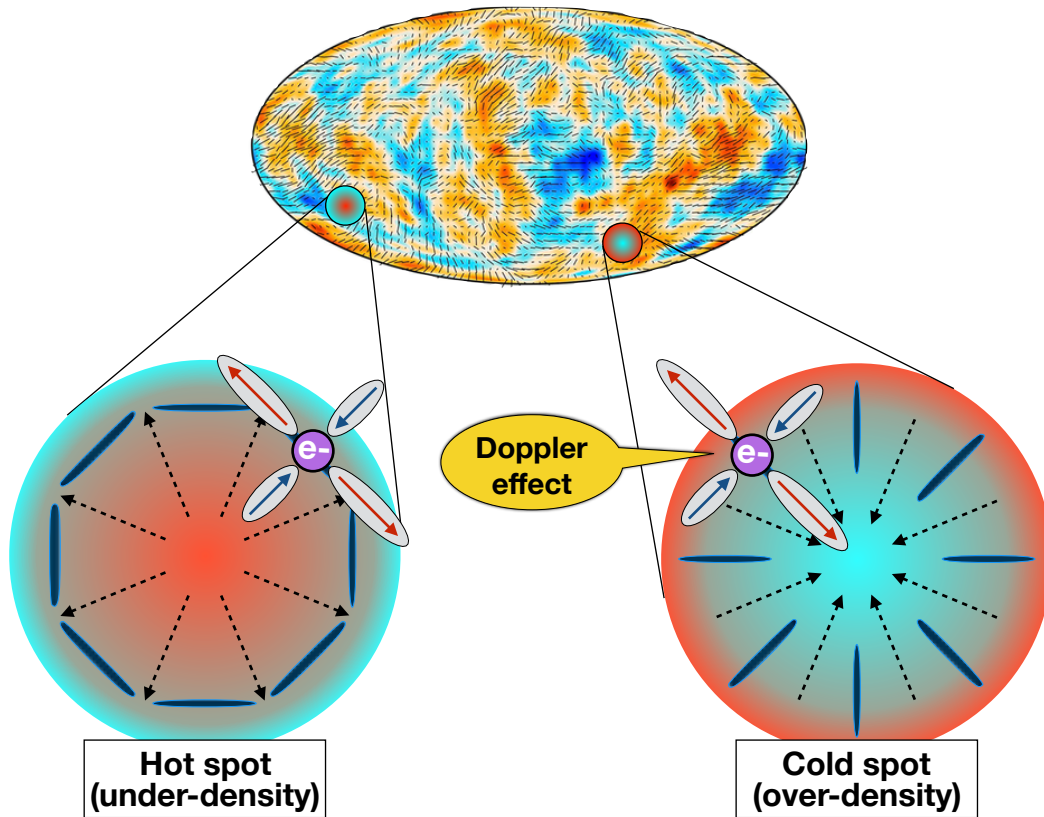


Figure 1.12: Behaviour of electrons near an under or over density of matter, seen respectively as hot and cold spots on the CMB surface. For under-densities, the electrons sees a quadrupole of temperature as a result of a Doppler effect : neighbouring electrons on the iso-latitude annulus are getting closer, while electrons parallel to the gradient of the gravitational potential well are going away from each other. The inverse phenomenon occurs for over-densities.

$$I = |E_x^2| + |E_y^2|, \quad (1.74a)$$

$$Q = |E_x^2| - |E_y^2|, \quad (1.74b)$$

$$U = E_x^* E_y + E_x E_y^* = 2\Re(E_x^* E_y), \quad (1.74c)$$

$$V = 2\Im(E_x^* E_y). \quad (1.74d)$$

The intensity of the photons is proportional to their temperature, $I \propto T$, and we generally make no distinction between both. Because Thomson scattering does not produce any circular polarisation V , we do not expect to observe any on the CMB. The polarisation state are shown in Fig. 1.14 for fully Q and U polarised photons.

Using Q and U Stokes parameters reveals to be useful to characterise the polarisation of light, for they depend on easily measurable intensities. However, in the context of CMB analysis, it is more convenient to decompose the polarisation field into a pure gradient component, and pure curl component. Those are shown in Fig. 1.15, and are respectively referred to as E-modes and B-modes, in analogy with electromagnetism.

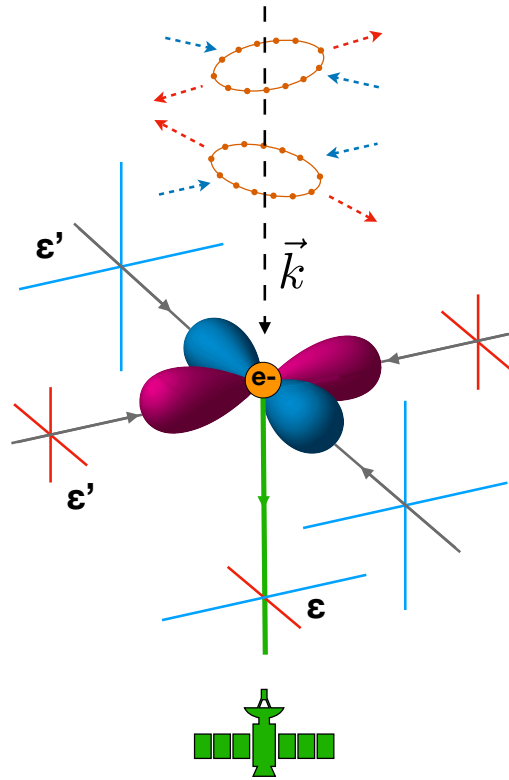


Figure 1.13: Temperature quadrupole induced by a gravitational wave with polarization h_+ , propagating along the wavevector \vec{k} . An electron positioned at the centre sees a quadrupole of temperature as a result of a Doppler effect : the GW alternatively stretches an annulus of test particles in perpendicular directions. The quadrupole pattern can be associated to the $\ell = 2, m = +2$ spherical harmonic, visualized by the lobe diagram at the centre.

A first and more practical reason to use this decomposition is that it does not depend on the orientation of the coordinate system, as the Stokes parameters does. The second and more physical motivation is that E and B modes production have distinct origins.

The scalar perturbations on the CMB can produce only two polarisation patterns on the CMB surface. Going back to Fig. 1.12, we see that only two polarisation orientations, perpendicular or parallel to the gradient of the potential, can be induced. Both are pure gradient fields, and therefore belong to the E-modes part of the CMB polarisation field.

On the other hand, a stochastic background of GWs produces both E and B modes. Since they can be sourced by GWs only, measuring B-modes on the CMB is therefore an efficient way to reveal the existence of a background of GWs in the early Universe. We discussed in Sec. 3.2 how the primordial GWs production is intimately related to the nature of inflation. Thus, characterising the CMB B-modes would be a unique probe to inflationary physics.

4.4 Polarization power spectra

The theoretical polarisation spectra can be computed using the scalar and tensor power spectra as initial conditions, and a transfer function which accounts for the evolutions of the perturbations as well as their geometrical projection on the CMB surface. We therefore define the

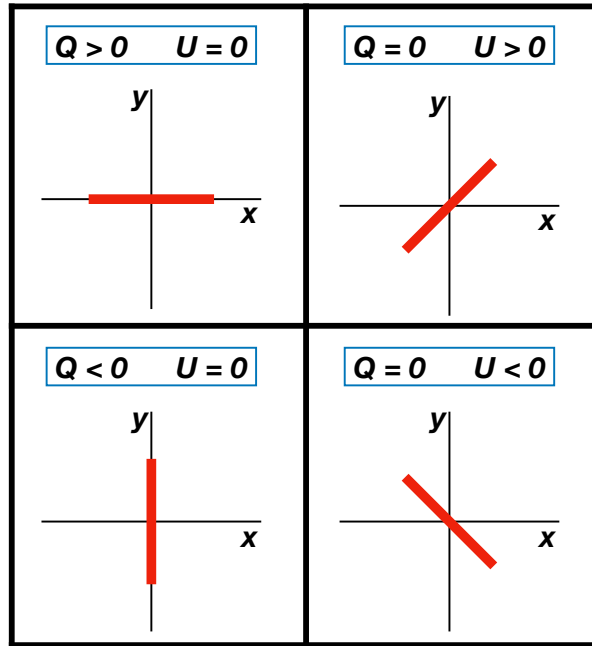


Figure 1.14: Stokes parameters for pure Q and U polarised light propagating in the \hat{z} direction.

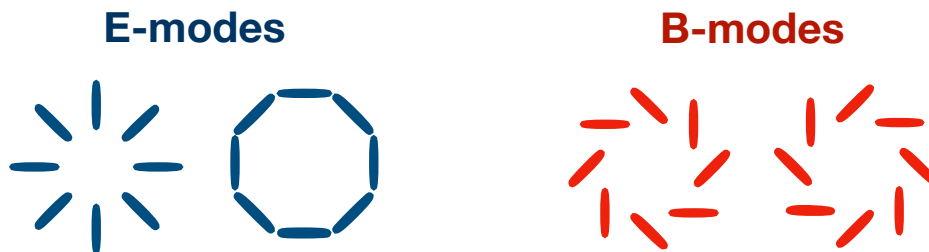


Figure 1.15: A vector field can be decomposed in a curl-free (E-modes) and a gradient-free (B-modes) patterns.

generic power spectrum,

$$C_\ell^{A,XY} = \int dk P_k^A \Delta_\ell^{A,X} \Delta_\ell^{A,Y}, \quad (1.75)$$

with P_k^A the usual matter power spectrum, and $\Delta_\ell^{A,X}$ the transfer function. The spectrum is sourced by \mathcal{A} -type perturbations, with $\mathcal{A} = \mathcal{S}$ for scalar perturbations, and $\mathcal{A} = \mathcal{T}$ for tensor perturbations. The CMB power spectrum quantifies the correlation between modes X and Y , with $X, Y = \{T, E, B\}$ respectively for temperature, E modes, and B modes.

The polarisation power spectra are computed using spin spherical harmonic functions, which are detailed in Sec. 2 of chapter 3.

We therefore list a total of four CMB power-spectra produced by the early Universe, C_ℓ^{TT} , C_ℓ^{EE} , C_ℓ^{BB} , and C_ℓ^{TE} , shown in Fig. 1.16. The lensing B-modes contribution will be introduced in Sec. 4.5. We expect the scalar EE spectrum to have an amplitude proportional but out of phase with the scalar temperature spectrum TT . Indeed, the latter's peaks correspond to each

oscillation rebound, while the former is sourced by a Doppler effect, which is maximal in-between two rebounds. This correlation between the temperature inhomogeneities amplitude and that of the E-modes is encoded in the C_ℓ^{TE} spectrum. The remaining cross-correlation spectra, C_ℓ^{EB} and C_ℓ^{TB} , are predicted to be null.

In chapter 3, we characterise and compares methods to estimate CMB power spectra, in the context of polarization and especially B-modes measurements.

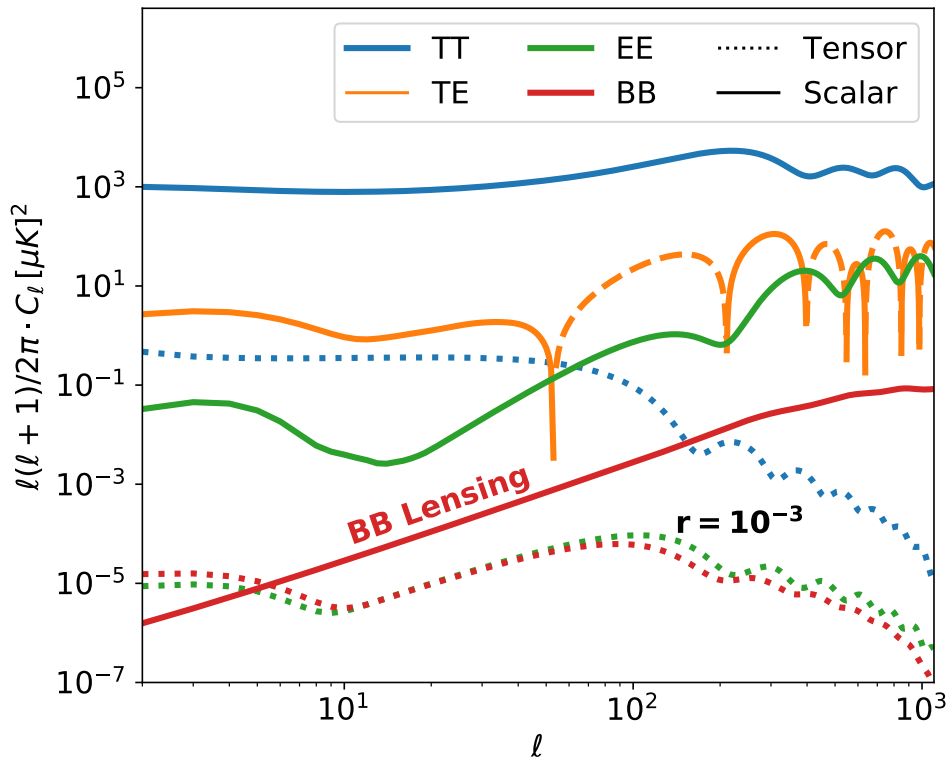


Figure 1.16: Theoretical CMB power spectra computed with CAMB (Lewis et al. 2000). Dashed TE is for the negative part of the spectrum. The tensor-to-scalar ratio is set to $r = 10^{-3}$. For polarisation spectra, the reionization bump is visible around $\ell \lesssim 10$.

4.5 Polarization secondary anisotropies

The polarization spectrum sourced by scalar fluctuations is expected to fall rapidly at large angular scales ($\ell \leq 100$), due to the lack of causality, hence the lack of coherent quadrupole at those scales. As for temperature, the CMB polarization is also sourced by secondary anisotropies. There is no polarization analogue to the Sachs-Wolfe effect, however, the polarisation signal is both sensitive to the reionization epoch, and to Silk damping effects. A fraction of the Sunyaev-Zel'dovich emission can also be polarised.

Reionization

The reionization period plays an important roll in the shape of the polarization spectra (Zaldarriaga 1997; Hu 2000; Doré et al. 2007). On one hand, because CMB photons re-scatter on free electrons, the signal they carry tend to be suppressed by a factor $e^{-\tau_{\text{re}}}$ at small scales. On the other hand, a new polarisation signal is produced by the electrons locally seeing the

CMB temperature anisotropies. Because the causal horizon is larger at the reionization epoch, the signal receives additional contribution at those scales, resulting in the so-called reionization bump at $\ell \lesssim 10$ on the polarization spectrum from Fig. 1.16.

Because of the higher sensitivity to the ionization era from the polarization compared to the temperature spectrum, the precise measurement of the former can greatly enhance the constraint on structures formations during this epoch, and helps distinguish between different reionization histories.

Lensing

Between the CMB last scattering surface and us, the photons undergo a weak lensing effect induced by their passage through the gravitational field of matter (Lewis et al. 2006). The CMB image is distorted, leading to an apparent transfer of E to B modes, and vice versa. The B-modes lensing signal amplitude is predicted to be quite high compared to the primordial B-modes, as shown on Fig. 1.16. It can therefore be seen as a source of noise compared to their primordial counterpart. A precise measurement of the primordial part of the B-modes at high ℓ 's would therefore require the subtraction of the lensing contribution. This can be achieved by measuring the lensing potential in order to remap the CMB photons to their original position.

The lensing B -modes has been detected by numerous experiments in the $100 \lesssim \ell \lesssim 1000$ range, as it will be discussed in Sec. 5.

4.6 Parameters measurements

The CMB reveals to be a powerful probe to constrain cosmological parameters. We enumerate the most standard ones, and we depict their contributions to the CMB spectra shape. Of course, this is only a qualitative description, as most of the parameters are correlated between each other (Dodelson 2003; Peter et al. 2009):

Hubble parameter today $H_0 \equiv h \text{ 100 km/s/Mpc}$

Since the horizon scale (or Hubble time) is given by $1/H_0$, the size of the fluctuations observed on the CMB directly depends on its value. Larger Hubble time would shift the CMB power spectra peaks to the smaller scales (higher ℓ 's).

Baryon density Ω_b

Boosting the baryon density increases the inertia to the photon-baryon fluid and therefore damp the acoustic rebound, resulting in the odd peaks being higher than the even peaks on the temperature power spectrum. Since it slows down the sound speed of the photon-baryon fluid, the oscillations frequency is reduced. It also shortens the mean free path of the photons, thus increasing the Silk damping at small scales.

Matter density $\Omega_m = \Omega_b + \Omega_c$

Since the total matter density is dominated by DM, it mainly changes the gravitational potentials, which affects among others the Sachs-Wolfe effect. Also, the redshift at which matter-radiation equality occurs increases with $\Omega_m h^2$.

Dark energy density Ω_Λ

Because DE plays a roll at late times, mainly large scales are affected by a change in its density, visible through the ISW effect.

Universe curvature Ω_K

The photons geodesics change weather the Universe is closed or open. The fluctuations on the CMB will respectively appear larger or smaller, and the peaks will shift toward large scales or small scales.

Neutrino density Ω_ν

In the early Universe, the neutrinos were relativistic. As the Universe expands, their momentum decrease, and neutrinos become non-relativistic. The time at which this transition occurs depends on the sum of the neutrinos masses. The effect of the neutrino mass on the CMB spectrum is minute, for they are still relativistic at the time of photons decoupling. However, at later times, they contribute to structure formation, which effect can be detected via weak lensing measurement (Lesgourgues et al. 2006). An upper limit on the sum of their mass can be obtained. Currently, $\sum m_\nu \leq 0.12 \text{ eV}$ (Planck 2018 Results. VI.).

Reionization optical depth τ_{re}

As discussed in Sec. 4.2, the epoch of reionization can be characterised by an optical depth τ_{re} . It changes the amplitude of the CMB temperature power spectra, and more generally the large scale shape of the polarization spectra, mainly observable via E-modes measurements.

Scalar and tensor amplitudes A_S and A_T , and spectral indexes n_s and n_t

The amplitudes of the scalar and tensor spectra introduced in Eq. (1.65) simply scale with the amplitude of CMB power spectra.

The value of the spectral indexes change the tilt of the primordial power spectra P_k , as well as the slope of the CMB power spectra. Increasing the number of measured multipoles therefore offers a good leverage to constrain those parameters. Current measurements of the scalar spectral indexes, $n_s = 0.9652 \pm 0.0042$, indicate that the spectrum is nearly scale invariant, but not quite, which is greatly in favour of the inflationary model (Planck 2018 Results. VI.).

The number of primordial B-modes multipoles primordial B-modes for measurements depends on the tensor signal amplitude. If $r \gtrsim 0.05$, one could hope measuring enough multipole to constrain the tilt of the B-modes primordial spectrum, n_t . If r reveals to be smaller, n_t would be challenging to measure in future experiments, for both the signal damping and the lensing B-modes erase any hope to make small scales primordial B-modes measurements (Abazajian et al. 2016).

Tensor-to-scalar ratio r

As discussed in Sec. 4.3, the detection of primordial B-modes could be a direct evidence of the existence of tensor perturbations in the metric. Since the amplitude of the primordial gravitational waves are related to the inflation energy, it would allow us to determine the inflation mechanism and its nature. If inflation is generated by a scalar field, precise measurements of

the B-modes spectrum would fix the shape of the inflaton potential.

Measuring the tensor-to-scalar ratio would have dramatic implications on high energy physics. Indeed, inflation is the only known mechanism capable of producing primordial gravitational waves in the early Universe. Detecting them would be the most direct evidence of the existence of quantum fluctuations in the gravitational field during inflation, and would provide insights into the quantum nature of gravity. The accessible energy scale would be at least 10^{11} higher than those probed by the LHC.

Best current upper limit provided by *Planck* alone is $r_{0.002} < 0.10$ when combining temperature, low- ℓ polarization, and lensing measurement. The limit is further tightened when combined with BICEP2/Keck Array BK14 data, which gives $r_{0.002} < 0.056$ ([Planck 2018 Results. X](#)). In chapter 4 we derive an upper limit on r using the *Planck* polarization maps made publicly available. The resulting constraint on $r_{0.002}$ and n_s is displayed in Fig. 1.17. In addition, some popular inflationary models are also indicated.

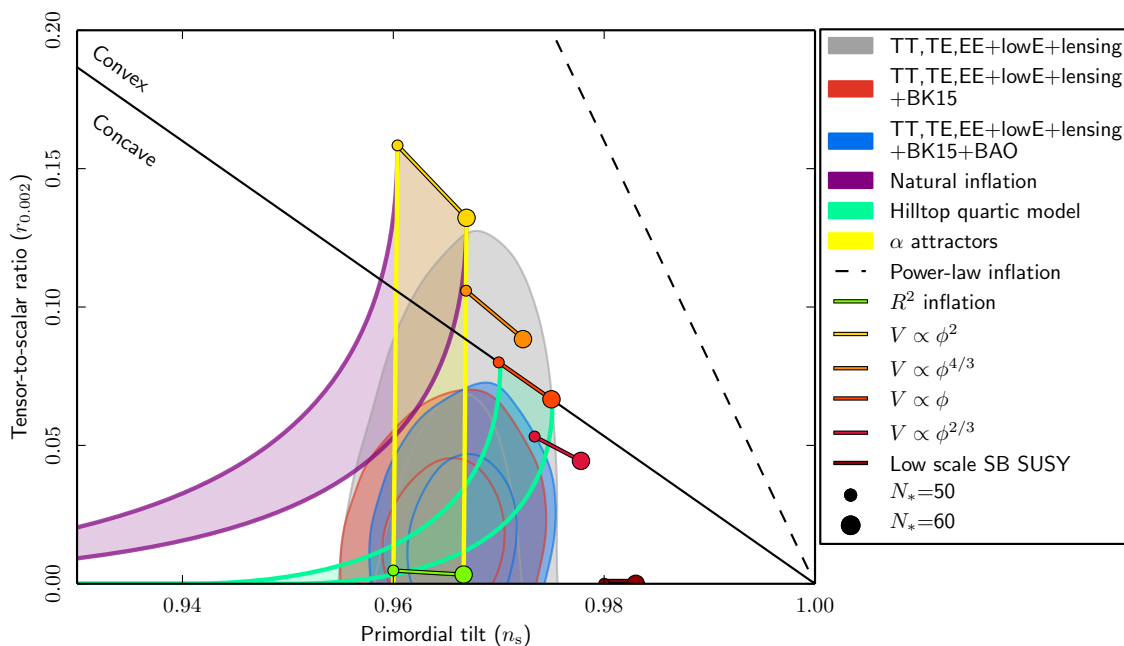


Figure 1.17: Marginalized joint 68 % and 95% confidence level regions for running index n_s and tensor-to-scalar ratio $r_{k_*=0.002}$ from *Planck* in combination with other data sets, compared to the theoretical predictions of some selected inflationary models. From Planck Collaboration et al. [2018e](#).

4.7 Λ CDM parametrization

The simplest Λ Cold Dark Matter cosmological standard model, Λ CDM, is based on six parameters : two parameters for the primordial matter spectrum, A_s and n_s , the Hubble expansion rate measured today H_0 , the baryonic and dark matter densities, Ω_b and Ω_c , and finally the reionization depth τ_{re} . The other parameters are assumed to be fixed, e.g. assuming a flat energy density, $\Omega_{\text{tot}} = 1$, a dark energy equation of state with $w_c = -1$, no running of the spectral index $dn_s/d \ln k = 0$, and no tensor modes $r = 0$.

5 Main CMB experiments

In this section, we enumerate some of the main past, current, and future CMB experiments. We especially focus on those targeting polarization and B-modes measurements.

5.1 Space-based missions legacy

Cosmic Background Explorer (COBE)

COBE is the first generation satellite mission dedicated to the CMB study, launched by NASA in 1989. It provided two key measurements in favour of the Big-Bang model. The CMB intensity spectrum measured by the FIRAS instrument follows exactly that of the Black-Body at 2.725 K (Smoot 1999) as shown in Fig. 1.4. The DMR instrument had a relatively limited effective angular resolution ($\sim 7^\circ$), but sufficient enough to find faint anisotropies in the CMB temperature field (e.g. Smoot 1999).

Wilkinson Microwave Anisotropy Probe (WMAP)

WMAP is the second generation of NASA CMB space mission. Launch in 2001, it mapped both the temperature and polarization CMB anisotropies during nine years. Thanks to its better angular resolution than COBE ($\sim 0.25^\circ$), it could measure the CMB spectrum up to $\ell \sim 1000$. It helped to tightly constrain the current Standard Model of Cosmology Λ CDM, providing error-bars on the parameters up to a few percent. Among others, WMAP helped to determine that we live in a geometrically flat Universe, with energy density content dominated at $\sim 71\%$ by dark energy, with some $\sim 5\%$ of baryonic matter, and $\sim 24\%$ of cold dark matter. It also provided evidences of the cosmic neutrino background, and with an effective number of neutrino species of 3.84 ± 0.40 , and evidence of inflation, measuring a scalar spectral index $n_s = 0.9608 \pm 0.0080$ (Bennett et al. 2013).

It observed the sky over five frequency bands, at 23, 33, 41, 61, and 94 GHz, to improve the subtraction of foreground contamination signals.

Planck

The latest mission to probe CMB anisotropies is the *Planck* satellite, sent by ESA. It had higher sensitivity and an improved angular resolution compared to WMAP, about ~ 5 -10 arc-minutes, allowing to measure the CMB spectrum up to $\ell \sim 2500$. *Planck* also covered a broader range of frequency channels, divided among two instruments: the Low Frequency Instrument (LFI) covering the 30, 44 and 70 GHz bands in both intensity and polarization; and the High Frequency Instrument (HFI) covering 100, 143, 217, 353, 545, and 857 GHz frequency bands. Of the HFI channels, only the lower four had the capability to measure the polarisation signal.

Thanks to its large frequency coverage, *Planck* also helped to better characterise the galactic foregrounds emissions in the microwave band. It provided the most precise measurements of the cosmological parameters, with sub-percent precision.

5.2 Recent ground-based experiments

Atacama Cosmology Telescope (ACT/ACTpol)

ACT is a telescope positioned in the Atacama Desert, a dry and high altitude (~ 5000 m) place in the north of Chile. It is designed to observe the CMB on a small patch of the sky in both temperature and polarization, simultaneously in three frequency bands centred on 148 GHz, 218 GHz, and 277 GHz. Thanks to ACT high-resolution, around 1 arc-minute, it can probe the CMB spectrum about $400 \lesssim \ell \lesssim 8000$. For instance, it can precisely measure the Sunyaev-Zeldovich effect or the lensing B-modes signal (Louis et al. 2017).

South Pole Telescope (SPT/SPTpol)

Similarly to ACT, the South Pole Telescope is a small angular resolution experiment. It makes deep resolution CMB temperature and polarization maps, ~ 500 square degrees, of the Southern sky. SPT observes at three different frequencies, 95 GHz, 150 GHz, and 220 GHz, with an angular resolution of 1 arc-minute, and roughly covers a $50 \lesssim \ell \lesssim 8000$ multipole range. (Henning et al. 2018)

POLARBEAR / Simons Array

Located in the Atacama Desert, POLARBEAR is designed to make small angular scales measurements of the CMB polarization. It has two main goals : to detect the B-modes (lensing and primordial), and to reconstruct the lensing potential of the CMB. With a resolution of 3.5 arc-minute, broader than ACT or SPT, POLARBEAR studies the CMB spectra over the range of multipoles $200 \lesssim \ell \lesssim 1400$. In order to increase the measurements sensitivity, it focuses on a relatively small patch of the sky, ~ 30 square degrees of the sky, compared to ACT or SPT (POLARBEAR Collaboration et al. 2014b; POLARBEAR Collaboration et al. 2014c; POLARBEAR Collaboration et al. 2014a).

BICEP/Keck array (BK)

The Bicep/Keck Array is a multi-frequency instrument comprised of four telescopes observing the polarization of the CMB around the South Celestial Pole at 30/40, 95, 150 and 220/270 GHz. Using a relatively broad angular resolution around $\sim 0.50^\circ$, the BK experiment aims at detecting the B-modes signal at large angular scales, $40 \lesssim \ell \lesssim 300$ (Hui et al. 2018). As already mentioned, the current best upper limit is provided by combining *Planck* temperature, low- ℓ polarization, and lensing measurement with BICEP2/Keck Array BK14 data, which gives $r_{0.002} < 0.056$ (Planck 2018 Results. X).

5.3 Future measurements

Simons Observatory (SO)

The Simons Observatory plans to deploy an array of telescopes in the Atacama Desert by the 2020s. It will measure the CMB in both temperature and polarization, over six frequency bands, 27, 39, 93, 145, 225 and 280 GHz. The array will be composed of three small-aperture telescopes (SATs) with $\sim 0.5^\circ$ angular resolution, and one large-aperture telescope (LAT) with arcminute angular resolution. The targeted sky coverage is about $\sim 40\%$ for the LAT, and $\sim 10\%$ with the SATs. (Galitzki 2018; The Simons Observatory Collaboration et al. 2019).

Stage-4 (S4)

Stage-4 (S4) regroups the next generation of ground-based experiments dedicated to the study of the CMB, by combining and expanding existing facilities in Chile, South Pole, and possibly in the northern hemisphere (Abazajian et al. 2016; Abitbol et al. 2017). By the 2020s, the total number of detectors involved will improve the sensibility of CMB measurement of one or two orders compared to previous experiments such as *Planck*, as shown in Fig. 1.18. As an element of comparison, the number of detectors will go from around 10 000 (currently Stage-3), to 100 000 for S4.

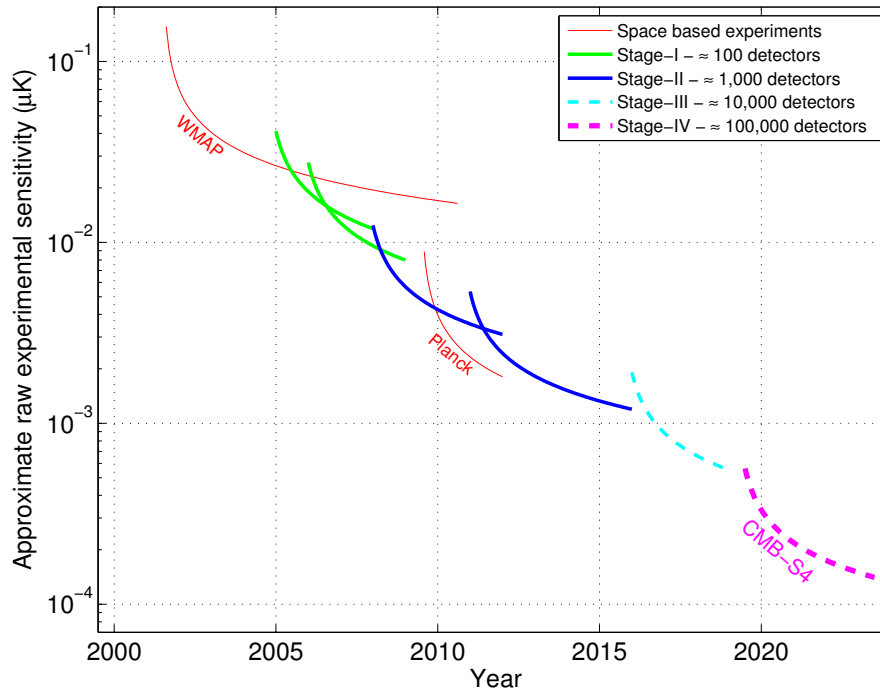


Figure 1.18: Improvement of the experimental sensitivity with CMB generations. From Abazajian et al. 2016.

S4 has numerous scientific goals. It aims at testing inflation, determining the masses and number of the neutrino species, to constrain the nature of dark energy, possibly to put light on new light relic particles, as well as testing general relativity on large scales. Among others, S4 could improve the lensing and Sunyaev–Zel’dovich effects measurements, or aid in delensing the primordial B-modes spectrum, allowing to probe the primordial part of the spectrum and therefore low value for the tensor-to-scalar ratio. This will be made possible by combining large sky coverage with degree angular scale measurements, and high resolution measurements made from sub-degree angular scales, hence covering most of the CMB spectrum from $\ell \approx 20$ to $\ell \approx 5000$ -10000.

Figure 1.19 shows all current CMB spectra measurements from *Planck*, ACT, SPT, BICEP/keck, and polarbear. The forecast on S4 measurement and sensibility on the spectra is also indicated.

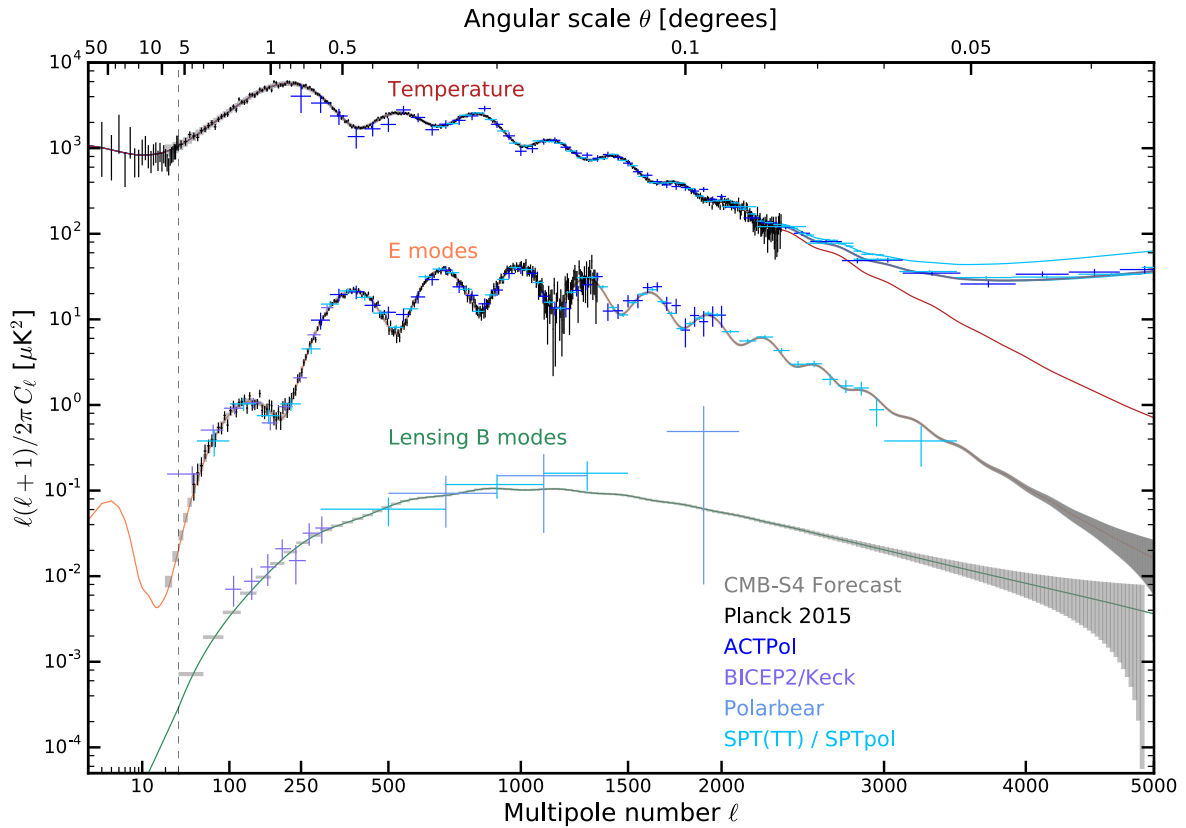


Figure 1.19: 2016 constraints on CMB power spectra from *Planck*, ACT, SPT, BICEP/keck, and polarbear. The forecast on S4 measurements and sensibilities on the spectra are also indicated in grey boxes. The horizontal axis scaled logarithmically in multipole ℓ left of the vertical dashed line ($\ell < 30$) and as $\ell^{0.6}$ at higher multipole. From Abazajian et al. 2016.

LiteBIRD

LiteBIRD is a satellite mission that would be deployed by the Japan Aerospace Exploration Agency (JAXA) in the middle of the 2020s. It will observe the CMB during a 3-year full sky survey. In order to measure and subtract galactic foregrounds, the satellite will use 15 frequency bands covering 32 GHz to 448 GHz, and with typical angular resolution of $\sim 0.5^\circ$. The mission is essentially designed to probe the primordial B-modes on large angular scales ($2 \leq \ell \leq 200$) and to achieve a total error $\delta r < 0.001$ on the tensor to scalar ratio (Hazumi et al. 2019).

6 Summary

In this introductory chapter, we described how the current standard cosmological model makes powerful predictions about the early Universe and its evolution, and how a probe like the CMB allows us to constrain it with high precision and understanding. A fundamental part of the model, the inflation era, elegantly solve at once several fundamental problems of the Big-Bang model : the horizon problem, the flatness problem, and the origin of primordial inhomogeneities. However, today, inflation is not well constrained, and the most promising probe to inflationary physics lies in the detection and observation of primordial B-modes polarization patterns in the CMB.

In the following chapters, we focus on the development of analysis tools of the primordial B modes. This task turns out to be complex, for the expected signal is small compared to other CMB polarization signals. Moreover, in practice, precise CMB polarization measurements are impeded with the presence of foreground contaminations and instrumental noise.

Foreground contaminations come in various form : terrestrial, galactic, or extra galactic. We further discuss their origin in chapter 2, where we also explore and adapt methods in the context of CMB polarization galactic foregrounds cleaning.

The instrumental noise can produce bias when estimating the CMB power spectra. The noise contribution can either be evaluated and removed, or averted by cross-correlating datasets that have uncorrelated noise. The latter technique will especially be described in chapter 3 in the context of power spectra estimators targeting precise polarisation measurements.

In chapter 4, we apply the cleaning and spectrum estimation approaches to the polarisation data and simulation maps publicly provided by *Planck*.

Astrophysical foreground removal

The CMB is not the only microwave emission that we observe in the sky. Multiple astrophysical objects are emitting in the microwave band, and thus contaminate any CMB measurement. Those foreground contaminations can have many origins, from human activities or atmosphere emissions, to galactic and extra galactic sources. Each foreground has variable intensity depending on the angular scale, the wavelength measurement, and the direction of the observation.

Balloon and space based experiments allow us to be free of contaminations from the atmosphere, ground emissions, and radio frequency interferences. The remaining components originate from astrophysical sources, such as solar system objects, galaxies and clusters of galaxies on small angular scales, as well as the Zodiacal light, the Milky Way, and the Cosmic Infrared Background (CIB) on larger scales.

Outlook

In this chapter, we first investigate in Sec. 1 the different galactic foreground emissions. In Sec. 2, we describe the tools that we use to simulate the foreground signal on the sky. In Sec. 3 we review some existing foreground cleaning algorithms. Inspired by those methods, we adapt and propose new algorithms, developed in the context of large scale polarisation CMB analysis. We especially work in the framework of *Planck* data. The motivation behind the choice of the class of methods is detailed in Sec. 4. The forecast on the impact of foreground contamination on the CMB signal detection is investigated in Sec. 5. A section is dedicated to each of our methods, from Sec. 6 to Sec. 8. We also investigate a possible detection of the foreground signal polarisation rotation in Sec. 9. The methods that we propose can be adapted to clean localised patches of pixels of the sky, as discussed in Sec. 10. We briefly discuss how to lower the uncertainty of the methods during the cleaning process in Sec. 11. Finally, the performance of the methods are compared and summarised in Sec. 12.

1 Astrophysical foregrounds

Multiple astrophysical foregrounds emissions have been identified. Depending on their physical origin, those can be classified in two types, galactic and extra-galactic. The spatial distribution of their emission on the sky can be highly inhomogeneous. Some astrophysical processes also induce a non-zero polarisation signal. The brightness of the temperature and polarisation foregrounds signals vary depending on the wavelength of emission.

1.1 Galactic sources

Figure 2.1 shows the spectral energy distributions (SED) in temperature and polarisation intensity for the Galactic foreground components currently identified.

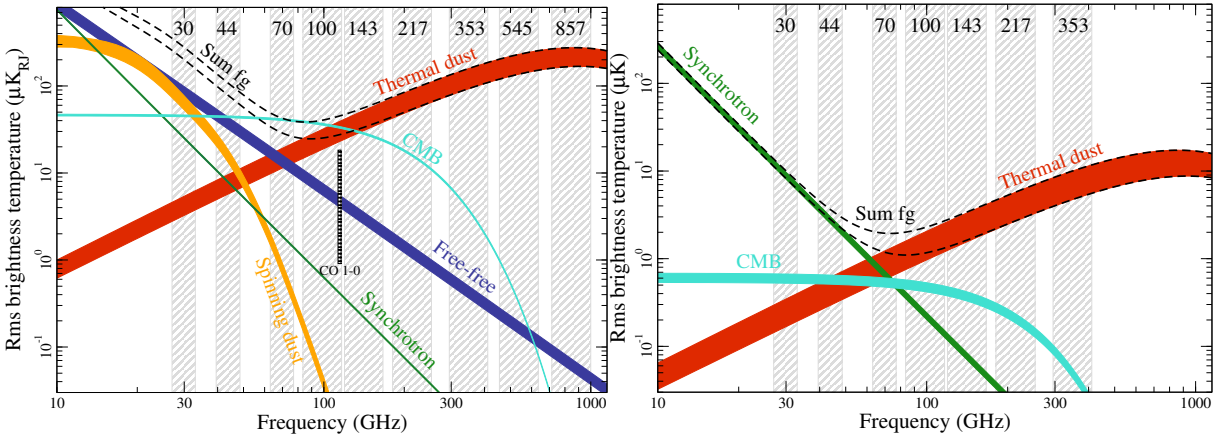


Figure 2.1: Spectral energy distribution (SED) of the galactic foregrounds in temperature (left) and polarization (right), respectively evaluated over 93% and 73% of the sky. From *Planck 2015 Results. X*.

Thermal Dust

The dominant source of foregrounds for frequencies $\gtrsim 70$ GHz are thermal emission from galactic silicate and carbonaceous dust grains. The ultra violet (UV) emission from the surrounding stars population heats up dust grains of the interstellar medium, which in turn re-emit in infrared frequency when cooling down. Although dust population and temperature vary across the sky, the thermal dust SED model for frequency up to ~ 850 GHz is empirically well fitted by a modified black-body (MBB) (or grey-body) spectrum,

$$I_{\nu}^d \propto \nu^{\beta_d(\hat{n})} B_{\nu}(T(\hat{n})), \quad \text{with} \quad B_{\nu}(T) = \frac{2h\nu^3/c^2}{\exp\left(\frac{h\nu}{k_B T}\right) - 1}, \quad (2.1)$$

which parameters can vary depending on the direction on the sky \hat{n} . $B_{\nu}(T_d)$ is the Planck law for a blackbody radiation at temperature T_d , and $\beta_d(\hat{n})$ is the dust spectral index. The measurement across the sky found the average values $T_d^I \sim 19.6$ K and $\beta_d^I \sim 1.55 \pm 0.05$ (*Planck 2018 Results. IV.*).

An alternative parametrisation of the thermal dust proposes instead multiple component grey-body model, for which two (or more) populations of thermal dust are considered along the line of sight. See for example Meisner et al. 2014 or Finkbeiner et al. 1999.

For aspherical dust grains, the major axis tend to statistically align with the galactic magnetic field. As a result, there is a dust emission polarization perpendicular to the galactic magnetic field. Modelling dust polarization is more complex, and it depends on the shape, the optical properties, and the size distribution of the aligned grain population. For the polarised dust SED, P_ν^d , the average temperature and spectral indexes are measured to be $T_d^P \sim 19.6$ K and $\beta_d^P = 1.53 \pm 0.03$, consistent with the value of the temperature spectral indexes (Planck 2018 Results. XI; Planck 2018 Results. IV.). The dust polarization fraction I^d/P^d mean value has been found to be around 10% at high latitude, with a maximum of 20% in some regions. The dust emission is the major contamination for CMB polarisation measurement at frequencies above 70 GHz.

The dust polarisation intensity, $\sqrt{Q^2 + U^2}$, is displayed in Fig. 2.2 for which we smoothed the 353 GHz *Planck* channel with a 2.6° Gaussian beam.

Synchrotron

At low frequencies, less than 80 GHz, the foreground contamination is dominated by synchrotron radiation from cosmic ray electrons. Under the influence of the local galactic magnetic field, electrons undergo an acceleration perpendicular to their velocity, which result in a spiral trajectory around the field lines, accompanied with the emission of radiations. The intensity and spectrum can show significant variations on the sky, since they depend on the cosmic ray number, their energy, and the magnetic field strength. For frequencies above 20 GHz, the synchrotron SED is well-approximated by a power-law,

$$I_\nu^s \propto \nu^{\beta_s^I(\hat{n})}, \quad (2.2)$$

with a mean spectral index measured at $\beta_s^I = -3.1 \pm 0.1$ (Planck 2018 Results. IV.).

The emission is also highly polarised, with a polarization fraction that can theoretically reach 75% in a regular and uniform magnetic field. In practice, because magnetic fields are generally non-uniform, and because of rotation depolarisation effect for frequencies under a few GHz, the fraction of polarization only reaches 10%-40%. Because of the limited polarization sensitivity of *Planck*, the polarised synchrotron spectral index is not significantly constrained. The best fit has a very broad distribution, with a weak preference between $\beta_s^P = -3.5$ to $\beta_s^P = -3$, consistent with the temperature value $\beta_s^I = -3.1 \pm 0.1$ (Planck 2018 Results. XI). The synchrotron emission is the most intense source of foreground contamination for CMB polarisation measurements at frequencies under 70 GHz.

The synchrotron amplitude is displayed in Fig. 2.2 for which we smoothed the 30 GHz *Planck* channel with a 5° Gaussian beam.

Spinning dust

Discovered relatively recently, another foreground component detected around 10–60 GHz, first identified as anomalous microwave emission (AME) (Kogut et al. 1996; Leitch et al. 1997), is now thought to arise from spinning dust grains whose rotation leads to a microwave emission. However, the origin of this signal is still debated, and a significant amount of the emission could also arise from magnetic dust radiation, described here after. Current constraints indicate that the spinning dust polarization is below a few percent at 30 GHz (Hoang et al. 2013).

Magnetic dust

An other candidate to the AME origin are radiation from thermal fluctuations of magnetic grain materials, such as ferromagnetic particles and inclusions into silicate dust grains. In such

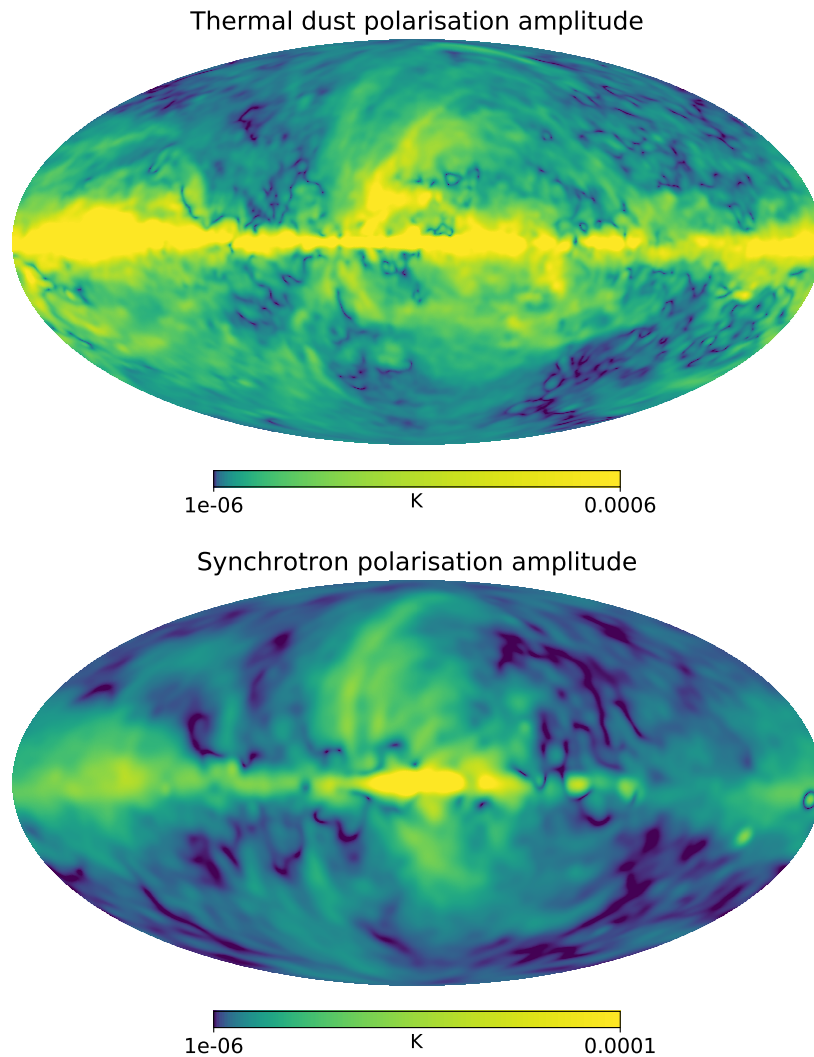


Figure 2.2: *Planck* polarisation amplitude maps, $P = \sqrt{Q^2 + U^2}$, at 353 (top) and 30 GHz (bottom), tracing respectively the dust and synchrotron signals. Color range is in log scale. Here and throughout, all maps are shown in Galactic coordinates using Mollweide projection

materials, a net magnetization arises from the spontaneously spins ordering of unpaired electrons. Thermal fluctuations caused by the astrophysical surrounding excite the magnetization of the materials, whose de-excitation to its initial magnetization state is accompanied by radiation emissions in the microwave band. Current predictions indicate that magnetic dust radiation polarization emission could be of the order of a few percent (Dickinson et al. 2018; Génova-Santos et al. 2017).

Molecular clouds

The interstellar medium is filled with molecular clouds, also known to be the nursery places for young forming stars, mainly confined close to the Galactic disk. The molecules can undergo internal quantum transitions accompanied with an emission of photons. For example, the rotational state transition $J = 1 \rightarrow 0$ of the carbon monoxide CO at 115.271 GHz (Penzias et al. 1972; Wilson et al. 1970), (Planck 2013 Results. XIII). Since those energies levels are quantified, the molecular cloud emission appears as a line in the frequency spectrum. Additional

transitions ($J = 2 \rightarrow 1$, $J = 3 \rightarrow 2$, ...) are also observed, as well as other lines emitted from other molecular origins (CN, HCO+, ...). The emission from molecular clouds, such as CO, is predicted to be polarized at a level up to a few percent (Goldreich et al. 1982; Li et al. 2011).

Free-free

Because of the interactions with ionised gazes of the interstellar medium, free electrons are decelerated, whose deceleration is accompanied with bremsstrahlung emissions (or free-free emissions). Since the Coulombic interactions direction is by nature random, with no significant alignment with the galactic magnetic field, the free-free foreground is expected to be unpolarised. Its polarization fraction has been measured to be less than a percent over the whole sky (Macellari et al. 2011).

1.2 Extra galactic sources

Point sources

On the frequency range used to observe the CMB, two point sources populations are expected, radio galaxies and dusty star-forming galaxies. The polarization amplitude of the later is expected to be low, as recently observed on the M82 source (Matthews et al. 2009). Radio galaxies are expected to have a higher polarization emission fraction (Battye et al. 2011; Tucci et al. 2012), which should therefore be taken into account for future small scale CMB polarization analysis.

The Cosmic Infrared Background

The CIB is a diffuse radiation associated to the emission from dust within galaxies from the young Universe (e.g. Béthermin et al. 2013). Studying the CIB provides unique informations about star formation processes at high redshifts. As for the CMB, the CIB is a diffuse emission, characterised by anisotropies in intensity, which correspond to variations in the clustering of galaxies. Thanks to its wide range of frequencies, *Planck* provided important improvements on the CIB measurements (see for example *Planck 2013 Results. XXX*).

Sunyaev-Zel'dovich effect

Already introduced in Sec. 4.2 of chapter 1, the SZ effect is the result of photons being inverse Compton scattered by high-energy electrons in galaxy clusters (Sunyaev et al. 1969; Sunyaev et al. 1980b). Dense clusters of galaxies can thus be observed using high resolution CMB observations. Because the effect is redshift-independent, it has attracted most interest to provides a powerful probe of the structures on large scales and to constrain the cosmological parameters. A fraction of the SZ emission can also be polarised (Sunyaev et al. 1980a).

2 Sky modelling and simulations

In this section, we first describe how the signal on the sky is modelled, then we introduce the datasets simulations against which the foreground cleaning methods will be tested. We will use the *Planck* polarized frequency channels. Those come as three bands from the Low Frequency Instrument (LFI), 30, 44 and 70 GHz; and four from the High Frequency Instrument (HFI), covering 100, 143, 217, and 353 GHz.

In addition to the experimental noise, the signal measured by the detectors results in the sum of the various sources that emit in the microwave band. A polarisation sky map, (or dataset) $d^{\text{obs}} \equiv (d^Q, d^U)$ measured at frequency ν contains n_{pix} pixels measuring Q and n_{pix} pixels measuring U components of the polarization. It can be modelled as a collection of observations in each direction \hat{n} , corresponding to the linear combination of the CMB signal s_ν^{CMB} , n_{fg} foreground contamination f_i^{fg} , and the experimental noise n^{noise} ,

$$d_\nu^{\text{obs}}(\hat{n}) = s_\nu^{\text{CMB}}(\hat{n}) + \sum_i^{n_{\text{fg}}} f_{i,\nu}^{\text{fg}}(\hat{n}) + n_\nu^{\text{noise}}(\hat{n}). \quad (2.3)$$

2.1 CMB signal

We will assume that the signal of each dataset is rescaled such that the CMB signal has a constant spectrum across all frequencies, $s_\nu = s_\mu = s$, $\forall \mu, \nu$. The maps are therefore expressed in K_{CMB} units.

The CMB input power spectra are generated using *CAMB* with *Planck* 2018 best fit parameters ([Planck 2018 Results. VI.](#)), and the reionization parameter $\tau = 0.06$. If not specified the tensor-to-scalar ratio is set to $r = 0$. The CMB signal on the sky is finally generated from the power spectra using the *Healpix* package.

2.2 Foregrounds modelling

As seen in [Fig. 2.1](#) (extracted from [Planck 2015 Results. X](#)), the polarization foregrounds can show very high amplitudes compared to the CMB signal. Their contribution is quite important when estimating the CMB power spectra, and it can highly bias the CMB measurement.

Quantifying the contribution of the foregrounds signal to the power spectra is a hard task, because the foregrounds properties and distribution over the sky are not fully understood and modelled. In order to improve the understanding of the foregrounds signal, the sky has to be mapped with high sensitivity over a broad frequency range. Latest measurements provided by *Planck* allowed to improve the foreground sky models. Based on sky measurements, and assuming a SED for each component, public codes allow to simulate the foreground signals in each frequency band.

The foregrounds signal $f^\nu(\hat{n})$ in a given direction \hat{n} and frequency ν is generally modelled as the product between the foreground SED encoding the spectral variation, $g_f(\nu, \hat{n})$, and the signal amplitude, $F_f(\hat{n})$,

$$f^\nu(\hat{n}) = g_f(\nu, \hat{n})F_f(\hat{n}). \quad (2.4)$$

If we have constraints on the average SED of each components, current measurements provide relatively poor constraints on spatial variation of the polarisation SED parameters ($T_d(\hat{n})$, $\beta_d(\hat{n})$, $\beta_s(\hat{n})$ presented in [Sec. 1](#)), ([Planck Intermediate Results. XXII.](#); [Planck 2018 Results. IV.](#)). We must therefore rely on models, in particular for polarisation signals.

2.3 The Python Sky Model

The *PySM* package offers several foreground modellings in both temperature and polarisation (Thorne et al. 2017).

Dust signal

We choose the single modified black-body component for the thermal dust modelling (referred to as the *d1 PySM* option), for which the polarization emission is generated using the 353 GHz *Planck* dust template map as a tracer for the signal amplitude (Planck 2015 Results. X). Therefore, $F_D(\hat{n}) = d^{353\text{ GHz Planck}}(\hat{n})$ in Eq. (2.4). To build their model, the 353 GHz map is degraded to $n_{\text{side}} = 512$, then smoothed with a 2.6° FWHM Gaussian beam, which removes the CMB and noise contaminations. The dust signal at other frequencies is then scaled using a MBB spectrum, a varying temperature T_d , and a spectral index β_d obtained from the *Planck* data (Planck 2015 Results. X).

Synchrotron

We select the synchrotron emission modelled by a simple power law (*s1 PySM* option). The amplitude of the signal based on the 23 GHz *WMAP* polarization maps (Bennett et al. 2013) and smoothed with a 5° FWHM Gaussian beam. Therefore, $F_S(\hat{n}) = d^{23\text{ GHz WMAP}}(\hat{n})$ in Eq. (2.4). The synchrotron emission at other frequencies is then scaled using a power law, with a varying spectral index β_s . The index map is built from the ‘Model 4’ of Miville-Deschenes et al. 2008, using a combination of the 23 GHz *WMAP* and the 408 MHz map observed by Haslam et al. 1982 and reprocessed in Remazeilles et al. 2014.

For both foreground models, small scales are added to the maps by drawing random Gaussian realisations using an extrapolation of the foreground power spectrum. This has no particular impact on our study as we focus on large-scale foreground contaminations. The map of the spectral parameters used in the PySM are shown in Fig. 2.3

2.4 The Planck sky model

The Full Focal Plane (FFP10) foreground simulations publicly available with *Planck* legacy archive (Planck Legacy Archive 2019), makes use of the Planck Sky Model (PSM) (Delabrouille et al. 2013) to simulate the foreground frequency dependency.

Dust

The dust polarisation signal is simulated by merging the *Planck* data with a realization of the statistical model of dust emission. In the galactic plane, and on the full sky large scales ($\ell \lesssim 10$), the dust amplitude is modelled using the 353 GHz *Planck* polarisation map, while the small scales at higher latitudes are simulated from a realization of the Vansyngel et al. 2017 model. The PSM assures that the transition between large and small scales, as well as between the galactic plane and higher latitudes is continuous. The dust signal at other frequencies is then scaled following a modified blackbody emission law that vary between each pixel.

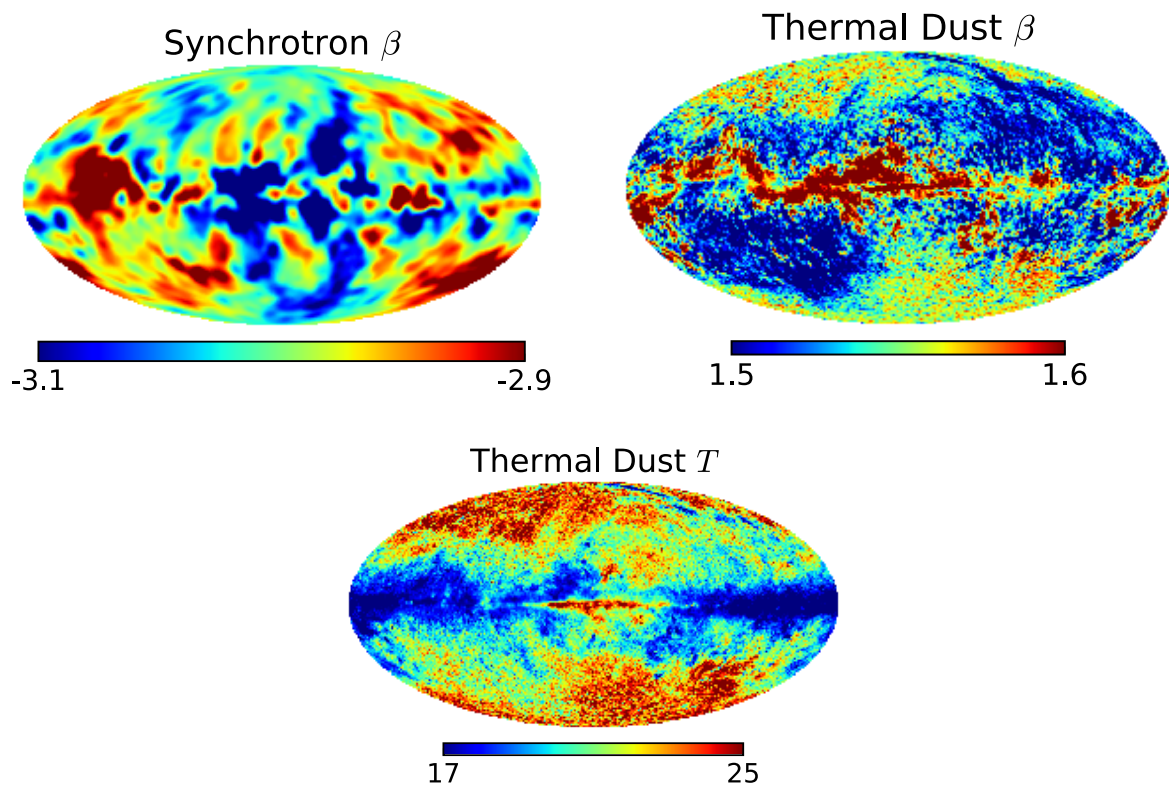


Figure 2.3: PySM spectral parameters maps, for the synchrotron (β_s) and the dust (β_s and T_d). Extracted from Thorne et al. 2017

Synchrotron

The amplitude of the polarised synchrotron signal is based on the 23 GHz WMAP polarisation data. The signal is extrapolated at other frequencies using a spectral index map from synchrotron intensity. The index map is built similarly than with the PySM. The PSM follows the ‘Model 4’ of Miville-Deschenes et al. 2008 with a combination of the 23 GHz WMAP and the 408 MHz map observed by Haslam et al. 1982 and reprocessed in Remazeilles et al. 2014.

The homogeneous model

We also consider a simplified model, assuming a spatially homogeneous SED dependency of the foregrounds, i.e. $g(\nu, \hat{n}) = g(\nu)$ in Eq. (2.4).

The dust and synchrotron foregrounds tracers $F_D(\hat{n})$ and $F_S(\hat{n})$ in Eq. (2.4) are generated using respectively the 353 GHz and 30 GHz *PySM* maps.

We first introduce the foreground coefficient $\alpha(\hat{n})$, using Eq. (2.4),

$$\alpha_f^\nu(\hat{n}) \equiv \frac{f^\nu(\hat{n})}{f^\mu(\hat{n})} \quad (2.5)$$

$$= \frac{g_f(\nu, \hat{n})}{g_f(\mu, \hat{n})}, \quad (2.6)$$

with $f^\nu \in \{D, S\}$ either the dust or the synchrotron signal at frequency ν . We choose a reference frequency $\mu = 353$ GHz for the dust, and $\mu = 30$ GHz for the synchrotron. The foregrounds

signal can thus be scaled to any frequency ν . For that purpose, we use the mean value of the coefficients α'_D and α'_S computed from the PSM model.

2.5 Foreground models comparison

We now confront the models with each other by comparing the foreground coefficient $\alpha(\hat{n})$ defined in Eq. (2.5), which reflects the spectral variation of the emissions. We select the same reference frequency as for the homogeneous model, that is to say, $\mu = 353$ GHz for α_D , and $\mu = 30$ GHz for α_S . The resulting maps and distributions of α'_D and α'_S are shown in Fig. 2.4 for the channel $\nu = 100$ GHz.

We observe that the maps of α_S are similar between the synchrotron the PSM and the PySM. This is expected as their modelling follow the same procedure. However, the mean value of the distributions are slightly different. We therefore shift the PySM distribution on top of that of the PSM to facilitate the comparison.

The maps and distribution of the dust coefficient, α_D , show much more differences between both models. Especially at high latitudes, for which the PSM model has wider variations. This is also visible on the distributions, for which the PySM is sharper.

An other difference between both models, which is not visible either on the distributions or the maps, is that the coefficients α for each pixel are not homogeneous between the Q and U components for the PSM, which is not the case for PySM.

We also noticed an important feature of the PSM, for which the distribution of the α 's of both signals have many outliers, localised on some isolated pixels, and distributed over the whole sky, as shown on the zoomed view in Fig. 2.4. For example, the dust coefficients can typically have values from $\alpha_D^{\min} \sim -16$ to $\alpha_D^{\max} \sim 5$, which is not physically acceptable, since by definition $0 \leq \alpha'_D \leq 1$ for $\nu < 353$. The synchrotron coefficient map $\alpha_S(\hat{n})$ is also impeded with some outlier, although we require α_S for $\nu > 30$. For this reason, in the following analysis, we select the PySM and homogeneous models only.

2.6 Noise

We consider one noise regime, generated from the *Planck* public noise covariance data. For each pixel, those come in $3 \times 3 \times n_{\text{pix}}$ noise temperature and polarization covariance matrices, from which we only select the $2 \times 2 \times n_{\text{pix}}$ polarization block,

$$\mathbf{N} = \begin{pmatrix} N^{QQ} & N^{QU} \\ N^{QU} & N^{UU} \end{pmatrix}. \quad (2.7)$$

This matrix allows to produce white but inhomogeneous noise in the pixel domain, while still including some correlations of the Q - U measurement in each pixel. In order to generate a Gaussian noise map $n \sim \mathcal{N}(0, \mathbf{N})$, we Cholesky-decompose the noise covariance matrix $\mathbf{H}\mathbf{H}^T \equiv \mathbf{N}$, and generate a $2 \times n_{\text{pix}}$ random vector $\mathbf{Z} \sim \mathcal{N}(0, 1)$. Finally, a Q - U noise map is obtained as

$$n \equiv \begin{pmatrix} n^Q \\ n^U \end{pmatrix} = \mathbf{H}\mathbf{Z}. \quad (2.8)$$

In general, we define the noise level σ_n , expressed in $[\mu\text{K}\cdot\text{arcmin}]$, which has the advantage to be independent of the map resolution. It is therefore to the noise per pixel as,

$$\sigma_{\text{pix}}^2 = \frac{\sigma_n^2 \cdot 10^{-12}}{60^2 \cdot A_{\text{pix}}} [\text{K}^2], \quad (2.9)$$

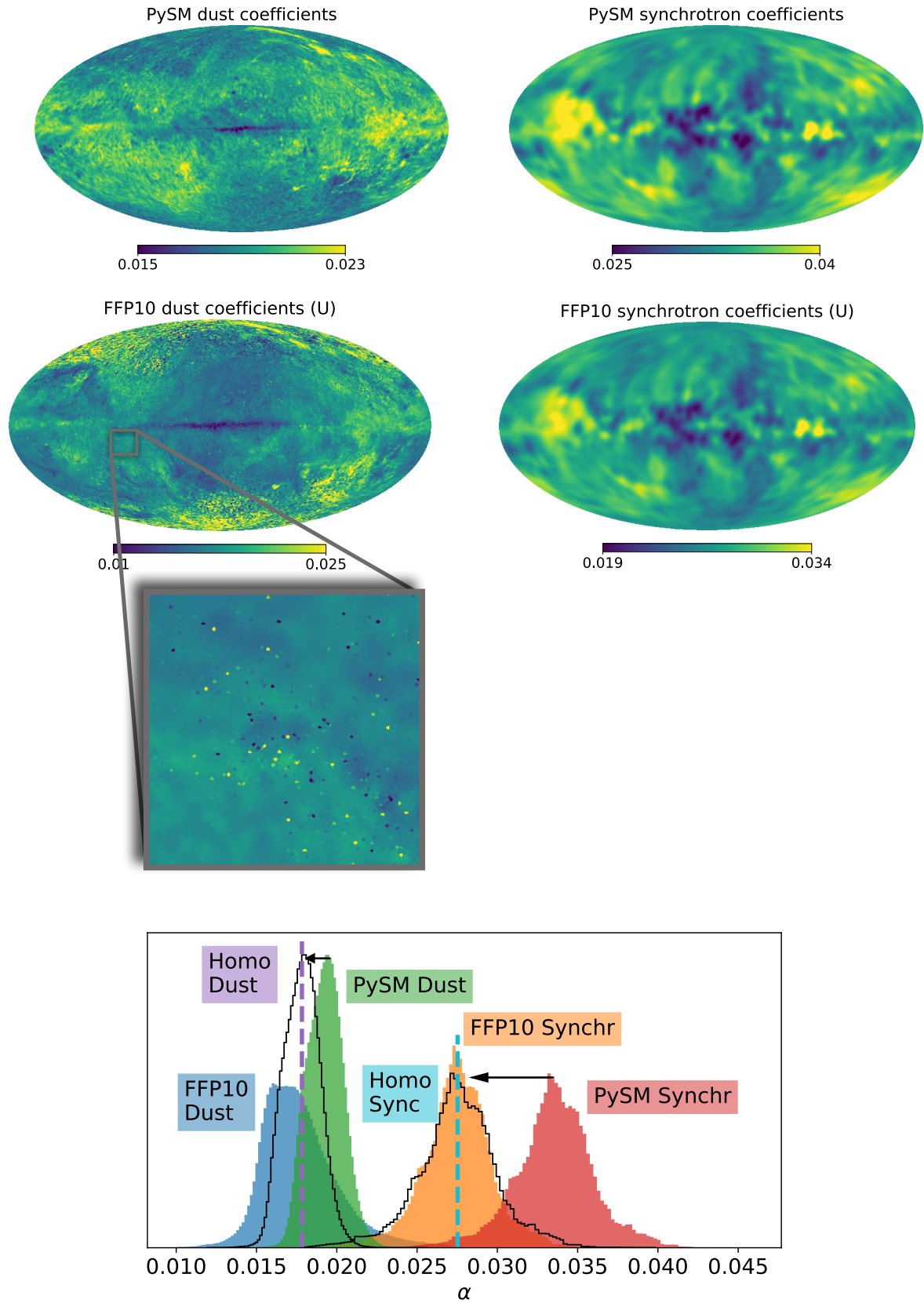


Figure 2.4: Dust and synchrotron foreground coefficients distribution on the sky, $\alpha^{100\text{GHz}}(\hat{n})$, for the different foregrounds models.

where A_{pix} is the pixel area expressed in degree squared. The corresponding noise power spectrum is given by

$$N_\ell = \frac{4\pi\sigma_{\text{pix}}^2}{n_{\text{pix}}} B_\ell^{-2} [\text{K}^2], \quad (2.10)$$

where B_ℓ encodes the deconvolution of the instrumental beam.

The noise level expressed in $\mu\text{K}\cdot\text{arcmin}$ for each *Planck* polarisation map are indicated on Table 2.1. The corresponding power spectrum are shown in Fig. 2.5.

Table 2.1: Planck polarisation noise levels (in $[\mu\text{K}\cdot\text{arcmin}]$) per frequency channel.

Freq [GHz]	30	44	70	100	143	217	353
σ [$\mu\text{K}\cdot\text{arcmin}$]	240	287	246	102	63	95	392

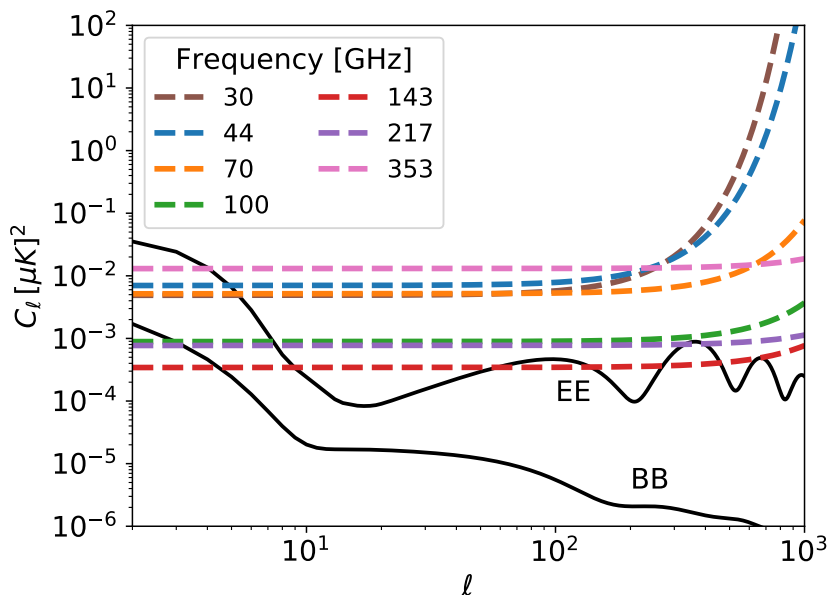


Figure 2.5: Planck polarisation noise spectrum, N_ℓ , for each frequency full mission dataset.

2.7 Dataset signals

Maps

For illustration purpose, we show in Fig. 2.7 the different simulated components from the PySM model at 100 GHz : the signal from the CMB, the dust and synchrotron, as well as the *Planck* noise. Following Eq. (2.3), all signals are linearly combined into a final map. One can already appreciate how the CMB polarisation measurement can be a hard task, as the galactic foregrounds contaminate most of the sky.

Spectra signals

As a forecast, the expected polarisation power spectra of foreground contaminations in all *Planck* frequencies are displayed in Fig. 2.6. The CMB E and B modes signal are generated using *CAMB*

with *Planck* best fit power spectra. We also display the primordial part of the B-modes for a tensor-to-scalar ratio with values $r = [10^{-3}, 10^{-2}, 10^{-1}]$.

We consider a sky fraction going from 40% to 90%, for which the sky-cut is applied mainly in the galactic plane, where the polarisation foregrounds amplitude is expected to be the highest. The E and B modes of the foregrounds are estimated on the PySM foregrounds simulations. The spectra are estimated using the pseudo-spectrum estimator *xPol* (Tristram et al. 2005), and the logarithmic value of the estimation is then fitted using a quadratic function. We note that the 353 and 217 GHz synchrotron signal almost perfectly overlap.

The amplitude of the E and B foregrounds signals are found to differ. In *Planck 2018 Results. IV.*, the ratio EE/BB evaluated on 78% of the sky is of the order of $E/B \sim 0.57$ for the dust signal, and $E/B \sim 0.34$ for the synchrotron. With the PySM we find that this ratio for the dust is of the order of $E/B \sim 0.61$, and does not depend on the sky coverage. While for the synchrotron we find $E/B \sim 0.18$ on 40% of the sky, and $E/B \sim 0.22$ on 90%.

We see that for frequencies above 70 GHz, the dust signal dominates that of the CMB E and B modes over the largest angular scales, $\ell < 10$. On those scales, the synchrotron dominates the E-modes signal for frequencies under 70 GHz. The primordial part of the B-modes is overwhelmed by both foregrounds for $r < 10^{-1}$, which is already under current limits (*Planck 2018 Results. X*). Foreground cleaning methods are therefore mandatory in the context of CMB polarisation analysis.

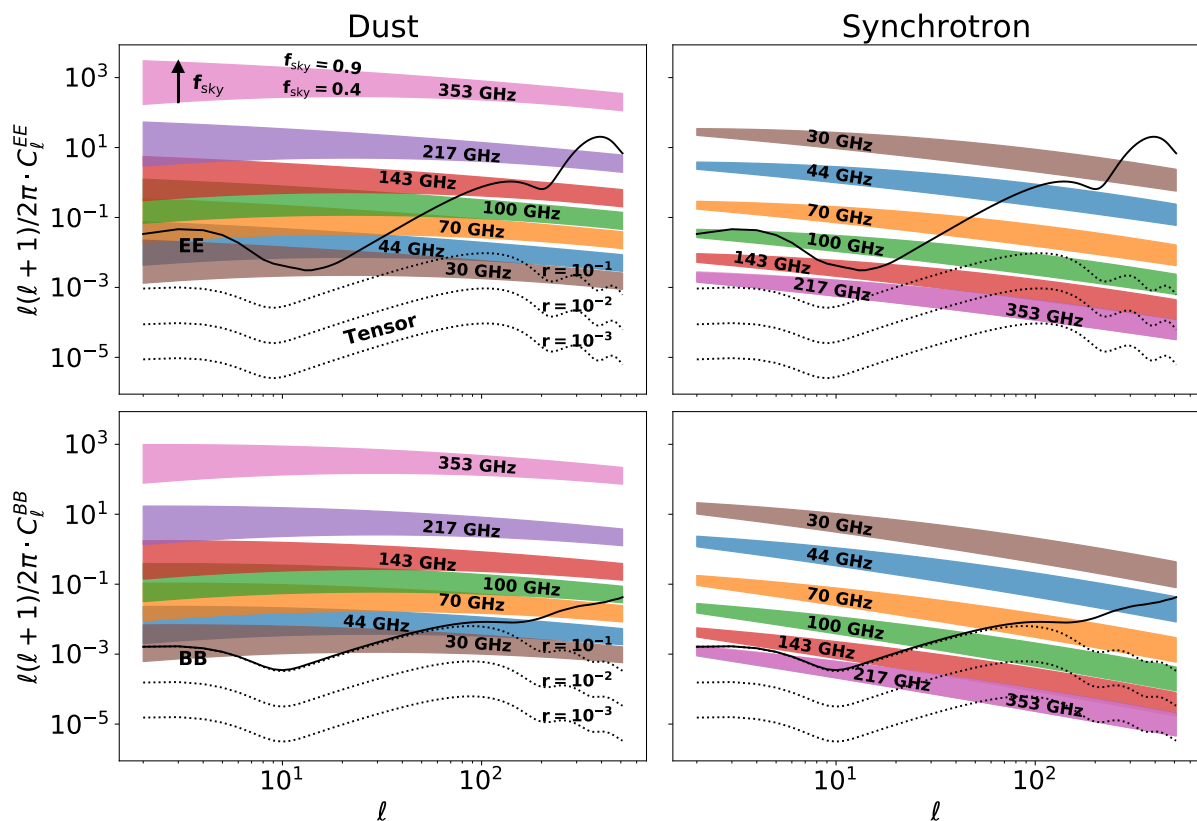


Figure 2.6: Foregrounds polarisation power spectra of the PySM foreground signals. The CMB spectra for the total E-modes and B-modes are in solid, while primordial B-modes are in dashed for three tensor-to-scalar ratio values, $r = [10^{-3}, 10^{-2}, 10^{-1}]$. The foreground signals are indicated by the coloured bands which span the signal between a sky fraction $f_{\text{sky}} = 0.4$ and $f_{\text{sky}} = 0.9$ (indicated by the black arrow).

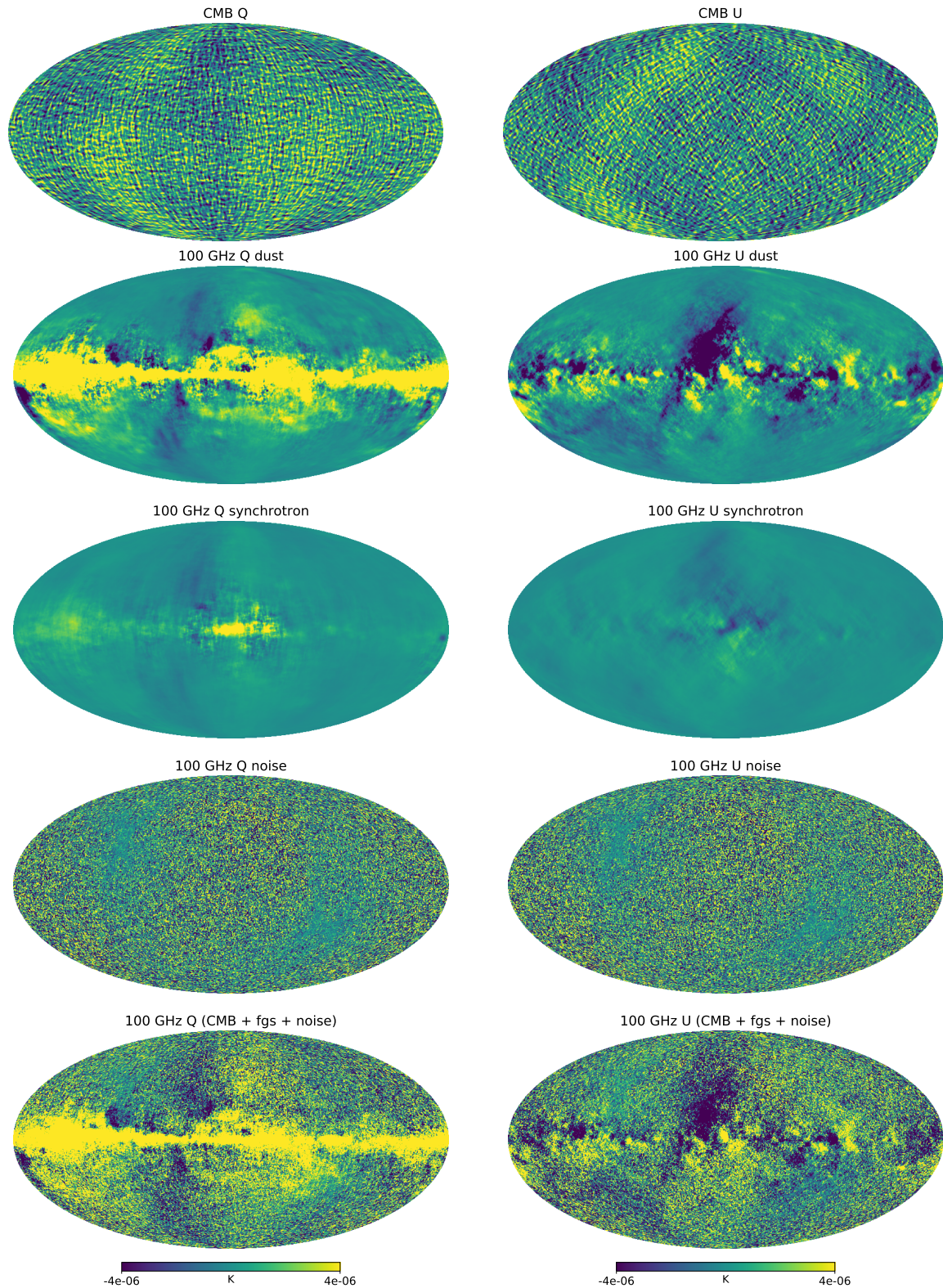


Figure 2.7: Sky simulations at 100 GHz of the CMB polarization signal (first row), the dust and synchrotron signals from PySM (second and third row), the *Planck*-like white noise simulation (fourth row), and finally the sum of all those components. All maps are smoothed with a 0.5° Gaussian beam.

3 Foregrounds removal methods

Disentangling foregrounds from the CMB signal is a domain of analysis on its own. Multiple methods have been proposed which generally depend on the datasets resolutions, the signal-to-noise level, and the number of observed frequency channels. They can work in the pixel and/or in the harmonic domain. Some methods focus on recovering the CMB signal only, while others, known as component separation methods, allow to retrieve all the signals (CMB and foregrounds). They are generally grouped in two categories, blind and non-blind (parametric) methods, depending on the assumption made on the foregrounds modelling and the CMB signal. In this section, we review the main classes of those methods.

In this context, the general data model is linear and reads

$$d(\hat{n}) = \mathbf{A} c(\hat{n}) + n(\hat{n}), \quad (2.11)$$

where the vector d contains the measured signal in each of the $n_\nu(\hat{n})$ frequency bands observed, the vector $c(\hat{n})$ contains the unknown CMB signal $s(\hat{n})$ and the foreground signals, while $n(\hat{n})$ is the vector quantifying the noise in each frequency channel. The $n_\nu \times n_c$ mixing matrix \mathbf{A} contains the information about the emission law of the n_c signals (CMB and foregrounds). Generally, for each dataset, the value for the pixels is rescaled such that the CMB signal intensity is common between all frequencies, $s_\nu = s_\mu = s$, $\forall \mu, \nu$, and the maps are therefore expressed in K_{CMB} units. In that case, the entries of the column corresponding to the CMB signal in \mathbf{A} are equal to 1.

3.1 CMB cleaning methods

Template removal

One simple and powerful solution to get an estimate of the CMB signal is to subtract from the measured dataset $d(\hat{n})$ a foreground templates $t(\hat{n})$ weighted by some coefficient α_i .

$$\hat{s}(\hat{n}) = d(\hat{n}) - \sum_i^n \alpha_i(\hat{n}) \cdot t_i(\hat{n}). \quad (2.12)$$

For example, for one template t , the coefficients $\alpha_i(\hat{n})$ are fitted by minimizing the residuals,

$$\min_{\alpha} (\|s^2\|) = \min_{\alpha} (s^T C^{-1} s) \quad \Rightarrow \quad \hat{\alpha} = \frac{d^T C^{-1} t}{t^T C^{-1} t}. \quad (2.13)$$

Where $C \equiv \text{Cov}[s]$ is the residual covariance matrix.

The templates can be external, or built internally from the datasets of an experiment (e.g. Katayama et al. 2011). Within this later approach, referred to as the Internal Template Fitting (ITF), the templates are preferably constructed using frequency channels for which the foreground signal is known to be the highest. Those generally contain a certain amount of experimental noise, as well as other signals, such as the CMB. This can biased the fitting of α , as we will see in Sec. 6.

Template removal was adopted by the WMAP and *Planck* teams for both temperature and polarization component separation (Eriksen et al. 2004), ([Planck 2015 Results. X](#)).

Internal Linear Combination

The Internal Linear Combination (ILC) is a non-parametric foreground subtraction method that aims at recovering clean CMB signal by combining n_ν frequency datasets $d(\hat{n})$ into one final

map

$$s(\hat{n}) = \sum_i^{n_\nu} w_i \cdot d_i(\hat{n}). \quad (2.14)$$

The minimal assumption here is that the CMB follows a black-body emission with a temperature $T_{\text{CMB}} = 2.725\text{K}$. In this context, the mixing matrix \mathbf{A} of Eq. (2.11) is simply a vector corresponding to the CMB spectral column.

The ILC constitutes a powerful tool while requiring only a few assumptions. The CMB signal is assumed to be uncorrelated with the foregrounds, and to be present in each map, which must have a common angular resolution. The weights \mathbf{w} are computed in order to minimise the total (foregrounds plus noise) variance of the resulting datasets combination,

$$\text{Var}[s] = \mathbf{w}^T \mathbf{C} \mathbf{w}. \quad (2.15)$$

where $\mathbf{C} \equiv \text{Cov}[\mathbf{d}]$ is a $n_\nu \times n_\nu$ dataset covariance matrix. Minimizing the variance defined in Eq. (2.15) under the condition that the CMB signal amplitude remains unchanged in the map, i.e. $\sum_i^n w_i = 1$, gives the general solution

$$w_i = \frac{\sum_j^{n_\nu} \mathbf{C}_{ij}^{-1}}{\sum_{i,j}^{n_\nu} \mathbf{C}_{ij}^{-1}}. \quad (2.16)$$

The ILC was first used during the WMAP analysis in pixel domain (Bennett et al. 2013), and harmonic domain (Tegmark et al. 2003). A hybrid approach developed in Delabrouille et al. 2009 allows to apply the ILC for temperature maps on localised regions on the sphere in the harmonic space, also identified as wavelets (or needlets). A generalization to spin-2 polarization signal $P = Q + iU$ is explored and compared to other ILC methods in Rogers et al. 2016 in the needlet domain, and in Fernández-Cobos et al. 2016 in the pixel domain.

3.2 Component separation methods

Independent Component Analysis

The Independent Component Analysis (ICA) allows to recover the astrophysical components by blindly reconstructing the \mathbf{A} matrix. The model assumes arbitrary components power spectra, frequency spectra, and correlations between the components. In order to recover the multiple components on the sky (CMB signal and foregrounds), the mismatch of the model to the power spectra of the frequency channel maps is minimized. The Spectral Matching Independent Component Analysis (SMICA) (Delabrouille et al. 2003; Cardoso et al. 2008), is an implementation of this method in the spherical harmonic domain, which has been used by the *Planck* collaboration (Planck 2015 Results. X).

Parametric likelihood minimisation

Among the parametric methods, the most popular are Bayesian components separation algorithms (Eriksen et al. 2006a; Brandt et al. 1994). Those make use of sampler to fit for the CMB signal and for the foreground components. Within this context, the mixing matrix of Eq. (2.11) depends on the amplitude and spectral parameters θ of the SED signals, $\mathbf{A} = \mathbf{A}(\theta)$. The parameters are estimated by minimizing the so-called spectral likelihood function $\mathcal{L}(d|\theta)$, which provides the probability density of the data given a model parametrised by θ . Additional cosmological parameters can be included in θ , which offers the advantage to fit for both the foregrounds and the cosmological parameters at the same time. Uncertainties can be rigorously propagated

through to CMB power spectrum and cosmological parameter estimation. This method remains however computationally expensive, and it is sensitive to bias when the foreground model is badly parametrised. The implementation of the Bayesian parametric method, known as Commander (Eriksen et al. 2006b; Eriksen et al. 2008), was used for the *Planck* analysis (Planck 2015 Results. X).

4 Single frequency channel cleaning

Generally, the component separation methods introduced in the previous section, such as the Bayesian parametric or the ICA, try to recover all the component maps as well as parameters of the mixing matrix \mathbf{A} by inverting the full system of Eq. (2.11) including all available channels. Therefore, they must also account for the correlations between the datasets and the different resolutions at which they are produced.

On the other hand, foregrounds cleaning using templates is generally simpler to perform. Those classes of methods require less assumptions in the model, and make use of less parameters. They allow to produce multiple cleaned datasets, but each with higher level of noise compare to usual component separation methods.

In order to extract the B-modes from the CMB, we choose to explore the second class of methodologies, the template cleaning methods, as they allow for more tractability of error propagation in the CMB estimate. The production of multiple ‘clean’ datasets can be particularly suited for B-modes analysis. Indeed, the use of cross-correlations between CMB maps has demonstrated its efficiency in removing noise bias and mitigating the systematic errors when estimating power spectra, as detailed in chapter 3. This can only be achieved using multiple CMB estimates, with uncorrelated errors, and the lowest amount of foregrounds residuals. Each CMB estimate must therefore be built independently, using different channels and templates. In the following sections, we explore and adapt foregrounds removing methods introduced before in order to produce multiple clean CMB maps that have uncorrelated noise. The application of the cleaning methods and spectrum estimation is performed on all polarisation channels of the public *Planck* data in chapter 4.

4.1 Datasets

For most, the methods that we will consider are based on template fitting in the pixel domain. Generally, we make use of one CMB dominated channel, and at least as many secondary channels as foregrounds that we seek to remove. Current observations indicate that only two types of polarised foreground dominate over the sky : synchrotron and dust emission. We therefore consider three observed channels. The maps measured at low and high frequency will serve as internal templates, labelled $t_S(\hat{n})$ and $t_D(\hat{n})$, and respectively serve as tracers for the synchrotron and dusts signals. For that purpose, we select the channels from *Planck*, measured at 30 GHz and 353 GHz. Note that they also contain the CMB signal, as well as non negligible amount of instrumental noise. The dust signal in the 30 GHz band, or the synchrotron signal in the 353 GHz band are both negligible. The map measured at the intermediate band is labelled $d(\hat{n})$, and *Planck* provides five of those, centred on 44, 70, 100, 143, and 217 GHz. We will present our results tested on the 100 GHz band.

Our model datasets can therefore be written as follow,

$$d = s + \alpha_D f_D + \alpha_S f_S + n^d, \quad (2.17)$$

$$t_D = s + f_D + n_D^t, \quad (2.18)$$

$$t_S = s + f_S + n_S^t. \quad (2.19)$$

The foreground coefficients α_D and α_S were already introduced in Sec. 2. Those are grouped into a vector, $\boldsymbol{\alpha} = (\alpha_D, \alpha_S)$. Their value depend on the frequency at which the map d is measured. With all generality, the coefficients are allowed to vary spatially $\boldsymbol{\alpha} = \boldsymbol{\alpha}(\hat{n})$, and can account for polarization rotation, which mix the Q and U components, as described hereafter.

4.2 Polarization rotation

With all generality, the spectral variations encoded in the function $g(\nu, \hat{n})$ of Eq. (2.4) allows for a change in amplitude of the signal as well as polarisation rotation. In that case, we write

$$f^\nu(\hat{n}) = g_f(\nu, \hat{n})F_f(\hat{n}), \quad (2.20)$$

$$\Leftrightarrow \begin{pmatrix} f_Q^\nu(\hat{n}) \\ f_U^\nu(\hat{n}) \end{pmatrix} = \rho_\nu(\hat{n}) \begin{pmatrix} \cos[\theta_\nu(\hat{n})] & -\sin[\theta_\nu(\hat{n})] \\ \sin[\theta_\nu(\hat{n})] & \cos[\theta_\nu(\hat{n})] \end{pmatrix} \begin{pmatrix} F_f^Q(\hat{n}) \\ F_f^U(\hat{n}) \end{pmatrix}. \quad (2.21)$$

For the foreground coefficient $\alpha(\hat{n})$ to account for the polarisation rotation between a frequency ν and μ , we write

$$g(\nu, \hat{n})F_f(\hat{n}) = \alpha(\hat{n})g(\mu, \hat{n})F_f(\hat{n}) \quad (2.22)$$

$$\Rightarrow \alpha(\hat{n}) = g(\nu, \hat{n}) \cdot [g(\mu, \hat{n})]^{-1} \quad (2.23)$$

$$\Leftrightarrow \alpha(\hat{n}) = \frac{\rho_\nu(\hat{n})}{\rho_\mu(\hat{n})} \begin{pmatrix} \cos[\theta_\nu(\hat{n}) - \theta_\mu(\hat{n})] & -\sin[\theta_\nu(\hat{n}) - \theta_\mu(\hat{n})] \\ \sin[\theta_\nu(\hat{n}) - \theta_\mu(\hat{n})] & \cos[\theta_\nu(\hat{n}) - \theta_\mu(\hat{n})] \end{pmatrix}. \quad (2.24)$$

We can therefore parametrise the foreground coefficient as

$$\alpha(\hat{n}) \equiv \begin{pmatrix} \alpha^R(\hat{n}) & -\alpha^I(\hat{n}) \\ \alpha^I(\hat{n}) & \alpha^R(\hat{n}) \end{pmatrix}, \quad (2.25)$$

with

$$\frac{\rho_\nu(\hat{n})}{\rho_\mu(\hat{n})} = \sqrt{\alpha^R(\hat{n})^2 + \alpha^I(\hat{n})^2}, \quad (2.26)$$

and

$$\theta_\nu(\hat{n}) - \theta_\mu(\hat{n}) = \arctan\left(\frac{\alpha^I(\hat{n})}{\alpha^R(\hat{n})}\right). \quad (2.27)$$

4.3 Clean CMB estimate

To obtain a clean estimation of the CMB signal s , the datasets are combined as

$$\hat{s} = \frac{d - \boldsymbol{\alpha}^\dagger \mathbf{t}}{1 - \boldsymbol{\alpha}^\dagger \mathbf{1}} \quad (2.28)$$

$$= \frac{d - \sum_i^{D,S} \alpha_i t_i}{1 - \sum_i^{D,S} \alpha_i}, \quad (2.29)$$

where $\mathbf{t} \equiv (t_D, t_S)^\dagger$. Here, the \dagger operator transposes the vectors $\boldsymbol{\alpha}$ and \mathbf{t} (i.e. in ‘foreground space’).

The pixel-pixel covariance C of the CMB estimate \hat{s} , or residual covariance matrix, is a combination of the CMB signal covariance S and the datasets noise covariances N ,

$$C_{mn} \equiv \text{Cov}[\hat{s}] \quad (2.30)$$

$$= S_{mn} + \frac{N_{mn}^d + \sum_i \alpha_i^2 N_{mn}^{t_i}}{(1 - \sum_i \alpha_i)^2}. \quad (2.31)$$

From Eq. (2.31), we note that the CMB estimate of Eq. (2.29) is mainly affected by the noise of the dataset to be cleaned, $d(\hat{n})$, with a factor proportional to $1/(1 - \mathbf{1}^\dagger \boldsymbol{\alpha})$, which is expected to be close to unity, since the α 's are expected to be small when the channel at which the dataset $d(\hat{n})$ is measured far from the template frequencies (here, 30 and 353 GHz). The CMB estimate is only affected at second order by the template noises, as their contribution is proportional to the square of the foreground coefficient in Eq. (2.31).

In the following, we will assume that the CMB signal covariance matrix S is mainly driven by the variance of the pixel, and therefore we will only consider its diagonal value. The noise in our simulations is only Q - U correlated for each pixel, and there is no correlation between different pixels. Thus, the residual covariance matrix C only consists of four square block matrices, each being diagonal. This highly simplifies the calculation as detailed in Sec. 11, and allows us to apply the methods on high resolution maps. Including the full CMB pixel-pixel correlation in S and C is investigated in Sec. 11.

4.4 Outline

In sections 6, 7, and 8 we will explore methods based respectively on the linear regressions, the maximum likelihood estimators, and the ILC formalism in order to estimate the foreground coefficients $\boldsymbol{\alpha}$. In Sec. 9 we consider which limit can be made on the detection of polarisation rotation.

Current measurements do not indicate much variation of the polarised foreground SED on the sky ([Planck Intermediate Results. XXII.](#)), meaning that the value of $\alpha(\hat{n})$ is almost independent of the position on the sky \hat{n} . We will therefore focus on the estimation of one global coefficient for each foreground. In Sec. 5 we quantify the impact on such approach, while in Sec. 10 we discuss the possibility and results of applying the cleaning methods on spatial local patches on the sky.

5 Foreground residuals

Firstly, we investigate the efficiency in removing the foregrounds signal using internal templates as we proposed in the Sec. 4. For that purpose, we first estimate a global foreground coefficient (introduced in Sec. 2) on sky, $\hat{\alpha}$, associate to each foreground component.

5.1 Contamination of the CMB map estimate

We suppose having access to two sets of measured frequency channels A and B with uncorrelated noise, i.e. $\langle n_{t_A}, n_{t_B} \rangle = \langle n_{d_A}, n_{d_B} \rangle = 0$. From each, a clean CMB map estimate as in Eq. (2.29) has been computed. The resulting estimation can be expanded in three main components : the CMB signal, the foreground residuals, and a noise term,

$$\hat{s}^A(\hat{n}) = s(\hat{n}) + \sum_i^{D,S} \frac{\alpha_i(\hat{n}) - \hat{\alpha}_i^A}{1 - \mathbf{1}^T \hat{\boldsymbol{\alpha}}^A} f_i(\hat{n}) + \sum_i^{D,S} \frac{\hat{\alpha} n_{t_i^A}(\hat{n}) + n_{d_A}(\hat{n})}{1 - \mathbf{1}^T \hat{\boldsymbol{\alpha}}^A}, \quad (2.32a)$$

$$\hat{s}^B(\hat{n}) = s(\hat{n}) + \sum_i^{D,S} \frac{\alpha_i(\hat{n}) - \hat{\alpha}_i^B}{1 - \mathbf{1}^T \hat{\boldsymbol{\alpha}}^B} f_i(\hat{n}) + \sum_i^{D,S} \frac{\hat{\alpha} n_{t_i^B}(\hat{n}) + n_{d_B}(\hat{n})}{1 - \mathbf{1}^T \hat{\boldsymbol{\alpha}}^B}. \quad (2.32b)$$

We can express the terms $\alpha(\hat{n}) - \hat{\alpha} = \delta(\hat{n}) + \epsilon$, where

- $\delta(\hat{n}) \equiv \alpha(\hat{n}) - \bar{\alpha}$ is the difference between the input coefficient distribution on the sky, $\alpha(\hat{n})$, and value averaged on the sky, $\bar{\alpha}$. To sum up, $\alpha(\hat{n})f(\hat{n})$ is the foreground signal contamination, and $\delta(\hat{n})f(\hat{n})$ is the residuals after cleaning.
- $\epsilon \equiv \bar{\alpha} - \hat{\alpha}$ is the uncertainty of the coefficient estimation $\hat{\alpha}$ on the mean value of the input distribution, $\bar{\alpha}$. If the estimator is not biased, $\langle \hat{\alpha} \rangle = \bar{\alpha}$, thus $\langle \epsilon \rangle = 0$.

As an example, the mean dust and synchrotron residuals amplitude, $\sqrt{[\delta(\hat{n})f^Q(\hat{n})]^2 + [\delta(\hat{n})f^U(\hat{n})]^2}$, are shown in Fig. 2.8 for the simulated 100 GHz channel using the PySM model and one global coefficient α .

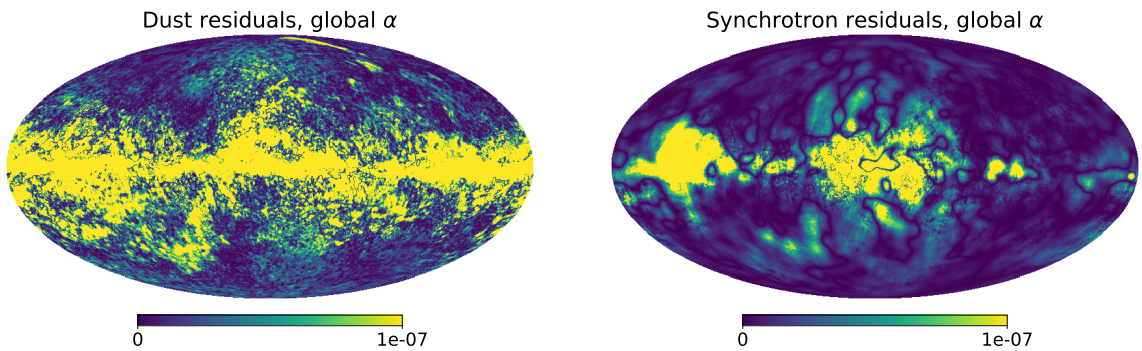


Figure 2.8: Mean foreground residuals power, $\sqrt{[\delta(\hat{n})f^Q(\hat{n})]^2 + [\delta(\hat{n})f^U(\hat{n})]^2}$, using one global coefficient α to cleaned the 100 GHz channel of the PySM.

5.2 Forecast on foreground residuals

We decompose the CMB estimates of Eqs. (2.32) into harmonics coefficients, $\hat{s}_{\ell m}^A$ and $\hat{s}_{\ell m}^B$, from which we can compute the cross-spectrum. Because the noise between both estimates are

supposed to be uncorrelated, the resulting mean power spectrum estimate is a combination of the CMB signal and foreground residuals. Considering only one foreground signal, f , we write

$$\hat{C}_\ell^{AB} \equiv \langle \hat{s}_{\ell m}^A \hat{s}_{\ell m}^B \rangle \quad (2.33)$$

$$= C_\ell^{\text{CMB}} + \frac{C_\ell[\delta f, \delta f] + (\epsilon_A + \epsilon_B)C_\ell[\delta f, f] + \epsilon_A \epsilon_B C_\ell[f, f]}{(1 - \hat{\alpha}_A)(1 - \hat{\alpha}_B)}, \quad (2.34)$$

where we defined $C_\ell[x, y]$ as the cross-power spectrum between the maps x and y . The model also assumes no correlation between the CMB and the foregrounds signals, $C_\ell[s, f] = 0$.

The second term of Eq. (2.34) quantifies the spectrum bias induced by the foreground residuals. The coefficient estimate error ϵ depends of course of the method used to estimate $\hat{\alpha}$.

Considering the case where $\epsilon = 0$, (i.e. $\hat{\alpha} = \bar{\alpha}$). We show in Fig. 2.9 the foreground residuals level, estimated on 40% and 90% of the sky, and for all *Planck* intermediate channels (44 to 217 GHz). The residuals maps are computed as $\delta_D(\hat{n})f_D(\hat{n})$ and $\delta_S(\hat{n})f_S(\hat{n})$, and their contribution to the spectra are estimated as in Eq. (2.34). The logarithmic value of the spectra are then quadratically fitted before being plotted. We also indicate the initial level of contamination, $\alpha_D(\hat{n})f_D(\hat{n})$ and $\alpha_S(\hat{n})f_S(\hat{n})$, which was already displayed in Fig. 2.6.

When using one global coefficient to remove the foregrounds, we see that the contamination is roughly decreased by two orders of magnitude. The foreground residuals amplitudes for all channels are under the CMB E-modes signal. For a sky fraction of $f_{\text{sky}} = 0.4$, the B-modes residual foreground level is of the same order as the CMB tensor contribution for $r = 10^{-2}$. Those results are quite encouraging, and show how a simple template subtraction technique can remove much of the contamination. We highlight that this forecast does not account for all the complexity of a complete dataset analysis, and it is highly model-dependent. Different level of spatial variations of the foreground SED will change significantly the impact of the residuals δf on the spectra. An end-to-end analysis from foreground cleaning to spectra estimate on *Planck* simulations and data is performed in chapter 4.

In order to further reduce the contamination residuals, one would seek to reduce the spread of the term δ for each foreground. This can be achieved by performing more localised cleaning, as discussed hereafter.

5.3 From global to patches

With upcoming CMB polarisation measurements, we expect to see more spatial variations of the foregrounds SED. Those experiments will allow to map the sky with high sensitivity over a wide range of frequency. We investigate how the estimation of the foreground coefficient α localised on patches of the sky can efficiently reduce the level of residual contaminations.

Methodology

For this purpose, the *Healpix* package (K. M. Gorski et al. 2005) offers a rather simple way to define patches over the sky. Within it, two pixel orderings are available. First, the ‘ring’ ordering, which simply counts the pixels from north to the south pole, along each isolatitude ring. Secondly, the ‘nested’ ordering, which is of special interest here, and for which the pixels are arranged in twelve regions on the sky. As shown in Fig. 2.10, each region is organised in a tree structure. As the map resolution is increased, each pixel is subdivided into four subpixels. The number of pixel per map for both orderings is defined as $n_{\text{pix}} = 12 n_{\text{side}}^2$ with $n_{\text{side}} = 2^n$ and $n \in \mathbb{N}$, as shown in Tab. 2.2. In the following, we will refer to the resolution value of the patches maps as p_{side} . We also define an additional resolution, $p_{\text{side}} = 0$, for when a global coefficient is estimated on the sky, which can thus be seen as a unique pixel.

Once the coefficients in each patch are estimated, it is straightforward to build a *Healpix* map of the $\hat{\alpha}(\hat{n})$'s. We then upgrade the resulting map resolution in order to match that of

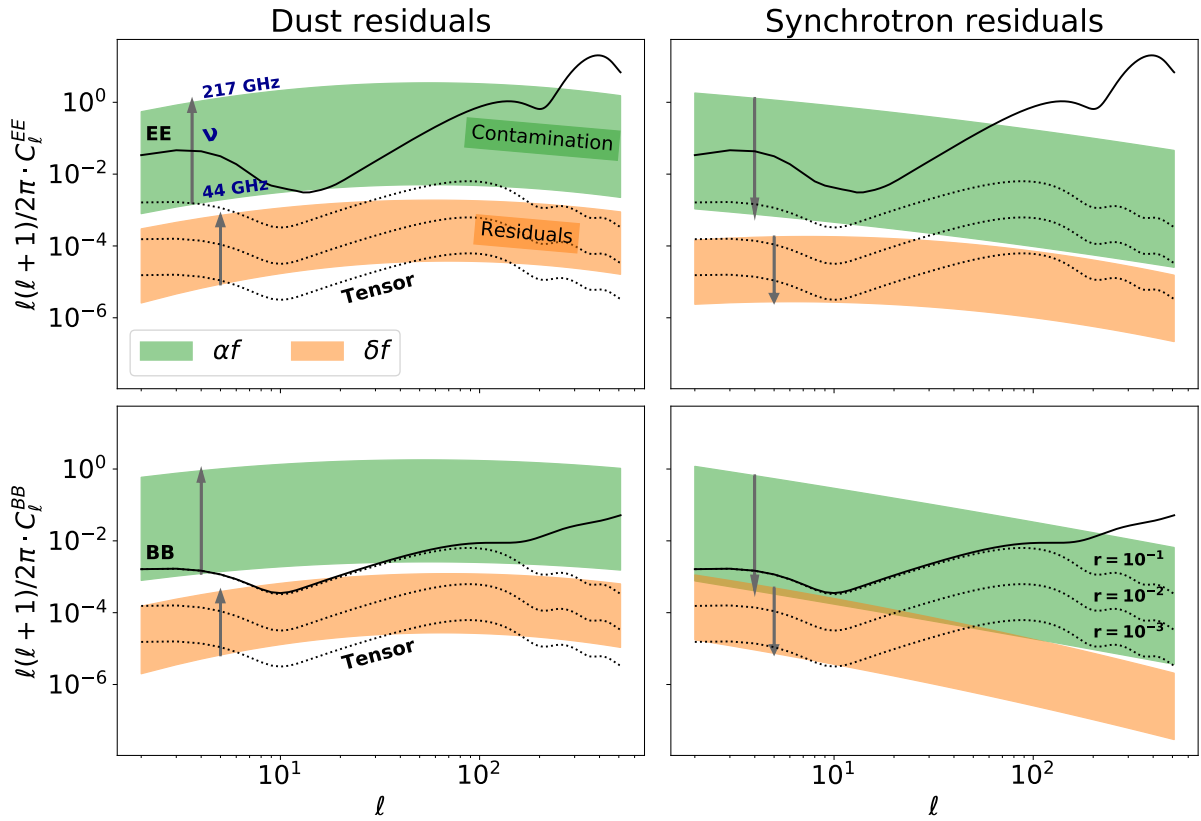


Figure 2.9: Forecast on the foreground residuals on 50% the sky for all intermediate *Planck* channels (44 to 217 GHz), based on the PySM foreground simulations. The arrows go from the lowest to the highest frequencies, and their signal is indicated by the coloured bands. The no-cleaning case (initial level of contamination), αf , corresponds to the green upper bands in each panel, while the lower orange bands correspond to the foregrounds residuals, δf .

the datasets, and generally smooth the map $\hat{\alpha}(\hat{n})$ with a Gaussian kernel. Finally, replacing α by the coefficients map in Eq. (2.29), we can compute a clean CMB map estimation. The smoothing of the coefficient map assures a continuous transition of the CMB estimate between the patches.

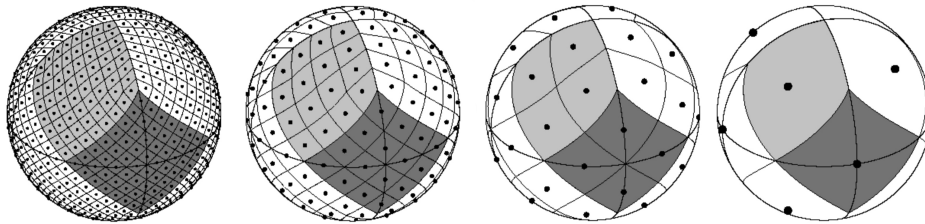


Figure 2.10: Healpix pixel nested resolution organization. Sub-pixels can always be grouped into pixels corresponding to one resolution below, down to 12 main regions (or ‘big’ pixels) displayed on the far right.

Table 2.2: Healpix correspondence between map resolution n_{side} and the number of pixels n_{pix} .

n_{side}	0	1	2	4	8	16	32	64	128	256	512
n_{pix}	1	12	48	192	768	3072	12288	49152	196608	786432	3145728

Forecast on patch-cleaning

We can perform a similar forecast on the foreground residuals as in Sec. 5.2, now considering patch cleaning. We select two resolutions, $p_{\text{side}} = 8$ and $p_{\text{side}} = 32$. To build the patch map of $\bar{\alpha}(\hat{n})$, we take the initial map of $\alpha(\hat{n})$ at $n_{\text{side}} = 256$, then we average the sub-pixels for each patch. Following the methodology proposed in Sec. 5.3, we smooth the patch map $\bar{\alpha}(\hat{n})$ using a 4° and 3° Gaussian beam respectively for $p_{\text{side}} = 8$ and $p_{\text{side}} = 32$. We then compute the foreground residuals as $\delta f(\hat{n}) = (\alpha(\hat{n}) - \bar{\alpha}(\hat{n}))f$ for the dust and the synchrotron signals. The residuals amplitude are shown in Fig. 2.11. Compared to Fig. 2.8, we see that the residual amplitude is drastically decreased.

The power spectra of the foreground residuals as computed in Eq. (2.34) are shown in Fig. 2.12 for frequencies between 44 and 217 GHz, and for two sky coverages, 40% and 90%. Compared to Fig. 2.9, we see that using a patch cleaning globally decreases the residuals level, especially at large angular scales ($\ell \lesssim 10$). For a patch resolution $p_{\text{side}} = 8$, the amplitude is reduced by two orders of magnitude at large angular scales, and one order of magnitude at intermediate scales ($\ell > 10$), which is below the primordial CMB B-modes signal for $r = 10^{-3}$. For a patch resolution $p_{\text{side}} = 32$, the residuals are even further reduced, by four and three orders of magnitude for large and intermediate scales respectively.

Those results on patch cleaning only serve as indications, and they highly depend on the foreground modelling used to simulate the signal foreground SED. Moreover, we supposed that the patch map of the coefficient α is precisely estimated, which can be difficult to achieve in practice. Moreover, we only average the value of the input $\alpha(\hat{n})$ of each sub-pixel in the patches. In practice, the cleaning methods will generally give more weight to the pixels for which the foreground signal is the highest, thus favouring estimates $\hat{\alpha}(\hat{n})$ that reduce even more the overall residuals amplitude. The performance of patch-cleaning methods using Monte-Carlo simulations will be further discussed in Sec. 10.

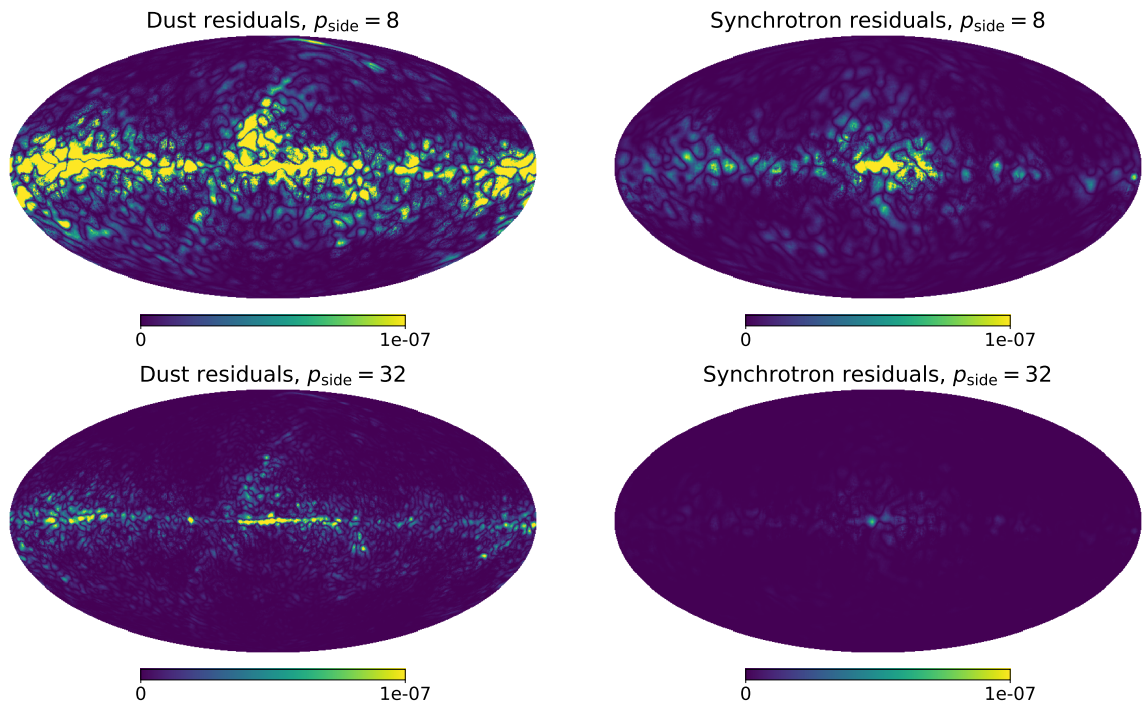


Figure 2.11: Foreground residuals as presented in Fig. 2.8, but using patch coefficient cleaning.

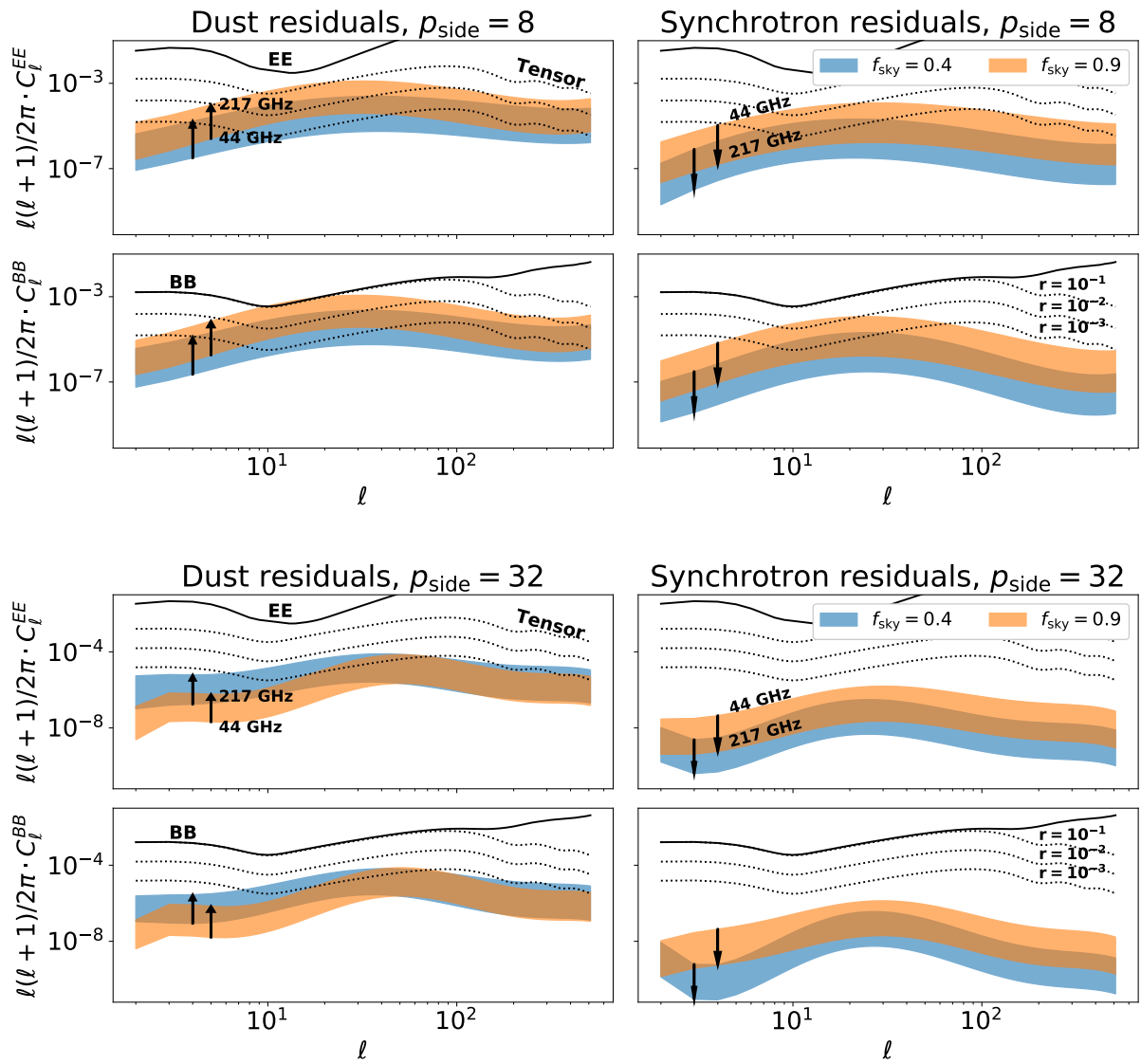


Figure 2.12: Forecast the foreground residuals using patch-cleaning for 40% and 90% of the sky on all intermediate *Planck* channels (44 to 217 GHz), and based on the PySM foreground simulations. We use two patch resolutions, $p_{\text{side}} = 8$ and $p_{\text{side}} = 32$. The spectra estimation is similar to what was presented in Fig. 2.9

6 Linear regression estimators

In this section we present a method to estimate the foreground coefficient α using linear regression methods. We consider one global coefficient on the sky, and no foreground polarisation.

6.1 Ordinary linear Regression

As a first approach for fitting $\alpha(\hat{n})$, we will consider the *ordinary* linear regression (referred to oLR hereafter), as adopted by the *WMAP* and *Planck* teams (Page et al. 2007; Bennett et al. 2013; Gold et al. 2011), (Planck 2015 Results. XI). We will see in this section that this method can produce biased estimates due to the presence of noise and CMB in the templates used in the fit. We therefore propose some solutions in order to obtain unbiased estimates.

Formalism

The oLR can be applied when assuming that the residuals covariance matrix C defined in Eq. (2.31) is fixed, using a fiducial value for the α 's, $C = C(\alpha^{\text{fid}})$. In that case, we can maximise analytically the likelihood, or equivalently minimise the following chi-square function,

$$\begin{aligned} -2 \ln \mathcal{L} &= \chi^2 \\ &= (d - \boldsymbol{\alpha}^\dagger \cdot \mathbf{t})^T C^{-1} (d - \boldsymbol{\alpha}^\dagger \cdot \mathbf{t}). \end{aligned} \quad (2.35)$$

Here, the T operator transposes the data vectors (i.e. in ‘pixel space’). Note that for the oLR estimator, the corresponding residual covariance matrix C defined in Eq. (2.31) must be rescaled by a factor of $1 - \sum \alpha$.

Minimizing for $\boldsymbol{\alpha}$, we obtain the following estimate

$$\begin{aligned} \frac{\partial \chi^2}{\partial \boldsymbol{\alpha}} &= 0 \\ \Leftrightarrow -2 \mathbf{t}^T C^{-1} [d - \boldsymbol{\alpha}^\dagger \cdot \mathbf{t}] &= 0 \\ \Leftrightarrow \mathbf{t}^T C^{-1} d &= \mathbf{t}^T C^{-1} \mathbf{t}^\dagger \boldsymbol{\alpha} \\ \Rightarrow \hat{\boldsymbol{\alpha}} &= \left(\mathbf{t}^T C^{-1} \mathbf{t}^\dagger \right)^{-1} \left(\mathbf{t}^T C^{-1} d \right). \end{aligned} \quad (2.36)$$

One foreground toy-model

Let us consider a toy-model with only one foreground component t , no Q - U correlation, and a homogeneous white noise for each pixel. The residual covariance matrix is thus diagonal, $C_{ij}^{-1} \equiv \delta_{ij} \sigma^{-2}$. The oLR solution of Eq. (2.36) reads

$$\hat{\alpha} = \frac{\sum_i^{n_{\text{pix}}} t_i d_i}{\sum_i^{n_{\text{pix}}} t_i^2}, \quad (2.37)$$

where the summation over the pixels is applied on both Q and U components, i.e. $\sum_i^{n_{\text{pix}}} t_i d_i = \sum_i^{n_{\text{pix}}} (t_i^Q d_i^Q + t_i^U d_i^U)$, and $\sum_i^{n_{\text{pix}}} t_i^2 = \sum_i^{n_{\text{pix}}} (t_i^Q t_i^Q + t_i^U t_i^U)$.

If we develop the mean of both terms of the ratio,

$$\sum_i^{n_{\text{pix}}} t_i d_i = \alpha \langle f^2 \rangle + \langle s^2 \rangle, \quad (2.38)$$

$$\sum_i^{n_{\text{pix}}} t_i^2 = \langle f^2 \rangle + \langle s^2 \rangle + \langle n_t^2 \rangle, \quad (2.39)$$

we observe that the estimator is biased by the CMB signal variance $\langle s^2 \rangle$ and template noise variance $\langle n_t^2 \rangle$,

$$\langle \hat{\alpha} \rangle \rightarrow \frac{\alpha \langle f^2 \rangle + \langle s^2 \rangle}{\langle f^2 \rangle + \langle s^2 \rangle + \langle n_t^2 \rangle}. \quad (2.40)$$

For a CMB (respectively noise) dominated template, the foreground coefficient α will be biased toward 1 (respectively 0).

This particular case, where both the data and the templates are noisy, is part of what is referred to as error-in-variables models¹. We propose some solutions to remove the bias in Sec. 6.3.

Two foregrounds toy-model

Let us develop the oLR considering two foreground components, the dust f_D and synchrotron f_S , for which we respectively use the two templates maps t_D and t_S . The oLR solution of Eq. (2.36) reads

$$\begin{pmatrix} \hat{\alpha}_D \\ \hat{\alpha}_S \end{pmatrix} = \begin{pmatrix} t_D^T C^{-1} t_D & t_D^T C^{-1} t_S \\ t_S^T C^{-1} t_D & t_S^T C^{-1} t_S \end{pmatrix}^{-1} \begin{pmatrix} t_D^T C^{-1} d \\ t_S^T C^{-1} d \end{pmatrix}. \quad (2.41)$$

If we develop the resulting estimations, we get

$$\hat{\alpha}_D = \frac{t_S^T t_S \cdot t_D^T d - t_D^T t_S \cdot t_S^T d}{t_D^T t_D \cdot t_S^T t_S - 2t_D^T t_S}, \quad (2.42)$$

$$\hat{\alpha}_S = \frac{-t_S^T t_D \cdot t_D^T d + t_D^T t_D \cdot t_S^T d}{t_D^T t_D \cdot t_S^T t_S - 2t_D^T t_S}. \quad (2.43)$$

For the seek of clearness, for the equation above only, every dataset products of the form $x^T y$, with $\{x, y\} \in \{d, t_D, t_S\}$, is weighted by the inverse covariance matrix C^{-1} (not written), meaning that $x^T y = x^T C^{-1} y$. On average, the estimations will tend to

$$\langle \hat{\alpha}_D \rangle \rightarrow \frac{(\langle f_S^2 \rangle + \langle n_S^2 \rangle + \langle s^2 \rangle) \cdot (\alpha_D \langle f_D^2 \rangle + \langle s^2 \rangle) - \langle s^2 \rangle \cdot (\langle s^2 \rangle + \alpha_S \langle f_S^2 \rangle)}{(\langle f_D^2 \rangle + \langle s^2 \rangle + \langle n_D^2 \rangle) \cdot (\langle f_S^2 \rangle + \langle s^2 \rangle + \langle n_S^2 \rangle) - 2 \langle s^2 \rangle}, \quad (2.44)$$

$$\langle \hat{\alpha}_S \rangle \rightarrow \frac{-\langle s^2 \rangle \cdot (\langle s^2 \rangle + \alpha_D \langle f_D^2 \rangle) + (\langle f_D^2 \rangle + \langle n_D^2 \rangle + \langle s^2 \rangle) \cdot (\alpha_S \langle f_S^2 \rangle + \langle s^2 \rangle)}{(\langle f_D^2 \rangle + \langle s^2 \rangle + \langle n_D^2 \rangle) \cdot (\langle f_S^2 \rangle + \langle s^2 \rangle + \langle n_S^2 \rangle) - 2 \langle s^2 \rangle}. \quad (2.45)$$

Both are biased by the CMB variance $\langle s^2 \rangle$ and the templates noise $\langle n_t^2 \rangle$.

6.2 Normalised-model linear regression

We found that 'normalising' the linear regression by $1 - \sum_i^{D,S} \alpha_i$ removes the CMB bias found in the oLR. In the following, we refer to this normalised linear regression as the nLR method.

One foreground example

Going back to our one-foreground toy-model, we now minimise the normalised chi-square,

$$\chi^2 = \frac{(d - t\alpha)^T}{1 - \alpha} C^{-1} \frac{(d - t\alpha)}{1 - \alpha}, \quad (2.46)$$

¹Here, the CMB signal is considered as a source of noise in the context of foreground linear regression.

which gives the solution

$$\hat{\alpha} = \frac{(d-t)^T C^{-1} d}{(d-t)^T C^{-1} t} \quad (2.47)$$

$$= \frac{d^T C^{-1} d - t^T C^{-1} d}{d^T C^{-1} t - t^T C^{-1} t}. \quad (2.48)$$

This estimator is still biased, but only because of the dataset and template noise terms. Indeed, considering a simplified case where C is proportional to the identity matrix, it is easy to show that

$$\langle \hat{\alpha} \rangle \rightarrow \frac{\alpha f^2 + \langle n_d^2 \rangle}{f^2 + \langle n_t^2 \rangle}. \quad (2.49)$$

Two foregrounds

The nLR method is easily generalisable to two foregrounds components. The solution reads

$$\hat{\alpha}_D = \frac{\mathbf{1}^T \mathbf{C}^{-1} \begin{pmatrix} 0 \\ 1 \\ 0 \end{pmatrix}}{\mathbf{1}^T \mathbf{C}^{-1} \begin{pmatrix} 1 \\ 0 \\ 0 \end{pmatrix}}, \quad \hat{\alpha}_S = \frac{\mathbf{1}^T \mathbf{C}^{-1} \begin{pmatrix} 0 \\ 0 \\ 1 \end{pmatrix}}{\mathbf{1}^T \mathbf{C}^{-1} \begin{pmatrix} 1 \\ 0 \\ 0 \end{pmatrix}}, \quad (2.50)$$

with the dataset covariance matrix defined as

$$\mathbf{C} \equiv \langle m C^{-1} m^T \rangle, \quad \text{with} \quad m \equiv \begin{pmatrix} d \\ t_1 \\ t_2 \end{pmatrix}. \quad (2.51)$$

The expansion of the coefficients estimation of Eq. (2.50) reads

$$\hat{\alpha}_D = \frac{(d^T f_S)^2 - d^T d \cdot (f_S^T f_S - f_D^T f_S) - d^T f_S \cdot f_D^T f_S - d^T f_D \cdot (d^T f_S - f_S^T f_S)}{f_D^T f_S \cdot (d^T f_D - f_D^T f_S + d^T f_S) - d^T f_D^T \cdot f_S^T f_S - f_D^T f_D \cdot (d^T f_S - f_S^T f_S)}, \quad (2.52)$$

$$\hat{\alpha}_S = \frac{(d^T f_D)^2 - d^T d \cdot (f_D^T f_D - f_D^T f_S) - d^T f_D \cdot f_D^T f_S - d^T f_S \cdot (d^T f_D - f_D^T f_D)}{f_D^T f_S \cdot (d^T f_D - f_D^T f_S + d^T f_S) - d^T f_D^T \cdot f_S^T f_S - f_D^T f_D \cdot (d^T f_S - f_S^T f_S)}, \quad (2.53)$$

where each dataset summation $x^T y$, with $\{x, y\} \in \{d, t_1, t_2\}$, is weighted by the inverse covariance matrix C^{-1} defined in Eq. (2.31) (not to be confused with \mathbf{C}^{-1} defined in Eq. (2.51)). Therefore, for the equation above only, $x^T y \equiv x^T C^{-1} y$.

As before, we can identify the terms that will cause a bias in the estimate. One can check that, on average, the CMB variance will not induce any bias for noiseless maps. We identify the usual datasets noise variance bias induced by the terms $d^T d$ and $f_i^T f_i$.

6.3 Bias removal

Interestingly, the bias for the nLR comes from the noise present both in the intermediate channel and in the templates, n_d and n_D, n_S . While for the oLR method, only the template noise variances play a role in the estimate bias, in addition to the CMB variance present in the maps. We propose three solutions to remove or mitigate the bias observed in both linear regression methods.

Variance subtraction

The bias terms can be evaluated and subtracted. Therefore, it requires an estimate of the noise and signal variances, $\langle n_i^2 \rangle$ and $\langle s^2 \rangle$. This is possible when the datasets noise variance is known with sufficiently high precision. The CMB signal variances is mainly driven by the E -modes amplitude. Since the E -modes signal is measured with sufficiently high precision, the CMB variance can fairly be evaluated and removed². This bias subtraction is a known solution for generic error-in-variable models (see for example Patriota et al. 2009 for heteroscedastic noise).

Practically, for any map $m_i \in \{d, t_i\}$ with $i \in \{D, S\}$, the product between two maps can be expanded as

$$\begin{aligned}
m_i^T C^{-1} m_j &= m_{iQ}^T [C^{-1}]_{QQ} m_{jQ} + m_{iU}^T [C^{-1}]_{UU} m_{jU} + m_{iQ}^T [C^{-1}]_{QU} m_{jU} + m_{iU}^T [C^{-1}]_{UQ} m_{jQ} \\
&= \sum_{p,p'}^{n_{\text{pix}}} (f_{iQ}^p f_{jQ}^{p'} + \delta_{ij} N_{i,QQ}^{pp'} + S_{QQ}^{pp'}) [C^{-1}]_{QQ}^{pp'} \\
&\quad + \sum_{p,p'}^{n_{\text{pix}}} (f_{iU}^p f_{jU}^{p'} + \delta_{ij} N_{i,UU}^{pp'} + S_{UU}^{pp'}) [C^{-1}]_{UU}^{pp'}, \\
&\quad + \sum_{p,p'}^{n_{\text{pix}}} 2(f_{iQ}^p f_{jU}^{p'} + \delta_{ij} N_{i,QU}^{pp'} + S_{QU}^{pp'}) [C^{-1}]_{QU}^{pp'},
\end{aligned} \tag{2.54}$$

where we have split the inverse residual covariance matrix into four square blocks,

$$C^{-1} = \begin{pmatrix} [C^{-1}]_{QQ} & [C^{-1}]_{QU} \\ [C^{-1}]_{UQ} & [C^{-1}]_{UU} \end{pmatrix}. \tag{2.55}$$

Thereby, to each occurrence of $m_i^T C^{-1} m_j$ in the linear regression estimator, one have to subtract the bias value

$$\begin{aligned}
b_{ij} &= \sum_{p,p'}^{n_{\text{pix}}} \left(\delta_{ij} N_{i,QQ}^{pp'} + S_{QQ}^{pp'} \right) [C^{-1}]_{QQ}^{pp'} \\
&\quad + \left(\delta_{ij} N_{i,UU}^{pp'} + S_{UU}^{pp'} \right) [C^{-1}]_{UU}^{pp'} \\
&\quad + 2 \left(\delta_{ij} N_{i,QU}^{pp'} + S_{QU}^{pp'} \right) [C^{-1}]_{QU}^{pp'}.
\end{aligned} \tag{2.56}$$

Map smoothing

An other solution consists in applying a spatial smoothing of the maps. This process mainly reduces small angular scale amplitudes, where the noise and CMB signal become dominant compared to the foreground signal. In Fourier space it is equivalent to convolve the spectrum with a squared beam function, b_l^2 . We draw some of them in Fig. 2.13, using a Gaussian beam with different value of the full width at half maximum (FWHM).

Smoothing the dataset maps can thus mitigate the variance bias induced at those small angular scales. One drawback is that it spatially correlates the foreground signals, which is not desired if the foreground cleaning must be performed locally.

Applying this technique to a map is warranted when the foreground signal amplitude is much higher than the noise and the CMB signal at large angular scales, for which the smoothing process has a more limited effect. This is the case for the template maps $t(\hat{n})$, which are especially selected for this feature. For the intermediate channel $d(\hat{n})$, things become more complicated.

²For datasets that have been smoothed, the noise bias must be re-evaluated using Monte-Carlo simulations

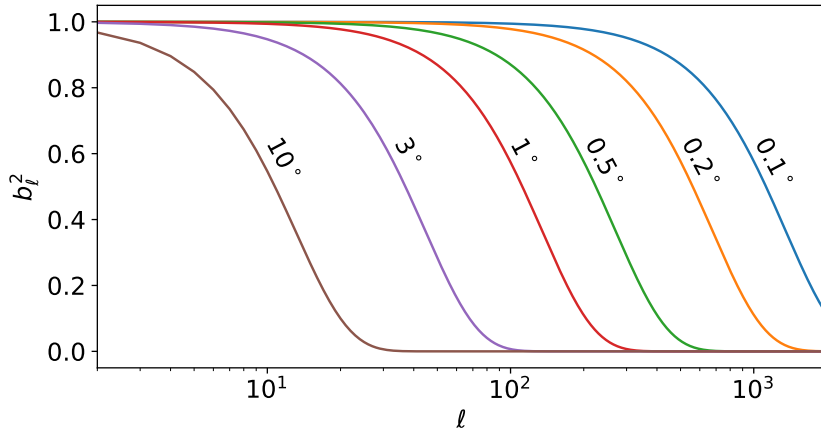


Figure 2.13: Squared Gaussian beam functions, b_ℓ^2 , from 0.1 to 10 deg.

Depending on which frequency channel is used, the foreground signal is not always above the CMB or the noise variance at large angular scales ($\ell \simeq 50$), as seen in Fig. 2.6.

The smoothing technique is actually only effective for the oLR estimator. Indeed, for this method, the bias are only produced by terms involving the map products of the form³ $\langle t^T t \rangle \rightarrow f^T f + \langle s^2 \rangle + \langle n_t^2 \rangle$ and $\langle t^T d \rangle \rightarrow \alpha f^T f + \langle s^2 \rangle$, see Eqs. (2.37), (2.42) and (2.43). After the datasets being smoothed, only the large angular scale will remain. Since $f^T f \gg \langle s^2 \rangle$ and $f^T f \gg \langle n_t^2 \rangle$, as well as $\alpha f^T f \gg \langle s^2 \rangle$ and $\alpha f^T f \gg \langle n_t^2 \rangle$, for those scales, the bias become negligible.

This is not the case for the nLR estimator, which is built from additional terms involving auto product of the intermediate channel $d(\hat{n})$, of the form $d^T d \rightarrow \alpha^2 f^T f + \langle s^2 \rangle + \langle n_t^2 \rangle$, see Eqs. (2.48), (2.52) and (2.53). Here, because in general $\alpha^2 \ll 1$, the term $\alpha^2 f^T f$ can have an amplitude comparable to $\langle s^2 \rangle$ or $\langle n_t^2 \rangle$, and the bias is not removed at large angular scales. Therefore, the higher the α , the lower this estimator is biased.

Cross correlation

A third solution, which only removes the noise variance bias, makes use of cross-correlations between datasets. At each frequency, we consider two sets of maps. Those, labelled d_A , d_B for the intermediate channel, and t_A , t_B for the templates, are assumed to have uncorrelated noise, i.e. $\langle n_{d_A} n_{d_B} \rangle = 0$ and $\langle n_{t_A} n_{t_B} \rangle = 0$. Such construction is easily possible by splitting the detector measurements in half, or select data measured during different period of times. By replacing every occurrences of both $d^T d$ (respectively $t^T t$) by $d_A^T d_B$ (respectively $t_A^T t_B$) in the linear regression estimators, we get rid of the noise bias when the number of pixels is sufficiently large. Indeed, in that case,

$$\langle d_A d_B \rangle \xrightarrow{\langle n_{d_A} n_{d_B} \rangle = 0} \langle s^2 \rangle + \alpha_D^2 f_D^2 + \alpha_S^2 f_S^2, \quad (2.57)$$

$$\langle t_A t_B \rangle \xrightarrow{\langle n_{t_A} n_{t_B} \rangle = 0} \langle s^2 \rangle + f^2. \quad (2.58)$$

For other cross-terms of the estimators which are of the form $d^T t$, we can simply average all four combinations $d_X^T t_Y$, with $\{X, Y\} \in \{A, B\}$.

This technique is especially suited for the nLR, since only the datasets noise variances are involved in the bias.

³For simplicity, we dropped the C^{-1} matrix, but the discussion is still general.

Nomenclature

To identify which bias subtraction process is combined with the methods, we use the following labels :

- the variance subtraction is identified by v_c , v_n , or v_{cn} , when subtracting respectively the CMB variance, the noise variance, or both.
- the smoothing solution is identified by s_θ , with θ the FWHM smoothing angle (in degree).
- the cross-correlation solution is identified by x .

For example, the normalised linear regression estimator using the cross-correlation solution will be referred to as $xnLR$, while the ordinary linear regression using a 3° Gaussian beam smoothing will be referred to as s_3oLR .

6.4 Methods results and comparison

We test the linear regression methods presented above (oLR and xLR) on the two sky models introduced in Sec. 2, i.e. the PySM and the homogeneous model. We consider two map resolutions, $n_{side} = 32$ and $n_{side} = 128$, and a *Planck*-like noise level equivalent to the 100 GHz channel. The distributions of the coefficients $\hat{\alpha}$ estimated from 1000 M-C simulations on $f_{sky} = 0.9$ (90% percent of the sky) are displayed in Fig. 2.14. We compare six estimations :

- oLR , the ordinary linear regression, for which no de-biasing process is applied.
- v_noLR , for which the template noise variance bias is subtracted.
- v_coLR , where the CMB variance bias is subtracted.
- v_cnoLR , for which both the CMB and noise variances bias are subtracted.
- s_3oLR , where we performed a 3° Gaussian smoothing of the maps.
- $xnLR$, the normalised linear regression using cross-datasets.

The first three cases are selected to highlight the possible bias discussed during the introduction of both linear regressions methods. The three remaining cases are expected to produce unbiased estimates of α , as each makes use of one of the three bias removing solutions proposed in Sec. 6.3.

For comparison, we also draw the distributions of the input coefficient values $\alpha(\hat{n})$ of the sky model for which they are allowed to vary spatially, i.e. the PySM skies. For this comparison the matrix C^{-1} used for each method only accounts for the sky masking, and the noise as well as the CMB variance on the sky. We discuss more complex weightings that take into account the CMB correlations in Sec. 11.

On Fig. 2.14, we first remark that, as expected, the oLR , v_noLR , and v_coLR estimators are biased. This is clearly visible on the simple homogeneous sky model. The dust coefficient is not much impacted by the CMB variance bias, since the distribution of both the v_coLR and the oLR estimators are similar. We can appreciate how the CMB variance brings the synchrotron coefficient toward 1 (v_noLR case), while the noise variance biases the estimation toward 0 (v_coLR case). The bias mainly impact the synchrotron coefficient α_S , and when the map resolution is high ($n_{side} = 128$). The latter effect is understandable, since the foreground signals dominate at large angular scales, while the CMB and noise contributions, and their induced bias, are expected to show up at smaller angular scale, i.e. for higher map resolutions.

For this model, the three other methods, namely v_cnoLR , s_3oLR , and $xnLR$, successfully produce unbiased estimates $\hat{\alpha}$, with similar precision. For each, the dust coefficient is estimated with a precision much smaller than its true spread on the sky for the PySM model. This is

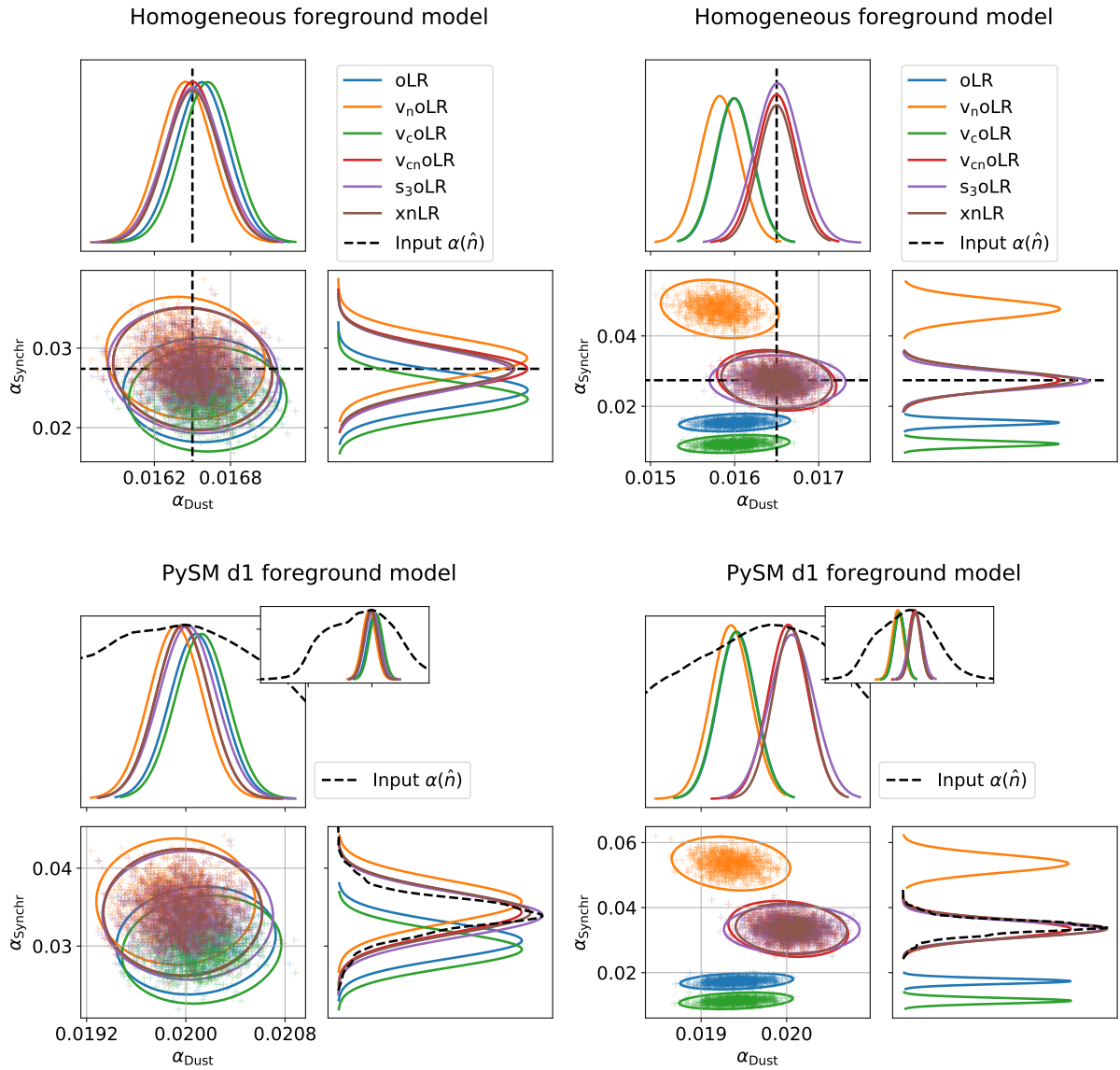


Figure 2.14: Foreground coefficient distributions for the linear regression methods at the resolution $n_{\text{side}} = 32$ (left), and $n_{\text{side}} = 128$ (right). Results are shown for the homogeneous foregrounds model (top), and the PySM model (bottom).

not the case for the synchrotron, for which the error on $\hat{\alpha}_S$ is of the same order as its input dispersion on the sky.

6.5 Summary and conclusion

In this section dedicated to the linear regression methods, we showed that the ordinary estimator, **oLR**, can be biased by both the CMB and the noise variances. We proposed some solutions by either evaluating and subtracting the bias (**v_{cn}oLR**), or by applying a 3° Gaussian smoothing on the maps (**s₃oLR**). An other approach was to normalise the model by a factor $1 - \sum_i \alpha_i$, whose solution is free from the CMB variance bias. The remaining noise variance bias can be removed by using cross-datasets, considering they have uncorrelated noise (**xnLR**).

Those unbiased methods all perform similar results on the PySM sky in term of precision and error on the estimation of the foreground coefficients α . All unbiasing processes have different characteristics :

- The maps smoothing can be quite powerful and simple to perform, and only mitigates the bias on the **nLR** method. However, the smoothing can spatially correlates the foregrounds signal, thus reducing the possibility to perform localised cleaning. Moreover, the degree of smoothing is arbitrary, and can also reduce the foreground signal amplitude, therefore increasing the uncertainty of the estimation of α .
- Subtracting the bias terms requires a high degree of confidence about the template noise and the CMB signal variance. For example, any systematic errors not included during the noise variance bias subtraction can lead to potential bias. Moreover, any pre-smoothing of the datasets will change the bias levels. The noise and CMB variance bias must thus be re-evaluated for each pixel.
- Finally, using the cross-correlation requires split-datasets to be provided, and their noise to be uncorrelated. It is especially effective on the **nLR** method, as it is affected by the maps noise variance only.

7 Maximum likelihood estimator

As we demonstrated in Sec. 6, the ordinary and normalised linear regressions are biased by the noise, the CMB variance, or both. One would therefore prefer to rely on writing the full likelihood in order to avoid any unbiasing processing such as map smoothing, cross-datasets, or bias subtractions. In this section, we develop a likelihood algorithm that allows to compute the foreground coefficients α for an error-in-variable model, that is, in our case, three datasets containing correlated noise (here, the CMB signal) and some noise. We consider one global coefficient α on the sky and no polarisation rotation.

7.1 One foreground model

Model

Let us first consider one foreground contamination. To express the likelihood we group all maps into a single $n_\nu n_{\text{pix}}$ -size vector m , with $n_\nu = 2$ the number of maps,

$$m \equiv \begin{pmatrix} d \\ t \end{pmatrix} = \begin{pmatrix} s + \alpha f + n_d \\ s + f + n_t \end{pmatrix}. \quad (2.59)$$

We consider $n_{\text{pix}} + 1$ unknowns : the foreground signal f with size n_{pix} , and α with size 1. The noise variables are n_p , n_t and the CMB s . The $n_\nu n_{\text{pix}} \times n_\nu n_{\text{pix}}$ residual covariance matrix reads

$$C \equiv \text{Cov}[m] = \begin{pmatrix} S + N_d & S \\ S & S + N_t \end{pmatrix}. \quad (2.60)$$

Maximizing the Likelihood function $\mathcal{L}(m|\alpha, f)$ is equivalent to minimize the following chi-square function,

$$-2 \ln \mathcal{L}(m|\alpha, f) = \chi^2(m|\alpha, f) \quad (2.61)$$

$$= \left(m - \sum_{\nu}^{n_\nu} B_\nu f \alpha^T e_\nu \right)^T C^{-1} \left(m - \sum_{\nu}^{n_\nu} B_\nu f \alpha^T e_\nu \right), \quad (2.62)$$

with $\alpha \equiv (\alpha, 1)^T$.

In Eq. (2.62), we defined the i -th canonical basis vector e_i for the n_ν -dimensional space as

$$e_i = (0, \dots, 0, 1, 0, \dots, 0)^T, \quad (2.63)$$

for which only the i 'th entry is non-zero, while

$$B_i \equiv (0_{n_{\text{pix}} \times n_{\text{pix}}}, \dots, 0_{n_{\text{pix}} \times n_{\text{pix}}}, 1_{n_{\text{pix}} \times n_{\text{pix}}}, 0_{n_{\text{pix}} \times n_{\text{pix}}}, \dots, 0_{n_{\text{pix}} \times n_{\text{pix}}})^T, \quad (2.64)$$

are $n_{\text{pix}} n_\nu \times n_\nu$ matrices, for which only the i 'th block-entry is non-zero.

The matrices B_i and vectors e_i are used to vectorize the product $f \cdot \alpha^T = (\alpha f, f)$, by staking their columns into a single vector. For $n_\nu = 2$, we thus have $e_0 = (1, 0)^T$, $e_1 = (0, 1)^T$, and $B_0 = (1_{n_{\text{pix}} \times n_{\text{pix}}}, 0_{n_{\text{pix}} \times n_{\text{pix}}})^T$, $B_1 = (0_{n_{\text{pix}} \times n_{\text{pix}}}, 1_{n_{\text{pix}} \times n_{\text{pix}}})^T$.

For the seek of compactness, we define the $n_{\text{pix}} n_\nu \times n_{\text{pix}}$ matrix $A(\alpha) \equiv \sum_{\nu}^{n_\nu} B_\nu \alpha_\nu$, which depends on the coefficient α .

We can thus write the signal terms in the χ^2 function of Eq. (2.62) as

$$\begin{aligned} \sum_{\nu}^{n_\nu} B_\nu f \alpha^T e_\nu &= \begin{pmatrix} \alpha f \\ f \end{pmatrix} \\ &= Af. \end{aligned} \quad (2.65)$$

Likelihood maximisation

By minimizing the χ^2 function with respect to f , one gets an estimate of the foreground signal,

$$-2A^T C^{-1}(m - Af) = 0 \quad (2.66)$$

$$\Leftrightarrow \hat{f} = (A^T C^{-1} A)^{-1} A^T C^{-1} m. \quad (2.67)$$

We can do the same for the coefficient α , and obtain

$$-2(B_0 f)^T C^{-1}(m - B_0 f \alpha - B_1 f) = 0 \quad (2.68)$$

$$\Leftrightarrow \hat{\alpha} = [(B_0 f)^T C^{-1}(B_0 f)]^{-1} (B_0 f)^T C^{-1}(m - B_1 f). \quad (2.69)$$

Since we focus on the foreground parameter coefficient only, α , we marginalise the likelihood over the foreground signal f . Since the A matrix depends on α , it is clear that injecting the solution for f of Eq. (2.67) into Eq. (2.69) provides a non-linear equation for α . We thus rely on numerical methods to solve this system of equations.

7.2 Linearisation and Newton-Raphson algorithm

The minimum of the log-likelihood can be computed by linearizing the model around a fixed value of α_0 assumed to be sufficiently close to its true value, taking $\alpha = \alpha_0 + \delta\alpha$, with $\delta\alpha$ the new unknown. The second-order Taylor-expansion of the chi-square,

$$\chi^2(\alpha_0 + \delta\alpha) = \chi^2(\alpha_0) + \partial_\alpha \chi^2(\alpha_0) \delta\alpha + \frac{1}{2} \partial_\alpha^2 \chi^2(\alpha_0) \delta\alpha^2 + \mathcal{O}(\delta\alpha^3), \quad (2.70)$$

can now be minimized for $\delta\alpha$,

$$\frac{\partial [\chi^2(\alpha_0 + \delta\alpha)]}{\partial(\delta\alpha)} \simeq \partial_\alpha \chi^2(\alpha_0) + \partial_\alpha^2 \chi^2(\alpha_0) \delta\alpha = 0 \quad (2.71)$$

$$\Rightarrow \boxed{\delta\alpha \simeq -J^{-1} \partial_\alpha \chi^2(\alpha_0)}, \quad (2.72)$$

where $J \equiv \partial_\alpha^2 \chi^2(\alpha_0)$ is the Jacobian of the function $\partial_\alpha \chi^2(\alpha_0)$. The Eq. (2.72) allows us to easily generalize the problem for multiple foregrounds f_j and variables α_{f_j} . The roots of the derivative of χ^2 can finally be approximated by iterating $\alpha_{i+1} = \alpha_i + \delta\alpha$, which is known as a Newton-Raphson (N-R) iterative algorithm.

Applying this linearisation to our one-foreground toy-model, we write the chi-square function of Eq. (2.62) as follow,

$$\chi^2 = [m - B_0 f(\alpha + \delta\alpha) - B_1 f]^T C^{-1} [m - B_0 f(\alpha + \delta\alpha) - B_1 f], \quad (2.73)$$

which we now minimize for $\delta\alpha$,

$$\delta\alpha = [(B_0 f)^T C^{-1}(B_0 f)]^{-1} (B_0 f)^T C^{-1}(m - Af), \quad (2.74)$$

and iterate while updating at each step the foreground signal estimate, \hat{f} , using Eq. (2.67).

7.3 Two foregrounds model

The model

It is straightforward to add a second foreground component to our model,

$$m \equiv \begin{pmatrix} d \\ t_D \\ t_S \end{pmatrix} = \begin{pmatrix} s + \alpha_D f_D + \alpha_S f_S + n_d \\ s + f_D + n_D \\ s + f_S + n_S \end{pmatrix}, \quad (2.75)$$

where we assumed that each template map t_D or t_S is dominated by one foreground component, such that the signal of the other can be neglected.

The residual covariance matrix now reads

$$C \equiv \text{Cov}[m] = \begin{pmatrix} S + N_d & S & S \\ S & S + N_D & S \\ S & S & S + N_S \end{pmatrix}. \quad (2.76)$$

We define the foreground coefficients vectors $\boldsymbol{\alpha}_D \equiv (\alpha_D, 1, 0)^T$ and $\boldsymbol{\alpha}_S \equiv (\alpha_S, 0, 1)^T$, such that the log-likelihood reads

$$\begin{aligned} \chi^2 &= \left(m - \sum_{\nu}^{n_{\nu}} B_{\nu} f_D \boldsymbol{\alpha}_D^T e_{\nu} - \sum_{\nu}^{n_{\nu}} B_{\nu} f_S \boldsymbol{\alpha}_S^T e_{\nu} \right)^T C^{-1} \left(m - \sum_{\nu}^{n_{\nu}} B_{\nu} f_D \boldsymbol{\alpha}_D^T e_{\nu} - \sum_{\nu}^{n_{\nu}} B_{\nu} f_S \boldsymbol{\alpha}_S^T e_{\nu} \right) \\ &= (m - A_D f_D - A_S f_S)^T C^{-1} (m - A_D f_D - A_S f_S), \end{aligned} \quad (2.77)$$

where we have introduced the matrices $A_i \equiv \sum_{\nu}^{n_{\nu}} B_{\nu} \boldsymbol{\alpha}_{i,\nu}$ for $i \in \{D, S\}$

Likelihood maximization

We minimize the log-likelihood for f_D and f_S , which gives the following estimates of the foreground signals,

$$\begin{pmatrix} f_D \\ f_S \end{pmatrix} = \begin{pmatrix} A_D^T C^{-1} A_D & A_D^T C^{-1} A_S \\ A_S^T C^{-1} A_D & A_S^T C^{-1} A_S \end{pmatrix}^{-1} \begin{pmatrix} A_D^T C^{-1} m \\ A_S^T C^{-1} m \end{pmatrix}. \quad (2.78)$$

As for the one-foreground case, we linearise the model, taking $\alpha_D = \alpha_D^{(0)} + \delta\alpha_D$ and $\alpha_S = \alpha_S^{(0)} + \delta\alpha_S$ ⁴. The likelihood minimization for $\delta\alpha_D$ and $\delta\alpha_S$ gives

$$\begin{pmatrix} \delta\alpha_D \\ \delta\alpha_S \end{pmatrix} = \begin{pmatrix} (B_0 f_D)^T C^{-1} (B_0 f_D) & (B_0 f_D)^T C^{-1} (B_0 f_S) \\ (B_0 f_S)^T C^{-1} (B_0 f_D) & (B_0 f_S)^T C^{-1} (B_0 f_S) \end{pmatrix}^{-1} \begin{pmatrix} (B_0 f_D)^T C^{-1} (m - A_D f_D - A_S f_S) \\ (B_0 f_S)^T C^{-1} (m - A_D f_D - A_S f_S) \end{pmatrix}. \quad (2.79)$$

Finally, we iterate until the $\delta\alpha_{\nu}$'s are sufficiently small, and injecting at each step the foreground signal estimate of Eq. (2.78) into Eq. (2.79). We remark that the square matrix on the right hand side of the equation is non-other than inverse Jacobian matrix J^{-1} of the chi-square derivative functions $\partial_{\alpha_D} \chi^2$ and $\partial_{\alpha_S} \chi^2$, thereby we recover Eq. (2.72).

7.4 Noise and algorithm convergence

We first noticed that the matrix C is not invertible in the case of noiseless data. Even if, in practice, this is never the case, the noise level can be sufficiently low such that the matrix is badly conditioned. A solution is to regularise C by adding a small constant noise level to its diagonal. We observed that the number of iteration required by the N-R algorithm increases as the noise level becomes small. About 2 to 5 iterations are needed for a *Planck*-like noise level and a precision $\delta\alpha/\alpha$ of 1%, while, for the same precision, around 30 iterations are needed with $1 \mu\text{K.arcmin}$ noise level.

⁴The subscript refers to the foreground component 1 or 2, while the superscript (i) indicates the iteration step.

7.5 Results

We test the likelihood maximization estimator (referred to as MLE hereafter) on the two sky models introduced in Sec. 2, and one dataset resolutions, $n_{\text{side}} = 128$. The results from 1000 M-C simulations on $f_{\text{sky}} = 0.9$ are displayed in Fig. 2.15, and show that the method is not biased for the basic sky model, i.e. a linear homogeneous SED of the foregrounds. For the PySM model, the MC distributions of the estimations properly lie under the input distributions of the coefficients. The method thus successfully recovers the mean value of α , even on more complex sky models.

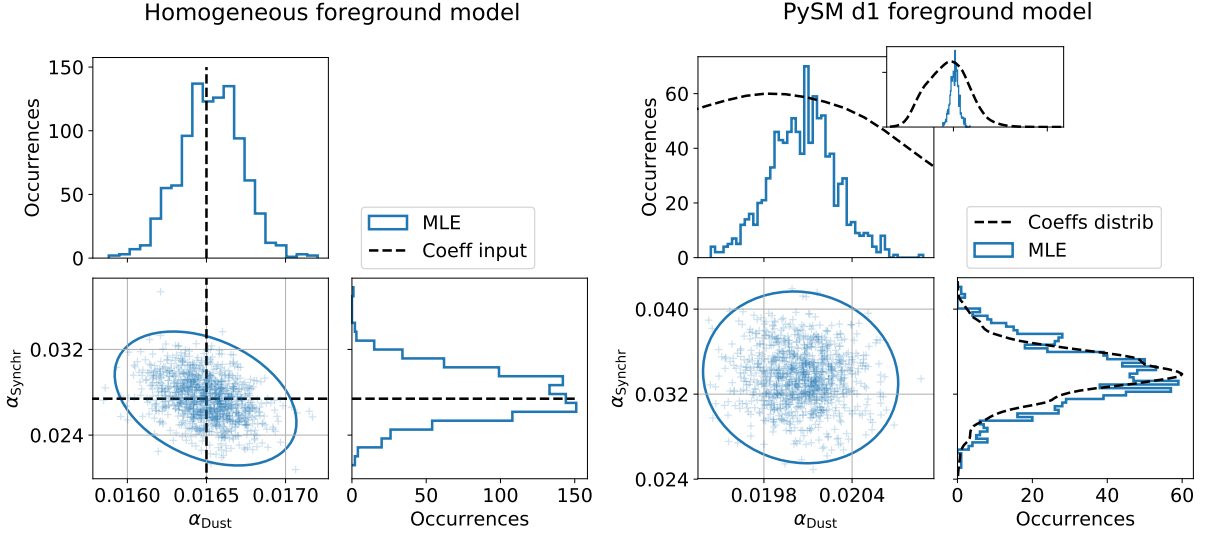


Figure 2.15: Foreground coefficient distributions for the MLE estimator at the resolution $n_{\text{side}} = 128$. Results are shown for the homogeneous foregrounds model (left), and the PySM model (right).

7.6 Conclusion and summary

There is some pros and cons using the MLE compared to the linear regressions methods previously proposed in the Sec. 6. By construction, the MLE provides the lowest error-bars on the estimation $\hat{\alpha}$, although the linear regression solutions seem to perform nearly just as good. The main advantage of the MLE is that it does not require any bias cancelling. The coefficients can be evaluated on each frequency maps independently, without using any cross-datasets as for the xnLR. However, the algorithm requires the inversion (or at least solving) for a larger covariance matrix, C , of size $3n_{\text{pix}} \times 3n_{\text{pix}}$, compared to the size $n_{\text{pix}} \times n_{\text{pix}}$ for the linear regression. The algorithm must be ran iteratively, which can be time consuming even for a few iterations ($\sim 3, 4$). Further comparison of all methods are made in sec. 12.

8 Internal Linear Combination

In this section, we introduce the ILC method, and adapt its implementations for our polarization datasets cleaning in the pixel domain. We discuss how the ILC can be parametrised to account for polarisation rotation at the end of the section.

8.1 Formalism

The ILC method estimates the CMB signal $s = (s^Q, s^U)^T$ by linearly combining n_ν frequency maps m_ν of size n_{pix} with some weight coefficients w_ν ,

$$\hat{s} = \sum_{\nu}^{n_\nu} w_\nu m_\nu \quad (2.80)$$

$$= \mathbf{w}^\dagger \mathbf{m}, \quad (2.81)$$

with \mathbf{w} an array of weight coefficients w_ν , and \mathbf{m} an array of the maps m_ν . The \dagger operator transposes in the map-space only (as opposed to pixel space).

The coefficients w_ν can be scalars (minimal parametrisation), or matrices, for example in order to weight independently the Q and U components of the maps, or to account for polarisation rotation of the signals with respect to a change of frequency at which the maps m_ν are measured. The choice of the weights parametrisation is discussed in Sec. 8.3. For now-on, we will keep the discussion as general as possible.

8.2 Optimal coefficients

In the case of pure temperature ILC, the weights \mathbf{w} are chosen such that they minimize the pixel variance of the CMB estimation. If we now write the variance of the polarization CMB estimation $\hat{P} \equiv \hat{s}^Q + i\hat{s}^U$, which leads to $\text{Var}[\hat{P}] = \langle \hat{P} \hat{P}^\dagger \rangle - \langle \hat{P} \rangle \langle \hat{P}^\dagger \rangle$, we see that this variance involves terms such as $\langle Q \rangle$ and $\langle U \rangle$, which are the pixel average of the Stokes components. However, those are only defined in the local frame, not as global quantities. Therefore, their mean value on the sky cannot be properly estimated. For this reason, the quantity that must be minimized is the *covariant* variance $\langle |\hat{P}|^2 \rangle = \langle (s^Q + is^U)(s^Q - is^U) \rangle$, which is independent of the local coordinate frame. We thus write

$$\langle |\hat{P}|^2 \rangle = \langle (\mathbf{s}^Q + i\mathbf{s}^U)(\mathbf{s}^Q - i\mathbf{s}^U) \rangle \quad (2.82)$$

$$= \mathbf{w}^T \mathbf{C} \mathbf{w}, \quad (2.83)$$

with the maps covariance matrix defined as

$$\mathbf{C} \equiv \text{Cov}[\mathbf{m}]. \quad (2.84)$$

The shape of \mathbf{C} depends on the parametrisation of the weights w_μ , and will be discussed in Sec. 8.3. In order for the estimator of Eq. (2.80) to fully recover the CMB signal, we introduce an additional condition,

$$\mathbf{w}^T \mathbf{U} = \mathbf{v}^T. \quad (2.85)$$

The choice of the \mathbf{U} matrix and \mathbf{v} vector depends on the weights parametrisation, and is discussed hereafter. They simply account for the fact that the CMB signal is present in each dataset, and that the weights w_μ have to be normalised accordingly.

Introducing the Lagrange multipliers $\boldsymbol{\lambda}$ (which size also depends on the weight parametrisation), we now wish to minimise

$$\mathcal{L} = \langle |P|^2 \rangle - [\mathbf{w}^T \mathbf{U} - \mathbf{v}^T] \boldsymbol{\lambda}, \quad (2.86)$$

which leads to the following system of equations,

$$\frac{\partial \mathcal{L}}{\partial \mathbf{w}} = (\mathbf{C} + \mathbf{C}^T) \mathbf{w} - \mathbf{U} \boldsymbol{\lambda}. \quad (2.87)$$

The solution for the weight coefficients is given by

$$\mathbf{w} = (\mathbf{C} + \mathbf{C}^T)^{-1} \mathbf{U} \boldsymbol{\lambda}. \quad (2.88)$$

Finally, by reinjecting in Eq. (2.85), we get

$$\boldsymbol{\lambda} = [\mathbf{U}^T (\mathbf{C} + \mathbf{C}^T)^{-1} \mathbf{U}]^{-1} \mathbf{v}. \quad (2.89)$$

Ultimately, the coefficients solution is

$$\boxed{\mathbf{w} = (\mathbf{C} + \mathbf{C}^T)^{-1} \mathbf{U} [\mathbf{U}^T (\mathbf{C} + \mathbf{C}^T)^{-1} \mathbf{U}]^{-1} \mathbf{v}}. \quad (2.90)$$

This solution that we developed here is completely general, and accounts for most of the weight parametrisations present in the literature, providing that the normalisation condition of Eq. (2.85) is expressed accordingly.

8.3 Weights parametrisations

The most general parametrisation of the weights reads

$$w_\nu = \begin{pmatrix} w_Q^R & -w_U^I \\ w_Q^I & w_U^R \end{pmatrix}_\nu. \quad (2.91)$$

In general, some or all of the coefficients are degenerated. We distinguish three main parametrisations.

Minimal

The minimal parametrisation considers no signal rotation, and no change in amplitude between the Q and U components. Therefore, $w_Q^I = w_U^I = 0$, and $w_Q^R = w_U^R$ (Kim et al. 2009). In that case, the maps covariance matrix is of size $n_\nu \times n_\nu$,

$$\mathbf{C}_{\mu\nu} = \langle m_\mu^Q m_\nu^Q + m_\mu^U m_\nu^U \rangle. \quad (2.92)$$

We also have $\boldsymbol{\lambda} \equiv \lambda$ (a scalar quantity), as well as $\mathbf{U} = \mathbf{1}_{n_\nu \times 1}$ and $\mathbf{v} = 1$, such that the condition of Eq. (2.85) translates into $\sum_\nu w_\nu = 1$, and the CMB signal amplitude in the estimator of Eq. (2.80) is conserved. This parametrisation choice is referred to as PRILC in Fernández-Cobos et al. 2016.

Q/U Stokes

Other implementations propose to use different coefficients w_Q^R and w_U^R for each Stokes parameters. In that case, $\mathbf{w} = (\mathbf{w}_Q, \mathbf{w}_U)$, $\boldsymbol{\lambda} \equiv (\lambda_Q, \lambda_U)^T$. In addition,

$$\mathbf{U} \equiv \begin{pmatrix} \mathbf{1}_{n_\nu \times 1} & \mathbf{0}_{n_\nu \times 1} \\ \mathbf{0}_{n_\nu \times 1} & \mathbf{1}_{n_\nu \times 1} \end{pmatrix}, \quad \text{and} \quad \mathbf{v} = \begin{pmatrix} 1 \\ 1 \end{pmatrix}, \quad (2.93)$$

such that $\sum_\mu w_{Q,\mu} = \sum_\mu w_{U,\mu} = 1$.

However, one can show that this choice, referred to as QUILC in Fernández-Cobos et al. 2016, is not orientation-preserving the foreground residuals, as discussed in the same reference.

Polarisation rotation

The polarisation rotation of the foreground signal can be accounted for by taking $w_Q^I = w_U^I$, and $w_Q^R = w_U^R$. In that case, $\mathbf{w} = (\mathbf{w}^R, \mathbf{w}^I)$. The covariance matrix of Eq. (2.83) is a $2n_\nu \times 2n_\nu$ symmetric matrix,

$$\mathbf{C} \equiv \begin{pmatrix} \mathbf{C}^+ & -\mathbf{C}^- \\ \mathbf{C}^- & \mathbf{C}^+ \end{pmatrix}, \quad (2.94)$$

for which we define the $n_\nu \times n_\nu$ blocks

$$C_{\nu\mu}^+ \equiv \langle m_\nu^Q m_\mu^Q + m_\nu^U m_\mu^U \rangle, \quad C_{\nu\mu}^- \equiv \langle m_\nu^Q m_\mu^U - m_\nu^U m_\mu^Q \rangle, \quad (2.95)$$

with $\mathbf{C}^{+T} = \mathbf{C}^+$ and $\mathbf{C}^{-T} = -\mathbf{C}^-$.

We also have $\boldsymbol{\lambda} \equiv (\lambda_R, \lambda_I)^T$, as well as

$$\mathbf{U} \equiv \begin{pmatrix} \mathbf{1}_{n_\nu \times 1} & \mathbf{0}_{n_\nu \times 1} \\ \mathbf{0}_{n_\nu \times 1} & \mathbf{1}_{n_\nu \times 1} \end{pmatrix}, \quad \text{and} \quad \mathbf{v} = \begin{pmatrix} 1 \\ 0 \end{pmatrix}, \quad (2.96)$$

such that $\sum_\mu w_\mu^R = 1$ and $\sum_\mu w_\mu^I = 0$.

As investigated in Sec. 9, considering polarisation rotation (non-zero w^I 's) does not impact the precision on the estimation of the change in amplitude. This parametrisation is referred to as PILC in Fernández-Cobos et al. 2016.

8.4 Foregrounds cleaning ILC

Originally, the ILC method aims at combining multiple frequency maps while reducing the variance induced by the noise and the foregrounds of the resulting combination. Indeed, if we develop the covariance matrix for the minimal parametrisation of Eq. (2.92) (PRILC),

$$C_{\nu\mu} = \langle s_\nu^Q s_\mu^Q + s_\nu^U s_\mu^U \rangle + \langle f_\nu^Q f_\mu^Q + f_\nu^U f_\mu^U \rangle + \langle n_\nu^Q n_\mu^Q + n_\nu^U n_\mu^U \rangle, \quad (2.97)$$

we observe that for the elements on the diagonal of \mathbf{C} , (i.e. $\nu = \mu$), the last term of Eq. (2.97), which quantifies the noise contribution to the variance, is non-zero. In the case where the foreground signal is low compared to the noise variance, the latter will dominate \mathbf{C} . As a result, the ILC will favour the reduction of the noise from the combination of the map ν in the resulting CMB estimate against the reduction of the foregrounds signal. As underlined in Efstathiou et al. 2009, in the noise dominated limit, the ILC solution simply corresponds to inverse noise-variance weighting, and the foregrounds contamination are not properly removed.

In order to primarily minimize the foreground residuals, Efstathiou et al. 2009 propose to subtract the noise variance terms from the covariance matrix, such that $\mathbf{C} \rightarrow \mathbf{C} - I\sigma^2$, where $\sigma^2 \equiv (\sigma_0, \dots, \sigma_{n_\nu})^T$ is a vector of the dataset variances. An other solution that we propose to avoid this foreground subtraction bias is to compute the variance using cross-correlation between maps. This solution is similar to the one proposed in Sec. 6 for the linear regression estimator noise bias mitigation : we select two sets of maps, $m_{\nu A}$ and $m_{\nu B}$, each measured by pair at the same channel ν , but that have uncorrelated noise, i.e. $\langle n_{\nu A}^Q n_{\nu B}^Q \rangle = 0$, and $\langle n_{\nu A}^U n_{\nu B}^U \rangle = 0$. Therefore, on average, the last term of Eq. (2.97) vanishes. We then define the block entries of this new ‘cross’ covariance matrix between the datasets A and B as

$$C_{\nu A, \mu B} \equiv \langle m_{\nu A}^Q m_{\mu B}^Q + m_{\nu A}^U m_{\mu B}^U \rangle. \quad (2.98)$$

We note that $\mathbf{C}_{AB} = \mathbf{C}_{BA}^T$. Finally, the weights are given by Eq. (2.88) using \mathbf{C}_{AB} as the \mathbf{C} matrix. They can be used to clean both the split datasets A and B . The resulting combination of maps will not have minimal total variance anymore, but only minimal foreground variance. We refer to this variant of the ILC as the ‘cross’ ILC, or xPRILC for our example of parametrisation.

8.5 Relation to the linear regression

Let us consider the same three datasets, d , t_D , t_S , as for the linear regression of Sec. 6. The pixel-based PRILC weights $\mathbf{w} = (w_d, w_D, w_S)$ are intimately connected to the coefficients α_D and α_S estimated by the linear regression methods. Indeed, by identifying the ILC CMB signal estimation of Eq. (2.80) with that of Eq. (2.29) for the linear regression, we can write the relation

$$\alpha_D \leftrightarrow \frac{w_D}{w_d}, \quad \alpha_S \leftrightarrow \frac{w_S}{w_d}. \quad (2.99)$$

The solution for both methods are actually almost mathematically equivalent. Indeed, let us consider a one-foreground toy-model. The normalised linear regression (nLR) solution of Eq. (2.48) is

$$\hat{\alpha} = \frac{d^T C^{-1} d - t^T C^{-1} d}{d^T C^{-1} t - t^T C^{-1} t}, \quad (2.100)$$

while the PRILC parametrisation becomes $\mathbf{w} = (w_d, w_f)$, which estimation provided by Eq. (2.90) reads

$$\hat{w}_d = \frac{d^T d - t^T d}{d^T d + 2d^T t + t^T t}, \quad \hat{w}_f = \frac{d^T t - t^T t}{d^T d + 2d^T t + t^T t}. \quad (2.101)$$

When using cross-datasets, and neglecting the CMB pixel-pixel correlations, the residual covariance C becomes diagonal, and can therefore be removed from the nLR solution. In that case, the relation of Eq. 2.99 between the nLR and the PRILC coefficients becomes an equality, $\alpha = w_f/w_d$, and both methods (ILC and nLR) are strictly equivalent. This observation holds for the two foregrounds case.

Therefore, the only difference resides in the inclusion of the C covariance matrix in the linear regression. For our particular case (three datasets), the linear regression can thus be seen as a weighted ILC solution. For this reason, we do not show any result of the pixel based ILC method tested on our set of datasets simulations, since those, as well as the associated discussion, is similar to that of the nLR estimator provided in Sec. 6.

9 Polarization rotation

In this section, we investigate possible account for signal polarisation rotation. The formalism was presented in Sec. 4, in which we parametrise the foreground coefficients as

$$\alpha f \equiv \begin{pmatrix} \alpha^R & -\alpha^I \\ \alpha^I & \alpha^R \end{pmatrix}_\mu \begin{pmatrix} f_i^Q \\ f_i^U \end{pmatrix}_\mu. \quad (2.102)$$

The foreground coefficients are related to the change in polarisation amplitude by

$$\rho \equiv \sqrt{\alpha_\mu^R{}^2 + \alpha_\mu^I{}^2}, \quad (2.103)$$

and to the rotation angle by

$$\theta \equiv \arctan\left(\frac{\alpha_\mu^I}{\alpha_\mu^R}\right). \quad (2.104)$$

We use the `xnLR` estimator developed in Sec. 6 and consider two parametrisations of this estimator :

- no polarisation rotation degree of freedom, in that case $\alpha^R \neq 0$ and $\alpha^I = 0$. Thereby, $\theta = 0$ and $\rho = \alpha^R$. We refer to this parametrisation as the standard `xnLR`.
- allowed polarisation rotation, in that case, $\alpha^R \neq 0$ and $\alpha^I \neq 0$. We refer to this parametrisation as `xnLRr`.

Using MC simulations on the PySM model (introduced in Sec. 2), we show the distribution of the dust and synchrotron coefficients amplitudes ρ_D and ρ_S , in Fig. 2.16. In addition, we display the distribution of the rotation angle, θ_i , computed using the `xnLRr` estimator.

Both parametrisations provide similar precision on the estimation of the amplitude ρ . We see that the error on the estimation of the dust polarization rotation is about $\sigma_\theta \simeq 0.43^\circ$ for *Planck*-like noisy datasets, and $\sigma_\theta \simeq 0.25^\circ$ for noiseless datasets. The estimation of polarization rotation on the synchrotron shows much more uncertainty, with a typical error of $\sigma_\theta \simeq 3.4^\circ$ for *Planck*-like noisy datasets, $\sigma_\theta \simeq 1.8^\circ$ for noiseless datasets. We see that a significant part of the uncertainties is driven by the CMB variance. Better precision in future, less noisy, experiments could be achieved by subtracting datasets by pair, in order to remove the CMB signal. In that case, the method must be slightly modified in order to account for the removed signal.

The amplitude uncertainty is the same whether including the rotation or not in the estimator. However, the resulting CMB estimate map can still be impacted by the uncertainty on the rotation angle, which are quite important, when the polarization rotation is small compared to the noise and the CMB signal. It is thus generally safer to estimate the amplitude only.

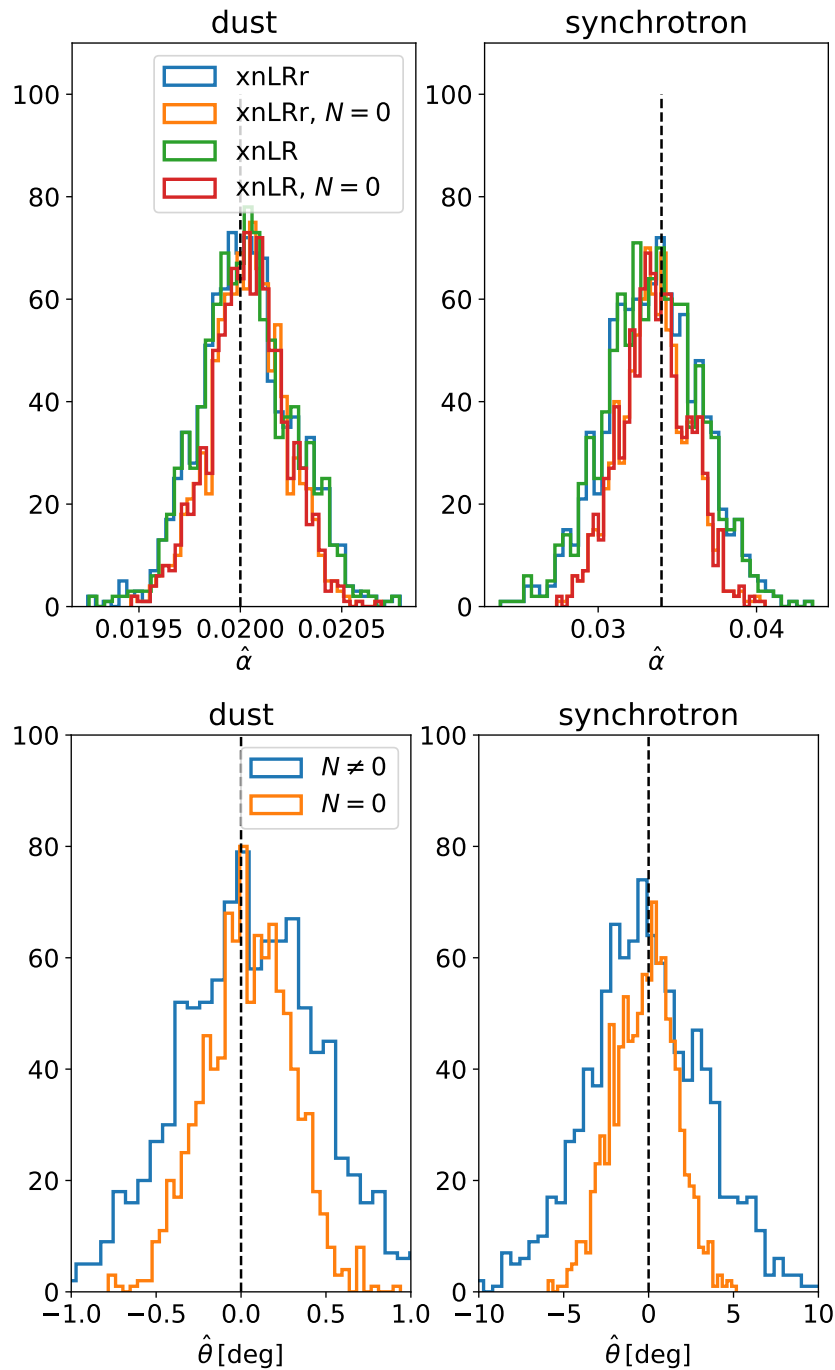


Figure 2.16: Top : amplitude distributions using the $xnLR$ and $xnLRr$ estimators. Bottom : foreground rotation angle θ estimated from the $xnLRr$ method. Simulations are generated using the PySM model, either using the 100GHz *Planck*-like noise level ($N \neq 0$), or no noise ($N = 0$).

10 Patches cleaning

Ideally, one would aim at estimating the full distribution of $\alpha(\hat{n})$ on the sky. In practice, because of the signal-to-noise limitation, we can only approximate $\alpha(\hat{n})$ by defining localised patches on the sky, and perform the estimation of one mean value of α for each patch. A forecast analysis on the foreground residuals using patch-cleaning was already investigated in Sec. 5. The results on MC simulations using the estimators proposed in the previous sections is presented here.

Using small patches allows us to track variations of $\hat{\alpha}(\hat{n})$ on the sky with a high resolution, however, as a result, the average signal-to-noise ratio per patch is lowered. Therefore, a compromise has to be found between the patch resolution, and the precision of the estimation of $\hat{\alpha}(\hat{n})$.

We apply the `xnLR` on patches to account for foreground spatial variations of the PySM foregrounds signals. We use *noiseless* simulations, with a patch resolution $p_{\text{side}} = 8$, which corresponds to 768 patches. Therefore, for our study case, the CMB is the only source of noise for the estimation of the foreground coefficients. The dataset resolution is $n_{\text{side}} = 256$, meaning that there is $12 \times 256^2 / 768 = 1024$ sub-pixels per patch.

10.1 Dust-synchrotron correlation

On Fig. 2.17, we compare the mean value of the estimation with the input coefficient on each patch. On average, the measured dust coefficient map is seen to accurately recover variations of the input coefficients $\alpha_D(\hat{n})$ on the sky. On the other hand, the synchrotron coefficient map seems noisier, with some mean values clearly away from the input coefficients α_S for some patches. We observed at least one effect that can drive the mean patch value away from the true input α distribution.

The effect is a dust-synchrotron correlation, observed for example on the patch number 343, which localisation on the sky is shown on the top right panel of Fig. 2.18. The top left and middle panels of the same figure shows the MC distribution of the foreground coefficient estimation, $\hat{\alpha}$. On the bottom left and middle panels, for each sub-pixel associated to a direction \hat{n} , we draw the input dust signal amplitude, $\sqrt{f_D^Q(\hat{n})^2 + f_D^U(\hat{n})^2}$, against the input coefficient, $\alpha(\hat{n})$.

We observe that the distribution of the estimation of α_D is driven by the dust pixels for which the signal is the highest (around $\alpha_D \sim 0.022$). This is expected from the `xnLR` method, since it naturally targets the pixels for which the foreground signal is the highest. However, as a result, the synchrotron MC distribution (top centre panel) is biased compared to the input value (centre bottom). This is because the dust residuals tend to drive the synchrotron coefficient away from its true value. This dust-synchrotron correlation between coefficients $\hat{\alpha}_D$ and $\hat{\alpha}_S$ is highlighted on the right panel, for which we plot the 2D-distribution of coefficients. To validate our observations, we simulated a sky with no dust, and verified that, in that case, the synchrotron is not biased (centre panel, red vertical line).

10.2 Cosmic variance

On Fig. 2.17, we also show the patch estimations for one simulation. The results are not encouraging, as the recovered coefficient map is highly noisy. The estimation successfully recovers the distribution in the galactic plane only, and for the dust coefficient only. It means that, for this patch resolution ($p_{\text{side}} = 8$), and at this frequency (100 GHz), a precise estimation is overwhelmed by the CMB present in the intermediate channel, which acts as a source of noise for the `xnLR`, and reduces the detection of foregrounds spatial variations.

A solution to recover precise estimations would be to remove the CMB from the datasets, for example by subtracting the datasets by pair to create templates. This, of course, is only

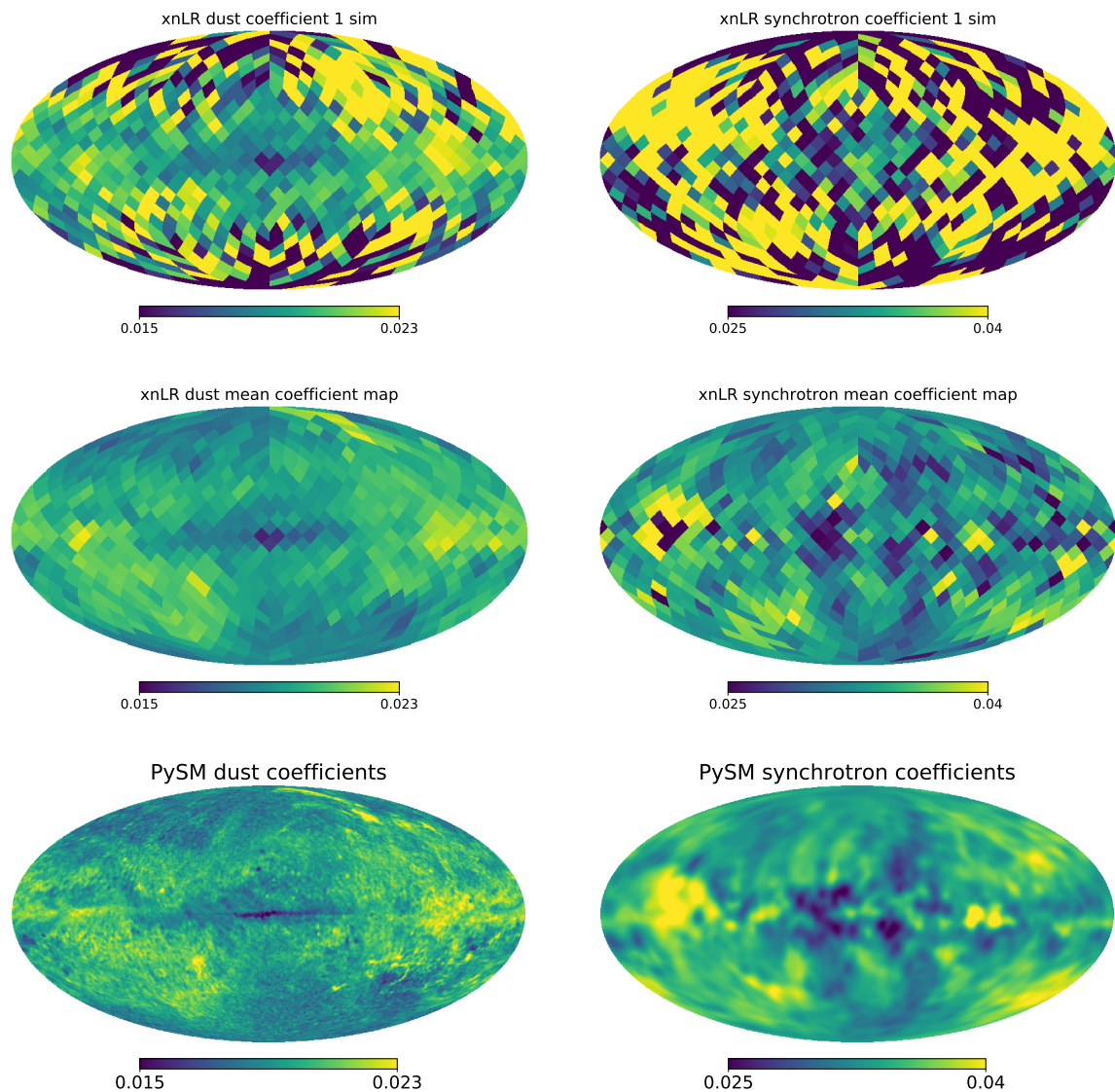


Figure 2.17: Coefficient estimate on patches for the PySM foreground model, for no experimental noise, using the cross LR method. The patch resolution is $p_{\text{side}} = 8$. Left column corresponds to the dust, and right to the synchrotron. First row shows the results for one simulation. The mean estimation over MC realisations are shown on the second row. For comparison, the third row corresponds to the input coefficient distribution in the PySM model.

advisable for low noise datasets. Since the noise of each dataset is summed when combined, one would seek to avoid inducing even larger uncertainties on the estimation of α in the patches.

10.3 Beyond cosmic variance

Given the results presented in this section, we conclude that the patch-cleaning method that we propose cannot be easily applied. We selected the worse-case frequency channel (100 GHz), for which the foreground amplitude is the lowest. In that case, even for noiseless datasets, the foreground coefficient estimations is still overwhelmed by the CMB variance present in the intermediate channel. This method is clearly not advisable for *Planck* data, for which the noise level of the datasets is even higher than the CMB polarisation signal amplitude (see Fig. 2.5).

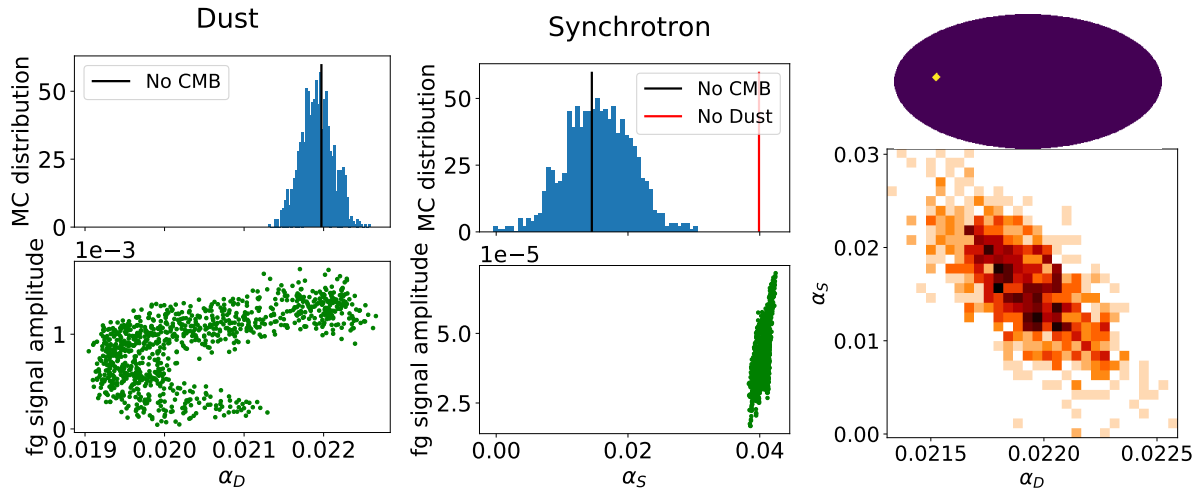


Figure 2.18: Distributions of foreground coefficients for the patch number 343 (showed on the top right mollview), for no experimental noise. The left and central panels respectively show the results of the dust and synchrotron. The MC distribution of the coefficients estimates $\hat{\alpha}$ are shown on the upper part of the panels. The bottom panels show the input foreground signal amplitude against the input coefficient $\alpha(\hat{n})$, for each sub-pixel of this patch. In addition, the estimate result for which no CMB are present in the datasets is indicated by a vertical black line. For synchrotron, the estimate for dust-free simulations is indicated by a solid red line. The right panel shows the 2D distribution of the dust and synchrotron MC coefficients estimates.

Patch cleaning on frequency channels that are closer to the templates will of course show more promising results. For example, the polarised dust SED spectral index estimation was performed on patches in *Planck 2018 Results. XI* combining all HFI polarisation channels (from 100 GHz to 353 GHz).

A solution for future, low noise measurements, is to subtract datasets by pair, in order to remove the CMB signal. In that case, the method must be slightly modified in order to account for the removed CMB component.

11 Residual covariance matrix

We investigate further the construction of the residuals covariance matrix, labelled C , defined in Eq. (2.31) for the linear regression, and in Eq. (2.76) for the maximum likelihood estimator.

Foreground mismatch

Let us consider a one-foreground toy model. The terms of the linear regressions estimators, such as $d^T C^{-1} t$ with $d = s + \alpha f$ and $t = s + f$, can be developed as follow

$$\langle d C^{-1} t \rangle = \langle s C^{-1} s \rangle + \alpha \langle f C^{-1} f \rangle + (1 + \alpha) \langle s C^{-1} f \rangle. \quad (2.105)$$

On average, the last term of Eq. (2.105) vanishes. However, it can be non-negligible for one sky realisation, and can greatly contribute to the uncertainty on the foreground coefficient estimation. It is identified as foregrounds mismatch, as already pointed out in the case of the pixel-based ILC methods (e.g. Efstathiou et al. 2009). A solution to mitigate the mismatch impact is to include the full CMB signal pixel-pixel correlation matrix S in the covariance matrix C . The estimator methods thus becomes semi-blind, as it requires a prior knowledge of the CMB signal. Anyway, S is dominated by the E -mode signal, which current measurement is achieved with enough precision. This, however limits the resolution at which the cleaning method can be performed, as it generally requires the inversion⁵ of the matrix C , which size of the order of $\sim n_{\text{pix}}$.

Diagonal approximation

The inversion of the matrix C limits the size at which the estimation of the α 's can be performed. A solution is to consider the variance of the pixels for the Q and U components, as well as the Q - U pixel correlation only. In that case, the 4 square blocks matrix C are diagonal for LR estimator (respectively 36 square blocks for the MLE). The matrix inversion can therefore be decomposed into multiple (n_{pix}) inversions of 2×2 matrices (respectively 6×6), which highly reduces the computational cost. As a result, the signals of smaller scales can be included, but the estimators are no more optimal, as they do not account for the full pixel-pixel correlation of the noise or the CMB signal.

Comparison between full and diagonal

We choose to compare two dataset resolutions. The lowest is at $n_{\text{side}} = 16$, for which we include the CMB correlation signal. The highest is at $n_{\text{side}} = 128$, for which we follow the diagonal approximation. We display in Fig. 2.19 the MC distribution of the xnLR and MLE estimations using both resolutions.

We notice that including the CMB signal in the covariance matrix reduces by half the uncertainty on $\hat{\alpha}$. When neglecting the off-diagonal terms of the C , increasing the resolution to $n_{\text{side}} = 128$ do not produce any better precision on the estimation compared to $n_{\text{side}} = 16$, but the uncertainty is still roughly twice larger than when including the CMB correlations and performing the cleaning at $n_{\text{side}} = 16$. We therefore advise using small resolution to estimate the foreground coefficients, in order to be able to include the full CMB correlation in the estimator and reduce the foreground mismatch.

⁵The matrix inversion is not mandatory, as the system $Cx = m$ can be solved numerically, with m a map and x the unknown.

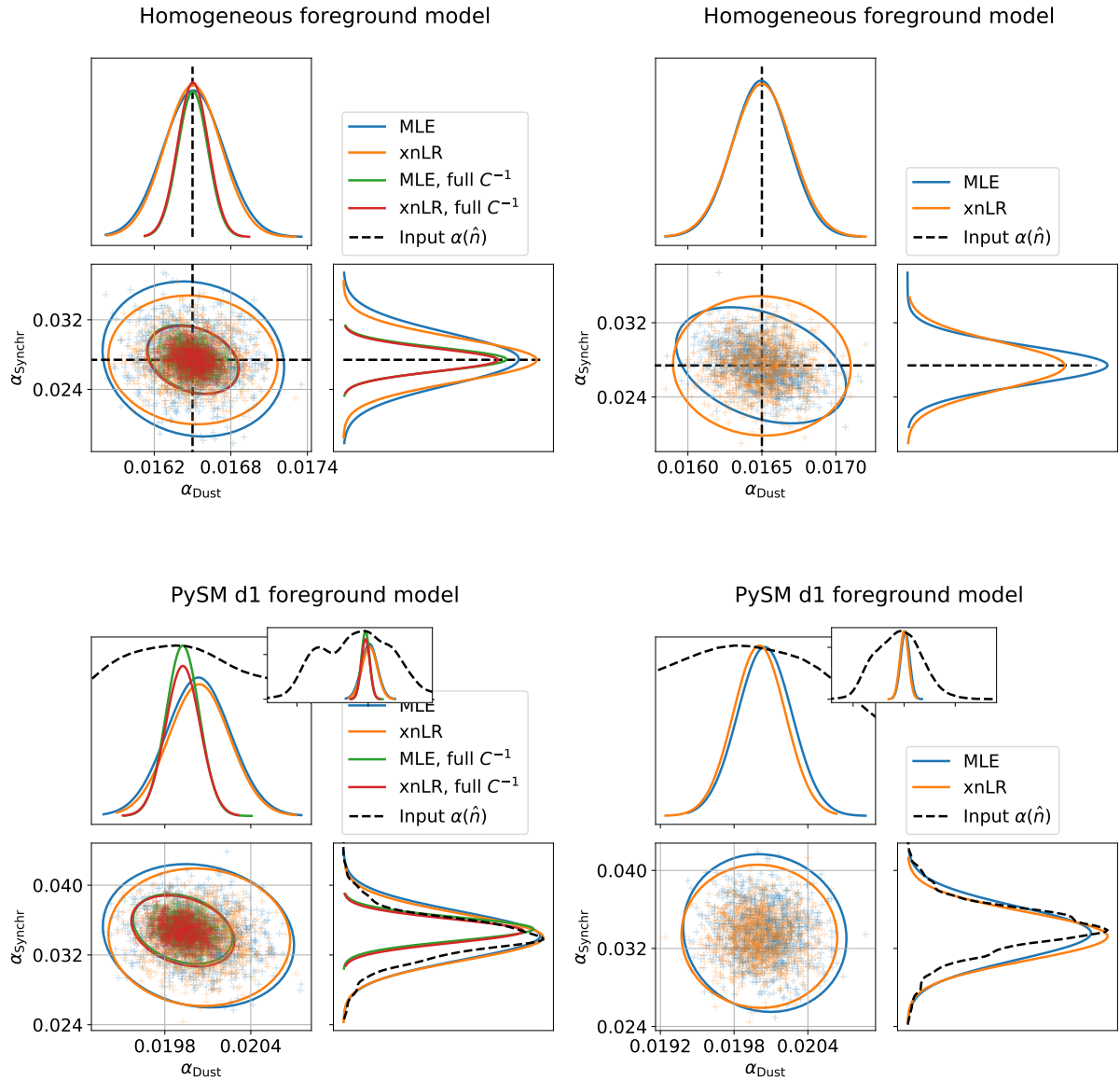


Figure 2.19: Foreground coefficient distributions for the xLR and MLE estimators at resolution $n_{\text{side}} = 16$ (left), and $n_{\text{side}} = 128$ (right). For the former resolution, the method is also performed when including the full CMB pixel-pixel correlations in the covariance matrix C . Results are shown for the homogeneous foregrounds model (top), and the PySM model (bottom).

12 Summary and method comparison

We summarise what we have learned about the methods developed to removed the foreground contamination of the datasets. We also compare their results in term of uncertainty on α .

12.1 Summary

In this chapter, we investigated the cleaning of the foreground contaminations using three datasets, including two templates, while considering two source of foregrounds contaminations, the dust and the synchrotron signals.

We showed in Sec. 6 that the linear regression estimator can be biased either by the noise, the CMB variance signal, or both. We provided some solution in order to mitigate the bias. In Sec. 7, we developed a maximum likelihood estimator, which is by construction unbiased, and optimal, but which must be ran iteratively and is more time consuming. In Sec. 8, we generalised the solution provided by the pixel-based ILC. In the context of three datasets and two foregrounds signals, we showed that the pixel based ILC PRILC and the normalised linear regression nLR are almost identical estimators.

As discussed in Sec. 9, the CMB signal can impact significantly the uncertainty on the polarisation rotation. In Sec. 11, we showed that including the full CMB signal correlation in the residual covariance matrix improves the uncertainty on the foreground coefficients α by a factor of two. For future work, we could investigate how including the full residual covariance matrix improves the measurement on the foreground polarisation rotation.

In addition, we considered applying the methods on patches of the sky, in order to account for the spectral variation of the foreground signal. For our case study, we showed that CMB signal can severely impede any precise patch-estimation of $\alpha(\hat{n})$. For future, low-noise, and multi-frequency experiments such as the LiteBIRD satellite, the CMB signal could be removed from the datasets before applying the patch cleaning. This could be done for example by subtracting datasets by pair. This solution deserves further investigations, which is left for future work.

12.2 Method comparison

The uncertainties on the estimation of the foreground coefficients α obtained thought all the methods presented in this chapter (except the ILC) are compared in Fig. 2.20, using the PySM model. We consider mainly four categories :

- the cross normalised linear regression, **xnLR**,
- the smoothed ordinary linear regression, **s₃oLR** ,
- the variance subtracted ordinary linear regression, **v_{cn}oLR**,
- the maximum likelihood estimator, obtained via the Newton-Raphson iterative algorithm, **MLE**.

As showed previously, the cross pixel-based xPRILC method is equivalent to the xnLR solution. Therefore, we do not include it in our comparison. We also do not consider any polarisation rotation.

For all methods, we consider a resolution of $n_{\text{nside}} = 128$, and we work using the diagonal approximation for which the residual covariance matrix only accounts for the noise and CMB variances (we refer to Sec. 11). We also consider including the full CMB correlation in the residual covariance matrix, but working at smaller map resolution, only for the xnLR ($n_{\text{nside}} = 32$) and MLE ($n_{\text{nside}} = 16$) estimators. For each foreground, the input distribution coefficients, $\alpha(\hat{n})$, is also displayed.

Of all methods, the `xnLR` and MLE estimators using the full C provide the lowest uncertainties. The `xnLR` is the easiest to implement, and computationally faster than the other methods which require either a pre-smoothing of the datasets as for the `s3oLR`, or an iterative implementation such as the MLE. However, it only provides one common coefficient for both split datasets, while the other methods allow to compute different α for each split-datasets. The `vcnoLR`, we believe, is the less safe method, as it must rely on precise estimate of the dataset noise and CMB variances to subtract the bias from the estimator.

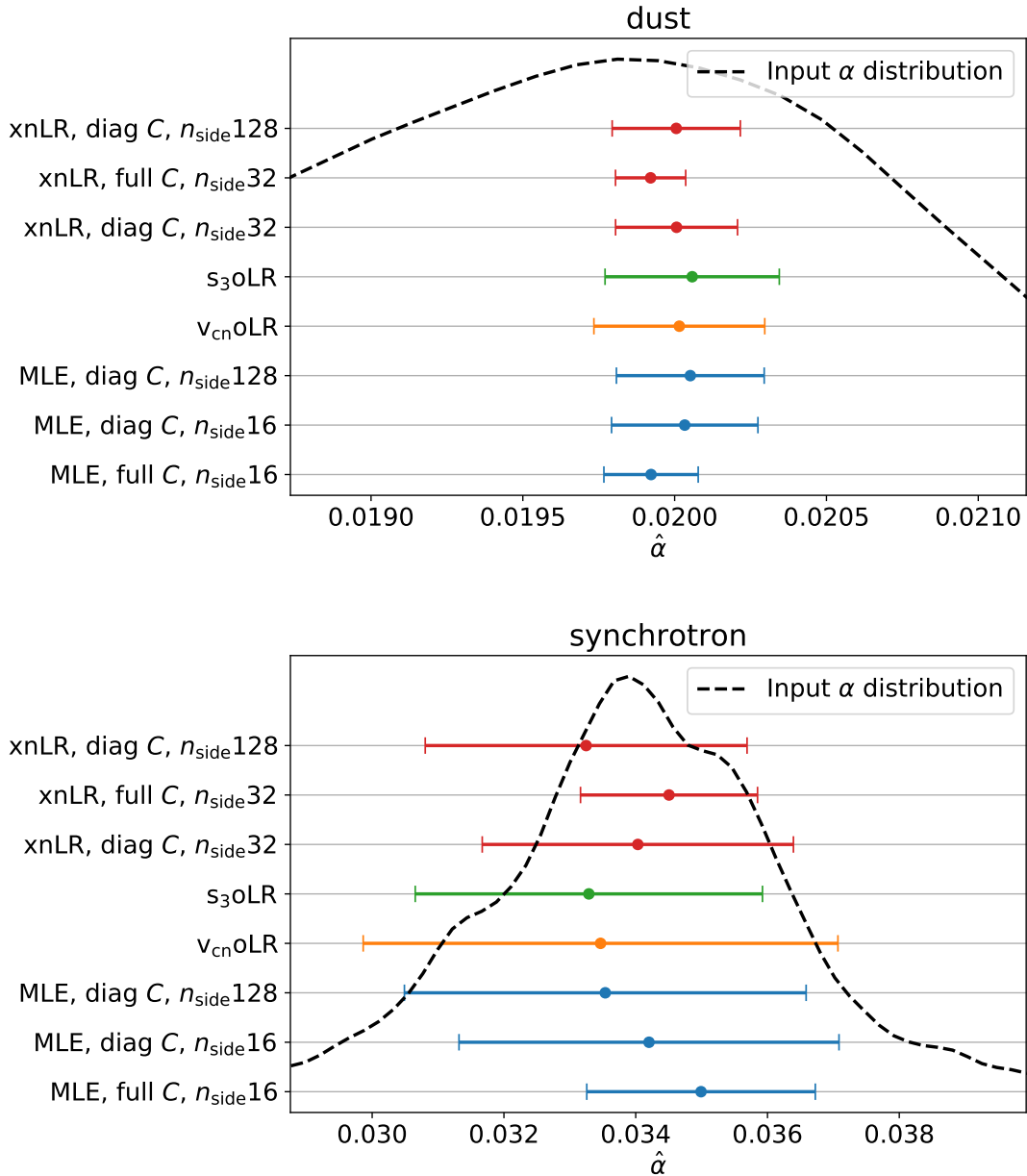


Figure 2.20: Comparison of the uncertainties for the dust (top), and synchrotron (bottom) coefficient estimations $\hat{\alpha}$ on the PySM foreground, at 100 GHz. In addition, the true distribution on the sky is displayed for each foreground signal.

Spectrum estimators

In order to constrain the cosmological model, the CMB anisotropies are conveniently projected in harmonic space, with their statistics encoded in the angular power spectra C_ℓ^{XY} , where ℓ is the multipole, and $X, Y \in \{T, E, B\}$. Since the anisotropies in the CMB are expected to be Gaussian distributed, all the cosmological information is contained in C_ℓ . The power spectra estimated from the CMB measurements, \hat{C}_ℓ , can be compared to the cosmological model $C_\ell(\theta)$ using a likelihood function, in order to estimate the cosmological model parameters θ . Using power spectra allows to compute the likelihood up to small angular scales on the sky in a reasonable amount of computational power, whereas a pixel-based likelihood is restricted to low resolutions CMB data due to its computational cost. In this chapter, we will focus on estimating the E and B polarization power spectra on large scales from Q and U polarization maps.

1 Context

1.1 Power spectrum estimator methods

Pseudo-spectrum

We generally define two categories of spectrum estimators. The first one, known as the pseudo-spectrum estimator (pCl), includes methods that work directly in the harmonics space (e.g. Tristram et al. 2005). The input map is firstly decomposed into a set of spherical harmonics coefficients $\tilde{a}_{\ell m}$, from which pseudo-spectra $\tilde{C}_\ell = \langle \tilde{a}_{\ell m} \tilde{a}_{\ell m} \rangle$ are computed, then corrected for sky coverage. For a dataset of N_d pixels, the pCl only demands $\mathcal{O}(N_d^{3/2})$ operations (Efstathiou 2004). The extension of the pCl method to cross-spectra formalism offers the advantage of being able to cross-correlate CMB maps, allowing us to remove the noise and mitigate the impact of systematic effects, providing that they are uncorrelated. However, the method has been showed to be sub-optimal for large and intermediate angular scales ($\ell \lesssim 100$) (Molinari et al. 2014; Efstathiou 2004; Efstathiou 2006).

Pixel-based

The second category includes power spectra estimators that use a pixel based approach. Those are known to be particularly suited for large angular scale analysis, but they have the drawback of being computationally more expensive. The spectrum Maximum Likelihood Estimator (MLE)¹ implemented in pixel space have the advantage of minimizing spectra uncertainties,

¹Not to be confused with the foreground MLE method defined in chapter 2, and used to estimate the foreground coefficient α .

but it requires to be ran iteratively, which quickly becomes infeasible for high resolution maps. See for example Borrill 1999; Bond et al. 1998 for a Newton-Raphson implementation of the spectrum MLE. The algorithm computational cost scales as $\mathcal{O}(N_{\text{d}}^3)$ operations since it requires the inversion of $N_{\text{d}}-N_{\text{d}}$ matrices. An other approach, developed in Tegmark 1997 and extended to polarization in Tegmark et al. 2001, is the so call Quadratic Maximum Likelihood (QML). The estimator requires less or none iteration, and it offers the same error bars as the spectrum MLE. At first sight, it also requires $\mathcal{O}(N_{\text{d}}^3)$, although it can be brought down $\mathcal{O}(N_{\text{d}}^2)$ as described in Tegmark 1997.

1.2 Polarization leakage

Because of experimental limitations and/or foreground contaminations, the effective CMB surveys sky coverage can be partial. In the context of polarization analysis, this introduces an ambiguity in the relationship between the Stokes parameters Q and U , and the E and B modes. Indeed, the E/B spectrum decomposition is inherently non-local, and is non unique in the presence of boundaries. In this context, the E and B modes are inevitably mixed and mislabeled (Lewis et al. 2001; Bunn 2003; Bunn et al. 2003). A new set of modes, called ‘ambiguous’, which receive contributions from both E and B modes, is introduced. This effect, known as *polarization leakage*, can be corrected on average (Chon et al. 2004; Kogut et al. 2003). However, the E/B mixing signals contribute to each other’s spectrum variance. The E modes thus act as a source of noise for the B modes estimation. Since the B-mode signal is expected to be much lower than that the E-mode signal, the impact of this ‘variance leakage’ is extremely problematic for the detection of B-modes and their precise measurement. Several methods have been developed in order to reduce the variance leakage impact.

The pure pseudo-spectrum (PpCl) method presented in Smith 2006; Bunn 2003; Lewis 2003 is an extension of the standard pCl and currently represents the most popular solution that reduces the amount of polarization variance leakage. It has been widely investigated in e.g. Grain et al. 2009; Grain et al. 2012; Ferte et al. 2015, and has been demonstrated to produce near-optimal variance power spectrum estimates for intermediate and small angular scales. However, the PpCl method requires particular sky mask apodizations, which depend on the scanning strategy and on the depth of the observed CMB field.

In this chapter, with a view to lower the polarization variance leakage, and more generally to lower the B modes spectrum variance, we will introduce the formalisms of two spectrum estimators, each belonging to one of the two categories introduced here above. Firstly, we will present the pure pseudo-spectrum (PpCl) method. Secondly, we will develop a method based on the QML approach that allows us to cross-correlate CMB maps that have common sky coverage, in analogy with the pseudo cross-spectra formalism. The formalism was first introduced in *Planck Intermediate Results: XLVI* for the 2016 Planck results. In this chapter, we propose to fully characterise the properties of such an estimator, extending the discussion published in Vanneste et al. 2018. Finally, the two estimators are compared on experimental survey simulations.

2 Power spectrum definitions and notations

First of all, we introduce the basic ideas behind the Fourier transform on the sky, and how the power spectrum is constructed from the temperature and polarization fields. We then develop how the spectrum uncertainty is impeded by the cosmic variance and the experimental noise.

2.1 Spherical Fourier transform

The CMB field measurement is generally parametrised by the Stokes parameters I , Q and U , which can be combined into a spin-1 temperature field T , and two spin- ± 2 polarization fields $P_{\pm 2}$,

$$I = T, \quad P_{\pm 2} \equiv Q \pm iU. \quad (3.1)$$

Those fields can thus be expressed in term of complex spin- s spherical harmonic functions ${}_s Y_{\ell m}$ weighted by the spin- s complex harmonic coefficients ${}_s a_{\ell m}$

$$T(\hat{n}) = \sum_{\ell m} a_{\ell m} Y_{\ell m}(\hat{n}), \quad a_{\ell m} = \int Y_{\ell m}^\dagger(\hat{n}) T(\hat{n}) d\hat{n}, \quad (3.2)$$

$$P_{\pm 2}(\hat{n}) = \sum_{\ell m} \pm 2 a_{\ell m} \pm 2 Y_{\ell m}(\hat{n}), \quad \pm 2 a_{\ell m} = \int \pm 2 Y_{\ell m}^\dagger P_{\pm 2}(\hat{n})(\hat{n}) d\hat{n}, \quad (3.3)$$

and

$$\int {}_s Y_{\ell m}^\dagger(\hat{n}) \cdot {}_s Y_{\ell' m'}(\hat{n}) d\hat{n} = \delta_{\ell \ell'} \delta_{m m'}, \quad (3.4)$$

with \hat{n} is the unit vector on the sky, and the integrals are taken over the entire celestial sphere. Generally, the following notation is adopted for spin-0 fields $a_{\ell m} \equiv {}_0 a_{\ell m}$ and $Y_{\ell m} \equiv {}_0 Y_{\ell m}$. The spinned spherical harmonics can be written in term of spin-0 spherical harmonics (Zaldarriaga et al. 1997),

$${}_s Y_{\ell m} \equiv \beta_{\ell, s} \bar{\partial}^s Y_{\ell m}, \quad -{}_s Y_{\ell m} \equiv \beta_{\ell, s} (-1)^s \bar{\partial}^s Y_{\ell m}, \quad (3.5)$$

where $\beta_{\ell, s} = \sqrt{(\ell - s)! / (\ell + s)!}$. The spin-raising and lowering differential operators acting on the spin- s quantity are defined on the sphere as

$$\bar{\partial}^s \equiv -(\sin(\theta))^s \left(\partial_\theta + i \frac{\partial_\varphi}{\sin \theta} \right) (\sin \theta)^{-s}, \quad (3.6a)$$

$$\bar{\partial}^s \equiv -(\sin(\theta))^{-s} \left(\partial_\theta - i \frac{\partial_\varphi}{\sin \theta} \right) (\sin \theta)^s, \quad (3.6b)$$

with $(\bar{\partial}^s f)^* = \bar{\partial}^s f^*$.

2.2 Power spectrum

It is usually convenient to express the polarization field in term of a (scalar) E and a (pseudo-scalar) B fields. This E/B decomposition is more natural, since from a physical point of view, the E/B decomposition is directly linked to the primordial cosmological perturbations and to the presently observed CMB anisotropies. The corresponding coefficients are expressed as

$${}_E a_{\ell m} = \frac{1}{2} ({}_+2 a_{\ell m} + {}_-2 a_{\ell m}) = \int {}_E \mathbf{Y}_{\ell m}^\dagger(\hat{n}) \mathbf{P}(\hat{n}) d\hat{n}, \quad (3.7a)$$

$${}_B a_{\ell m} = -\frac{i}{2} ({}_+2 a_{\ell m} - {}_-2 a_{\ell m}) = \int {}_B \mathbf{Y}_{\ell m}^\dagger(\hat{n}) \mathbf{P}(\hat{n}) d\hat{n}, \quad (3.7b)$$

with $\mathbf{P} = (Q, U)^T$. From Eqs. (3.5), the associated E/B spherical harmonics

$$\begin{aligned} {}_E\mathbf{Y}_{\ell m} &= \frac{1}{2} \begin{pmatrix} +2Y_{\ell m} + -2Y_{\ell m} \\ -i(+2Y_{\ell m} - -2Y_{\ell m}) \end{pmatrix} \\ &= \frac{\beta_{\ell,2}}{2} \begin{pmatrix} \partial^2 + \bar{\partial}^2 \\ -i(\partial^2 - \bar{\partial}^2) \end{pmatrix} Y_{\ell m} \\ &\equiv \mathbf{D}_2^E Y_{\ell m}, \end{aligned} \quad (3.8)$$

and

$$\begin{aligned} {}_B\mathbf{Y}_{\ell m} &= \frac{1}{2} \begin{pmatrix} i(+2Y_{\ell m} - -2Y_{\ell m}) \\ +2Y_{\ell m} + -2Y_{\ell m} \end{pmatrix} \\ &= \frac{\beta_{\ell,2}}{2} \begin{pmatrix} i(\partial^2 - \bar{\partial}^2) \\ \partial^2 + \bar{\partial}^2 \end{pmatrix} Y_{\ell m} \\ &\equiv \mathbf{D}_2^B Y_{\ell m}, \end{aligned} \quad (3.9)$$

thus define two orthogonal subspaces, E and B, such that

$$\mathbf{D}_2^E \cdot \mathbf{D}_2^B = 0, \quad \text{and} \quad \int {}_E\mathbf{Y}_{\ell m}^\dagger(\hat{n}) \cdot {}_B\mathbf{Y}_{\ell m}(\hat{n}) d\hat{n} = 0. \quad (3.10)$$

The operators $\mathbf{D}_2^{E(B)}$ can be seen as projectors, which filtering out all B (E) modes from the polarization dataset \mathbf{P} in Eqs. (3.7). For each ℓ , there are only $2\ell + 1$ Fourier coefficients $a_{\ell m}$ on the sky. The power spectrum is obtained by computing the variance of the Fourier coefficients over the modes m ,

$$\boxed{\frac{1}{2(\ell+1)} \sum_{m=-\ell}^{\ell} X a_{\ell m} Y a_{\ell m} = C_\ell^{XY} \delta_{\ell\ell'}, \quad X, Y \in \{T, E, B\}} \quad (3.11)$$

where, for each ℓ , the operator $\langle \rangle$ is the average over the $2\ell + 1$ modes m .

2.3 Spectrum variance

When the power spectrum \hat{C}_ℓ is estimated from a set of measured coefficients $\tilde{a}_{\ell m}$, the estimation has a variance induced by both the datasets noise and the finite number of modes available on the sky. One can compute the covariance between two cross-power spectra, each respectively estimated from the cross-correlation of the datasets A & B , and C & D ,

$$\begin{aligned} \text{Cov} \left[\hat{C}_\ell^{AB}, \hat{C}_\ell^{CD} \right] &= \langle \hat{C}_\ell^{AB} \hat{C}_\ell^{CD} \rangle - \langle \hat{C}_\ell^{AB} \rangle \langle \hat{C}_\ell^{CD} \rangle \\ &= \frac{1}{(2\ell+1)^2} \sum_{mm'} (\langle \hat{a}_{\ell m}^A \hat{a}_{\ell m}^B \hat{a}_{\ell m'}^C \hat{a}_{\ell m'}^D \rangle - \langle \hat{a}_{\ell m}^A \hat{a}_{\ell m}^B \rangle \langle \hat{a}_{\ell m'}^C \hat{a}_{\ell m'}^D \rangle) \\ &= \frac{1}{(2\ell+1)f_{sky}} (C_\ell^{AB} C_\ell^{CD} + C_\ell^{AC} C_\ell^{BD} + C_\ell^{AD} C_\ell^{BC} - C_\ell^{AB} C_\ell^{CD}) \\ &= \frac{1}{(2\ell+1)f_{sky}} (C_\ell^{AC} C_\ell^{BD} + C_\ell^{AD} C_\ell^{BC}), \end{aligned} \quad (3.12)$$

where $\langle \rangle$ is the average over the multipoles ℓ , and C_ℓ is the true spectrum. The factor $f_{sky} \in [0, 1]$ accounts for the loss of power due to the partial sky coverage of the measurements. In the case for which the datasets have some instrumental noise, such that $\hat{a}_{\ell m} = a_{\ell m} + n_{\ell m}$, we simply have to replace $C_\ell^{XY} \rightarrow C_\ell^{XY} + N_\ell^{XY}$ in the above expression, with $N_\ell^{XY} \equiv \langle n_{\ell m}^X n_{\ell m}^Y \rangle$ the noise spectrum.

Even for full sky coverage, $f_{sky} = 1$, and no noise, $N_\ell = 0$, we see that the power spectrum estimate is still impeded by an intrinsic variance proportional to $C_\ell^2/(2\ell + 1)$. This so-called cosmic variance is a natural consequence of the finite number of modes available on the sky, and particularly impacts the large scales (low ℓ 's).

3 Simulations

In the following sections, in order to test and compare the spectrum estimators, we consider two simulated surveys. Firstly, a full sky experiment aiming at the measurement of the reionization signal ($\ell \lesssim 10$). The foreground contaminations are assumed to be removed, and their residuals, which are assumed to be strong in the galactic plane, are masked. The second survey covers a smaller sky fraction, aiming at the measurement of the recombination bump ($\ell \simeq 100$), and for which the foregrounds contamination is assumed to be removed. Both surveys sky fractions are shown in Fig. 3.2. We generate $n_{MC} = 10^5$ CMB simulations from the *Planck* 2015 best fit spectrum model (*Planck 2015 Results. XIII.*) shown in Fig. 3.1, with a tensor-to-scalar ratio $r = 10^{-3}$, and a reionization optical depth $\tau = 0.06$. The two surveys are treated completely independently. For each of them, in order to estimate the power spectrum, we cross-correlate two simulation maps with common CMB signal, but different noise realisation from the same level. The noise levels are chosen between $0.1 \leq \sigma_n \leq 50 \mu\text{K}\cdot\text{arcmin}$ indicated in Fig. 3.1. This choice roughly covers the characteristics of future ground experiments from CMB Stage 4 (S4) (Abazajian et al. 2016) ($\sim 1 \mu\text{K}\cdot\text{arcmin}$), or satellites such as LiteBIRD (Hazumi et al. 2019), CORE, and PICO (between 1 and $5 \mu\text{K}\cdot\text{arcmin}$) (Matsumura et al. 2014; Delabrouille et al. 2018; De Zotti 2018), up to *Planck* noise level (around $50 \mu\text{K}\cdot\text{arcmin}$) (*Planck 2015 Results: VI.*).

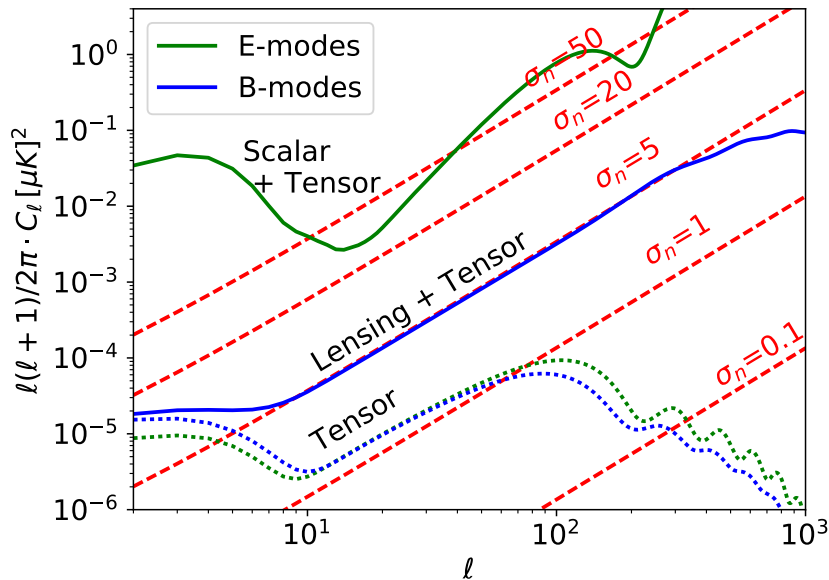


Figure 3.1: Tensor (dashed) and total (solid) components of the E-modes (green), and B-modes (blue) spectra $\ell(\ell + 1)/(2\pi) C_\ell$ as a function of the multipole ℓ , based on *Planck* 2015 best fit model with an optical depth $\tau = 0.06$. The primordial (tensor) polarization spectra are indicated for a tensor-to-scalar ratio $r = 10^{-3}$. Various experimental noise levels $\sigma_n [\mu\text{K}\cdot\text{arcmin}]$ are also indicated.

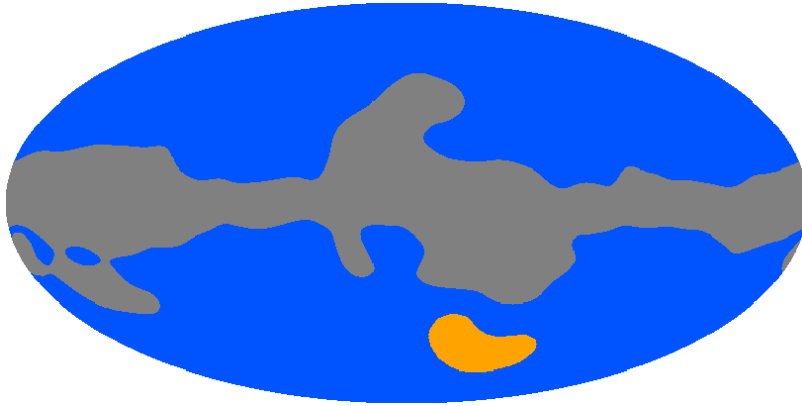


Figure 3.2: Mollweide projection of the sky coverages for the reionization (yellow + blue areas), and the recombination (yellow area) surveys. The latter corresponds to the $\sim 1\%$ sky fraction from *BICEP2* public mask. The grey area corresponds to the 30% where *Planck* dust polarization amplitude is the highest, mostly located in the galactic plane.

3.1 Reionization survey

For the large angular scales analysis, referred as the 'reionization survey', we consider an observed sky fraction $f_{\text{sky}} \simeq 70\%$. A binary mask is built from the 353 GHz *Planck* polarization maps, for which pixels with the highest polarization amplitude, $\sqrt{Q^2 + U^2}$, accurately traces the galactic polarized dust. The map is pre-smoothed using a Gaussian window function in order to remove the experimental noise bias. A cut is then applied on the pixels with the highest amplitude, and the resulting binary mask is smoothed with a Gaussian beam window to avoid sharp edge. We choose to follow the instrumental specifications of the satellite mission LiteBIRD (Matsumura et al. 2014), considering a beam-width of 0.5 deg, and a white homogeneous noise. The analysis is considered over the multipoles range $\ell \in [2, 47]$.

3.2 Recombination survey

The 'recombination survey' sky patch is based on the public *BICEP2* (*Keck Array/BICEP2 October 2015 Data Products 2018*) apodized mask $M \in [0, 1]$. We build a binary mask using all pixels i for which $M_i \geq 0.1$. Rather than considering a homogeneous noise as for the reionization survey, we apply an inverse noise weighting distribution based on the mask M . The effective sky fraction is therefore $f_{\text{sky}} = (\sum_i M_i^2)^2 / \sum_i M_i^4 \simeq 1\%$, as defined in (Hivon et al. 2002). Our analysis considers a beam-width of 0.5 deg. Because of the limited sky fraction, individual multipoles are strongly correlated. We thus reconstruct the spectrum on multipoles bins. We show the results starting from $\ell = 48$ to account for the low sensitivity to large angular scales due to the small coverage, and we define 24 bins up to $\ell = 383$ with a constant bin-width $\Delta_b = 14$.

4 Pure pseudo spectra

In this section we develop the formalism of the pure pseudo spectrum estimator. We discuss its possible implementations and optimisations of the power spectra ‘purifications’. The methods are tested on the simulations set presented in the previous section.

4.1 Formalism

Pseudo spectrum

In the context of partial sky integration or noise weighting, with $W(\hat{n}) \in [0, 1]$ a window function accounting for both, the observed temperature and polarization fields can be replaced by $T \rightarrow TW$ and $\mathbf{P} \rightarrow \mathbf{P}W$ in the expressions introduced in Sec. 2. As a consequence, the measured Fourier coefficients $\tilde{a}_{\ell m}$ do not correspond to the true coefficients $a_{\ell m}$ anymore. Their variance over m , the so called pseudo-spectrum \tilde{C}_ℓ^{XY} , is biased compared to the true power spectrum C_ℓ . Indeed, for temperature and polarization spectra, the terms of \tilde{C}_ℓ^{XY} involves a mixture between the different true multipoles ℓ . In addition, the polarization spectra \tilde{C}_ℓ^{XY} receive additional contributions from both polarization types. By introducing the so-called mixing kernel $M_{\ell\ell'}^{XX',YY'}$, the pseudo-spectrum relation to the true power spectrum C_ℓ is recovered as

$$\tilde{C}_\ell^{XY} = \langle_X \tilde{a}_{\ell m} \tilde{a}_{\ell' m'} \rangle \quad (3.13)$$

$$= \sum_{\substack{\ell', \\ X'=E,B \\ Y'=E,B}} M_{\ell\ell'}^{XY,X'Y'} C_{\ell'}^{X'Y'} + N_\ell^{XY}. \quad (3.14)$$

This aliasing only occurs between polarization modes, i.e. $\{X, Y\} \in \{E, B\}$. The term N_ℓ^{XY} accounts for the experimental noise contribution to the estimate, which can be either evaluated and subtracted when the experimental measurement is sufficiently characterised, or removed by cross-correlating two datasets as discussed further. By removing the noise term and inverting Eq. (3.14), one can recover an unbiased estimator \hat{C}_ℓ^{XY} , the so called pseudo-spectrum estimator. The mixing kernel $M_{\ell\ell'}^{XY,X'Y'}$ thus accounts for the cut-sky effect, the noise weighting, as well as instrumental beams effects. The relevant expressions to build it can be found for example in (Kogut et al. 2003; Alonso et al. 2019).

Cross spectrum

CMB survey datasets are generally a combination of CMB, foregrounds signal, and experimental noise. The measured spherical Fourier coefficients (for temperature or polarization) can thus be written as

$$\hat{a}_{\ell m} = a_{\ell m}^{\text{CMB}} + a_{\ell m}^{\text{Fg}} + a_{\ell m}^{\text{N}}. \quad (3.15)$$

Although the foregrounds signal can be subtracted and/or masked, the noise contribution must be removed in order to obtain unbiased CMB power spectra. This can be achieved by estimating and subtracting the noise power spectrum N_ℓ from the estimate \hat{C}_ℓ . An other solution, first used for the WMAP data analysis (Bennett et al. 2013), consists in cross-correlating two datasets A and B that have uncorrelated noise, such that $\langle a_{\ell m}^{\text{N}_A} a_{\ell m}^{\text{N}_B} \rangle = 0$, and $\hat{C}_\ell^{AB} \equiv \langle a_{\ell m}^A a_{\ell m}^B \rangle$ has vanishing noise bias on average. This second approach, unlike the first one, does not require any prior knowledge of the datasets noise. It also helps mitigating systematic error potentially present in the datasets, providing that they are uncorrelated.

Polarisation purification

As already pointed out, the kernel $M_{\ell\ell'}^{XY, X'Y'}$ in Eq. (3.14) will, in general, mix different modes as well as E and B polarization types,

$$\tilde{C}_\ell^{EE} = M_{\ell\ell'}^{EE, EE} C_{\ell'}^{EE} + M_{\ell\ell'}^{EE, BB} C_{\ell'}^{BB}, \quad (3.16)$$

$$\tilde{C}_\ell^{BB} = M_{\ell\ell'}^{BB, EE} C_{\ell'}^{EE} + M_{\ell\ell'}^{BB, BB} C_{\ell'}^{BB} \quad (3.17)$$

Though such a mixing is removed on average by inverting Eq. (3.14), the leaked ‘ambiguous’ modes will still contribute to the variance of the estimated power spectra. We say that the power spectrum $C_\ell^{E/B}$ are non-pure, as they receive contributions from both E and B modes. For noise dominated datasets, this variance leakage has a small impact since both polarizations have the same noise, and their mutual contributions are equivalent. Conversely, when the noise is much lower than the signal level, the uncertainty is limited by the intrinsic ‘cosmic variance’, arising from the finite number of modes that can be sampled on the sky. In that case, the spectrum variance is proportional to the signal. The E-modes signal, thus its cosmic variance, is much higher than that of B-modes. As a consequence, even for small polarization mixing, the E-to-B leakage drastically exaggerates the B modes power spectrum estimation uncertainty.

Several methods have been developed in order to reduce the contribution of ambiguous modes to the power spectrum estimate. In general, the strategy is to remove the polarization mixing terms of the kernel, such that $M_{\ell\ell'}^{XY, X'Y'} = M_{\ell\ell'}^{XY, X'Y'} \delta_{X'Y'}$, i.e. to make the kernel diagonal in the polarization subspace. This can be achieved by recovering the orthogonality relation of Eq. (3.10), i.e. by reconstructing pure E/B projections ${}_{E/B}\mathbf{Y}_{\ell m}^\dagger$, such that ${}_{E/B}a_{\ell m}$ do not receive any contribution from ambiguous Fourier modes. One can notice that ${}_{E/B}\mathbf{Y}_{\ell m}^\dagger = W\mathbf{D}_2^{E/B}(Y_{\ell m})$ are not pure E/B mode projections, while $\mathbf{D}_2^{E/B}(WY_{\ell m})$ are. Using Eqs. (3.8) and (3.9), the Eqs. (3.7) can be integrated by parts, in order to move the mask weighting field W to the right of the $\mathbf{D}_2^{E/B}$ differential operators (Smith et al. 2007; Bunn 2003),

$${}_{E}a_{\ell m} = \int \mathbf{P}(\hat{n}) [\mathbf{D}_2^E(W(\hat{n})Y_{\ell m}(\hat{n}))]^\dagger d\hat{n}, \quad (3.18)$$

$${}_{B}a_{\ell m} = \int \mathbf{P}(\hat{n}) [\mathbf{D}_2^B(W(\hat{n})Y_{\ell m}(\hat{n}))]^\dagger d\hat{n}. \quad (3.19)$$

The $\mathbf{D}_2^{E/B}(WY_{\ell m})$ terms are now orthogonal subspace to each other, and the resulting Fourier coefficients ${}_{E/B}a_{\ell m}$ are purified from polarization leakage. This transformation is only valid if the line integral terms resulting from the integration by parts vanishes. Since it involves terms proportional to W and ∂W , the weighting mask must satisfies simultaneously the Neumann and Dirichlet boundary conditions. In other words, the pixel mask must have vanishing boundaries and first derivative near the cut sky region. Practically, this is achieved by applying an apodization to the initial mask, a process described in the next section.

A variant method consists in integrating by part to rather move the polarization field \mathbf{P} to the right of the $\mathbf{D}_2^{E/B}$ differential operators (Smith 2006; Grain et al. 2009; Ferte et al. 2013). However, it involves explicit calculation of derivatives of noisy sky maps, while the first method requires the differentiation of a presumably smooth window function. Moreover, it has been shown in (Ferte et al. 2013) that this approach currently does not allow for a pixel mask apodization optimisation, which greatly improves the final B modes spectrum estimate variance as we will see.

Spin weighted windows

We can expand Eq. (3.19) for the B mode Fourier coefficients, and get

$${}_B a_{\ell m} = \mathcal{B}_{2,\ell m} + 2 \frac{\beta_{\ell,2}}{\beta_{\ell,1}} \mathcal{B}_{1,\ell m} + \beta_{\ell,2} \mathcal{B}_{0,\ell m}, \quad (3.20)$$

with

$$\mathcal{B}_{s,\ell m} \equiv \frac{i}{2} \int {}_{+s} Y_{\ell m}^\dagger P_{+2} W_{s-2} - (-1)^s {}_{-s} Y_{\ell m}^\dagger P_{-2} W_{2-s} d\hat{n}, \quad (3.21)$$

where

$$W_s = \partial^s W, \quad (3.22)$$

$$\Leftrightarrow w_{s,\ell m} = \beta_{\ell,s}^{-1} w_{\ell m}, \quad (3.23)$$

are the spin-weighted window functions respectively in the pixel and harmonic domain. Any pure pseudo spectrum implementation thus requires the computation of the spin-1 and spin-2 windows of the spin-0 field W . Those can be computed numerically from W , going back and forth in the pixel and harmonics domain using the Eq. (3.23).

4.2 Window function apodization

As mentioned in the previous section, the B mode purification in Eq. (3.19) is only valid when the window function is sufficiently apodized (smooth), with vanishing boundaries and first derivative near the cut sky region. This condition ensures that the polarization leakage is cancelled, although, in practice, some residual leakage would still be present due to the sky discretization. In the context of B modes analysis, minimizing the polarization leakage does not necessarily imply that the total B mode spectrum variance is minimal. Indeed, for realistic (meaning noisy) datasets, the polarization leakage is not the only source of uncertainty in the resulting spectrum estimate. In some regions, it is possible that the variance induced leakage is subdominant compared to the experimental noise. In that case, the window apodization process is superfluous since it reduces the available effective sky fraction, thus increasing the resulting spectrum estimate variance. An equilibrium has to be found between the variance leakage reduction, and the available sky fraction.

Isotropic

An easy-to-implement solution to apodize the window function is to apply an analytical smoothing function. Following Smith 2006 and Grain et al. 2009, we consider two ‘pure’ analytic apodizations functions that are applied on each pixel of an input binary mask,

$$f_{C1} = \begin{cases} \frac{1}{2} \left[1 - \cos \left(\pi \frac{r}{r_*} \right) \right] & r < r_* \\ 1 & r > r_* \end{cases} \quad (3.24)$$

$$f_{C2} = \begin{cases} \frac{r}{r_*} - \frac{\sin \left(2\pi \frac{r}{r_*} \right)}{2\pi} & r < r_* \\ 1 & r > r_* \end{cases} \quad (3.25)$$

where $r \equiv \sqrt{(1 - \cos \theta)}$ is the distance between the pixel and the closest masked pixel, and r_* is an apodization length parameter. This parameter must be adapted depending on experimental noise, as well as the measured angular scale of the power spectrum. Typically, since the

signal-to-noise ratio decreases as smaller angular scales are probed, the polarization leakage also becomes subdominant compared to the experimental noise induced variance. Smaller apodization lengths r_* are generally required. Ideally, the apodization process must be optimised for each bin of the power spectrum, which can be done for example via Monte-Carlo simulations. A comparison of both apodization functions performed in (Grain et al. 2009) showed that the C2 function produces better performances on the resulting power spectrum uncertainty. In the noise-dominated limit, the inverse-noise weighting window functions can be built by multiplying the inverse square-noise variance with the apodized mask.

We note that the application of those isotropic apodizations does not guarantee the differentiability of the resulting window function. Especially for complex mask shapes having sharp corners. The resulting power spectrum estimate is thus subject to bias because to this non-differentiability.

Optimisation

An optimised apodization process, proposed in (Smith et al. 2007), consists in finding for each bin of multipoles the adequate window function that lower the total (noise and leakage) B pseudo-spectrum variance. As already mentioned, when estimated on a cut sky, the pseudo-spectrum estimator at one given multipole of a polarization mode consists of a mixture of the signal and noise of all true multipoles from both polarisations. The amount of mixing depends directly on the window function shapes. The method proposed in (Smith et al. 2007) aims at reducing the signal+noise contribution from the multipoles different from ℓ (or aliasing). Equivalently, it aims at minimizing the pseudo spectrum expectation value for each multipole ℓ ,

$$\langle \tilde{C}_\ell \rangle = \left\langle \sum_{i,j}^{N_d} \mathbf{d}_i W_i \mathbf{P}_{ij}^\ell W_j \mathbf{d}_j \right\rangle \quad (3.26)$$

$$= \sum_{i,j}^{N_d} W_i \mathbf{C}_{ij} \mathbf{P}_{ij}^\ell W_j, \quad (3.27)$$

$$= W^T (\mathbf{C} * \mathbf{P}^\ell) W, \quad (3.28)$$

where $\mathbf{C} \equiv \langle \mathbf{d}^2 \rangle$ is the pixel covariance matrix of the dataset \mathbf{d} , and $\mathbf{P}_{ij}^\ell = \frac{\partial \mathbf{C}^{ij}}{\partial C_\ell}$ (see appendix A for further definition of the \mathbf{P}_ℓ matrices). We also used the operator $*$ defined as the element-wise matrix multiplication $\mathbf{C} * \mathbf{P}^\ell = \mathbf{C}_{ij} \mathbf{P}_{ij}^\ell$ (with no summation over the i, j indices). Requiring $\sum W_i = \beta$, with $\beta \neq 0$, and introducing the Lagrange multiplier λ , we differentiate

$$\mathcal{L} = W^T (\mathbf{C} * \mathbf{P}^\ell) W + \lambda (W^T \mathbf{1} - \beta) \quad (3.29)$$

with respect to the window function W . The solution reads

$$W = \lambda (\mathbf{C} * \mathbf{P}^\ell)^{-1} \mathbf{1}, \quad (3.30)$$

and we can select the value of β such that $\lambda = 1$. The above equation requires the inversion of a $N_d \times N_d$ matrix², which quickly become computationally costly for large datasets. The equation can still be solved using an iterative Preconditioned Conjugate Gradient (PCG) solver as implemented in Smith et al. 2007; Grain et al. 2009. In this framework, the relation of Eq. (3.22) between the spin-0 window function and its higher spins is relaxed. Eq. (3.30) is then solved simultaneously for all window functions of higher spin. The optimisation procedure can be implemented in both pixel and harmonics domain. The pixel-based approach is preferred

²Typically, N_d is of the order of the number of pixels ($\sim 10^6$ - $\sim 10^8$)

since it accounts for complex mask shapes, holes, and complicated map noise properties (Grain et al. 2009), and is thus our optimisation choice for the simulations tests.

This apodization optimisation method requires a prior knowledge of the experimental noise, and especially of the CMB signal, to build the \mathbf{C} matrix. It has been shown in Grain et al. 2009 that the window apodization optimisation from the perspective of E-to-B leakage reduction mainly depends on the E modes signal, which current characterisation is known with sufficiently high precision on intermediate and small angular scales. As for the B mode, the dominant component of the signal at small angular scales comes from the lensing of E modes, which is well modelled. The impact on the signal prior is investigated in Grain et al. 2009, for which they conclude that the assumption on the B modes signal has almost no impact on the resulting spectrum variance.

4.3 Results

Mask apodizations

We consider both mask apodization processes introduced above. Firstly, an isotropic apodization using the C2 function defined in Eq. (3.25), as this function showed better performance on the power spectra (Grain et al. 2009). For this purpose, we use the *NaMaster* package Alonso et al. 2019, which provides a pure cross-pseudo spectra estimator. Secondly we use the pixel-based mask optimisation obtained through the Preconditioned Conjugate Gradient (PCG) solver used in Grain et al. 2009, implemented in the package *Xpure* 2019. The solver convergence highly depends on the signal and noise levels, and it is typically observed to decrease as the input noise level is low. We found however that the convergence is reached with a reasonable amount of time when the windows are optimised over bins of multipoles rather than on each multipole. For this analysis, we choose to optimise six window functions, with a bin-width of ten multipoles for the reionization survey, and around a hundred for the recombination survey. The mixing kernel is then computed ‘row-by-row (i.e. bin-per-bin) using each window function, from which the unbiased estimator is finally built. For the large scale analysis only, the PCG does not converge in a reasonable amount of time for a fiducial noise level under $3 \mu\text{K}\cdot\text{arcmin}$. We thus use optimised window functions at $3 \mu\text{K}\cdot\text{arcmin}$ to estimate the power spectrum for simulations with noise level under $3 \mu\text{K}\cdot\text{arcmin}$.

The real part (Q component) of the window functions used for the analysis at $1 \mu\text{K}\cdot\text{arcmin}$ are displayed in Fig. 3.3 and 3.4 respectively for the reionization and recombination surveys. We observe that the first and second derivative (spin-1 and spin-2) window map computed for both surveys present scratchy features when using the C2 apodization function. Those reflect the non-differentiability of the window function, which is due to the complex shapes of the large scale binary mask. The impact in terms of potential bias on the reconstructed power spectrum is discussed hereafter. On the other hand, the optimised apodization produces significant smoother spinned maps. We will see that the spectrum estimate present no bias, and a lower variance, which emphasises the interest of this technique against a simple isotropic apodization function applied on the sky.

Mixing kernel

Following (Grain et al. 2012), we adopt a hybrid approach, where the E-modes are obtained using the standard pseudo-spectrum, and the B-modes using the pure method. Indeed, the B-to-E leakage has almost negligible impact on the E estimate variance given the B mode signal level. It is thus advised to keep the ambiguous modes to estimate the E spectrum.

The mixing kernel for both surveys are shown in Fig. 3.5. We only display the polarization block entries for the optimised apodization at $1 \mu\text{K}\cdot\text{arcmin}$ noise level. Each mixing kernel

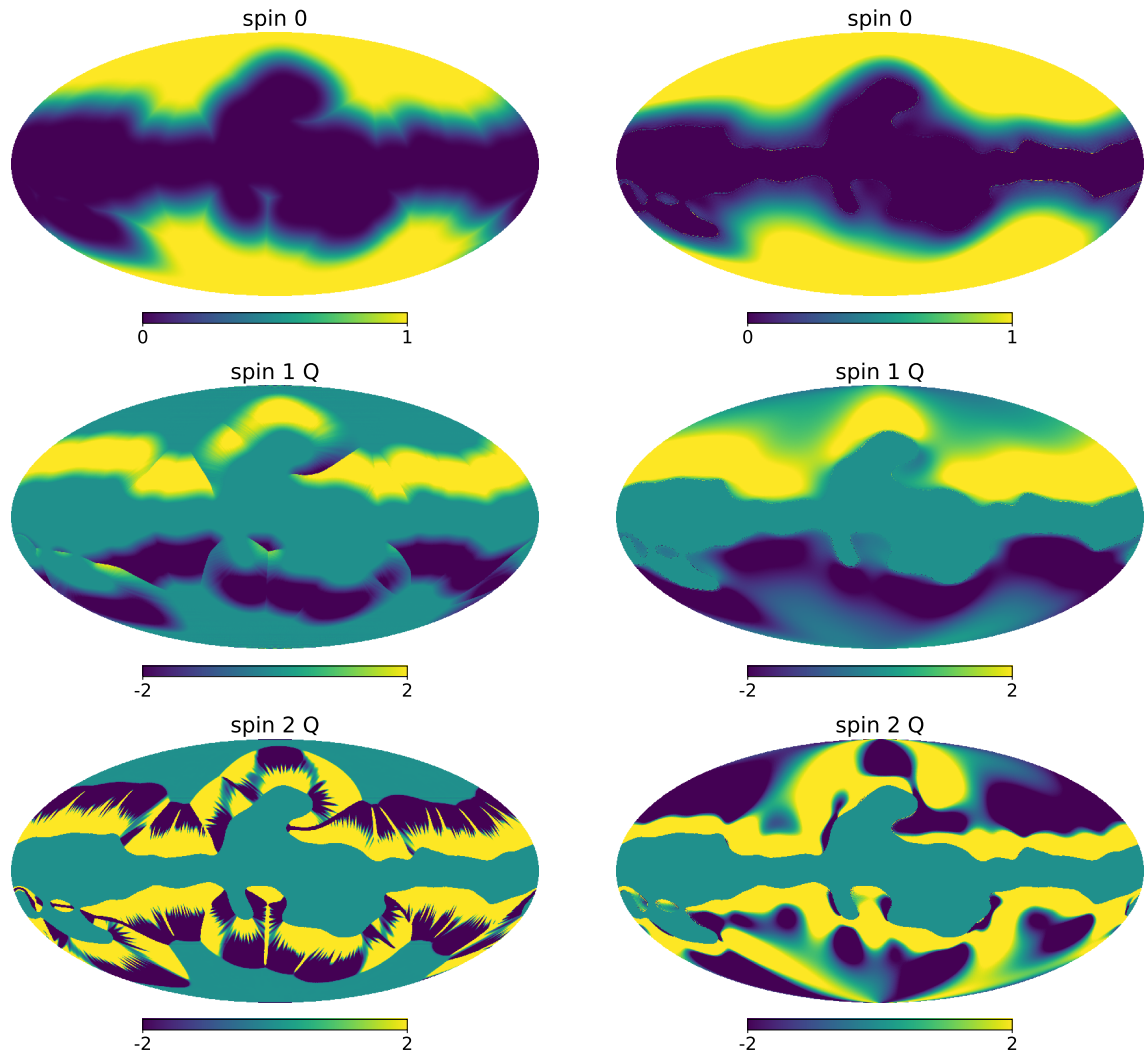


Figure 3.3: Spin-weighted window functions used for the large-scale (reionization) pure pseudo spectrum simulations. The windows using the C2 apodization function with an apodization angle $\theta_* = 30^\circ$ are displayed on the left column. The pixel-optimised windows for $3 \mu\text{K.arcmin}$ are displayed on the right column.

made of four blocks reflecting each of the four pseudo-multipole mixing combination EE-EE, EE-BB, BB-EE, and BB-BB. As already mentioned, the mixing matrix $M_{\ell,\ell}^{XY,X'Y'}$ translates the amount of modes ℓ' from the $X'Y'$ polarization power spectrum leaking into the XY polarization spectrum estimated at the multipole ℓ . Thus, with this definition, we understand that the amount of E modes leaking into B modes is quantified by the bottom left block of the mixing matrix. Conversely, the amount of B mode leaking into E modes is quantified by the top right block.

We observe that the E-to-B leakage is successfully reduced, as the BB-EE block of both surveys contains smaller mixing values. Only a small mixing is observed on the first bin $\ell \sim 2$. On the other hand, the B-to-E leakage is not reduced, which is in agreement with our choice to adopt a hybrid pure pseudo-spectrum estimation. We note that the overall amount of mode-mixing is smaller for the recombination survey.

We also notice that the first multipoles of the BB-BB block can be highly correlated with small scales ℓ' of the same block.

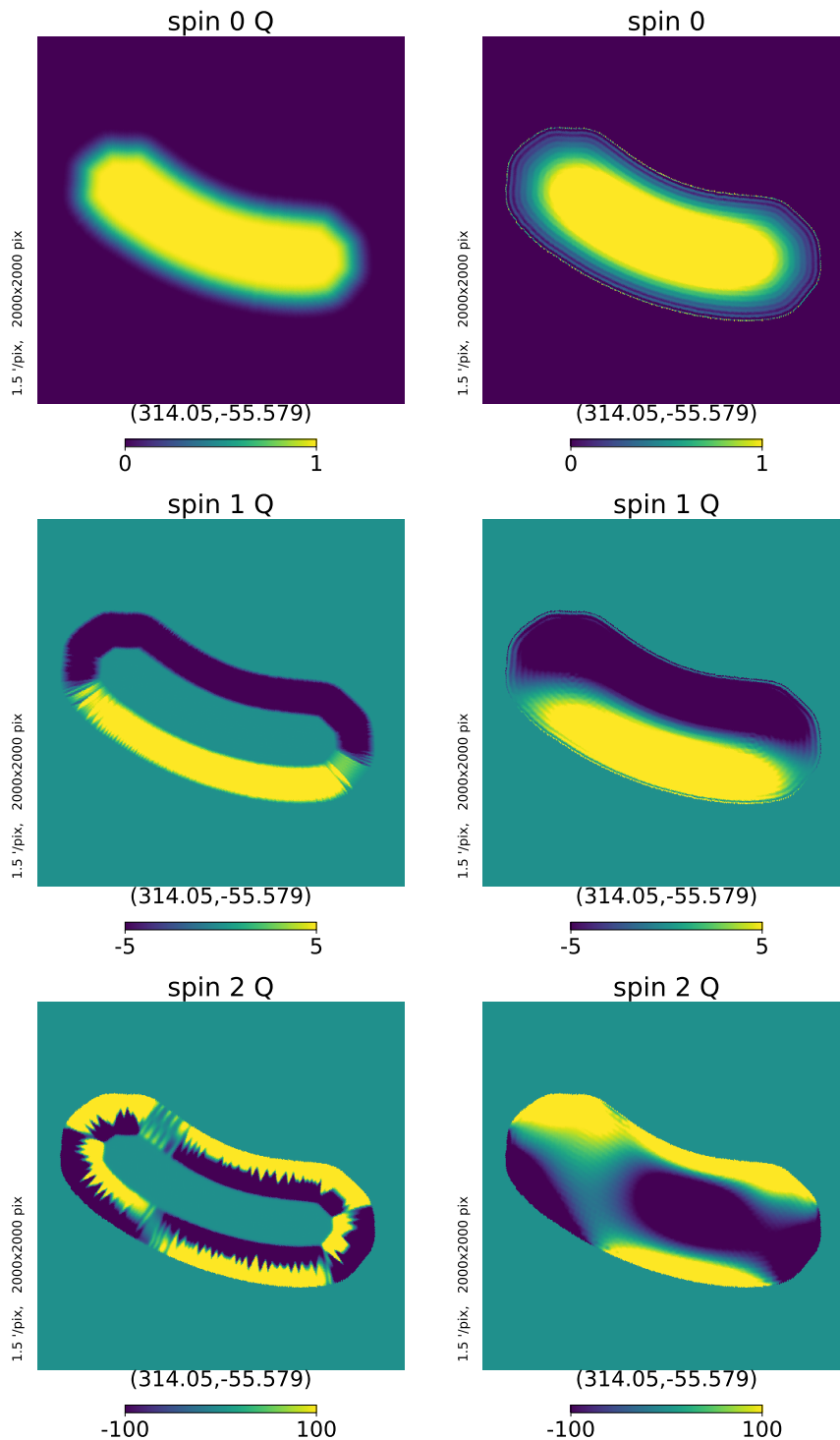


Figure 3.4: Spin-weighted window functions used for the small-scale (recombination) pure pseudo spectrum simulations. The windows using the C2 apodization function with an apodization angle $\theta_* = 30^\circ$ are displayed on the left column. The pixel-optimised windows for $1 \mu\text{K.arcmin}$ are displayed on the right column

Spectrum

In this subsection we compare the spectrum estimations from the standard pseudo-spectrum (pCl) using the xPol estimator (Tristram et al. 2005), and the (pure) pseudo-spectrum ap-

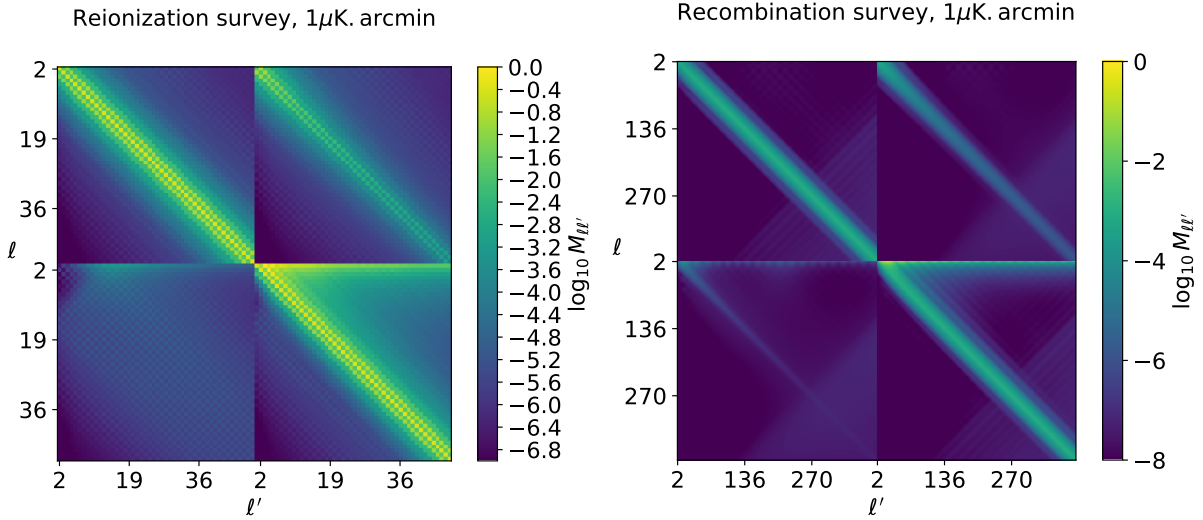


Figure 3.5: Pure pseudo spectrum polarization mixing kernel (log-scale) for the reionization (left) and recombination (right) surveys, with a noise level $\sigma_n = 1\mu\text{K.arcmin}$.

proaches. For that purpose, we make use of 10^4 MC simulations based on the surveys introduced in Sec. 3.

For each apodization angle θ_* , the power spectrum uncertainty using the C2 apodization is shown in Fig. 3.6. We observe that broader apodization lengths reduce the amount of leakage at large angular scales ($\ell \lesssim 15$ for the reionization survey, and $\ell \lesssim 90$ for the recombination survey), but also reduces the effective observed sky fraction, thus rising the sampling variance at the remaining higher multipoles. For each multipole, we select the apodization length θ which produces the lowest variance. We then combine the estimated multipole to reconstruct an unbiased spectrum estimation

$$\hat{C}_\ell^{\text{combi}} = \hat{C}_\ell^\theta \quad \text{such that} \quad \sigma(\hat{C}_\ell^\theta) = \min \left\{ \sigma(\hat{C}_\ell^{\theta_0}), \dots, \sigma(\hat{C}_\ell^{\theta_n}) \right\}. \quad (3.31)$$

The resulting spectrum uncertainty is therefore equal to the joined spectra minimum variances, that is to say,

$$\sigma(\hat{C}_\ell^{\text{combi}}) = \min \left\{ \sigma(\hat{C}_\ell^{\theta_0}), \dots, \sigma(\hat{C}_\ell^{\theta_n}) \right\}. \quad (3.32)$$

In order to fully visualize the apodization effect, we also show PpCl errors for each apodization length value. Longer apodization lengths do not improve further the large scale spectra uncertainties ($\theta_* \geq 30^\circ$ for the reionization, and $\theta_* \geq 10^\circ$ for the recombination survey). The C2 apodization is also observed to cause bias on the spectrum estimate. The bias is induced by the non-differentiability of the spin-window function discussed previously. It is mainly present on the first tenth multipoles of the reionization survey when using a small apodization angle θ_* , and it tends to disappear as a larger apodization angle is used. We note that using the other apodization function C1 does not produce significant changes in these results.

As expected, the standard pCl leads to much higher uncertainties, for which the E-modes variance leakage contribution is visible on the recombination survey B-modes variance.

Similarly, we show the spectrum estimate results for the optimised apodization procedure in Fig. 3.7, and we compare with the C2 case. For both surveys, the pixel domain optimisation provides the lowest spectra uncertainty over the whole multipole range, particularly at large angular scales. This is in accordance with previous studies (Ferte et al. 2013; Smith et al. 2007; Grain et al. 2009).

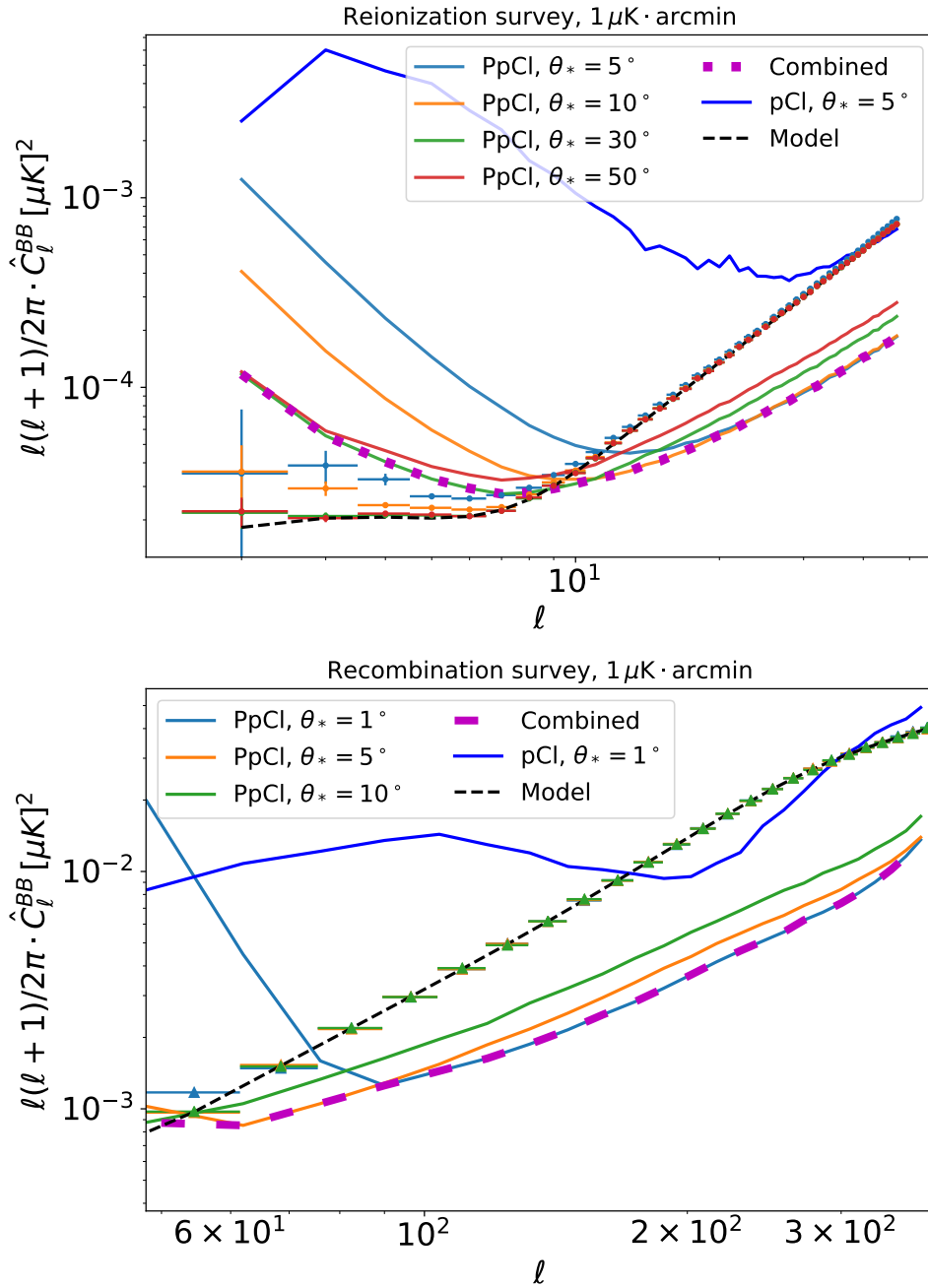


Figure 3.6: BB spectrum C_ℓ (error-bars) and uncertainty $\sigma(C_\ell)$ (plain) using the standard pseudo-Cl (pCl) and the pure pseudo-Cl (PpCl) with a 'C2' apodization. Left : reionization survey. Right : recombination survey. The PpCl results are shown for each apodization angle, θ_* . The combined PpCl uncertainty is indicated in plain dashed magenta. The simulation are generated with a noise level $\sigma_n = 1 \mu\text{K} \cdot \text{arcmin}$. Vertical error-bars are divided by the square root of the number of simulations (10^4), while horizontal error-bars account for the binning width.

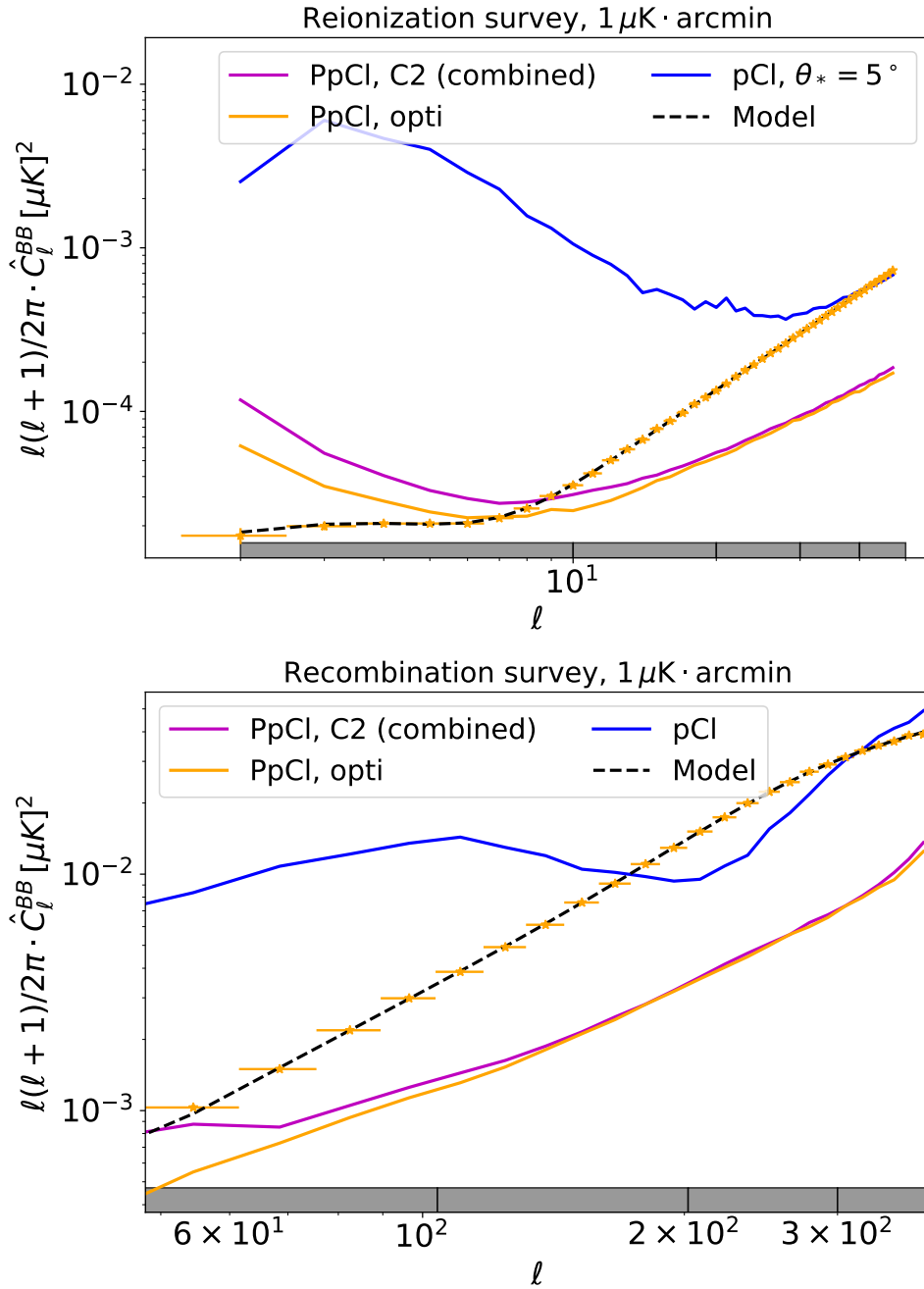


Figure 3.7: BB spectrum (error-bars) and uncertainty (plain) for the pure pseudo-Cl (PpCl) using the 'C2' and optimised apodizations. Top : reionization survey. Bottom : recombination survey. The PpCl spectrum estimates (error-bars) and uncertainty are shown for each apodization angle, θ_* . The combined PpCl uncertainty is indicated in plain dashed magenta. The simulation are generated with a noise level $\sigma_n = 1 \mu\text{K} \cdot \text{arcmin}$. Error-bars are divided by the square root of the number of simulations (10^4). The grey boxes indicate the bins used to optimise the window function.

4.4 Summary

In this section, we have presented the pseudo-spectrum estimator, and more specifically the pure formalism. Compared to the standard approach, the latter allows to separate ambiguous modes from pure polarization modes when estimated on a cut sky. This technique is particularly suited for B-mode power spectrum estimation, since it reduces the amount of E-to-B leakage. Though the leakage can be corrected on average by computing a mixing kernel matrix, the uncertainty on the ambiguous modes still contributes to the total variance of the BB spectrum. The polarization mixing terms in the kernel matrix can be reduced by redefining an appropriate window function on the sky. In particular, the pure method requires that the window function, as well as its first derivative should continuously vanish near the border of the mask. In order to do so, we presented two apodization processes. The first one consists in applying a constant apodization function C2 on the sky, but that can lead to spectrum bias due to the non-differentiability of the window function. The second technique consists in optimising the window function in the pixel domain in order to reduce the amount of modes mixing. It has the advantage in accounting for the pixel-noise weighting or complex mask shapes. However, the PCG solver that optimises the window functions was observed to lose convergence as lower noise levels were considered. The current solution that we propose is to estimate the window functions with higher noise fiducial level. Anyway, the optimisation successfully provides lower spectrum variance, especially at large scales.

A very high variance is also present at low multipoles ($\ell \lesssim 10$), on the reionization survey. We observed that it appears as soon as the tensor-to-scalar ratio becomes small ($r \lesssim 10^{-3}$), while it is not visible on the previous papers cited in this section since they used a fiducial value $r \gtrsim 10^{-2}$, which is one order of magnitude higher than ours.

5 Cross Quadratic maximum likelihood estimator

As described in the introduction of this chapter, the Quadratic Maximum Likelihood (QML) is a pixel-based estimator that allows to obtain spectra with minimum variance. However, it does not allow to cross-correlate datasets, as the pCl formalism does. In this section, we describe a pixel-based spectrum estimator, based on the QML approach, that allows us to cross-correlate CMB maps that have common sky coverage. This cross QML (xQML) formalism was first mentioned in *Planck Intermediate Results: XLVI* for the 2016 Planck results, and we deepened its characterisation in Vanneste et al. 2018. More specifically, we estimated the degree of optimality of the xQML compared to the QML, and tested the algorithm on large and small scales simulated surveys. We also estimated its efficiency at mitigating polarization variance leakage impact on the B-modes power spectrum, and compared the results with the pure pCl spectrum estimator. The following discussion resumes and completes our study published in Vanneste et al. 2018. A public implementation of the xQML estimator has been made available on GitLab: <https://gitlab.in2p3.fr/xQML>.

5.1 Formalism

Firstly, we review the most important steps that lead to the definition of the QML estimator, following what has been done in (Tegmark 1997; Tegmark et al. 2001). We then derive a cross-spectrum QML estimator (xQML) and compare its properties with the QML. Finally, we discuss in depth the implementation of the algorithm.

In the following sections, lower case characters correspond to vectors and upper case characters correspond to matrices. Bold font, Latin indices, the trace and transpose operators are used for elements in the pixel domain, while normal font and ℓ indices are used in the multipole domain.

Standard QML

We consider a dataset \mathbf{d} , of dimension $N_d = 3n_{\text{pix}}$ which encodes temperature T and Stokes parameters Q and U measurements,

$$\mathbf{d} \equiv \begin{pmatrix} \mathbf{T} \\ \mathbf{Q} \\ \mathbf{U} \end{pmatrix}. \quad (3.33)$$

The pixel covariance matrix \mathbf{C} of the dataset is given by

$$\mathbf{C} \equiv \langle \mathbf{d}, \mathbf{d}^T \rangle = \mathbf{S} + \mathbf{N}, \quad (3.34)$$

with \mathbf{N} the pixel noise covariance matrix, and \mathbf{S} the signal covariance matrix defined as

$$\mathbf{S} \equiv \sum_{\ell} \mathbf{P}_{\ell} C_{\ell}, \quad \text{with} \quad \mathbf{P}_{\ell}^{ij} = \frac{\partial \mathbf{C}^{ij}}{\partial C_{\ell}}. \quad (3.35)$$

The vector C_{ℓ} can encode all six power spectra TT , EE , BB , TE , TB , and EB . For temperature, the P_{ℓ}^{ij} matrices correspond to the Legendre polynomial functions,

$$\mathbf{P}_{\ell}^{ij,T} = \frac{4\pi}{2\ell+1} \sum_m Y_{\ell m}(\hat{n}_i) Y_{\ell m}^*(\hat{n}_j). \quad (3.36)$$

The expression and computation of \mathbf{P}_{ℓ} is detailed for polarization in appendix A.

Following (Tegmark 1997; Tegmark et al. 2001), we write the power spectrum estimator as a quadratic function of the pixels

$$\hat{y}_{\ell} \equiv \mathbf{d}^T \mathbf{E}_{\ell} \mathbf{d} - b_{\ell}. \quad (3.37)$$

The \mathbf{E}_ℓ ($\ell = 2, \dots$) are Hermitian $N_d \times N_d$ matrices, and b_ℓ are arbitrary constants. From Eqs. (3.34) and (3.35), the estimator ensemble average reads

$$\langle \hat{y}_\ell \rangle = \text{Tr} [\mathbf{E}_\ell \langle \mathbf{d}, \mathbf{d}^T \rangle] - b_\ell, \quad (3.38)$$

$$= \sum_{\ell'} W_{\ell\ell'} C_{\ell'} + \text{Tr} [\mathbf{E}_\ell \mathbf{N}] - b_\ell, \quad (3.39)$$

with

$$W_{\ell\ell'} \equiv \text{Tr} [\mathbf{E}_\ell \mathbf{P}_{\ell'}] \quad (3.40)$$

as the 'mode-mixing' matrix. Choosing $b_\ell = \text{Tr} [\mathbf{E}_\ell \mathbf{N}]$, the unbiased estimator of the true power spectrum C_ℓ thus reads

$$\hat{C}_\ell \equiv \sum_{\ell'} [W^{-1}]_{\ell\ell'} \hat{y}_{\ell'}, \quad (3.41)$$

and has the following covariance

$$\langle \Delta \hat{C}_\ell, \Delta \hat{C}_{\ell'} \rangle = [W^{-1}]_{\ell\ell_1} \langle \Delta \hat{y}_{\ell_1}, \Delta \hat{y}_{\ell_2} \rangle [W^{-1}]_{\ell_2\ell'}, \quad (3.42)$$

where $\Delta \hat{C}_\ell = \hat{C}_\ell - \langle \hat{C}_\ell \rangle$. The summation over repeated indices is implied. *The resulting power spectrum estimate is unbiased, regardless of the choice of the \mathbf{E}_ℓ matrices.* The \mathbf{E}_ℓ are usually constructed in order to minimize the estimator variance

$$\langle \Delta \hat{y}_\ell, \Delta \hat{y}_\ell \rangle = 2 \text{Tr} [\mathbf{C} \mathbf{E}_\ell \mathbf{C} \mathbf{E}_\ell], \quad (3.43)$$

which gives the trivial solution $\mathbf{E}_\ell = \mathbf{0}$. We thus impose the mode-mixing matrix diagonal to be non-zero, that is for each ℓ , we have $W_{\ell\ell} = \beta$, with β an arbitrary constant. The problem can be solved using the method of Lagrange multipliers. We require the derivative of the Lagrange function

$$\mathcal{L} = \langle \Delta \hat{y}_\ell, \Delta \hat{y}_\ell \rangle - 2\lambda (\text{Tr} [\mathbf{E}_\ell \mathbf{P}_\ell] - \beta), \quad (3.44)$$

with respect to \mathbf{E}_ℓ vanishes, where λ is the Lagrange multiplier. The solution reads³

$$\mathbf{E}_\ell = \frac{\lambda}{2} \mathbf{C}^{-1} \mathbf{P}_\ell \mathbf{C}^{-1}. \quad (3.45)$$

Finally, imposing $W_{\ell\ell} = \text{Tr} [\mathbf{E}_\ell \mathbf{P}_\ell] = \beta$ gives

$$\frac{\lambda}{2} \text{Tr} [\mathbf{C}^{-1} \mathbf{P}_\ell \mathbf{C}^{-1} \mathbf{P}_\ell] = \beta. \quad (3.46)$$

We choose β such that $\lambda = 1$ and \mathbf{E}_ℓ is well defined. With this choice, the mode-mixing matrix is equal to the Fisher information matrix

$$W_{\ell\ell'} = F_{\ell\ell'} \quad (3.47)$$

$$\equiv \frac{1}{2} \text{Tr} [\mathbf{C}^{-1} \mathbf{P}_\ell \mathbf{C}^{-1} \mathbf{P}_{\ell'}], \quad (3.48)$$

with $\langle \Delta \hat{y}_\ell, \Delta \hat{y}_{\ell'} \rangle = F_{\ell\ell'}$ and $\langle \Delta \hat{C}_\ell, \Delta \hat{C}_{\ell'} \rangle = [F^{-1}]_{\ell\ell'}$.

The \mathbf{E}_ℓ matrices are thus constructed such that the spectrum estimator has minimal variance, i.e. the Fisher variance. However, the QML estimator requires a precise knowledge of the pixel noise matrix \mathbf{N} to compute the bias term b_ℓ in Eq. (3.37). In practice, estimating the noise model of an experiment is difficult and requires an exquisite knowledge of instrument properties. In the next section, we develop a method that allows us to compute a cross-spectrum estimator that is unbiased independently of the choice of \mathbf{N} .

³Using matrix identities $\partial_{\mathbf{E}} \text{Tr} [\mathbf{C} \mathbf{E} \mathbf{C} \mathbf{E}] = 2 \mathbf{C}^T \mathbf{E}^T \mathbf{C}^T$.

Cross QML

Following the same formalism as for the 'auto'-spectrum QML estimator detailed in the Sec. 5.1, we now consider two datasets \mathbf{d}^A and \mathbf{d}^B from which the pixel covariance matrix reads

$$\mathbf{C}^{AB} \equiv \langle \mathbf{d}^A, \mathbf{d}^{B^T} \rangle = \mathbf{S} + \mathbf{N}^{AB}. \quad (3.49)$$

We assume uncorrelated noise between the two datasets, such that the cross pixel noise covariance matrix vanishes $\mathbf{N}^{AB} = 0$.

The cross estimator now reads

$$\hat{y}_\ell^{AB} \equiv \mathbf{d}^{A^T} \mathbf{E}_\ell \mathbf{d}^B - b_\ell^{AB}, \quad (3.50)$$

with $b_\ell^{AB} = \text{Tr}[\mathbf{E}_\ell \mathbf{N}^{AB}] = 0$. As in Eqs. (3.41) and (3.42) for the QML method, the unbiased estimator reads

$$\hat{C}_\ell \equiv \sum_{\ell'} [W^{-1}]_{\ell\ell'} \hat{y}_{\ell'}^{AB}, \quad (3.51)$$

and its covariance

$$\langle \Delta \hat{C}_\ell, \Delta \hat{C}_{\ell'} \rangle = [W^{-1}]_{\ell\ell_1} \langle \Delta \hat{y}_{\ell_1}^{AB}, \Delta \hat{y}_{\ell_2}^{AB} \rangle [W^{-1}]_{\ell_2\ell'}. \quad (3.52)$$

The central term of Eq. (3.52) is computed using Wick's theorem,

$$\begin{aligned} \langle \Delta \hat{y}_\ell^{AB}, \Delta \hat{y}_{\ell'}^{AB} \rangle &= [\langle d_i^A, d_k^A \rangle \langle d_j^B, d_n^B \rangle + \langle d_i^A, d_n^B \rangle \langle d_j^A, d_k^B \rangle] \mathbf{E}_\ell^{ij} \mathbf{E}_{\ell'}^{kn} \\ &= \text{Tr}[\mathbf{C}^{AA} \mathbf{E}_\ell \mathbf{C}^{BB} \mathbf{E}_{\ell'}^T + \mathbf{C}^{AB} \mathbf{E}_\ell \mathbf{C}^{AB} \mathbf{E}_{\ell'}], \end{aligned} \quad (3.53)$$

where summation on the pixels indices i, j, k, n is implied. Matrices $\mathbf{C}^{AA} = \mathbf{S} + \mathbf{N}^{AA}$ and $\mathbf{C}^{BB} = \mathbf{S} + \mathbf{N}^{BB}$ are respectively the pixel covariance matrix of the datasets A and B .

As in Eq. (3.44) for the QML, we seek for the \mathbf{E}_ℓ matrices that minimize the estimator variance of Eq. (3.53). We get the equation⁴

$$\mathbf{C}^{AA} \mathbf{E}_\ell \mathbf{C}^{BB} + \mathbf{C}^{AB} \mathbf{E}_\ell^T \mathbf{C}^{AB} = \lambda \mathbf{P}_\ell, \quad (3.54)$$

which is a generalized form of the Sylvester equation (De Terán et al. 2016). Although the exact solution exists, as discussed in Sec. 5.3, it requires us to solve a system of N_d^2 equations, which is computationally prohibitive for large datasets. For this reason, we derive an approximate solution by considering two extreme signal-to-noise ratio (SNR) cases :

- HS : High SNR, such that $\mathbf{S} \gg \mathbf{N}$, and $\mathbf{C}^{AA} \sim \mathbf{C}^{BB} \sim \mathbf{S}$.
- LS : Low SNR, such that $\mathbf{S} \ll \mathbf{N}$, and $\mathbf{C}^{AA} \sim \mathbf{N}^{AA}$, $\mathbf{C}^{BB} \sim \mathbf{N}^{BB}$.

For both limits, Eq (3.54) admits a solution of the form⁵

$$\mathbf{E}_\ell \simeq \frac{\lambda}{\alpha} (\mathbf{C}^{AA})^{-1} \mathbf{P}_\ell (\mathbf{C}^{BB})^{-1}, \quad (3.55)$$

where α is a normalization coefficient that depends on the SNR, with $\alpha = 2$ for the HS regime, and $\alpha = 1$ for the LS regime. The impact of the approximation made in Eq. (3.55) on the spectrum variance is discussed in Sec 5.3. Finally, imposing $W_{\ell\ell} = \text{Tr}[\mathbf{E}_\ell \mathbf{P}_\ell] = \beta$ gives

$$\frac{\lambda}{\alpha} \text{Tr}[(\mathbf{C}^{AA})^{-1} \mathbf{P}_\ell (\mathbf{C}^{BB})^{-1} \mathbf{P}_\ell] = \beta. \quad (3.56)$$

⁴Using matrix identities $\partial_{\mathbf{E}} \text{Tr}[\mathbf{AEBE}] = \mathbf{A}^T \mathbf{E}^T \mathbf{B}^T + \mathbf{B}^T \mathbf{E}^T \mathbf{A}^T$ and $\partial_{\mathbf{E}} \text{Tr}[\mathbf{AEBE}^T] = \mathbf{A}^T \mathbf{E} \mathbf{B}^T + \mathbf{A} \mathbf{E} \mathbf{B}$.

⁵We remark that when $\mathbf{C}^{AA} \sim \mathbf{C}^{BB}$, and more specifically for a high signal-to-noise ratio, $\mathbf{E}_\ell \simeq \mathbf{E}_\ell^T$.

We choose β such that $\lambda/\alpha = 1/2$, and we recover the QML solution for $A = B$. Inserting \mathbf{E}_ℓ of Eq. (3.55) in the mode-mixing matrix defined in Eq. (3.40), one obtains

$$W_{\ell\ell'} = \frac{1}{2} \text{Tr} [(\mathbf{C}^{AA})^{-1} \mathbf{P}_\ell (\mathbf{C}^{BB})^{-1} \mathbf{P}_{\ell'}]. \quad (3.57)$$

Using Eqs. (3.53), (3.52), (3.55) and (3.57), the cross-spectrum estimator covariance reads

$$\begin{aligned} \langle \Delta \hat{C}_\ell, \Delta \hat{C}_{\ell'} \rangle &= \frac{1}{2} [W^{-1}]_{\ell\ell_1} (W_{\ell_1\ell_2} + G_{\ell_1\ell_2}) [W^{-1}]_{\ell_2\ell'} \\ &= \frac{1}{2} ([W^{-1}]_{\ell\ell'} + [W^{-1}]_{\ell\ell_1} G_{\ell_1\ell_2} [W^{-1}]_{\ell_2\ell'}) \\ &\equiv V_{\ell\ell'}, \end{aligned} \quad (3.58)$$

where we define the additional mode-mode matrix

$$G_{\ell\ell'} \equiv \frac{1}{2} \text{Tr} [(\mathbf{C}^{AA})^{-1} \mathbf{P}_\ell (\mathbf{C}^{BB})^{-1} \mathbf{C}^{AB} (\mathbf{C}^{AA})^{-1} \mathbf{P}_{\ell'} (\mathbf{C}^{BB})^{-1} \mathbf{C}^{AB}]. \quad (3.59)$$

In the HS regime $G_{\ell\ell'} \sim W_{\ell\ell'}$, such that $V_{\ell\ell'} = [W^{-1}]_{\ell\ell'}$. In the LS regime, the second term $[W^{-1}]_{\ell\ell_1} G_{\ell_1\ell_2} [W^{-1}]_{\ell_2\ell'}$ in Eq. (3.58) contributes at second order of the cross-spectrum variance. As a representative example, the diagonal elements of those two terms are compared in Fig. 3.8 for the EE and BB spectra, with a $10 \mu\text{K.arcmin}$ noise level. With this choice, the E-mode is signal dominated, and corresponds to the HS regime, while the B-mode SNR is low for most of the multipoles ($\ell \gtrsim 10$), and corresponds to the LS case.

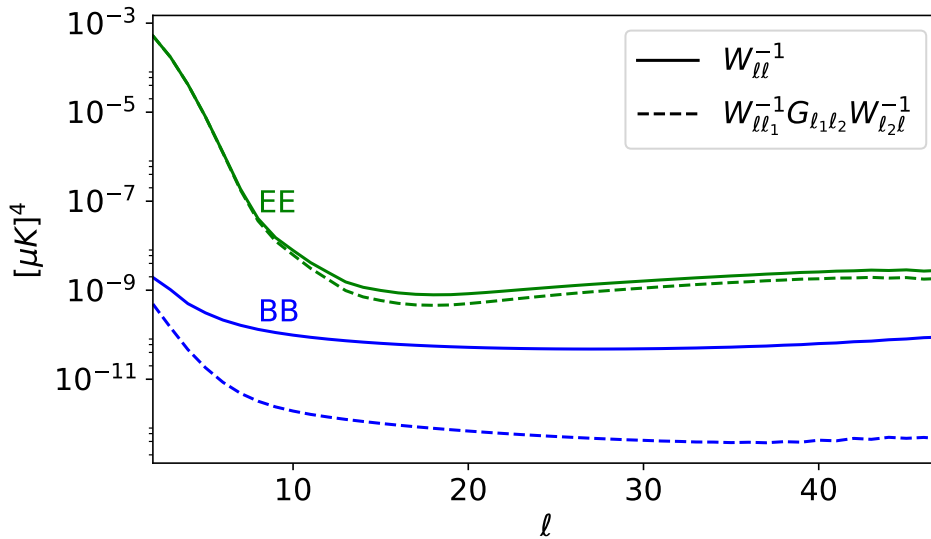


Figure 3.8: Diagonals of the covariance matrix terms $W_{\ell\ell_1}^{-1} G_{\ell_1\ell_2} W_{\ell_2\ell}^{-1}$ (dashed) and $W_{\ell\ell}^{-1}$ (plain) of Eq. (3.58). EE and BB components are plotted in green and blue respectively. The noise level is $10 \mu\text{K.arcmin}$.

We thus successfully defined a quadratic estimator based on datasets cross-correlation which does not require the subtraction of noise bias. Moreover, we derived an approximation of the \mathbf{E}_ℓ matrices that minimizes its variance. We also note that we recover the QML estimator when $A = B$, with a nonvanishing noise bias term b_ℓ .

5.2 Relation with the maximum likelihood estimator

The spectrum MLE, in its initial form, consists in finding the maximum of the Likelihood for the parameter \tilde{C}_ℓ ,

$$\mathcal{L}(\tilde{C}_\ell|\mathbf{d}) = -\frac{1}{2}(\mathbf{d}\tilde{\mathbf{C}}^{-1}\mathbf{d} + \text{Tr}[\ln \tilde{\mathbf{C}}]), \quad (3.60)$$

with $\tilde{\mathbf{C}} = \mathbf{N} + \tilde{\mathbf{S}}$ the pixel covariance matrix, and $\tilde{\mathbf{S}}$ is constructed from the fiducial spectra \tilde{C}_ℓ . First we Taylor expand Eq. (3.60) up to second order,

$$\mathcal{L}(\tilde{C}_\ell + \delta\tilde{C}_\ell) = \mathcal{L}(\tilde{C}_\ell) + \frac{\partial\mathcal{L}}{\partial\tilde{C}_\ell}\delta\tilde{C}_\ell + \frac{1}{2}\frac{\partial^2\mathcal{L}}{\partial\tilde{C}_\ell\partial\tilde{C}_{\ell'}}\delta\tilde{C}_\ell\delta\tilde{C}_{\ell'}, \quad (3.61)$$

where summation over repeated ℓ is assumed. The first derivative of the Likelihood is written as

$$\begin{aligned} \frac{\partial\mathcal{L}}{\partial\tilde{C}_\ell} &= \frac{1}{2}\left(\mathbf{d}^T\tilde{\mathbf{C}}^{-1}\frac{\partial\tilde{\mathbf{S}}}{\partial\tilde{C}_\ell}\tilde{\mathbf{C}}^{-1}\mathbf{d} - \text{Tr}\left[\tilde{\mathbf{C}}^{-1}\frac{\partial\tilde{\mathbf{S}}}{\partial\tilde{C}_\ell}\right]\right) \\ &= \frac{1}{2}\left(\mathbf{d}^T\tilde{\mathbf{C}}^{-1}\mathbf{P}_\ell\tilde{\mathbf{C}}^{-1}\mathbf{d} - \text{Tr}\left[\tilde{\mathbf{C}}^{-1}\mathbf{P}_\ell\right]\right), \end{aligned} \quad (3.62)$$

and the second derivative, also known as the curvature matrix, as

$$\begin{aligned} \frac{\partial^2\mathcal{L}}{\partial\tilde{C}_\ell\partial\tilde{C}_{\ell'}} &\equiv \mathcal{F}_{\ell\ell'} = -\mathbf{d}^T\tilde{\mathbf{C}}^{-1}\frac{\partial\tilde{\mathbf{S}}}{\partial\tilde{C}_\ell}\tilde{\mathbf{C}}^{-1}\frac{\partial\tilde{\mathbf{S}}}{\partial\tilde{C}_{\ell'}}\tilde{\mathbf{C}}^{-1}\mathbf{d} + \frac{1}{2}\text{Tr}\left[\tilde{\mathbf{C}}^{-1}\frac{\partial\mathbf{S}}{\partial C_\ell}\tilde{\mathbf{C}}^{-1}\frac{\partial\mathbf{S}}{\partial C_{\ell'}}\right] \\ &= -\mathbf{d}^T\tilde{\mathbf{C}}^{-1}\mathbf{P}_\ell\tilde{\mathbf{C}}^{-1}\mathbf{P}_{\ell'}\tilde{\mathbf{C}}^{-1}\mathbf{d} + \frac{1}{2}\text{Tr}\left[\tilde{\mathbf{C}}^{-1}\mathbf{P}_\ell\tilde{\mathbf{C}}^{-1}\mathbf{P}_{\ell'}\right]. \end{aligned} \quad (3.63)$$

By maximizing Eq. (3.61) with respect to $\delta\tilde{C}_\ell$, the solution for $\delta\tilde{C}_\ell$ reads

$$\delta\tilde{C}_\ell = -\left[\frac{\partial^2\mathcal{L}}{\partial\tilde{C}_\ell\partial\tilde{C}_{\ell'}}\right]^{-1}\frac{\partial\mathcal{L}}{\partial\tilde{C}_{\ell'}}. \quad (3.64)$$

The MLE can be implemented as a Newton-Raphson algorithm that iterates over $\delta\tilde{C}_\ell$, see for example Borrill 1999. The curvature matrix, $\mathcal{F}_{\ell\ell'}$, can be replaced by the Fisher matrix $F_{\ell\ell'}$, as in Bond et al. 1998, which does not impact the convergence of the algorithm to a solution.

With $\mathbf{E}_\ell \equiv \mathbf{C}^{-1}\mathbf{P}_\ell\mathbf{C}^{-1}$, we can rewrite Eq. (3.64) as

$$\delta\tilde{C}_\ell = -\frac{1}{2}\mathcal{F}_{\ell\ell'}^{-1}\left(\mathbf{d}^T\mathbf{C}^{-1}\mathbf{P}_{\ell'}\mathbf{C}^{-1}\mathbf{d} - \text{Tr}[\mathbf{C}\mathbf{C}^{-1}\mathbf{P}_{\ell'}\mathbf{C}^{-1}]\right) \quad (3.65)$$

$$= -\frac{1}{2}\mathcal{F}_{\ell\ell'}^{-1}\left(\mathbf{d}^T\mathbf{E}_{\ell'}\mathbf{d} - \text{Tr}[(\mathbf{S} + \mathbf{N})\mathbf{E}_{\ell'}]\right) \quad (3.66)$$

$$= -\frac{1}{2}\mathcal{F}_{\ell\ell'}^{-1}\left(\mathbf{d}^T\mathbf{E}_{\ell'}\mathbf{d} - \text{Tr}[\mathbf{N}\mathbf{E}_{\ell'}] - \text{Tr}[\mathbf{P}_{\ell''}C_{\ell''}\mathbf{E}_{\ell'}]\right). \quad (3.67)$$

At the maximum of the likelihood, i.e. $\tilde{C}_\ell = C_\ell$, it is straightforward to show that the ensemble average of the first derivative of likelihood Eq. (3.62) vanishes, and the curvature matrix Eq. (3.63) is equal to minus the Fisher matrix, $\langle\mathcal{F}_{\ell\ell'}\rangle = -F_{\ell\ell'}$. Hence,

$$\langle\delta\tilde{C}_\ell\rangle = 0 \quad (3.68)$$

$$\Leftrightarrow \langle\mathcal{F}_{\ell\ell'}\rangle^{-1}\langle\mathbf{d}^T\mathbf{E}_{\ell'}\mathbf{d} - \text{Tr}[\mathbf{N}\mathbf{E}_{\ell'}]\rangle = \langle\mathcal{F}_{\ell\ell'}\rangle^{-1}F_{\ell\ell''}C_{\ell''} \quad (3.69)$$

$$\Leftrightarrow F_{\ell\ell'}^{-1}\langle\mathbf{d}^T\mathbf{E}_{\ell'}\mathbf{d} - \text{Tr}[\mathbf{N}\mathbf{E}_{\ell'}]\rangle = \delta_{\ell\ell''}C_{\ell''}. \quad (3.70)$$

We thus recover the quadratic estimator $\hat{C}_\ell = F_{\ell\ell'}^{-1}(\mathbf{d}^T\mathbf{E}_{\ell'}\mathbf{d} - \text{Tr}[\mathbf{N}\mathbf{E}_{\ell'}])$, which corresponds to the solution that maximizes the likelihood.

This correspondence between the MLE and the standard QML cannot be extended to **xQML**, since the likelihood cannot be written in term of two different datasets \mathbf{d}^A and \mathbf{d}^B . Moreover, the matrices \mathbf{E}_ℓ are generally not Hermitian (as it is the case for the QML), so that it is not a quadratic estimator either. Anyway, we keep the appellation cross-‘QML’ because of the close formalism to the standard auto-spectrum approach.

5.3 Implementation

We provide a public code of the **xQML** method, available on GitLab : <https://gitlab.in2p3.fr/xQML>. In this section we detail some important steps of the **xQML** implementation. We first discuss the pixel covariance matrix construction. We then derive an exact solution for the Sylvester Eq. (3.54). Finally, we describe a method for binning the **xQML** spectrum estimator.

Instrumental beam and pixel window function

The construction of the \mathbf{P}_ℓ matrices in Eq. (3.35) are described in appendix A. For realistic data analysis, we must account for the datasets pixel window and beam transfer functions. They impact the measured cross-spectrum by smoothing the small scales, which is equivalent to convolve the true power spectrum with the product of the datasets effective beam functions $B_\ell^A B_\ell^B$. We therefore have

$$\langle \hat{C}_\ell \rangle = C_\ell (B_\ell^A B_\ell^B). \quad (3.71)$$

A simple solution to correct for the beam is to multiply the matrices \mathbf{P}_ℓ by each of the effective beam transfer functions in the multipole domain,

$$\mathbf{P}_\ell \rightarrow \mathbf{P}_\ell B_\ell^A B_\ell^B. \quad (3.72)$$

Indeed, applying Eq. (3.72) implies the following transformations,

$$W_{\ell\ell'} \rightarrow W_{\ell\ell'} B_\ell^A B_\ell^B B_{\ell'}^A B_{\ell'}^B, \quad (3.73)$$

$$y_\ell \rightarrow y_\ell B_\ell^A B_\ell^B, \quad (3.74)$$

or, from the definition of the estimator in Eq. (3.51),

$$\hat{C}_\ell \rightarrow \sum_{\ell'} [W^{-1}]_{\ell\ell'} (B_\ell^A B_\ell^B B_{\ell'}^A B_{\ell'}^B)^{-1} \hat{y}_{\ell'} (B_{\ell'}^A B_{\ell'}^B) \quad (3.75)$$

$$= \hat{C}_\ell (B_\ell^A B_\ell^B)^{-1}. \quad (3.76)$$

Therefore, from Eq. (3.71), we get $\langle \hat{C}_\ell \rangle \rightarrow C_\ell$, and the estimator is successfully corrected from the instrumental beam.

Pixel covariance matrix

The covariance matrix \mathbf{C} introduced in Eq. (3.34) includes correlations between pixels for each of the Stokes parameters,

$$\mathbf{C} = \begin{pmatrix} C^{TT} & C^{TQ} & C^{TU} \\ C^{QT} & C^{QQ} & C^{QU} \\ C^{UT} & C^{UQ} & C^{UU} \end{pmatrix}. \quad (3.77)$$

We can separate the temperature and polarization measurements by using an approximated pixel covariance matrix

$$\tilde{\mathbf{C}} = \begin{pmatrix} C^{TT} & 0 & 0 \\ 0 & C^{QQ} & C^{QU} \\ 0 & C^{UQ} & C^{UU} \end{pmatrix}. \quad (3.78)$$

This matrix does not mix temperature with polarization estimates. As a result, the \hat{C}_ℓ estimator is not optimal anymore, while it is still an unbiased estimator of the true C_ℓ . As shown in (Tegmark et al. 2001), the price to pay is a slight error bar increase of the order of one percent. Using this choice, the polarization spectra are protected from temperature systematics error that could propagate through the TQ and TU terms of Eq. (3.77). For the rest of the discussion, we focus our analysis on polarization measurement only. The method can be implemented for the temperature spectrum estimation following the same approach.

In Eq. (3.35), the summation over ℓ is theoretically infinite. It can however be truncated at a given ℓ_{max} as long as the remaining contributions from $C_{\ell > \ell_{max}}$ are negligible. This can be accomplished manually by smoothing the dataset \mathbf{d} (e.g. by convolving the spectrum with a decreasing function). In the framework of our analysis, we simply generated CMB simulations while filtering all $C_{\ell > \ell_{max}}$.

In the Sec. 5.1, the xQML variance has been shown to be minimal if the fiducial $\tilde{\mathbf{C}}$ matrix is built from the true \mathbf{C} . In practice, it is not always possible to estimate precisely the latter. Indeed, since $\mathbf{C} = \mathbf{S} + \mathbf{N}$, it requires an estimation of the CMB signal covariance $\mathbf{S} = \sum_\ell \mathbf{P}_\ell C_\ell$, and thus the CMB signal, as well as the experimental noise \mathbf{N} . It is not difficult to express the estimator variance as defined in Eq. (3.52) for any fiducial $\tilde{\mathbf{C}}$,

$$\begin{aligned} \langle \Delta \hat{C}_\ell, \Delta \hat{C}_{\ell'} \rangle &= [\tilde{W}^{-1}]_{\ell\ell_1} \text{Tr} \left[\mathbf{C}^{AA} \tilde{\mathbf{E}}_{\ell_1} \mathbf{C}^{BB} \tilde{\mathbf{E}}_{\ell_2}^T \right] [\tilde{W}^{-1}]_{\ell_2\ell'} \\ &+ [\tilde{W}^{-1}]_{\ell\ell_1} \text{Tr} \left[\mathbf{C}^{AB} \tilde{\mathbf{E}}_{\ell_1} \mathbf{C}^{AB} \tilde{\mathbf{E}}_{\ell_2} \right] [\tilde{W}^{-1}]_{\ell_2\ell'}, \end{aligned} \quad (3.79)$$

where $\tilde{\mathbf{E}}_\ell$ and $\tilde{W}_{\ell\ell'}$ are computed using the fiducial matrix $\tilde{\mathbf{C}}$ instead of \mathbf{C} in Eqs. (3.55) and (3.57).

Impact of pixel covariance matrix estimate

To estimate the impact on the spectra estimations variance of small deviations of the fiducial $\tilde{\mathbf{C}}$ from the true \mathbf{C} , we consider a simplified toy model with $\mathbf{C}^{AA} = \mathbf{C}^{BB} = \mathbf{C}$. We also restrict our calculation to the first term of Eq. (3.79), since we previously showed that, depending on the noise level, the second term is either negligible, or either equal to the first one. Any small perturbation to the fiducial $\tilde{\mathbf{C}}$ around the true \mathbf{C} can be written as

$$\tilde{\mathbf{C}} = \mathbf{C} + \mathcal{E}, \quad \text{with} \quad \mathcal{E} \ll \mathbf{C}, \quad (3.80)$$

and thus

$$\tilde{\mathbf{C}}^{-1} = \mathbf{C}^{-1} - \mathcal{D}, \quad \text{with} \quad \mathcal{D} \equiv \mathbf{C}^{-1} \mathcal{E} \mathbf{C}^{-1} \ll \mathbf{C}^{-1}. \quad (3.81)$$

At the first order in \mathcal{D} ,

$$\mathbf{C} \tilde{\mathbf{E}}_\ell \mathbf{C} \tilde{\mathbf{E}}_\ell = \mathbf{C}^{-1} \mathbf{P}_\ell \mathbf{C}^{-1} \mathbf{P}_\ell - 4 \mathbf{C}^{-1} \mathbf{P}_\ell \mathcal{D} \mathbf{P}_\ell + \mathcal{O}(\mathcal{D}^2), \quad (3.82)$$

and

$$\tilde{\mathbf{E}}_\ell \mathbf{P}_\ell = \mathbf{C}^{-1} \mathbf{P}_\ell \mathbf{C}^{-1} \mathbf{P}_\ell - 2 \mathbf{C}^{-1} \mathbf{P}_\ell \mathcal{D} \mathbf{P}_\ell + \mathcal{O}(\mathcal{D}^2). \quad (3.83)$$

Since in Eq. (3.79) we take the inverse square of $\tilde{W}_{\ell\ell} = \text{Tr} \left[\tilde{\mathbf{E}}_\ell \mathbf{P}_\ell \right]$, we get from Eq. (3.83)

$$\tilde{W}_{\ell\ell}^2 = (\text{Tr} [\mathbf{C}^{-1} \mathbf{P}_\ell \mathbf{C}^{-1} \mathbf{P}_\ell] - 2 \text{Tr} [\mathbf{C}^{-1} \mathbf{P}_\ell \mathcal{D} \mathbf{P}_\ell] + \mathcal{O}(\mathcal{D}^2))^2 \quad (3.84)$$

$$= \text{Tr} [\mathbf{C}^{-1} \mathbf{P}_\ell \mathbf{C}^{-1} \mathbf{P}_\ell] (\text{Tr} [\mathbf{C}^{-1} \mathbf{P}_\ell \mathbf{C}^{-1} \mathbf{P}_\ell] - 4 \text{Tr} [\mathbf{C}^{-1} \mathbf{P}_\ell \mathcal{D} \mathbf{P}_\ell]) + \mathcal{O}(\mathcal{D}^2). \quad (3.85)$$

Finally, inserting Eqs. (3.82) and (3.85) in Eq. (3.79),

$$\langle \Delta \hat{C}_\ell, \Delta \hat{C}_\ell \rangle \simeq \frac{\text{Tr} [\mathbf{C}^{-1} \mathbf{P}_\ell \mathbf{C}^{-1} \mathbf{P}_\ell] - 4 \text{Tr} [\mathbf{C}^{-1} \mathbf{P}_\ell \mathcal{D} \mathbf{P}_\ell]}{\text{Tr} [\mathbf{C}^{-1} \mathbf{P}_\ell \mathbf{C}^{-1} \mathbf{P}_\ell] (\text{Tr} [\mathbf{C}^{-1} \mathbf{P}_\ell \mathbf{C}^{-1} \mathbf{P}_\ell] - 4 \text{Tr} [\mathbf{C}^{-1} \mathbf{P}_\ell \mathcal{D} \mathbf{P}_\ell])} \quad (3.86)$$

$$\simeq \text{Tr} [\mathbf{C}^{-1} \mathbf{P}_\ell \mathbf{C}^{-1} \mathbf{P}_\ell]^{-1} \quad (3.87)$$

$$= V_{\ell\ell}. \quad (3.88)$$

We see that a fiducial $\tilde{\mathbf{C}}$ sufficiently close to the true \mathbf{C} induces only second order deviations of the spectrum estimation variance from the optimal variance $V_{\ell\ell}$. For a low SNR, the choice of the fiducial \tilde{C}_ℓ has little impact on $\tilde{\mathbf{C}}$. For signal dominated datasets, deviations of \tilde{C}_ℓ can still have an impact on the spectrum error if chosen far from the true. A solution is to run the **xQML** method iteratively as recommended in Tegmark et al. 2001, with previous spectrum estimation as the new fiducial model.

However, even if the variance of the spectrum estimation is only slightly impacted when the fiducial $\tilde{\mathbf{C}}$ differs from the true dataset covariance matrix, the analytical estimate of the variance,

$$\tilde{V}_{\ell\ell'} = \frac{1}{2} \left([\tilde{W}^{-1}]_{\ell\ell'} + [\tilde{W}^{-1}]_{\ell\ell_1} \tilde{G}_{\ell_1\ell_2} [\tilde{W}^{-1}]_{\ell_2\ell'} \right), \quad (3.89)$$

is biased. Taking, for example, $\tilde{\mathbf{C}} = \gamma \mathbf{C}$, for any constant γ , it is straightforward to calculate that the variance of the estimator $\langle \Delta \hat{C}_\ell, \Delta \hat{C}_{\ell'} \rangle = V_{\ell\ell'}$ is still minimal, but the estimated variance $\tilde{V}_{\ell\ell'} = \gamma^2 V_{\ell\ell'}$ diverges from the true variance by a factor γ^2 . One must thus be cautious when estimating the spectrum variance analytically.

Fiducial tensor-to-scalar ratio

We now wish to measure the impact on the estimator variance depending on the choice of the fiducial tensor-to-scalar ratio parameter r_{fidu} used to build the fiducial power spectrum. The latter being then used to construct the signal covariance matrix \mathbf{S} . The amplitude of r_{fidu} impacts the shape of the B-modes spectrum at large angular scales. Since the signal at higher multipoles is driven by the lensing B-modes, we do not expect any significant impact on this range of multipoles.

We remind that, by construction, the **xQML** estimator is not biased regardless the change of the fiducial spectrum used to build S . Only the variance of the estimation is impacted. The results of the spectra estimation applied on simulations is discussed in Sec. 5.4.

Considering the reionization survey only, with $f_{\text{sky}} = 0.7$, a resolution of $n_{\text{side}} = 8$, and a noise level of $1 \mu\text{K.arcmin}$, we compare the optimal variance with the estimator variance by computing the uncertainty ratio,

$$\Delta\sigma_\ell \equiv \frac{\sigma[C_\ell(\tilde{\mathbf{E}}_\ell)] - \sigma[C_\ell(\mathbf{E}_\ell)]}{\sigma[C_\ell(\mathbf{E}_\ell)]}, \quad (3.90)$$

where the $\tilde{\mathbf{E}}_\ell$ matrices are built using the fiducial model r_{fidu} , and \mathbf{E}_ℓ are from the true parameter r_{input} . The estimator built from the \mathbf{E}_ℓ matrices is therefore optimal in term of error-bars, and serves as a point of comparison. For different choices of r_{input} , we display the ratio in Fig. 3.9.

Focusing on the auto-spectra results first, we observe that the uncertainties on the largest scales are the most impacted. This is expected since the primordial B modes signal is the highest for those multipoles. Therefore, any change in the fiducial primordial C_ℓ^{BB} via r_{fidu} will mainly impact the variance optimality at low ℓ 's. At $\ell \leq 5$, the uncertainty deviation from optimality can reach as much as 50% when $r_{\text{input}} = 0$ and $r_{\text{fidu}} \simeq 10^{-3}$. We observed that this fraction only drops to 40% for a $5 \mu\text{K.arcmin}$ noise level. This observation about the fiducial model construction is crucial to keep in mind for future large angular scale experiments that

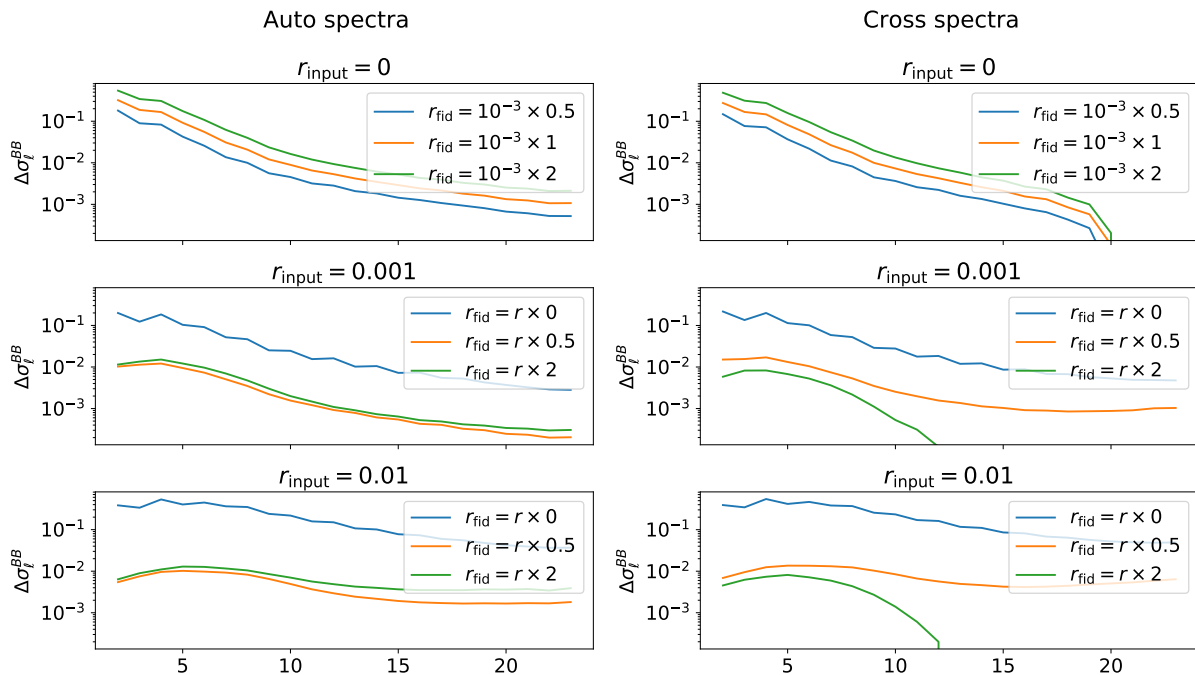


Figure 3.9: Deviation of the BB power spectrum uncertainty from optimality depending on the fiducial tensor-to-scalar ratio r_{fidu} used to construct S for different input r_{input} .

will produce low noise datasets and probe small values of r . As already mentioned, one solution would be to run the estimator iteratively, narrowing the choice for the fiducial tensor-to-scalar ratio at each step.

The cross spectra results are very similar to those of the auto-spectra. With the difference that the ratio can become negative at the higher multipoles (green curves for $r_{\text{input}} = 0.001$ and $r_{\text{input}} = 0.01$). This unexpected behaviour is actually caused by the approximation that we used to compute \mathbf{E}_ℓ in Eq. (3.54) introduced in Sec. 5.1. The slight non-optimality of the approximation is counter-acted by the deviation of the fiducial r_{fidu} . As a result, the variance of the estimator is less than what we defined as the optimal case, i.e. when $r_{\text{fidu}} = r_{\text{input}}$. However, this effect is completely negligible as it impacts less than 1% of the spectrum uncertainty. We verified this hypothesis at low n_{side} using an exact solution of the \mathbf{E}_ℓ matrix (whose solution is proposed here-after). The resulting ratios of the cross-spectra uncertainties are positive for the whole range of multipole (not shown).

Sylvester equation solution

We discuss the approximate solution of Eq. (3.54) introduced in Sec. 5.1, also known as a generalized form of the Sylvester equation, and we compare it with the exact solution described in (De Terán et al. 2016). To find the exact solution, we use the Kronecker product property $\text{vec}(\mathbf{AXB}) = (\mathbf{B}^T \otimes \mathbf{A})\text{vec}(\mathbf{X})$, under the condition that the product \mathbf{AXB} is well defined. The operator $\text{vec}()$ vectorizes a matrix (by stacking its columns), and \otimes is the Kronecker matrix product. We also introduce the permutation matrix Π such that $\text{vec}(\mathbf{X}^T) = \Pi \text{vec}(\mathbf{X})$. One can show that $\text{vec}(\mathbf{AX}^T\mathbf{B}) = \Pi(\mathbf{A}^T \otimes \mathbf{B})\text{vec}(\mathbf{X})$ (Horn et al. 1991). The Sylvester Eq. (3.54) can thus be written as a set of linear equations

$$[\mathbf{C}^{BB} \otimes \mathbf{C}^{AA} + \Pi(\mathbf{C}^{AB} \otimes \mathbf{C}^{AB})] \text{vec}(\mathbf{E}_\ell) = \text{vec}(\mathbf{P}_\ell). \quad (3.91)$$

We can then solve it exactly for $\text{vec}(\mathbf{E}_\ell)$ using the least-squares method. However, the equation system is of dimension N_d^2 , which is computationally costly for large datasets.

Approximation impact on spectrum uncertainty

We can use the Eq. (3.79) to compute the variance of the estimator with the approximate solution of Eq. (3.55) as the $\tilde{\mathbf{E}}_\ell$ matrices. Following Eq. (3.90), we compute the deviation of the spectrum variance using the approximation solution $\tilde{\mathbf{E}}_\ell$, with the optimal one, \mathbf{E}_ℓ . The latter is computed using the exact solution of Eq. (3.91).

The power spectra displayed in Fig.3.1 as input, and proceed to the same computation, shown in Fig. 3.10. For the reionization survey, on half of the sky, we observe a maximum

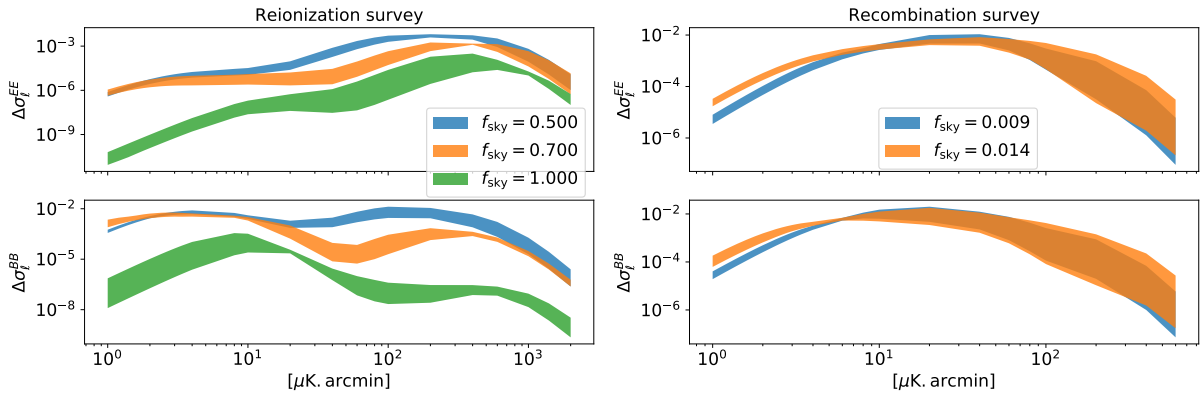


Figure 3.10: Deviation of the power spectrum uncertainty from optimality relative to the noise level, for E (up panel) and B modes (bottom). The reionization survey is computed on a resolution of $n_{\text{side}} = 2$ ($\ell_{\text{max}} = 5$), and the recombination survey of $n_{\text{side}} = 16$ ($\ell_{\text{max}} = 47$). The input polarization power spectra are from Planck best fit 2015. The width of the curves shows the values associated with the multipoles for which the deviation is minimum and maximum.

deviation from the optimality of about 1.3% for the B modes uncertainty, and 0.6% for the E modes uncertainty. Those values respectively drop to 0.6% and 0.2% at $f_{\text{sky}} = 0.7$, and around 0.03% on full sky. Those peaks appear when the signal and the noise levels are of the same order at those multipoles range, i.e. $\ell \sim 3$. The maximum deviation is at around $\sim 200 \mu\text{K.arcmin}$ for the E modes, and $\sim 10 \mu\text{K.arcmin}$ for the B modes signal, as displayed in Fig. 3.1.

The deviation for the recombination survey is observed to be the highest between $\sim 10 \mu\text{K.arcmin}$ and $\sim 40 \mu\text{K.arcmin}$, which also corresponds to the signal level of the E modes at those multipoles range, $\ell_{\text{max}} \simeq 30$. In that case, the deviation is at 1.5% for $f_{\text{sky}} = 0.009$, and around 1% for $f_{\text{sky}} = 0.014$.

Given the low level of deviation from optimality, at most 2% in the worse case, we can thus safely use the approximated solution of Eq. (3.55) for the implementation of the xQML method, and we will consider it as optimal. Further analysis on higher resolution should also be explored. A wealth of literature exists that propose algorithms to solve particular cases of Sylvester equation using reasonable computation resources, without using the Kronecker product. See for example Ding et al. 2005; Lin et al. 2010; Ramadan et al. 2015; Simoncini 2016 and especially De Terán et al. 2017 for our case.

Binning

CMB observations are only available on a limited sky fraction, and as a result, individual multipoles can be strongly correlated when reconstructing the CMB spectra. It is thus convenient to bin the power spectra in multipoles band powers, labelled b hereafter. We define the binning operators,

$$R_{b\ell} = \begin{cases} \Delta_b^{-1} \\ 0 \end{cases}, \quad Q_{\ell b} = \begin{cases} 1 & \text{if } \ell \in b \\ 0 & \text{otherwise} \end{cases}, \quad (3.92)$$

with Δ_b the width of the b th bin, which can be varied from one bin to another. The binned estimator is written

$$\hat{y}_b \equiv \sum_{\ell} R_{b\ell} \hat{y}_{\ell}, \quad (3.93)$$

for which the covariance reads

$$\begin{aligned} \langle \Delta \hat{y}_b, \Delta y_{b'} \rangle &= \text{Tr} [\mathbf{C}^{AA} \mathbf{E}_b \mathbf{C}^{BB} \mathbf{E}_{b'}^T + \mathbf{C}^{AB} \mathbf{E}_b \mathbf{C}^{AB} \mathbf{E}_{b'}] \\ &= \frac{1}{2\Delta_{b'}} (W_{bb'} + G_{bb'}), \end{aligned} \quad (3.94)$$

with $W_{bb'} = R_{b\ell} W_{\ell\ell'} Q_{\ell'b'}$, and $G_{bb'} = R_{b\ell} G_{\ell\ell'} Q_{\ell'b'}$. The true binned spectrum is thus

$$C_b \equiv \sum_{\ell, \ell', b'} [W^{-1}]_{bb'} R_{b'\ell} W_{\ell\ell'} C_{\ell'}, \quad (3.95)$$

and its unbiased binned estimation becomes

$$\hat{C}_b \equiv \sum_{\ell'} [W^{-1}]_{bb'} \hat{y}_{\ell'}, \quad (3.96)$$

with covariance

$$V_{bb'} = \frac{1}{2\Delta_{b'}} ([W^{-1}]_{bb'} + [W^{-1}]_{bb_1} G_{b_1 b_2} [W^{-1}]_{b_2 b'}). \quad (3.97)$$

We remark that the binning can also be achieved by computing $\mathbf{P}_b \equiv \sum_{\ell \in b} \mathbf{P}_{\ell}$ directly (without the normalization term Δ_b), or equivalently $\mathbf{P}_b \equiv \sum_{\ell} \mathbf{P}_{\ell} Q_{\ell b}$. With this definition of \mathbf{P}_b , the xQML components can be computed as usually defined in Eqs. (3.50), (3.51), (3.55) and (3.57) for the spectrum estimate \hat{C}_{ℓ} , and Eqs. (3.58), (3.59) and (3.57) for its analytical covariance (replacing all subscripts ℓ by b). This method is computationally more efficient compared to the method presented above.

5.4 Power spectra reconstruction

We verify with simulations that the reconstructed power spectra are unbiased with respect to the input model C_{ℓ} . From the central limit theorem, as n_{MC} is large, we expect the mean spectra residues,

$$R_{\ell}[\hat{C}_{\ell}] \equiv \frac{C_{\ell} - \langle \hat{C}_{\ell} \rangle}{\sqrt{\sigma^2(\hat{C}_{\ell}^{\text{MC}})/n_{\text{MC}}}}, \quad (3.98)$$

to be normally distributed around zero, for all ℓ if the spectra are unbiased, with $\sigma^2(\hat{C}_{\ell}^{\text{MC}})/n_{\text{MC}}$ the MC variance of the mean spectra. We carefully checked that this is the case for all noise levels $0.1 \leq \sigma_n \leq 50 \mu\text{K.arcmin}$.

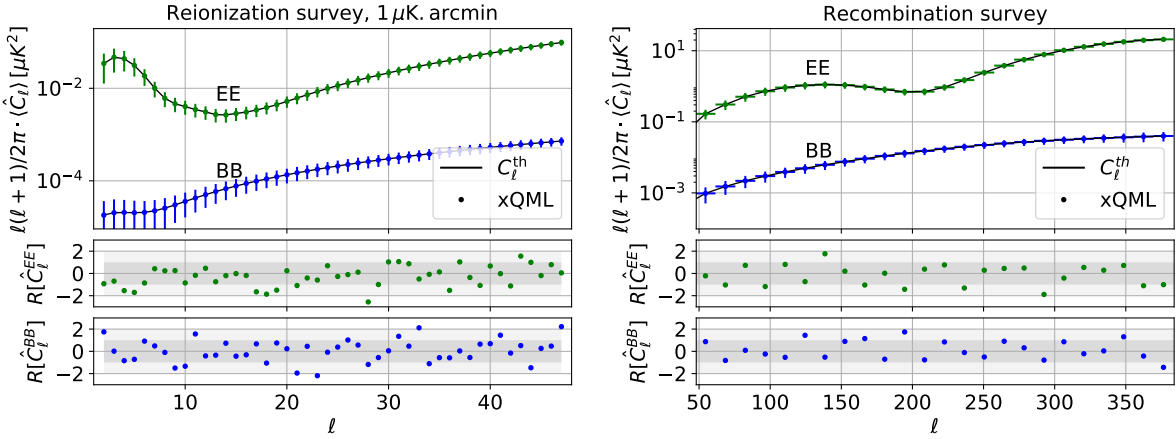


Figure 3.11: EE (green) and BB (blue) mean power spectra $\ell(\ell + 1)/2\pi \cdot \langle \hat{C}_\ell \rangle$, and residues $R_\ell[\hat{C}_\ell]$ from Eq. (3.98), computed from $n_{\text{MC}} = 10^5$ MC simulations. Spectra models are plotted in black solid lines. Left panel corresponds to the reionization survey simulations ($n_{\text{side}} = 16$, $f_{\text{sky}} \simeq 0.7\%$), right panel corresponds to the recombination survey simulations ($n_{\text{side}} = 128$, $f_{\text{sky}} \simeq 1\%$). Noise level is $\sigma_n = 1 \mu\text{K}\cdot\text{arcmin}$ for both surveys.

EE and BB signals

Power spectra and their residues are shown in Fig. 3.11 for $1 \mu\text{K}\cdot\text{arcmin}$. Given the residues distribution for $n_{\text{MC}} = 10^5$ simulations, we conclude that the spectra bias level is less than one percent of the spectra errors.

EB signal

Although first order primordial E-B and T -B correlations are predicted to be null in the frame of the ΛCDM model, nonstandard cosmological mechanisms, such as cosmic birefringence, could induce non-zero correlation spectra (Lue et al. 1999; Carroll 1998; Loeb et al. 1996; Kahniashvili et al. 2005; Campanelli et al. 2004; Caprini et al. 2004; Pogosian et al. 2002). In addition to providing an important probe to nonstandard physics, measuring EB, TB spectra could also help to diagnose instrumental systematic effects (Yadav et al. 2010; Hu et al. 2003).

We focus on the EB signal, which can be computed by including a new set of \mathbf{P}_ℓ matrices in the estimator. Their computation can be found in appendix A. As a consequence, the $W_{\ell\ell'}$, and generally all mode-mode matrices related to the estimator are also extended. The estimated spectrum from the xQML are shown in Fig. 3.12, with a null EB spectrum as input. The results are consistent with the input, and no bias are observed.

Spectrum variances

The MC spectra variance, and that derived analytically $\sigma^2(\hat{C}_\ell^{\text{ana}}) = V_{\ell\ell}$ in Eq. (3.58) are shown to be in excellent agreement, as displayed in Fig. 3.13 for E and B modes. The correlation matrix,

$$\bar{V}_{\ell\ell'} = \frac{V_{\ell\ell'}}{\sqrt{V_{\ell\ell}V_{\ell'\ell'}}}, \quad (3.99)$$

showed in Fig. 3.14, is band diagonal over the whole multipoles range, meaning that correlations only occur between neighbouring bins. Typically, $\bar{V}_{\ell\ell'}$ is of the order of ten percent for adjacent bins. This value drops to a few percent for $|\ell - \ell'| = 2, 3$, and becomes almost negligible for $|\ell - \ell'| > 3$.

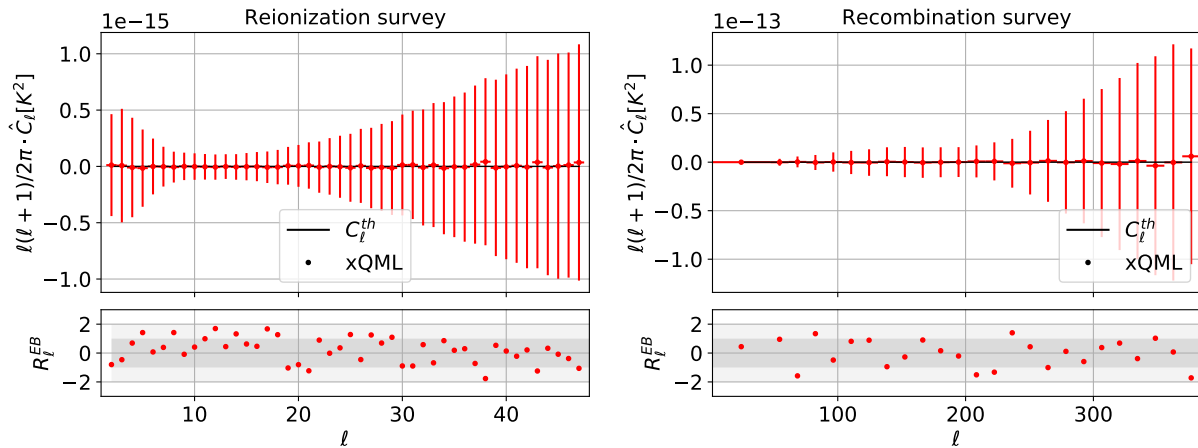


Figure 3.12: EB mean power spectrum xQML estimates $\ell(\ell+1)/2\pi \cdot \langle \hat{C}_\ell \rangle$, and residues $R_\ell[\hat{C}_\ell]$ from Eq. (3.98), computed from $n_{MC} = 10^3$ MC simulations.

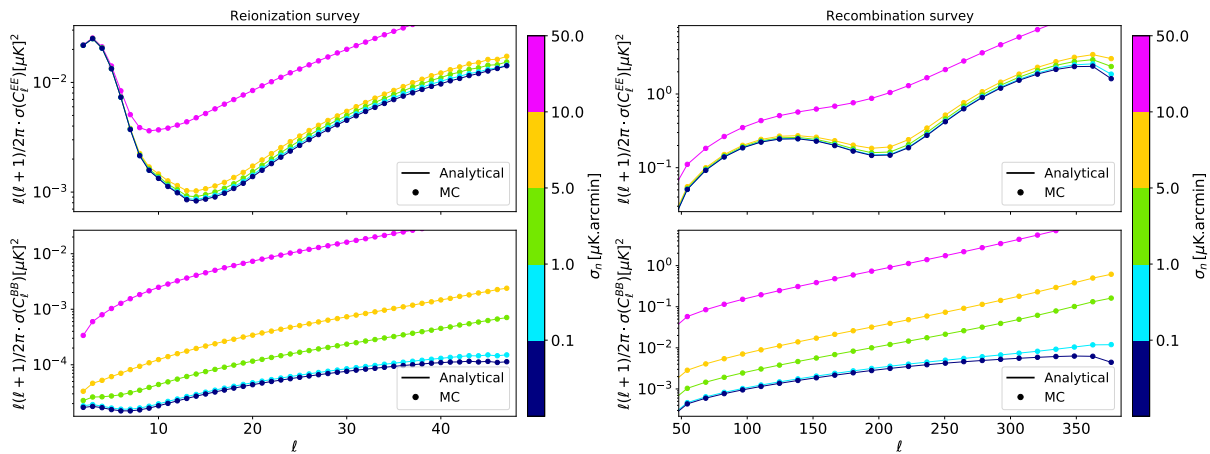


Figure 3.13: Monte-Carlo (dots) and analytical (plain) errors of polarization spectra EE (up) and BB (bottom), for the reionization (left) and recombination (right) surveys, with noise levels $0.1 \leq \sigma_n \leq 50 \mu\text{K} \cdot \text{arcmin}$.

5.5 Modes mixing and leakage

Mixing matrix

The mode-mixing matrix $W_{\ell\ell'}$ introduced in Eq. (3.40) quantifies the contribution of all ℓ' -modes to the spectrum estimator at angular scale ℓ . The rescaled matrix

$$\bar{W}_{\ell\ell'} = \frac{W_{\ell\ell'}}{\sqrt{W_{\ell\ell}W_{\ell'\ell'}}}, \quad (3.100)$$

is displayed in Fig. 3.15 in log-scale for $\sigma_n = 1 \mu\text{K} \cdot \text{arcmin}$. The off-diagonal blocks quantify the E/B modes mixing, also known as polarization leakage. This mixing appears as soon as maps are partially masked, making some modes ambiguously belong to both E and B polarization patterns.

The modes mixing matrix appears to be mainly band diagonal, which means that the multipoles mixing occurs only between neighbouring bins. This highlights an important property of the QML method. It can be used to estimate spectra over ranges of multipoles only, without being affected too much by the lack of multipoles outside the estimation range. In other words,

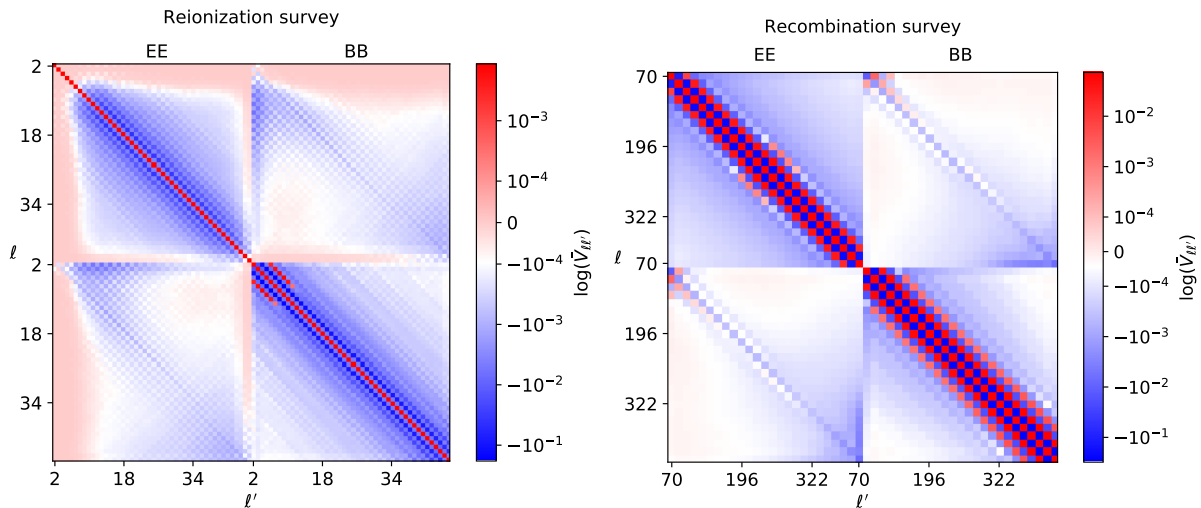


Figure 3.14: The spectrum correlation matrix $\bar{V}_{\ell\ell}$ defined in Eq. (3.98) in log scale, for the reionization (left) and recombination (right) surveys, for $\sigma_n = 1 \mu\text{K}\cdot\text{arcmin}$.

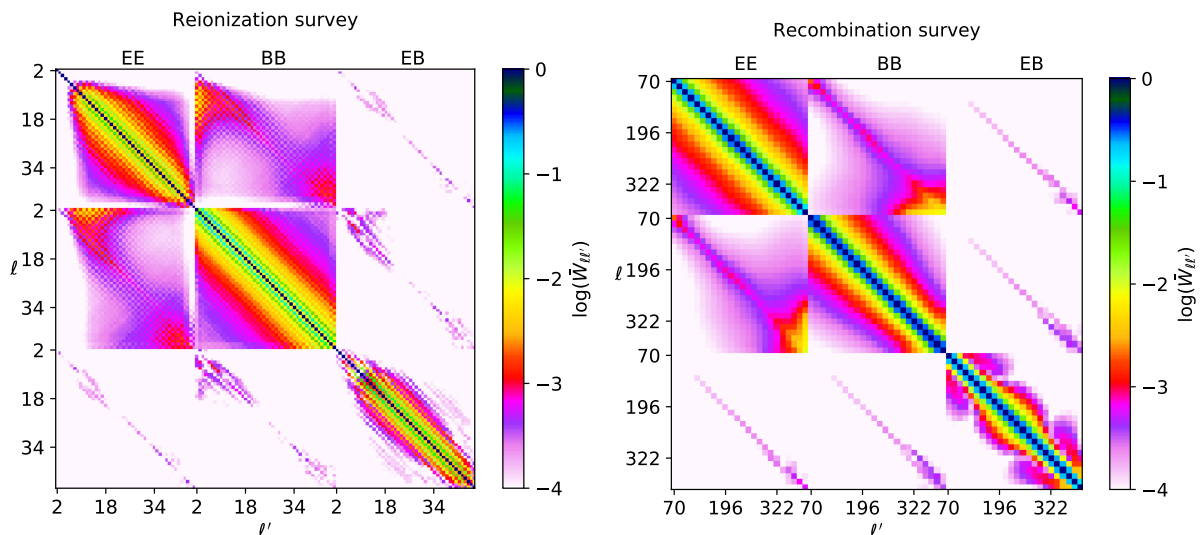


Figure 3.15: The normalized mode-mixing matrix $\bar{W}_{\ell\ell}$ defined in Eq. (3.100) in log scale, for the reionization (left) and recombination (right) surveys, for $\sigma_n = 1 \mu\text{K}\cdot\text{arcmin}$.

only the multipoles estimated near the edge of the estimation range would be affected by a bias. To test this property, we estimate the EE and BB polarization power spectra only on half of the modes that we generated for the simulation (up to ℓ_{max}). The estimation is computed on the first half, then on the second half of the multipoles. However, in order to build the estimator, we still use the full covariance signal matrix \mathbf{S} , for which the fiducial signal include all multipoles up to ℓ_{max} . The resulting joint spectra are shown in Fig. 3.16. At first glance, the overall spectra are well reconstructed. We observe a bias in the residuals, near the multipole cut, as we would have expected. At a distance of 5 bins from the cut, the spectrum bias drops at a few percent already.

Returning to Fig. 3.15, we remark that the E/B mixing (bottom left block) is on average very low. Most of the E-to-B leakage is localized at $\ell \lesssim 10$ for the reionization survey. The recombination survey also suffers from a polarization mixing increase at $\ell \gtrsim 250$. We suspect that this effect is caused by the pixel resolution of the maps. It appears when the multipole

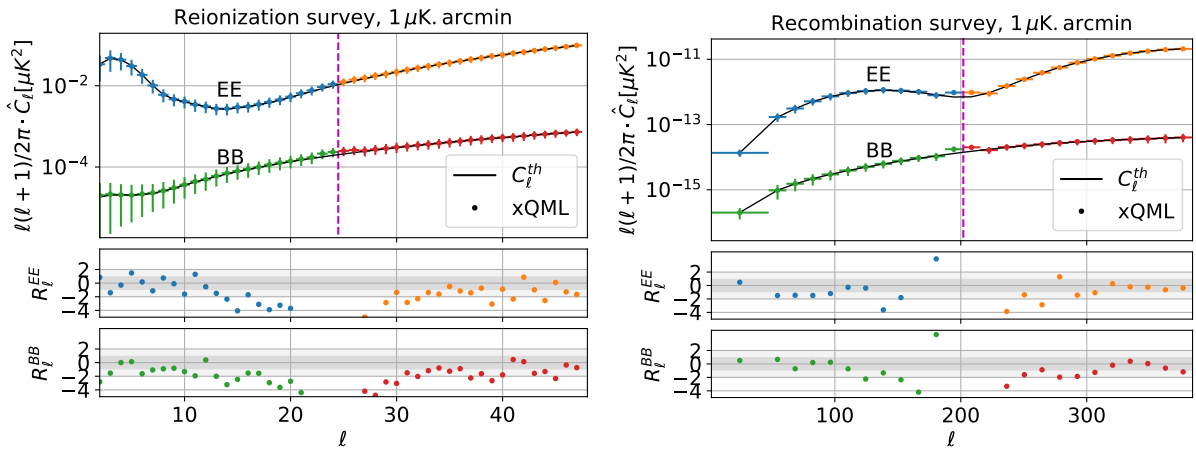


Figure 3.16: Truncated EE (green) and BB (blue) mean power spectra xQML estimates and residues computed from $n_{\text{MC}} = 10^3$ MC simulations, and a noise level of $\sigma_n = 1 \mu\text{K}.\text{arcmin}$. Left panel corresponds to the reionization survey simulations, right panel corresponds to the recombination survey simulations. The vertical magenta line indicates where the estimated spectra is truncated. Of the multipoles, only the first half is estimated, then only the second half is estimated. Each half is then jointly plotted.

angular scale is close to the typical pixel scale, and disappears as soon as we change the datasets pixel resolution. Moreover, we checked that it is not caused by the mask by going full sky. When reducing the resolution from $n_{\text{side}} = 128$ to $n_{\text{side}} = 64$, we observe in Fig. 3.17 that the aliasing appears at multipoles where the mixing was previously non-existent for the $n_{\text{side}} = 128$ case, hence confirming our hypothesis. The effect remains however very small. For the multipoles ranges of interest, it induces a negligible increase of variance as shown hereafter.

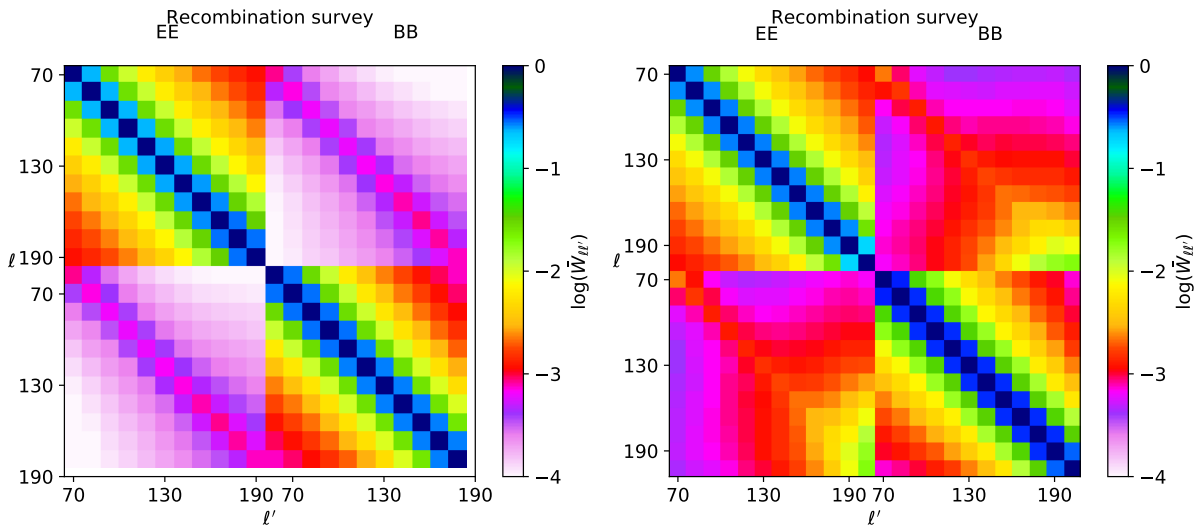


Figure 3.17: The normalized mode-mixing matrix $\bar{W}_{\ell\ell'}$ defined in Eq. (3.100) in log scale, for the recombination surveys at $n_{\text{side}} = 128$ (left) and $n_{\text{side}} = 64$ (right), and $\sigma_n = 1 \mu\text{K}.\text{arcmin}$. The bins for the $n_{\text{side}} = 128$ matrix is selected such that they match that of the $n_{\text{side}} = 64$ matrix.

Variance induced leakage

Because of polarization leakage, E and B modes respective uncertainty contributes to each other variance. For noise dominated datasets, this variance leakage has a small impact since both polarizations have the same noise, and their mutual contributions are equivalent. Conversely, when the noise is much lower than the signal level, the uncertainty is limited by the intrinsic 'cosmic variance', arising from the finite number of modes that can be sampled on the sky. The E-modes signal, thus its cosmic variance, is much higher than that of B-modes. As a consequence, even for small polarization mixing, the impact of the E-to-B variance leakage can become non-negligible.

Since, by construction the error of the \mathbf{xQML} estimator is minimal, it also minimizes the amount of variance leakage. The BB uncertainty is represented in Fig. 3.18, for which we compare the cases with and without leakage. The latter is obtained by simulating CMB polarization maps using null EE and TE spectra. We also show the absolute level of variance leakage $[\sigma(\hat{C}_\ell^{\text{leak}}) - \sigma(\hat{C}_\ell^{\text{no leak}})]/\sigma(\hat{C}_\ell^{\text{no leak}})$. We observe that the recovered spectra uncertainties for $\sigma_n = 0.1$ and $\sigma_n = 1 \mu\text{K.arcmin}$ are both mostly cosmic variance limited by the lensing B-modes signal. We also recover that the impact of the variance leakage gets less important as the SNR decreases.

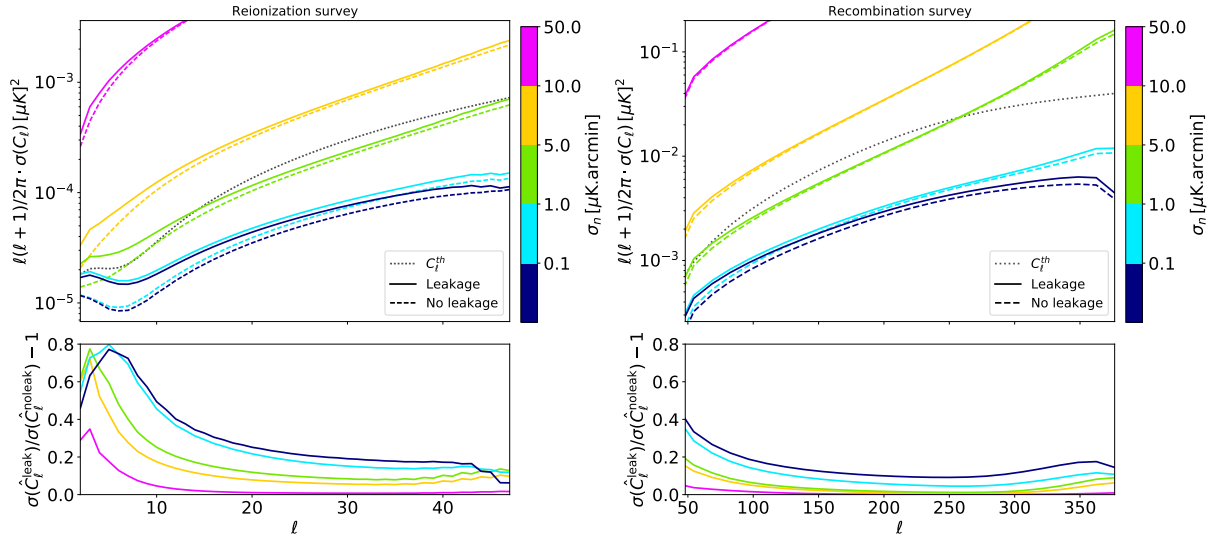


Figure 3.18: Top panels show the BB -spectrum uncertainty with variance leakage (solid) and without (dashed), for the reionization (left) and recombination (right) surveys, at noise levels $0.1 \leq \sigma_n \leq 50 \mu\text{K.arcmin}$. Bottom panels quantify the absolute variance leakage, computed from $[\sigma(\hat{C}_\ell^{\text{leak}}) - \sigma(\hat{C}_\ell^{\text{no leak}})]/\sigma(\hat{C}_\ell^{\text{no leak}})$.

For the reionization survey, the variance leakage is observed to be maximal at large angular scales, up to a 80% increased uncertainty around $\ell \lesssim 10$, which quickly drops to 30% for higher ℓ 's. This is not surprising since, for this multipole's range, the EE cosmic variance as well as the E-to-B mixing in $\bar{W}_{\ell\ell'}$ are maximal.

For the recombination survey, the impact is maximal for the first bins. This is again related to the higher polarization mixing in $\bar{W}_{\ell\ell'}$ at those multipoles. It then drops to 20% for $\ell \gtrsim 90$, followed by a slight increase at $\ell \gtrsim 250$. This is consistent with the previous E/B mixing observations made on $\bar{W}_{\ell\ell'}$ for this multipoles range. The impact at low ℓ 's remains however smaller since the E-modes cosmic variance level is much lower for those angular scales.

We conclude that, even if the mixing between polarization modes is minimized when using the \mathbf{xQML} estimator, the induced variance increase can however be non-negligible, especially at

large angular scales.

5.6 Summary

In this section, we derived a pixel-based spectrum estimator that allows us to cross-correlate CMB datasets. The method is very similar to the QML, but does not require a precise knowledge of the datasets noise covariance matrices to subtract the noise bias. We also provided an approximation to the Sylvester equation that has little impact on the optimality of the estimator, which, by construction, provides near-minimal error bars. The estimator variance is shown to be sensitive to only second order perturbations of the fiducial pixels covariance matrix. Moreover, using no TQ and TU correlations for the construction of this matrix, temperature and polarization analysis can be done completely separately. We provide a public implementation of the `xQML` method, available on GitLab: <https://gitlab.in2p3.fr/xQML>.

We showed that the `xQML` estimator is unbiased, and that the error bars on the recovered spectrum, obtained from Monte-Carlo simulations, correspond to the analytically derived variance. We presented two CMB surveys aiming at the reionization and recombination polarized signals measurement, with a fiducial tensor-to-scalar ratio $r = 10^{-3}$. The source of polarization leakage can be identified in the mode-mixing matrix $W_{\ell\ell'}$. We showed in Sec. 5.5 that it is consistent with the increase of variance in B -modes when compared to the no-leakage case. The reionization survey BB uncertainty at low noise levels is particularly impacted by the polarization mixing, with a maximum of an 80% increase for large angular scales at $0.1 - 1 \mu\text{K.arcmin}$. Since the `xQML` method minimizes bins correlations as well as polarization mixing, the resulting error bars thus correspond to the minimal uncertainty achievable when aiming to polarization variance leakage reduction. A comparison with the pure pseudo-spectrum formalism is performed in the next section.

6 Methods comparison

6.1 B-modes

In this section we compare the xQML with other methods such as the standard (pCl) and pure pseudo-spectrum (PpCl) approaches introduced in the Sec. 4. The discussion of B-mode variance performed in Sec. 4.3 is extended to include the xQML results. The uncertainty on the reconstructed B-mode power spectrum for all methods are illustrated in Fig. 3.19 based on 10^4 MC simulations.

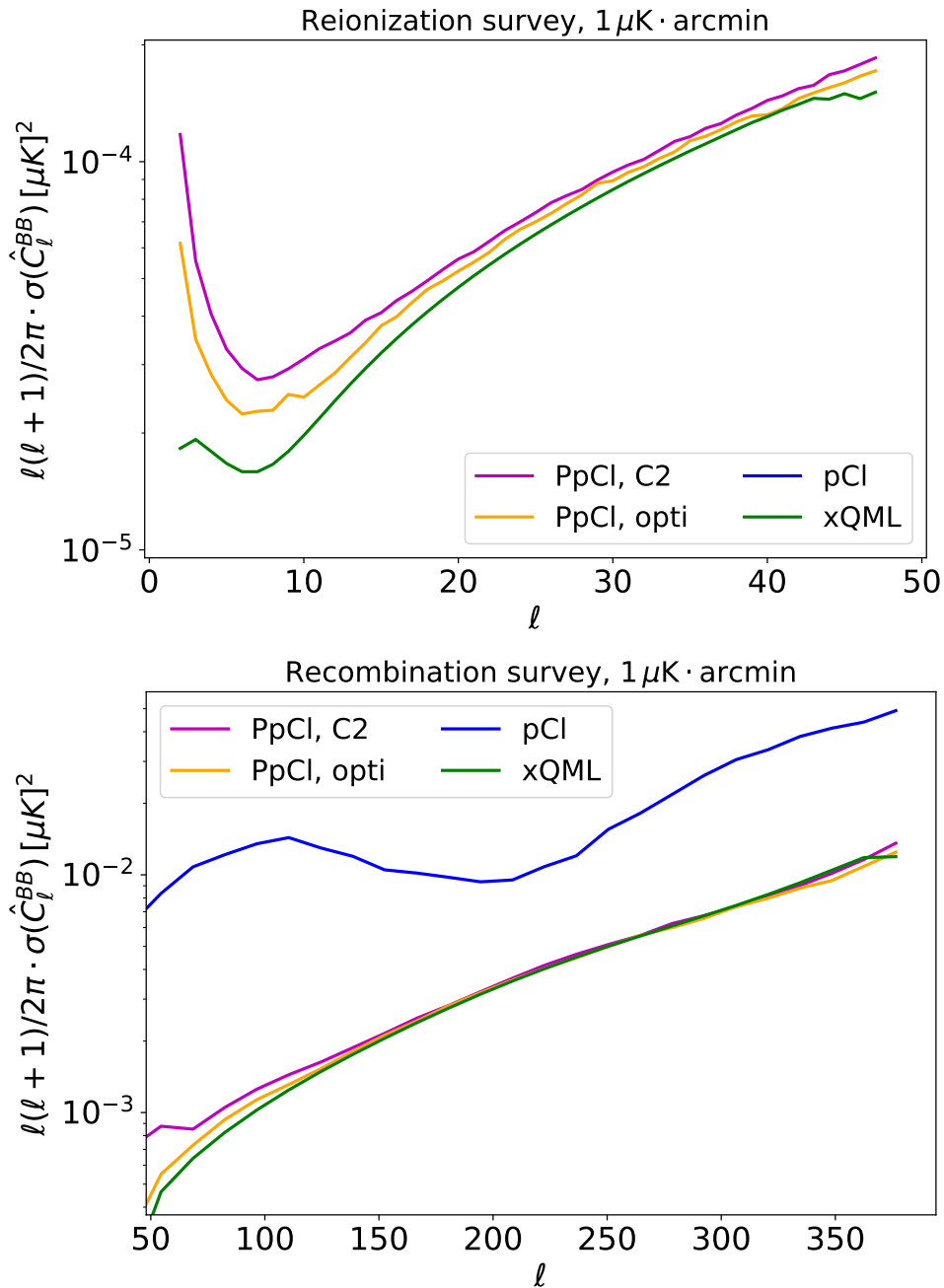


Figure 3.19: BB spectrum errors from xQML, standard pCl estimators, PpCl (pure pCl) using the C2 and optimised apodization, for the reionization (top) and recombination (bottom) surveys, with a noise level $\sigma_n = 1 \mu\text{K} \cdot \text{arcmin}$, and $r = 10^{-3}$. The pure pseudo-spectrum results were already shown in Fig. 3.7.

The pure methods PpCl allow to recover much lower error bars than the pCl. The two apodizations gives similar results at high multipoles but an optimised apodization is required to obtain better results at large angular scales. As expected, the pixel domain cross-correlation **xQML** provides the lowest spectra uncertainty over the whole multipole range. This is particularly visible at large angular scales. As discussed in Sec. 4.4, the uncertainty from the PpCl methods is observed to be high for low ℓ 's, then decreases as smaller scales are probed. This feature is much less present when using the **xQML** method. We observe that this difference on the B-mode uncertainty between the two formalisms is less visible when considering higher value of r ($\gtrsim 10^{-2}$), and it increases as smaller value are considered.

6.2 E-B correlation spectrum

We focus on the E-B correlation, for which we compute the $EB + BE$ spectrum variance. The rescaled mode-mixing matrix introduced in Eq. (3.100) is extended to EB multipoles as displayed in Fig. 3.15 for $1 \mu\text{K.arcmin}$. We observe almost no mixing between EB and EE, BB , apart from a very small effect at large scale for the reionization survey, and a resolution effect for high ℓ 's. However, we found that this property is lost when we consider particular fiducial models with non-zero \tilde{C}_ℓ^{EB} .

As in the previous section for the BB uncertainty, we compare our results with the pCl and PpCl methods. The latter is computed using the hybrid approach proposed in (Grain et al. 2012), where the E-modes are obtained using the standard pseudo-spectrum, and the B-modes using the pure method. Variances are shown in Fig. 3.20 for $1 \mu\text{K.arcmin}$. The PpCl uncertainty is about 20%-60% higher than that of the **xQML** for the reionization survey. Longer mask apodization lengths improve the PpCl error for $\ell \lesssim 10$. On the recombination survey, the **xQML** gives significant lower EB uncertainty only for $\ell \lesssim 100$. The conclusion is similar as for the BB -spectrum analysis. The **xQML** method provides an efficient estimator for large angular scales analysis.

6.3 Tensor-to-scalar ratio

As a forecast analysis, we show in Fig. 3.21 the uncertainty of r , obtained from 10^4 simulations for each method introduced previously, as a function of the noise level. We also proceed to a comparison with the mode-counting formula, which can be derived from Eq. (3.12),

$$\sigma_{\text{m.c.}}^2 = \frac{1}{(2\ell + 1)\Delta_\ell f_{\text{sky}}} \left[2\tilde{C}_\ell^2 + \tilde{C}_\ell(N_\ell^A + N_\ell^B) + N_\ell^A N_\ell^B \right], \quad (3.101)$$

where \tilde{C}_ℓ is the power spectrum fiducial model, $N_\ell = n_\ell/B_\ell^A B_\ell^B$ is the noise spectrum of the dataset convolved by the corresponding beam functions B_ℓ . This formulae gives a naive estimate of the lowest achievable variance, neglecting correlations and leakage induced by the sky coverage. We use the Low- ℓ Likelihood on Polarized Power-spectra, **Lollipop**, presented in Mangilli et al. 2015, which is a cross-spectra extended version of the Hamimeche&Lewis likelihood for large angular scales (Hamimeche et al. 2008). The methodology is further detailed in Sec. 6.1 of chapter 4.

The pure method spectrum covariance matrix is computed using MC as described in the introduction to the pure formalism. We consider only two datasets, no foreground contamination and/or residuals, nor de-lensing, and a perfect instrument. For low SNR, the impact of the polarization mixing is small, and all (standard and pure) pseudo-spectrum methods give the same error on r . For high SNR, the uncertainty of r is cosmic variance limited, which corresponds to the plateau from $\sigma_n = 0.1$ to $\sigma_n = 1 \mu\text{K.arcmin}$. In this range of noise level, the pure pseudo-spectrum method with optimised apodization and the **xQML** gives the same uncertainty on r for

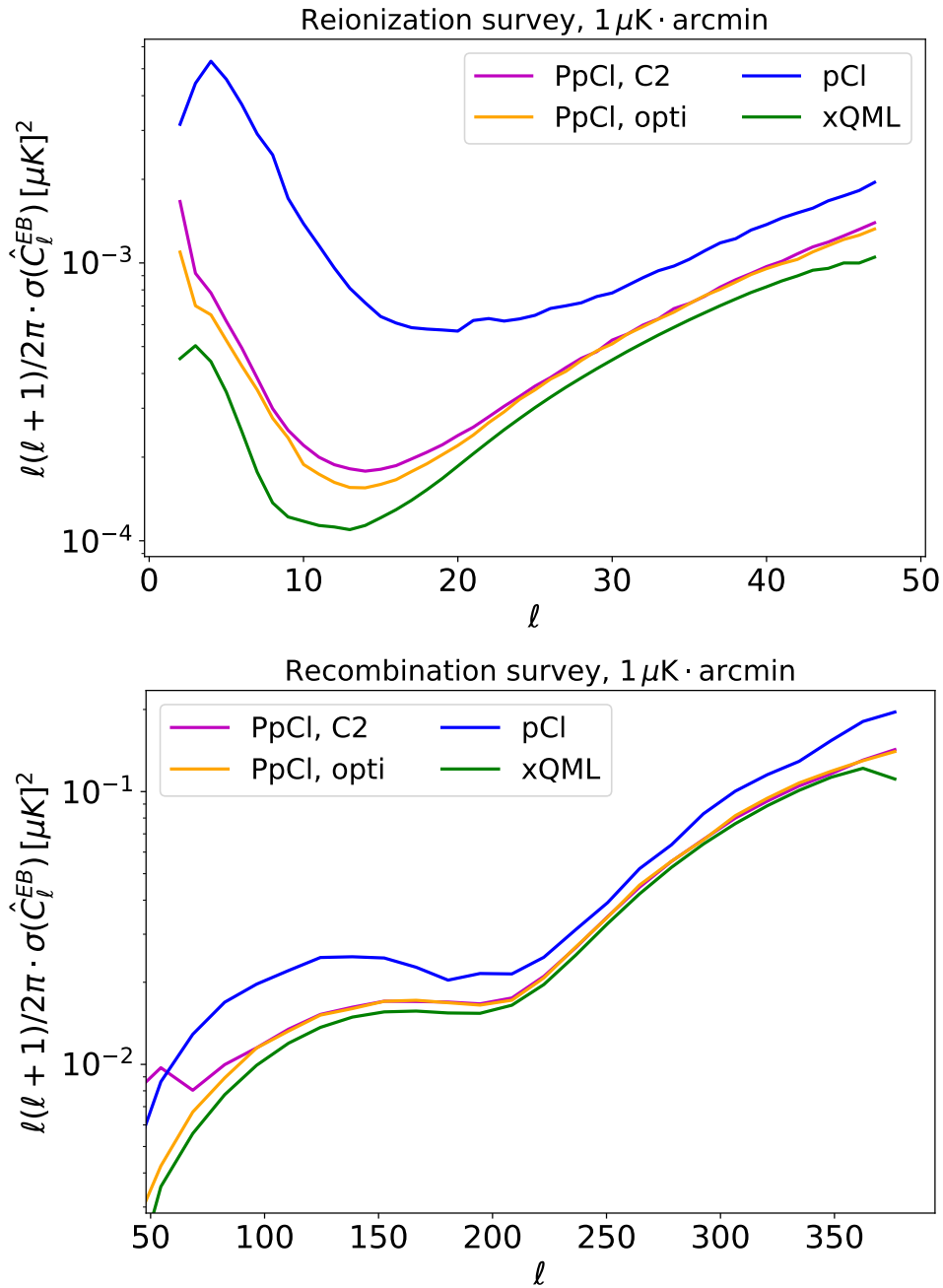


Figure 3.20: EB spectrum errors from $xQML$, standard pCl estimators, and $PpCl$ (pure pCl) using the $C2$ and optimised apodization, for the reionization (top) and recombination (bottom) surveys, with a noise level $\sigma_n = 1 \mu\text{K} \cdot \text{arcmin}$.

the recombination survey, while the $xQML$ uncertainty is $\sim 20\%$ lower than the optimised $PpCl$ method for the reionization survey.

6.4 Summary & conclusion

We saw in Sec. 4.3 that mask apodization is a non-trivial task for complex mask shapes. The naive isotropic apodization can produce window functions that are non-differentiable. This, in turn, induces a bias on the resulting spectra estimate, mainly visible at large angular scales. The other apodization process, which uses an optimisation PCG solver, provides much smoother

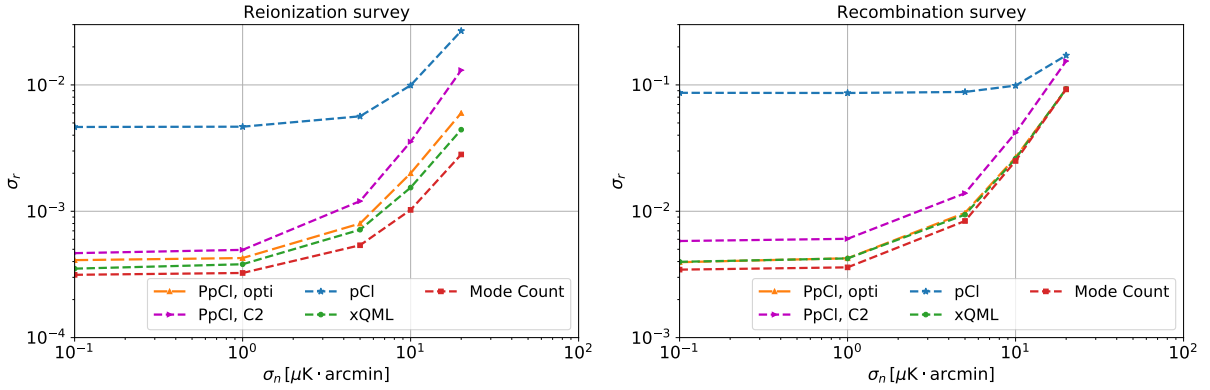


Figure 3.21: Error on the tensor-to-scalar ratio with a input $r = 10^{-3}$, for the reionization (left) and recombination (right) surveys as a function of the noise levels $0.1 \leq \sigma_n \leq 20 \mu\text{K}\cdot\text{arcmin}$. We compare the uncertainty obtained from the standard pseudo-spectrum (blue), the pure pseudo-spectrum using C2 (magenta) and optimised apodization (orange), the cross quadratic pixel based (green), and the mode-counting formula (red), based on 10^4 simulations.

window functions and no visible bias. However, one disadvantage is that, in order for the solver to converge, the windows must be optimised over bins of multipoles rather than on each multipole. The binning is arbitrary, and its optimal choice must be defined based on MC simulations. Moreover, the optimisation must be performed as soon as new sky coverages or noise levels are considered. We also observed that the solver loses convergence when considering large scales and low noise levels. Finally, in general, the pseudo methods show much higher variance at low ℓ 's ($\lesssim 10$) than the **xQML**. This effect is all the more visible as low tensor-to-scalar ratio r are considered.

Compared to the pseudo-spectrum formalism, the **xQML** shows significant improvements on the error bars and correlations for both BB and EB . The particular advantage relative to pure methods is that it does not require any special mask processing. Due to the higher computational cost of the latter ($\mathcal{O}(N_d^3)$ operations) relative to pseudo-spectra ($\mathcal{O}(N_d^{3/2})$ operations), the **xQML** cannot be run on as many multipoles as for the pseudo-spectra. For all those reasons, we conclude that the **xQML** estimator is particularly suited for large and intermediate angular scales analysis.

Planck data analysis

The *Planck* mission provides legacy products including polarisation measurements of the sky in the millimetre wavelength. This chapter focuses on the extraction of two cosmological parameters: the tensor-to-scalar ratio r via B-modes measurements, and the reionization parameter τ via E-modes measurements. In addition to *Planck* data, we also apply our analysis pipeline to the end-to-end (E2E) noise simulations that include realistic systematic errors. The validation on realistic simulations including systematics is a crucial step to assess the robustness of our analysis pipeline and to propagate the uncertainty through all the steps up to the cosmological parameters estimation. It also allows us to estimate the cross-spectra covariance matrix which will be used to constrain and estimate the posteriors on the cosmological parameters through likelihood analysis.

In Sec. 1, we present the *Planck* legacy data. We make use of the algorithms developed in chapter 2 to estimate the level of foreground contaminations in Sec. 2, and to remove it from the simulations and datasets in Sec. 4. In Sec. 3, using our methods, we also constrain the foreground spectral indices from *Planck* data. In Sec. 5, the polarisation power spectra are estimated on the cleaned maps using the xQML algorithm developed in chapter 3. Finally, in Sec. 6, the reionization and tensor-to-scalar ratio are estimated using a large-scale likelihood analysis.

1 Planck legacy

In this section, we describe the public data products made available by the European Space Agency’s *Planck* mission. Those are part of the third *Planck* release (PR3), available on the *Planck Legacy Archive 2019* (PLA).

1.1 Datasets

The bottom of the *Planck* satellite was always facing the Sun, while spinning on its vertical axis at the speed of one rotation per minute to scan the sky. The so-called rings (or *HEALPix* rings) consist of binned time ordered information (TOI) data measured during a stable pointing period of the spacecraft, which are about 60 minutes each. Using a map-making algorithm, the rings are then combined to get the final map products. Additional maps including several data splits are also delivered. Those are built using different period of the mission, different detectors, or different rings.

Planck carried two scientific instruments: the High Frequency Instrument (HFI), and the Low Frequency Instrument (LFI).

High Frequency Instrument

The HFI mission provided polarisation measurements in five channels, 100, 143, 217, 353 GHz, at maximum resolution of $n_{\text{side}} = 2048$. For each channel, the mission provides :

- a map for the full mission by combining all the rings.
- two half-mission maps (hm1 and hm2) which correspond to the first and second half of the ring sets from the full mission.
- two maps that are built from odd and even numbering of the rings (oe1 and oe2) from the full mission.

Low Frequency Instrument

The LFI mission measured polarisation in three channels, 30, 44, 70 GHz, at a maximum resolution of $n_{\text{side}} = 1024$. For each channel, the mission provides:

- a map for the full mission by combining all the rings.
- two half-ring maps (hr1 and hr2), generated from the first and second half of each stable pointing.
- four maps based on year-combination, year 1+2, year 1+3, year 2+4, and year 3+4.

1.2 FFP10 noise simulations

The *Planck* team identified systematic errors due to uncertainty in the calibration of the LFI and HFI instruments. Although negligible for the CMB temperature measurement, they can seriously impact the polarisation measurement of the instrument due in particular to intensity-to-polarisation leakage. In order to quantify their impact, the PLA provides 300 E2E simulations that include systematic uncertainties based on the modelling of all known instrumental and astrophysical effects.

HFI simulations

The E2E HFI simulation pipeline, detailed in *Planck 2018 Results. III*, simulates the time-ordered information (TOI) by proceeding to the main following steps which include the systematics effects :

1. White noise is generated to simulate the photon, phonon, and electronic noise.
2. The first white noise is convolved with the detector time response, and an additional white noise is added to mimic the electronics noise.
3. The timeline is deglitched similarly to what was applied due to the presence of cosmic rays.
4. The resulting data timeline is then combined with a fiducial sky signal including the CMB and foreground realisations from the PSM.
5. The signal in analog-to-digital units (ADU) is evaluated then fed through a simulator of a non-linear analogue-to-digital converter, where complexity is added into the signal by inducing time variation of the response and gain differences of the detector.
6. A 1/f noise component is added to the signal.
7. The TOI are then projected into *HEALPix* rings.
8. The resulting signals are fed to the map-making algorithm to produce the final maps.

Ultimately, from each final maps simulated, the input sky (CMB and foregrounds) is subtracted to build the noise and residual systematics frequency maps.

LFI simulations

The E2E LFI simulation pipeline is detailed in *Planck 2018 Results. II*. It includes systematic effects partially at the time-line level and partially at the ring-set level.

1. Firstly, separate ring-sets are produced for each signals : the CMB, Galactic foregrounds, extra-galactic diffuse signals, point sources, as well as the solar and orbital dipoles. The signals are then convolved with the suitable instrumental beam, and added to white and 1/f noises ring-sets. The resulting signals are combined and the signal calibration is computed.
2. Those calibration are therefore impeded by systematic errors. They are then applied to timelines data that include the same sky simulations as the one used for the ring-sets. The resulting timelines are then fed to the same map-making algorithm as the one use for the real data product, but including calibration errors.

The full pipeline of systematic simulations is also applied on the noise-only time-stream. The resulting 300 pure-noise simulations thus include the same systematic errors as the full (signal+noise) LFI simulations.

1.3 White noise simulations

In order to check the impact of systematics in the final results, we also generate white noise simulations following the same procedure as the one described in Sec. 2 of chapter 2. Our simulations are based on the pixel variance of the maps provided with PR3.

2 Foregrounds cleaning

This section is dedicated to the foregrounds cleaning methods applied on the *Planck* data and our simulations. The approaches that we follow have been described in details in chapter 2.

2.1 Pre-smoothing and resolution degradation

The datasets are loaded at their full resolution, then pre-smoothed using a cosine window function, as suggested in Benabed et al. 2009; Keskitalo et al. 2010,

$$b_\ell = \begin{cases} 1 & \ell \leq \ell_1 \\ \frac{1}{2} \left[1 + \cos \left(\pi \frac{\ell - \ell_1}{\ell_2 - \ell_1} \right) \right] & \ell_1 < \ell \leq \ell_2 \\ 0 & \ell_2 < \ell \end{cases} . \quad (4.1)$$

We choose $\ell_1 = 2n_{\text{side}} - 1$ and $\ell_2 = 3n_{\text{side}} - 1$, with $n_{\text{side}} = 16$. With that parametrisation, we assure that all signals above $\ell = 3 \times 16$ are erased by the smoothing process, as shown in Fig. 4.1. The datasets can therefore be safely downgraded to $n_{\text{side}} = 16$ while avoiding any aliasing coming from the signal at high multipoles. The resulting maps are then fed to the cleaning methods listed here-after.

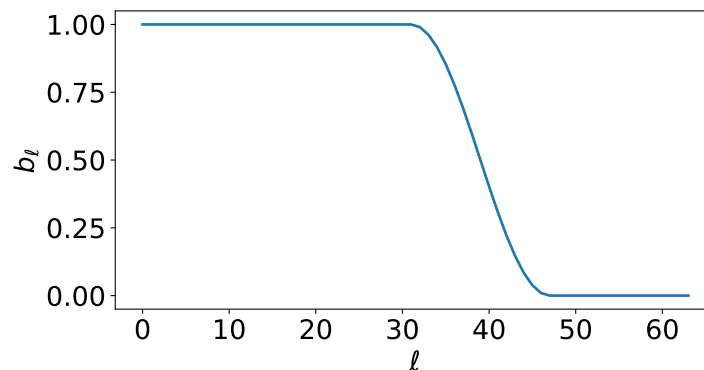


Figure 4.1: Cosine beam window from Eq. (4.1), with $\ell_1 = 2n_{\text{side}} - 1$, $\ell_2 = 3n_{\text{side}} - 1$, and $n_{\text{side}} = 16$.

2.2 Cleaning methods

We follow the prescription proposed in Sec. 4 of chapter 2. In order to clean the intermediate channels (44 GHz, 70 GHz, 100 GHz, 143 GHz, and 217 GHz), we use one low and one high frequency channel (30 GHz and 353 GHz) as tracers to remove respectively the synchrotron and the dust contaminations. We refer to the intermediate channels as the $d(\hat{n})$ maps, while the dust and synchrotron template are respectively labelled $t_D(\hat{n})$ and $t_S(\hat{n})$.

We consider three methods to estimate one global foreground coefficient α on the sky (the coefficient α was introduced in Sec. 2 of chapter 2):

Ordinary linear regression

The oLR is described in Sec. 6 of chapter 2. In order to mitigate the bias induced by the noise and the CMB variance, we proposed to smooth the datasets before applying the linear regression.

Such smoothing is already provided by the pre-smoothing using the beam window in Eq. (4.1). We therefore do not apply any additional smoothing to the datasets.

Cross normalised linear regression

The **xnLR** is described in Sec. 6 of chapter 2. For this method, we use the full covariance matrix, C defined in Eq. (2.31), that includes the dataset noise and CMB correlation signal, as this choice was shown to provide the lowest error-bars for this method. We note that it can only be applied on the data-split, since it relies on the cross-correlation between maps that have uncorrelated noise. For that purpose, we either use the half-missions or the odd/even rings of the HFI channels. We always use the half-rings for the LFI channels. We thus get two estimations of α : one for the half-missions, and one for the odd/even rings.

Maximum Likelihood Estimator

The MLE method is described in Sec. 7 of chapter 2. Again, we use the full covariance matrix defined in Eq. (2.76), including the dataset noise and CMB correlation signal. The method can either be applied on the full datasets, or each data-split.

For this method, we consider five possible combinations of dataset in order to estimate α . We always use the full mission map for the intermediate channels. For the templates, we either use the full missions or one of the four data-splits : hm1, hm2, oe1, oe2 for the 353 GHz dust template map, and hr1 or hr2 for the 30 GHz synchrotron template map. For both templates, we always use either the first split pair (hm1/oe1, hr1), or the second (hm2/oe2, hr2). Other combinations such as (hm2/oe2, hr1) or (hm1/oe1, hr2) provide very similar results.

2.3 Masks

We consider three masks, with a coverage going from $f_{\text{sky}} = 0.5$ to $f_{\text{sky}} = 0.9$, as shown in Fig. 4.2 for a resolution $n_{\text{side}} = 256$. To build the masks, we use the 353 GHz polarisation map that we smooth with a 5° Gaussian beam window. We then apply a cut based on the pixels with the highest amplitude, $\sqrt{Q^2 + U^2}$. The resulting binary map is then smoothed with a 3° Gaussian beam window, then downgraded to the required resolution, $n_{\text{side}} = 16$.

2.4 Monte-Carlo simulations

Method comparison

We test the three estimators on two sets of 300 simulations. Both sets include the PySM foreground model, combined either with white noise, or the FFP10 noise simulations which include systematic effects. The maps are loaded at¹ $n_{\text{side}} = 128$, then pre-smoothed and degraded to $n_{\text{side}} = 16$ before estimating α . We use the half-missions maps for the **xnLR** method, and the full missions maps for the MLE and **oLR** methods.

The results for all intermediate frequency channels are shown in Fig. 4.4. The grey bands indicate the input foreground coefficient distribution, each referring to 1, 2, or 3 standard deviation level of the input coefficient distribution based on the PySM realisations, as pictured in Fig. 4.3.

The triangles markers in Fig. 4.4 are the results for the white noise simulations, while the dots are for the FFP10 noise. As expected, we observe that the error-bars using the FFP10 noise are

¹We observed that MC results are not impacted by the choice of the initial resolution of the maps. We therefore select $n_{\text{side}} = 128$ and not the maximum resolution of *Planck* data.

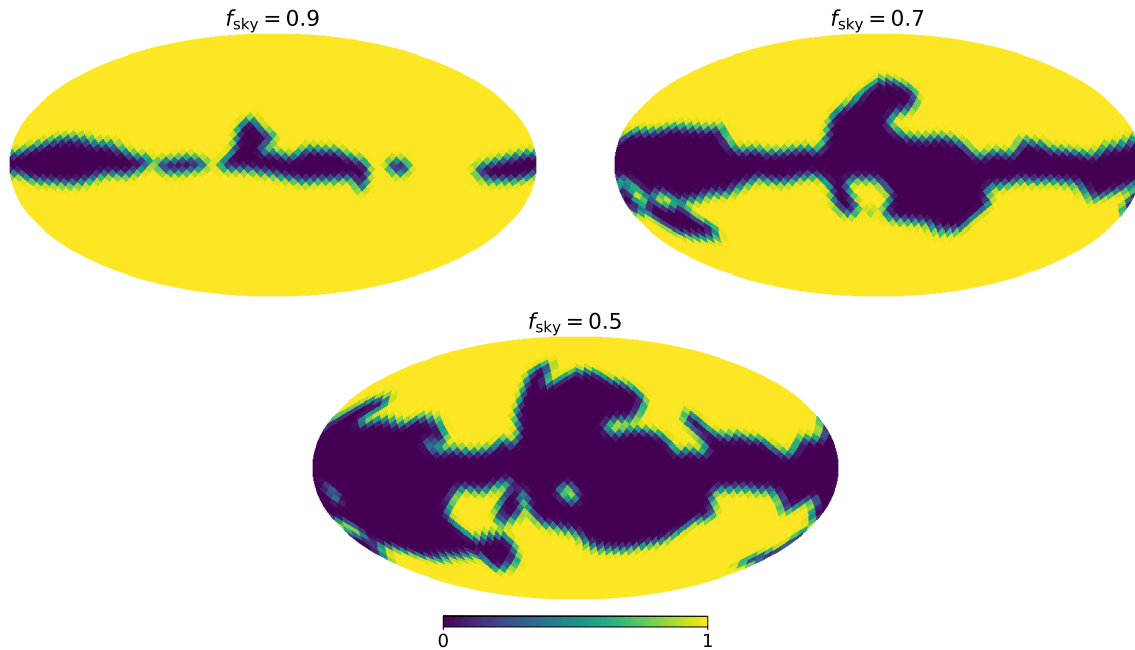


Figure 4.2: Masks used at $n_{\text{side}} = 16$, for three sky coverages : 90%, 70%, and 50%.

systematically larger than for the white noise case. For both sets of simulations, compared to the two other methods, the `oLR` is slightly more shifted from the input dust coefficient distributions at 44 GHz. This is due to the high noise level for this channel (we refer to Fig. 2.1), combined with a low amplitude of the dust signal. The dataset pre-smoothing is therefore not sufficient to remove the noise variance bias for this estimator.

For the two other methods, `xnLR` and `MLE`, we observe no bias using the white noise simulations, except for a slight shift at 217 GHz on the synchrotron coefficient α_S at $f_{\text{sky}} = 0.5$, induced by the reduced sky coverage combined with a loss of the synchrotron signal amplitude.

Globally, the results on the FFP10 noise simulations show higher variations of the coefficient estimations than for the white noise case. The most impacted channel is at 143 GHz, for which α_S is completely out of the input distribution. The coefficients on the remaining channels are relatively well recovered.

MLE only

In addition, we show in Fig. 4.5 the full distribution for the `MLE` estimations tested on the PySM sky + FFP10 noise simulations.

The results on the LFI datasets are relatively stable when changing the sky coverage. This is not the case for the HFI channels, for which relatively important variations of the distributions are observed depending on the sky fraction used to estimate α . Those variations are particularly visible on the 143GHz channel. Nevertheless, the overall estimations of the coefficients are in relatively good agreement with the input sky signal.

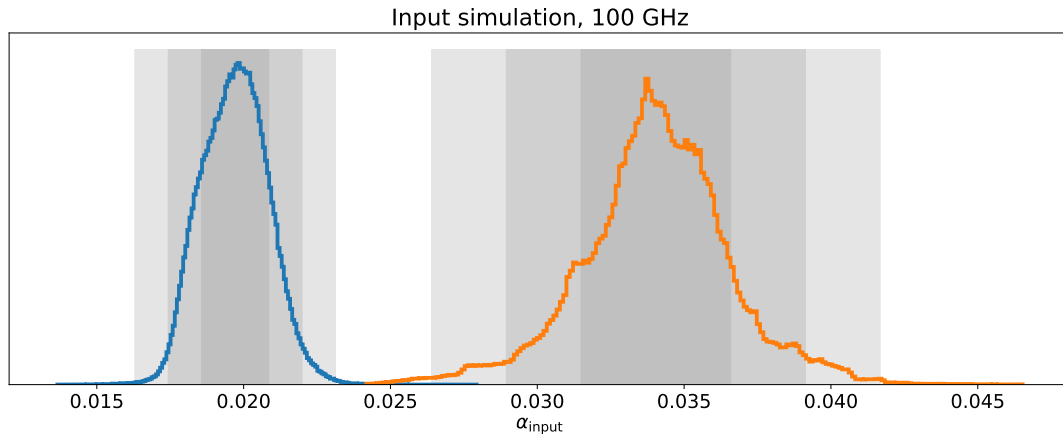


Figure 4.3: Input distributions of the coefficients α_D (left, blue) and α_S (right, orange) for the PySM at 100 GHz. The grey bands indicate 1, 2, and 3 standard deviations of the distribution.

2.5 Results on *Planck* data

Method comparison

For the *Planck* data, the results depending on the sky fraction considered are shown in Fig. 4.7 for all intermediate frequency channels. Again, we compare the three methods previously tested on Monte-Carlo simulations. For each data-point, we always show two error-bars: those obtained using white noise simulations (smaller and wider), and those using the FFP10 noise (thinner and longer).

The oLR presents very different estimates than the other methods, adding to the fact that this method performs poorer results on the Monte-Carlo simulations, we focus our discussion on the two other approaches.

We observe that both the xnLR and the MLE provides very similar results, whereas their implementations are fundamentally different. This adds to our confidence in the results. For those two methods, the estimations of α_D on HFI data are nearly constant for most of the sky coverages considered, while α_S is observed to decrease as smaller fraction of the sky are used. The inverse behaviour is observed on the LFI maps, for which α_D increases with the sky coverage, and α_S is relatively constant.

We also test for any variation of the coefficient estimated depending on which part of the mission (half, odd/even rings, or full) is used for the templates of the MLE. The results are shown only for the 100 GHz in Fig. 4.6, and they are very similar for all other channels. We observe that the estimations are stables for all the template mission used.

Fiducial noise variance

We investigated the impact of using different noise models to construct the residual covariance matrix C of the MLE method. We either use the public *Planck* noise covariance data introduced in Sec. 2 of chapter 2, or we build our own estimate of the pixel variance using the 300 FFP10 noise simulations. We found no major difference between both cases.

We also considered using mean pixel noise, instead of inverse-weighting the pixels. In the former approach, the datasets noise covariance matrices used to build the residuals covariance

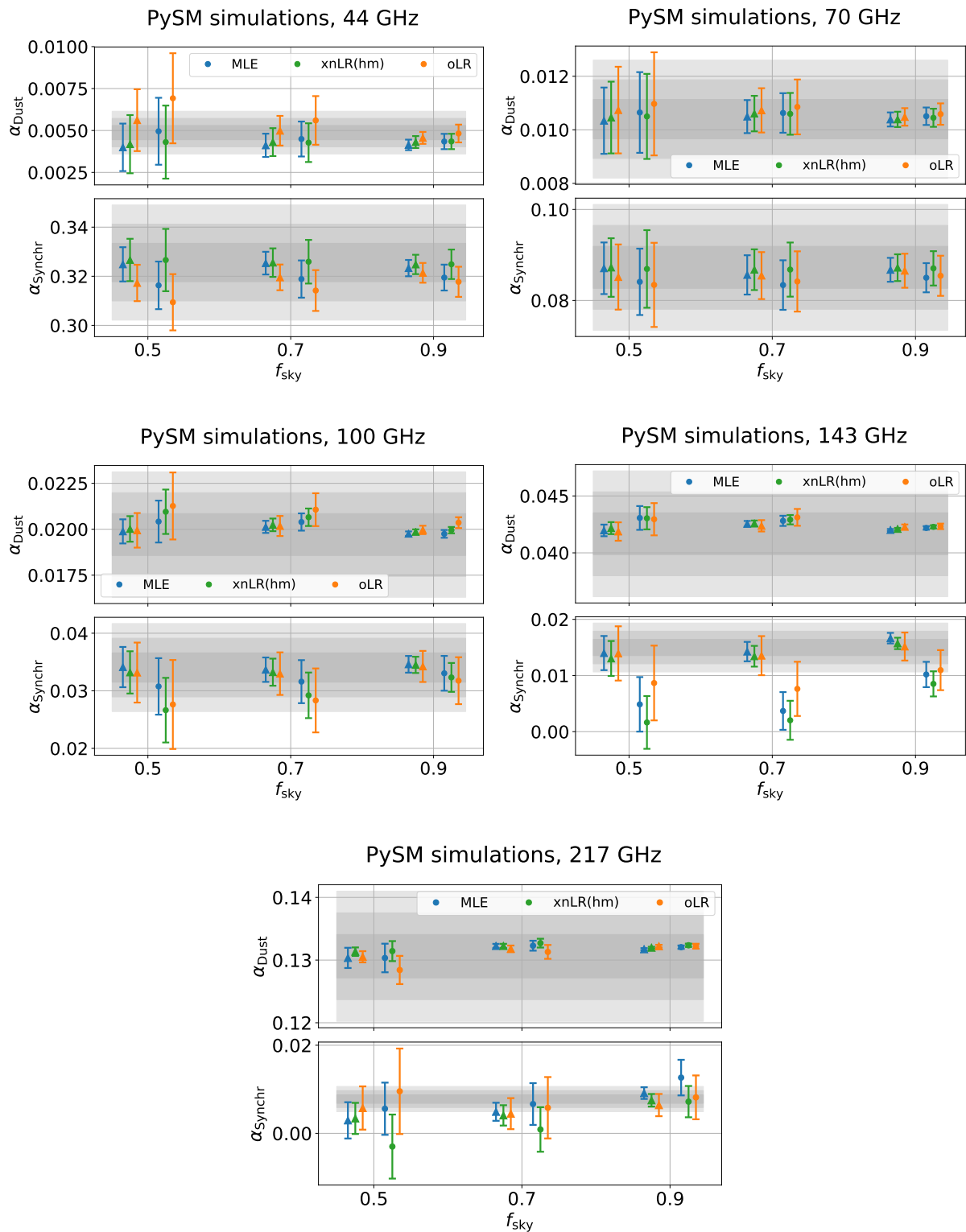


Figure 4.4: Foreground coefficients α estimated on 300 simulations, using the PySM foreground sky combined either with white noise simulations (triangles) or FFP10 noise simulations (dots). The MLE and oLR make use of the full missions, while the xnLR only uses the half-missions. We consider three different sky coverages, $f_{\text{sky}} = 0.5, 0.7, 0.9$.

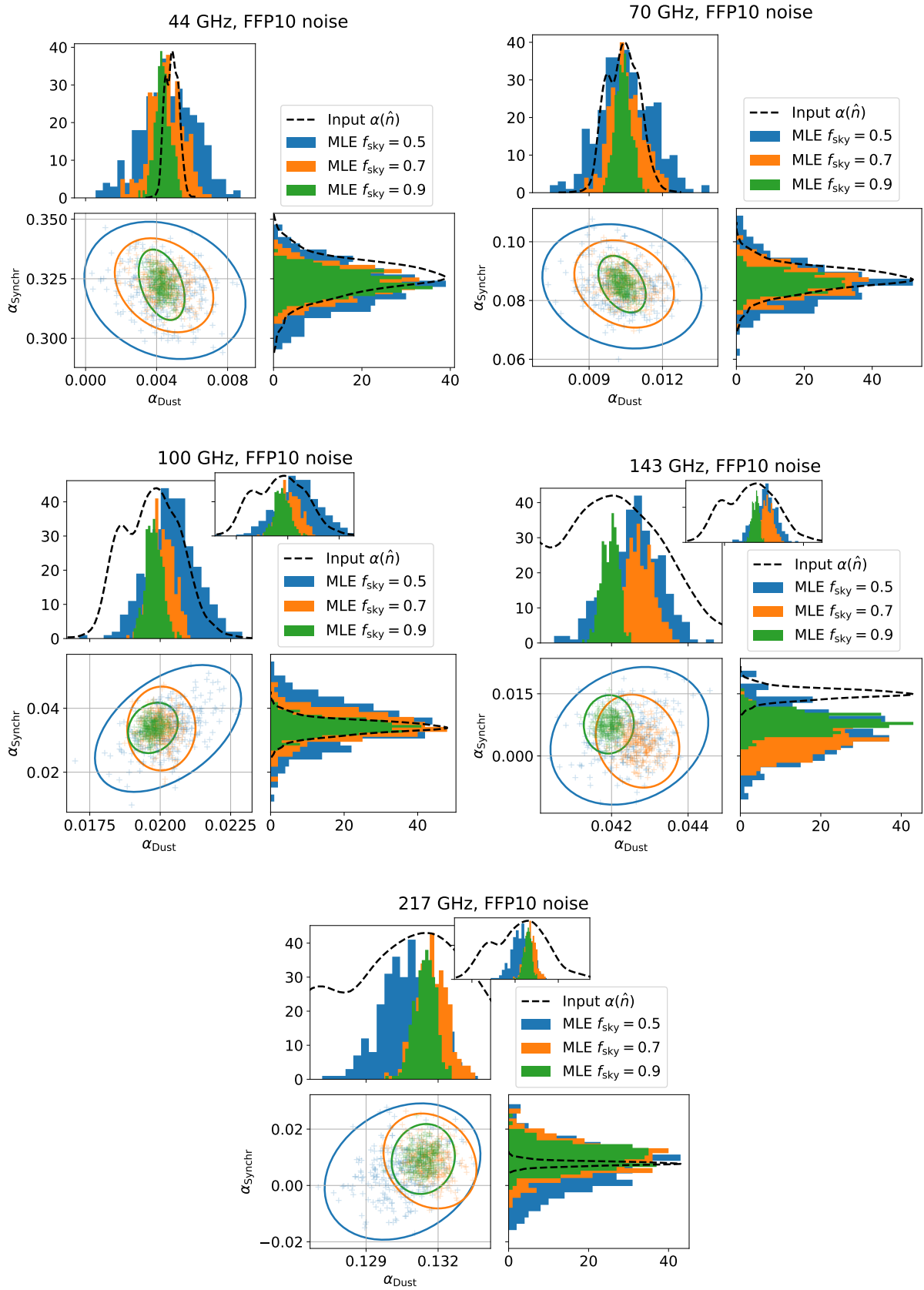


Figure 4.5: Foreground coefficients α estimated on 300 PySM + FFP10 noise simulations, using the MLE estimator on the full missions. We consider three different sky coverages, $f_{\text{sky}} = 0.5, 0.7, 0.9$.

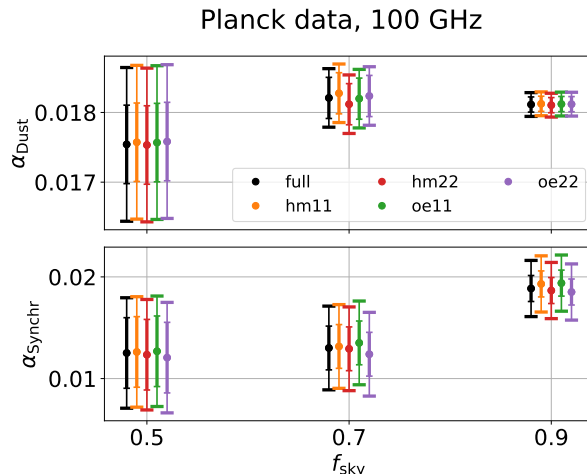


Figure 4.6: Foreground coefficients estimation on *Planck* 100 GHz full channel using the MLE method. Five missions are considered for both templates maps: full mission (full); half-mission 1 (hm11) or 2 (hm22); odd/even rings 1 (oe11) or 2 (oe22).

matrix of Eq. (2.76) are diagonals with constant value,

$$N_x \rightarrow \left(\sum_p^{N_{\text{pix}}} \frac{1}{N_x^p} \right)^{-1}, \quad x \in \{d, D, S\}. \quad (4.2)$$

Using either a pixel noise weighting or a constant noise for all pixels does not significantly change the precision of the estimator on α , nor does it impacts the results presented on *Planck* data.

Conclusion

In this section, we showed the consistency and robustness of our template cleaning method. As expected, the FFP10 simulations produce larger uncertainty on the foreground coefficient estimations than for the white noise. The results obtained on *Planck* data are coherent with those derived from the simulations. The choice of the template mission has little impact on the results.

Since the MLE provides the most stable results, we select this method for the rest of the *Planck* data analysis. We use the coefficients estimated on the full missions and considering 70% of the sky.

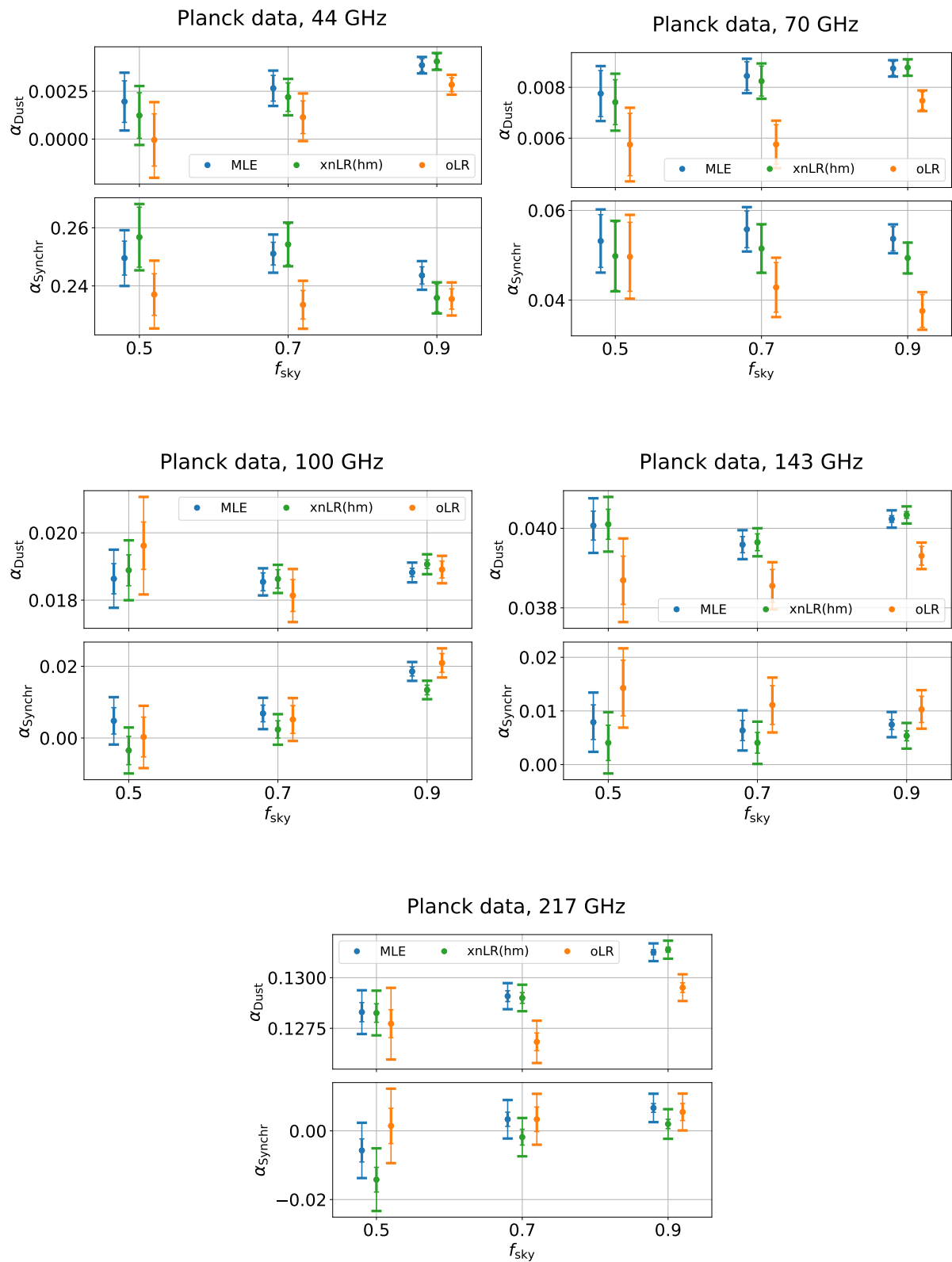


Figure 4.7: Same as Fig. 4.4 for *Planck* data. Two error-bars are shown for each data point: those obtained using white noise simulations (smaller and wider), and those using the FFP10 noise (thinner and longer).

3 Constraints on foreground spectral indices

3.1 From foreground coefficients to spectral indices

The dust and synchrotron SED are well approximated respectively by a modified black-body and a power law, as in Eq. (2.1) and Eq. (2.2). The foreground coefficients α that we measure can therefore be related to the spectral indices used to parametrise the foreground SEDs.

For the dust, we have

$$\alpha_D^\nu(\hat{n}, \beta_d, T_d) = \frac{\nu^{\beta_d(\hat{n})-2} B_\nu(T_d(\hat{n})) U_c^\nu C_c^\nu}{(353)^{\beta_d(\hat{n})-2} B_{353}(T_d(\hat{n})) U_c^{353} C_c^{353}}, \quad (4.3)$$

and for the synchrotron,

$$\alpha_S^\nu(\hat{n}, \beta_s) = \frac{\nu^{\beta_s(\hat{n})} U_c^\nu C_c^\nu}{(30)^{\beta_s(\hat{n})} U_c^{30} C_c^{30}}. \quad (4.4)$$

The unit conversion factor $U_c^\nu [K_{\text{CMB}}/K_{\text{RJ}}]$ transposes the signal observed at frequency ν from Rayleigh-Jeans temperature to CMB temperature units. The colour-correction coefficients, C_c^ν , account for spectral variations of the foreground signals within a photometric channel.

3.2 Methodology

In order to estimate the spectral indices, we minimise the log-likelihood of the foregrounds coefficients,

$$-2 \log \mathcal{L}(\hat{\boldsymbol{\alpha}} | \boldsymbol{\alpha}(\beta_s, \beta_d, T_d)) = [\hat{\boldsymbol{\alpha}} - \boldsymbol{\alpha}(\beta_s, \beta_d, T_d)]^T \boldsymbol{\Xi}^{-1} [\hat{\boldsymbol{\alpha}} - \boldsymbol{\alpha}(\beta_s, \beta_d, T_d)], \quad (4.5)$$

where

$$\boldsymbol{\alpha}(\beta_s, \beta_d, T_d) = (\alpha_d^{\nu_1}(\beta_d, T_d), \dots, \alpha_d^{\nu_{n_\nu}}(\beta_d, T_d), \alpha_s^{\nu_1}(\beta_s), \dots, \alpha_s^{\nu_{n_\nu}}(\beta_s))^T, \quad (4.6)$$

is the model, $\hat{\boldsymbol{\alpha}}$ the coefficients estimated on the data (PLA or simulations), and $\boldsymbol{\Xi} \equiv \text{Cov}[\boldsymbol{\alpha}]$ the $2n_\nu \times 2n_\nu$ covariance matrix of the foregrounds coefficients estimated from MC simulations.

3.3 Results

Simulations maps

We first discuss the results on simulations. We use either white or FFP10 noise simulations, and the PySM foreground sky. Since we do not simulate bandpass when generating the PySM foreground sky, we do not apply any colour correction to the datasets. For delta-bandpass, the unit conversion coefficient are computed as

$$U_c^\nu = \frac{2k_B \nu^2}{c^2 b'_\nu}, \quad \text{with} \quad b'_\nu \equiv \left. \frac{\partial B_\nu(T)}{\partial T} \right|_{T_{\text{CMB}}}, \quad (4.7)$$

and $T_{\text{CMB}} = 2.725 \text{ K}$. The resulting coefficients are listed in Table. 4.1.

We draw the distribution of the posterior maximum for the spectral parameters in Fig. 4.8, for which we display the 1σ and 2σ 2D contours of the distribution. For each set of simulations, we select two sampling procedures when minimising the likelihood function of Eq. (4.5). We either let the dust MBB temperature T_d free, or we fix it to the white-noise simulations best-fit

value. The latter choice is warranted, because the dust temperature T_d and spectral index β_d are highly correlated, as shown on the right panel Fig. 2.3.

The variation across the sky of the PySM input spectral indices are shown in Fig. 2.3 (Sec. 2 of chapter 2). For the PySM, the input synchrotron spectral index lies between $-3.1 < \beta_s < -2.9$, while the dust spectral index and its MMB temperature lies respectively between $1.5 < \beta_d < 1.6$ and between $17\text{K} < T_d < 25\text{K}$. The mean value accompanied with the 1σ error are listed in Table. 4.3. In addition, we also include the correlation between the dust and synchrotron spectral indices, $\rho(\beta_d, \beta_s)$. The synchrotron results are compatible with the PySM input, with $\beta_s \approx -3$, independently of the sky coverages or simulation datasets. The dust spectral index is badly fitted on the FFP10 simulation datasets for $f_{\text{sky}} = 0.5$ and T_d free. For the remaining cases, the results are compatibles with the PySM input. We see how the value of the dust spectral index grows from $\hat{\beta}_d \approx 1.5$ to $\hat{\beta}_d \approx 1.57$ when considering larger sky fraction, thus including more signal from the galactic plane. This feature is expected, since the input value of β_d is larger near the galactic plane (we refer to Fig. 2.3). Finally, we observe that the dust-synchrotron spectral correlation can be quite high, reaching $\rho(\beta_d, \beta_s) \approx 20\%$ for $f_{\text{sky}} = 0.9$ and considering white noise simulations. We also notice that the error-bars of the FFP10 simulations are roughly twice larger than that of the white noise simulations.

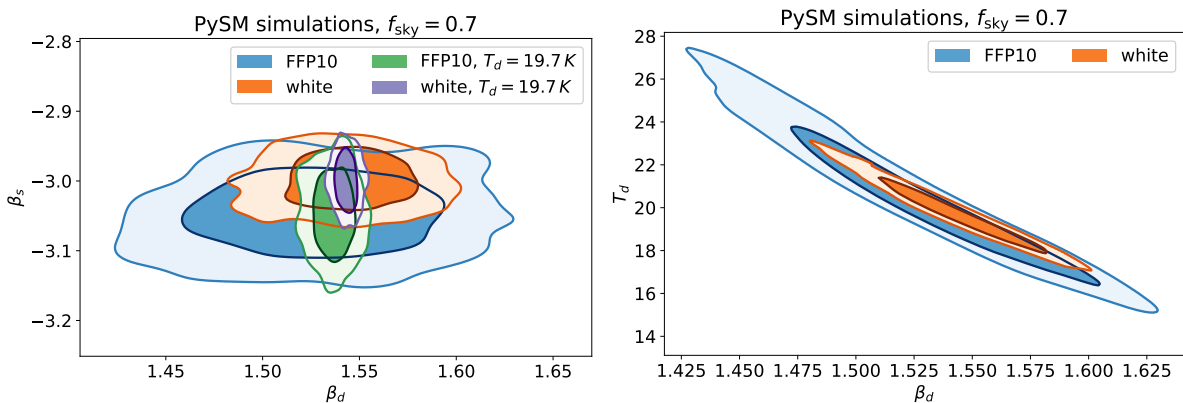


Figure 4.8: Distribution of the posterior maximums for the spectral parameters based on 300 white or FFP10 noise simulations, and evaluated on 70% of the sky. Left : 1σ and 2σ 2D dispersion of the dust and synchrotron spectral coefficients, β_d and β_s . The dust MMB temperature parameter is either free, or fixed to 19.7 K. Right: 1σ and 2σ 2D dispersion of the dust MMB temperature T_d and the dust spectral index β_d .

Planck data

For *Planck* data, the values of the colour coefficients are computed assuming spectral law of the foreground signals which is then integrated over the detector frequency bandpass. We select the unit conversions U_c^ν and colour correction factors C_c^ν found in Table 2 of *Planck 2018 Results. XI*. Their value are listed in Table. 4.2. The colour correction coefficients for the HFI are computed for a modified black-body SED with fiducial spectral index $\beta_d \approx 1.5$ and temperature $T_d \approx 19\text{K}$. The colour correction coefficients for the LFI are computed for a power-law SED using a fiducial spectral index $\beta_s \approx -3$. For both simulation sets, we observe an anti-correlation between α_D and α_S (off-diagonal blocks), reaching 30% at low frequency (44 and 70 GHz).

To compute the likelihood of Eq. (4.5), we use the α -covariance matrix Ξ , computed from the simulations, which include either white noise or the FFP10 noise set of maps. The correlation matrices derived from Ξ are shown in Fig. 4.9. For the white-noise simulations, we observe a

high level of correlation between the high frequency channel coefficients for both α_D and α_S . Such feature is less present for the FFP10 simulations.

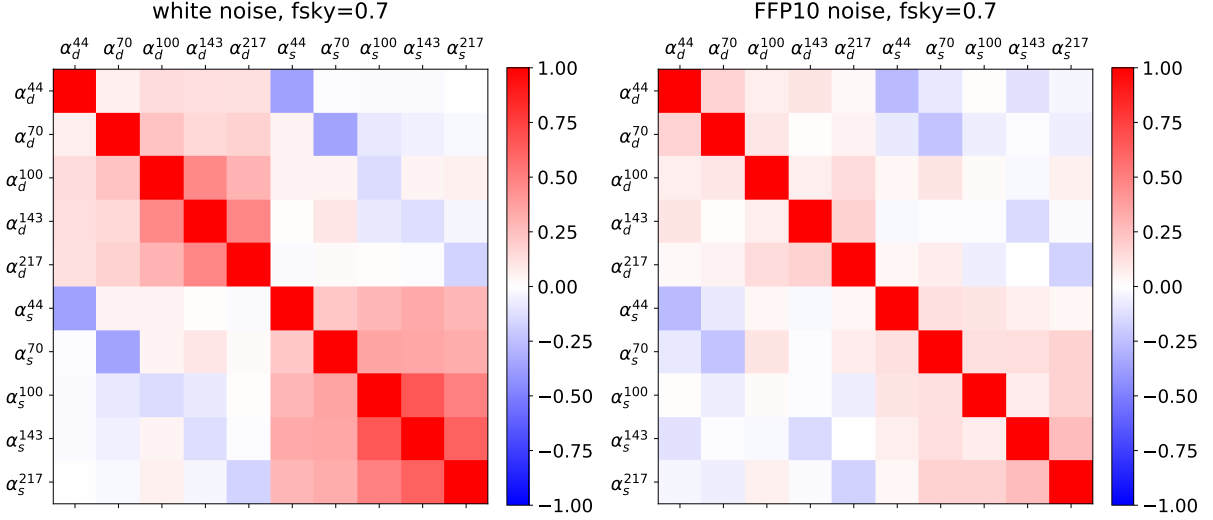


Figure 4.9: Foreground coefficients correlation matrices, $\text{Corr}[\Xi]$. We use 300 white or FFP10 noise simulations to estimate α on 70% of the sky.

Because the dust temperature and spectral index are highly correlated, we choose a fixed value $T_d = 19.6$ K for the best fit derived from (Planck Collaboration et al. 2015), and following the same procedure as in *Planck 2018 Results. XI*. All results for the sky coverages $f_{\text{sky}} = 0.5, 0.7$ and 0.9 are summarised in Table. 4.4. We also include the *Planck* results from *Planck 2018 Results. XI* which, in addition to *Planck* polarisation channels, also includes the 23 GHz and 33 GHz WMAP datasets. Although they also use the FFP10 simulations, their approach is completely different than ours, as they work in the harmonic domain using half-mission maps to compute the cross-spectra over the multipole range $4 \leq \ell \leq 148$, while our method is pixel-based and makes use of the full missions datasets. The mask used is not the same, although their effective sky fraction is close to one of ours ($\sim 70\%$). In addition to the spectral index, the results from *Planck* also fit for the foreground amplitudes and a correlation coefficient between the dust and the synchrotron. We note that our error-bars on the estimated spectral parameters include the uncertainty induced by the noise and CMB variance only. We do not include for variation of the foreground SED across the sky. All these differences explain why our error-bars from the FFP10 simulations are almost three times smaller than for the *Planck* results.

We display our results for $f_{\text{sky}} = 0.7$ in Fig. 4.10. When using the covariance matrix Ξ derived from white-noise simulations, all values of the dust coefficient $\beta_d^{f_{\text{sky}}}$ are found to be close to *Planck* results, $\beta_d^{\text{Pl}} = 1.53 \pm 0.02$ from *Planck 2018 Results. XI*. We obtain $\beta_d^{0.9} = 1.551 \pm 0.002$ and $\beta_d^{0.7} = 1.551 \pm 0.004$. This value slightly decreases when less signal from the Galactic plane is included, with $\beta_d^{0.5} = 1.546 \pm 0.007$. Our synchrotron spectral index gives $\beta_s^{0.7} = -3.229 \pm 0.027$ and $\beta_s^{0.5} = -3.315 \pm 0.04$. Those are also consistent with *Planck* results $\beta_s^{\text{Pl}} = -3.13 \pm 0.13$, as well as other measurements (Choi et al. 2015; Fuskeland et al. 2014; Krachmalnicoff et al. 2018). When considering 90% of the sky, our estimation gives a lower value, with $\beta_s^{0.9} = -3.430 \pm 0.018$.

When using the covariance matrix Ξ derived from FFP10-noise simulations instead of the one derived from white-noise, we observe an overall boost of all the spectral index estimations compared to the white-noise case. We find $\beta_d^{0.5} = 1.586 \pm 0.013$, $\beta_d^{0.7} = 1.599 \pm 0.007$, and $\beta_d^{0.9} = 1.613 \pm 0.005$ for the dust spectral index, and $\beta_s^{0.5} = -3.458 \pm 0.027$, $\beta_s^{0.7} = -3.373 \pm 0.040$, and $\beta_s^{0.9} = -3.458 \pm 0.027$ for the synchrotron spectral index.

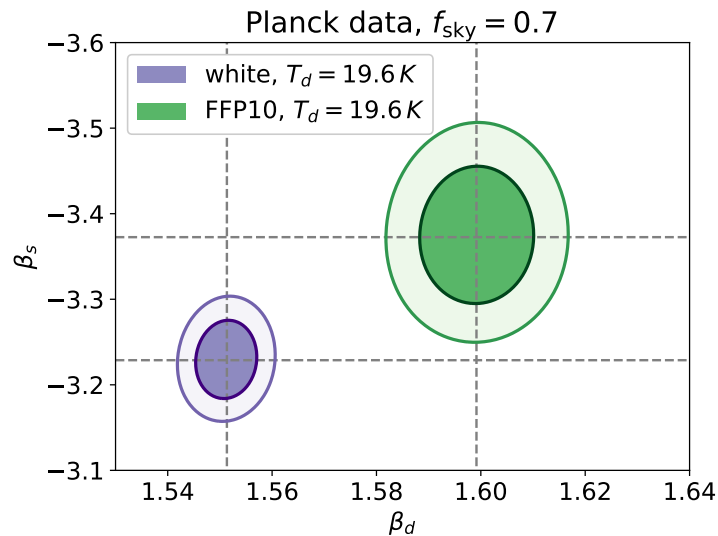


Figure 4.10: 1σ and 2σ 2D contours of the spectral parameter β_d and β_s measured on *Planck* data, evaluated on 70% of the sky. The dust MMB temperature parameter is fixed to 19.6 K.

3.4 Conclusion

In this section, we provided a simple approach allowing us to connect the spectral parameters of the foreground signal with the coefficient that we estimate for the template fitting. Our results are in good agreement with those provided by *Planck* and other studies. The observed variation of the spectral indices with the sky coverage is directly related to the variation of the foreground coefficient estimates α , and it translates the inhomogeneity of the foreground signals across the sky.

Further work would allow us to highlight the foreground signal variations across the sky by choosing different masks, or focusing on patches of the sky. We could also include other datasets such as those provided by WMAP to improve the constraints on the spectral parameters.

Table 4.1: PySM unit conversion and colour correction coefficients U_c^ν and C_c^ν for the datasets simulation (using delta-bandpass).

Reference frequency ν [GHz]	30.0	44.0	70.0	100.0	143.0	217.0	353.0
$U_c^\nu [K_{\text{CMB}}/K_{\text{RJ}}]$	0.9770	0.9514	0.8824	0.7771	0.6046	0.3341	0.0774
C_c^ν	1.0	1.0	1.0	1.0	1.0	1.0	1.0

Table 4.2: *Planck* data unit conversion and colour correction coefficients U_c^ν and C_c^ν . From Planck Collaboration et al. 2015.

Reference frequency ν [GHz]	28.4	44.1	70.4	100.0	143.0	217.0	353.0
$U_c^\nu [K_{\text{CMB}}/K_{\text{RJ}}]$	0.949	0.932	0.848	0.794	0.592	0.334	0.075
C_c^ν	1.000	1.000	0.981	1.088	1.017	1.120	1.098

Table 4.3: Spectral estimation on simulations using white and FFP10 noise datasets. For each case, the dust temperature parameter T_d is either free, or fixed to the white-noise best-fit value.

f_{sky}	noise	$\hat{\beta}_s$	$\hat{\beta}_d$	\hat{T}_d [K]	$\rho(\beta_d, \beta_s)$
0.9	White	-3.015 ± 0.018	1.569 ± 0.002	18.5	19.8%
	White	-3.015 ± 0.018	1.569 ± 0.010	18.498 ± 0.455	14.4%
	FFP10	-3.044 ± 0.027	1.571 ± 0.005	18.5	-1.7%
	FFP10	-3.045 ± 0.027	1.567 ± 0.023	18.772 ± 1.150	-2.3%
0.7	White	-3.000 ± 0.027	1.543 ± 0.004	19.7	9.9%
	White	-3.000 ± 0.027	1.543 ± 0.022	19.724 ± 1.099	2.0%
	FFP10	-3.047 ± 0.040	1.537 ± 0.007	19.7	-1.8%
	FFP10	-3.047 ± 0.040	1.528 ± 0.040	20.409 ± 2.354	-7.5%
0.5	White	-3.000 ± 0.040	1.535 ± 0.007	20.3	-3.6%
	White	-3.000 ± 0.040	1.535 ± 0.038	20.552 ± 2.018	7.2%
	FFP10	-3.050 ± 0.061	1.533 ± 0.013	20.3	-2.7%
	FFP10	-3.047 ± 0.062	1.450 ± 0.067	29.220 ± 10.407	-6.5%

Table 4.4: Spectral estimation on *Planck* data using the Ξ covariance matrix computer from simulations sets with either white or FFP10 noise. The dust temperature is fixed to $T_d = 19.6$ K for the fit. The *Planck* results are extracted from *Planck 2018 Results. XI*.

f_{sky}	Ξ	$\hat{\beta}_s$	$\hat{\beta}_d$
~ 0.7	<i>Planck</i> results	-3.13 ± 0.13	1.53 ± 0.02
0.9	White	-3.430 ± 0.018	1.551 ± 0.002
	FFP10	-3.458 ± 0.027	1.613 ± 0.005
0.7	White	-3.229 ± 0.027	1.551 ± 0.004
	FFP10	-3.373 ± 0.040	1.599 ± 0.007
0.5	White	-3.315 ± 0.040	1.546 ± 0.007
	FFP10	-3.339 ± 0.061	1.586 ± 0.013

4 Cleaned polarisation maps

In this section, we present the results when using the foreground internal templates to clean the polarisation maps. The results are shown both for the simulations and the *Planck* data. For each channel, we use Eq. (2.29) to estimate the CMB signal, with the MLE method performed on 70% of the sky.

4.1 Cleaned datasets

Considering two intermediate channels A and B , the cleaned maps are built following

$$\hat{s}^{A11} = \frac{d^A - \alpha_D^A t_{353}^1 - \alpha_S^A t_{30}^1}{1 - \alpha_D^A - \alpha_S^A}, \quad (4.8)$$

$$\hat{s}^{B22} = \frac{d^B - \alpha_D^B t_{353}^2 - \alpha_S^B t_{30}^2}{1 - \alpha_D^B - \alpha_S^B}, \quad (4.9)$$

with t^1 and t^2 the templates computed respectively from the half-mission 1 and 2.

In this section, we present the results of the full mission set, \hat{s}^{A11} , which are built using the first half-split of the templates. The other combinations show very similar results.

4.2 Simulations

We compare the white and FFP10 noises residual in pixel space at resolution $n_{\text{side}} = 256$ using the coefficients estimated at $n_{\text{side}} = 16$ in Sec. 2. The average and standard deviation of each pixel for the Q and U components is first computed then smoothed by a 5° Gaussian beam. Because we average over many different realisations, most of the CMB signal as well as the noise residuals are reduced. The remaining signal mainly comes from the foreground residuals as well as systematics.

We also compute the map amplitude of the residuals, $P \equiv \sqrt{\langle Q \rangle^2 + \langle U \rangle^2}$, and similarly the map amplitude of the residuals standard deviation, $P_\sigma \equiv \sqrt{\sigma_Q^2 + \sigma_U^2}$. The Q and U residuals are shown for a range $\pm 1 \mu\text{K}$. The amplitudes, P , are shown for a range $[0, 1] \mu\text{K}$. The scale of the standard deviation maps are based on each dataset white noise level. For each channel, we use the same colour range between the white noise and FFP10 maps.

Residuals

The foreground residuals are displayed in Fig. 4.11 and 4.12 respectively for the white noise and FFP10 simulations. Some contaminations are observed in the galactic plane and the variations on the sky are very similar between both types of noise simulations. We observe almost no residuals for the white-noise at higher latitudes. This is not the case for the FFP10, where systematic residuals are visible on the whole sky for the HFI channels. We do not observe such residuals for the LFI channels.

Standard deviations

The standard deviations are similarly displayed on the Fig. 4.13 and 4.14. Those are in excellent agreement between white noise and FFP10 simulations. We note a slight boost of the variance is observed in the Galactic plane for the HFI FFP10 simulations. However, we observe that the 100 GHz channel shows less variance for the FFP10 than for the white noise simulations.

This result is surprising since the variance of the FFP10 simulations (which include white noise) should be at least of the same level as the pure white noise simulations. Masking 30% of the galactic plane, we find that the 100 GHz white noise standard deviation is about 20% higher than that of the FFP10 noise.

4.3 *Planck* data

We show the non-cleaned polarisation Q and U maps in Fig. 4.15, at resolution $n_{\text{inside}} = 256$, and smoothed with a 5° Gaussian window function. The resulting cleaned map with our method are shown in Fig. 4.16. In addition, we also display the initial *Planck* data. We see that much of the initial contaminations are removed. Some residuals foreground signal is still visible, mainly in the galactic plane. We also see how the 44 and 70 and 217 GHz are much noisier than the 100 or 143 GHz channels (we also refer to Fig. 2.1 for the noise levels).

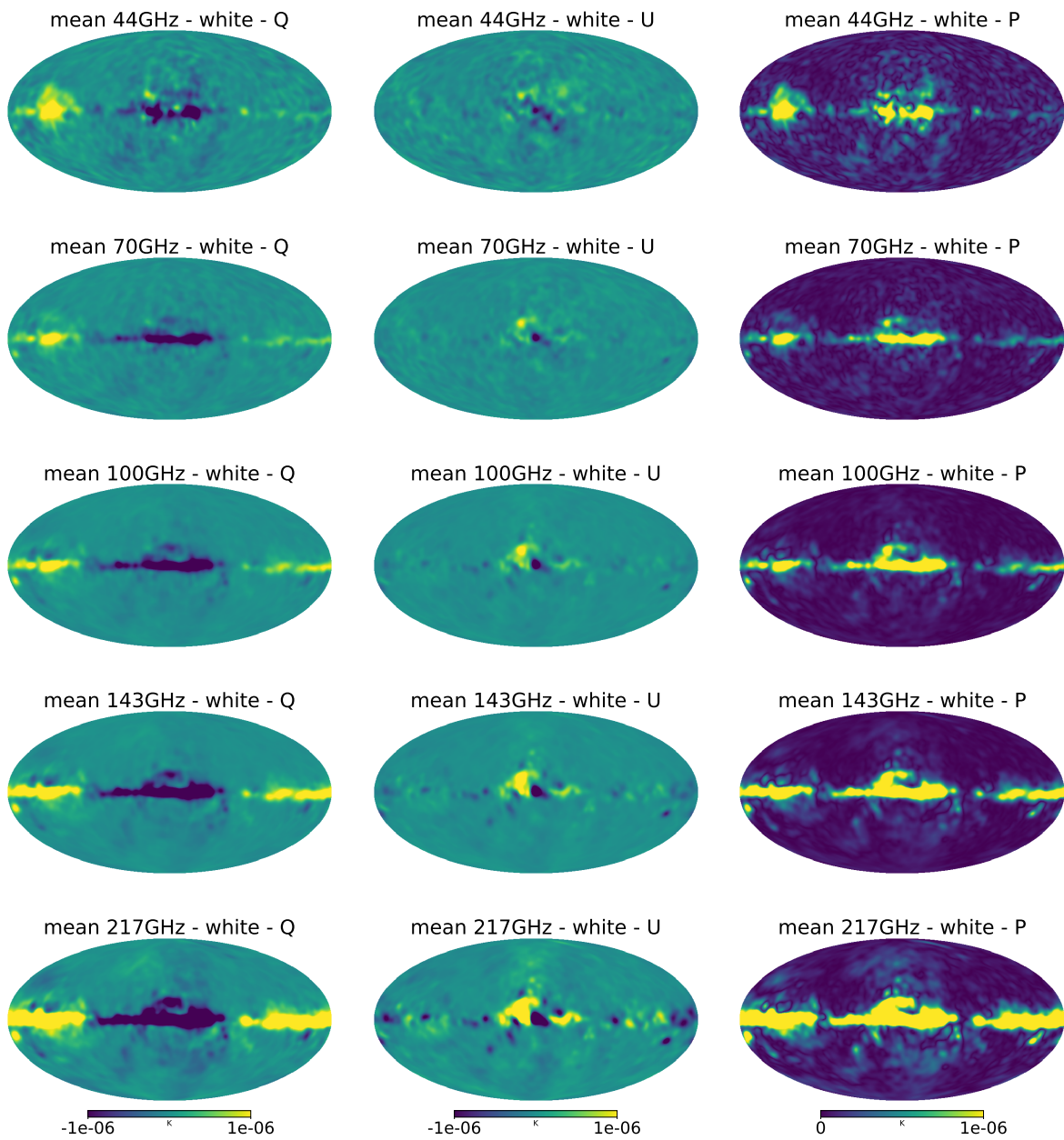


Figure 4.11: White noise simulations mean residuals Q and U Stokes components as well as total intensity power.

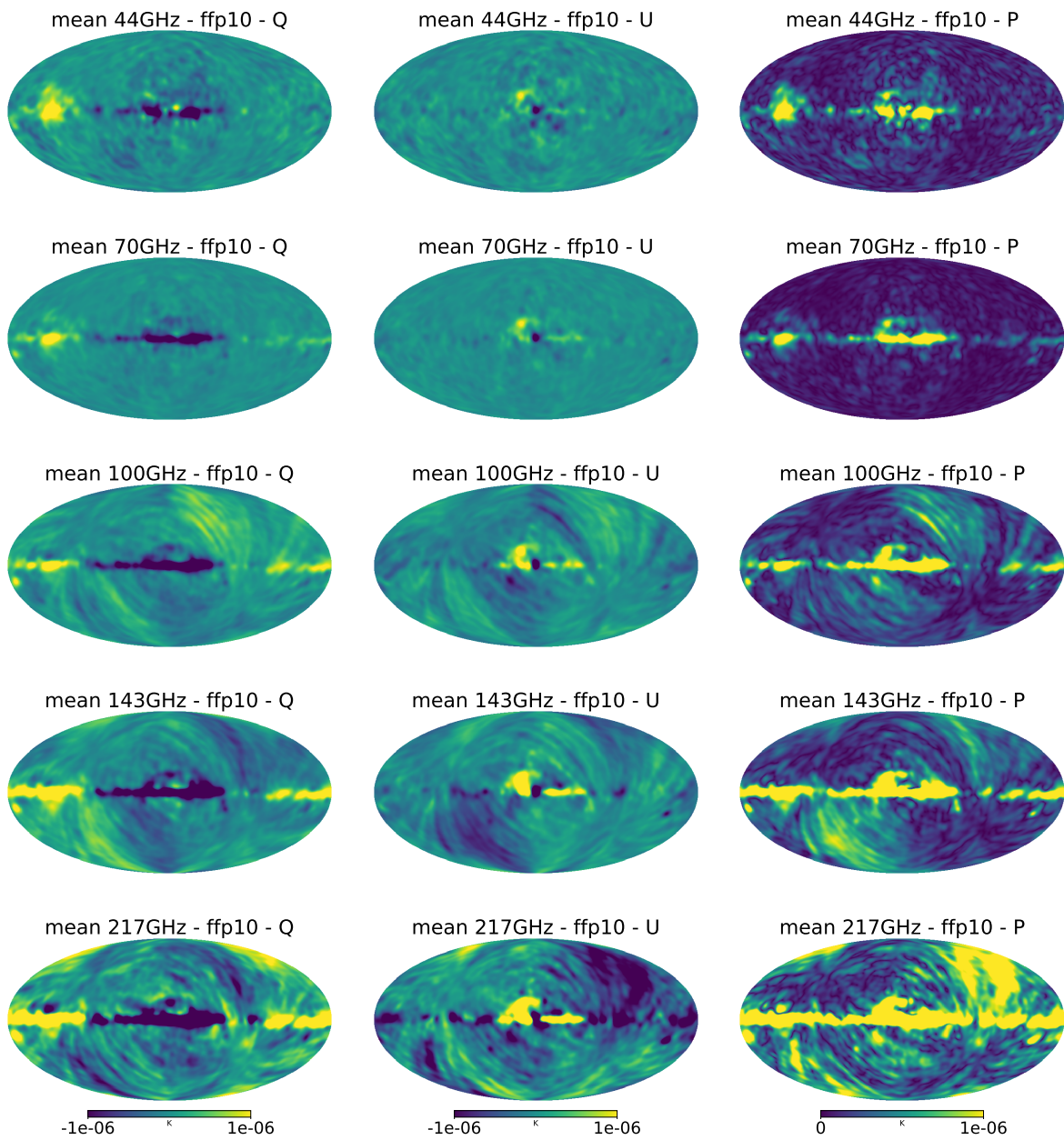


Figure 4.12: FFP10 noise simulations mean residuals Q and U Stokes components as well as total intensity power.

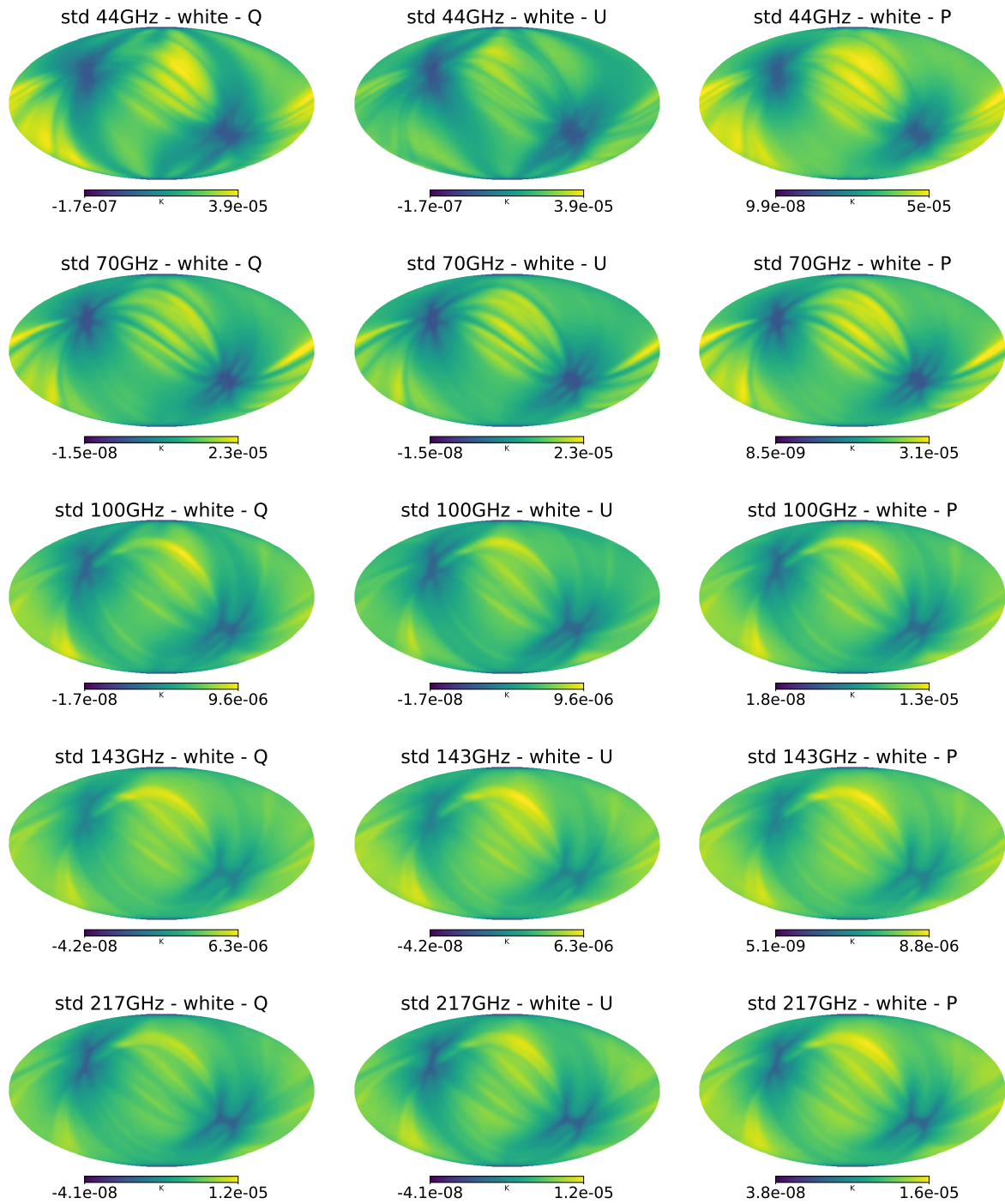


Figure 4.13: White noise simulations standard deviation of the residuals Q and U Stokes components as well as total power.

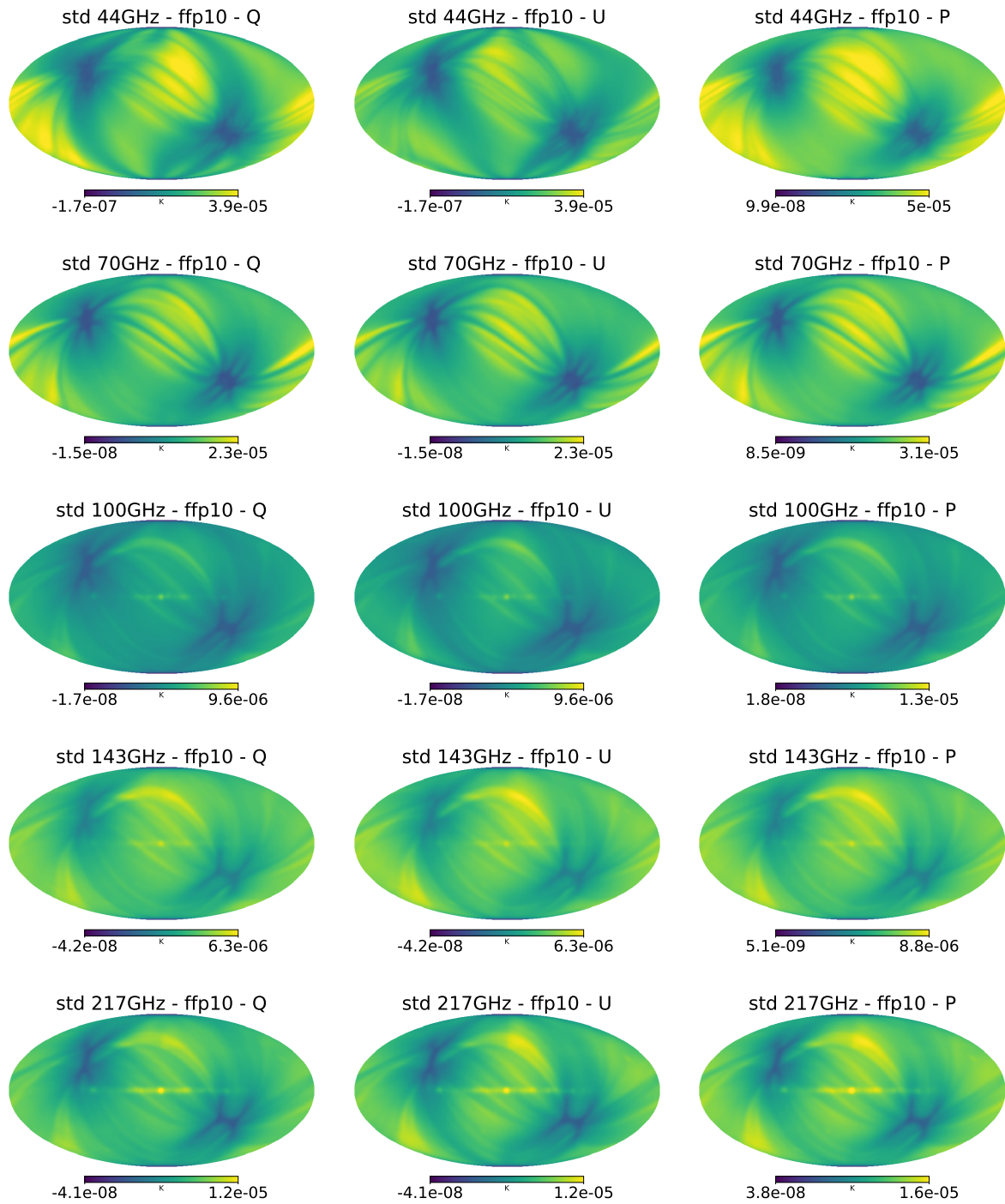


Figure 4.14: FFP10 noise simulations standard deviation of the residuals Q and U Stokes components as well as total power.

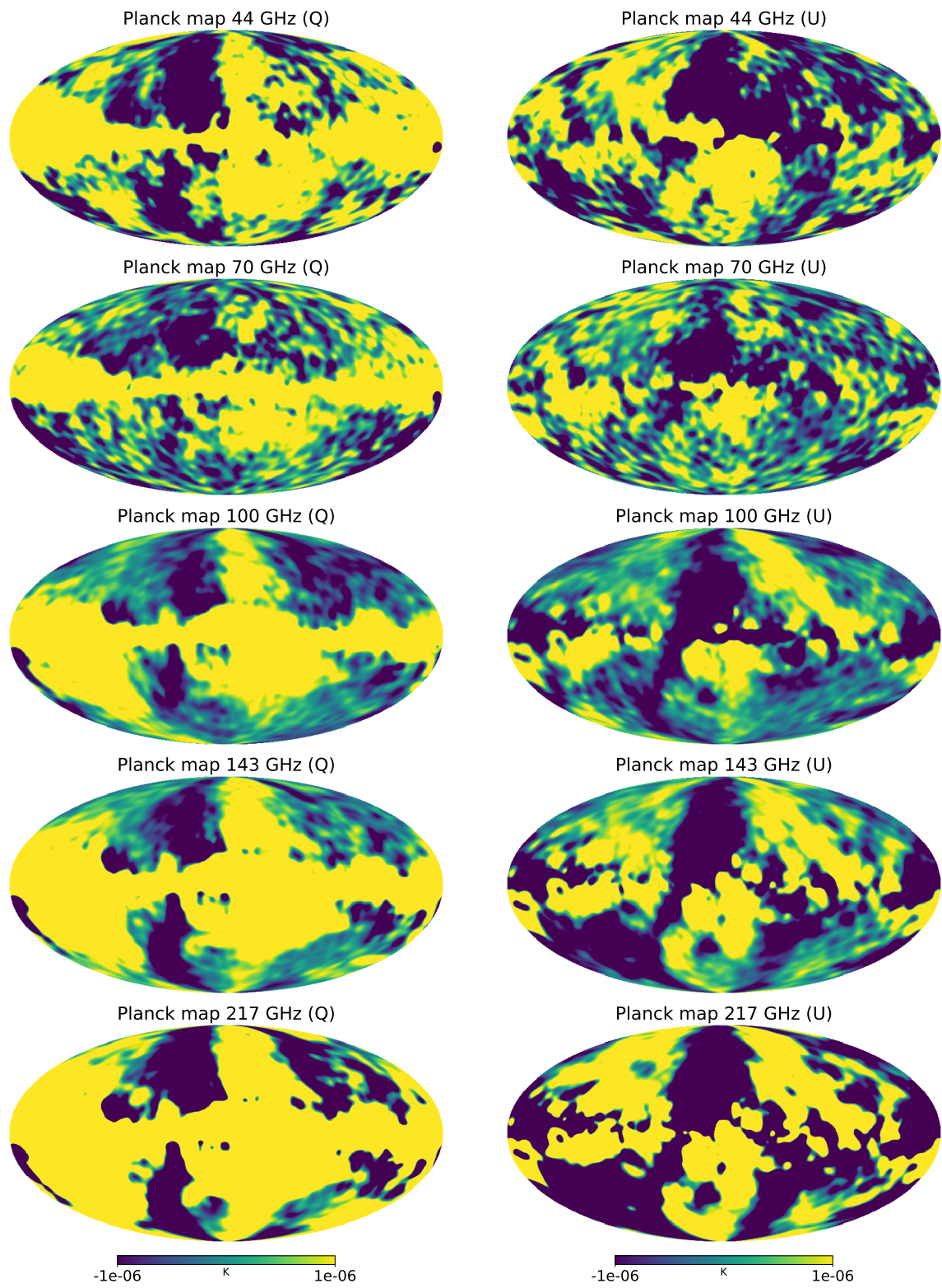


Figure 4.15: Public *Planck* polarisation maps smoothed with a 5° Gaussian beam.

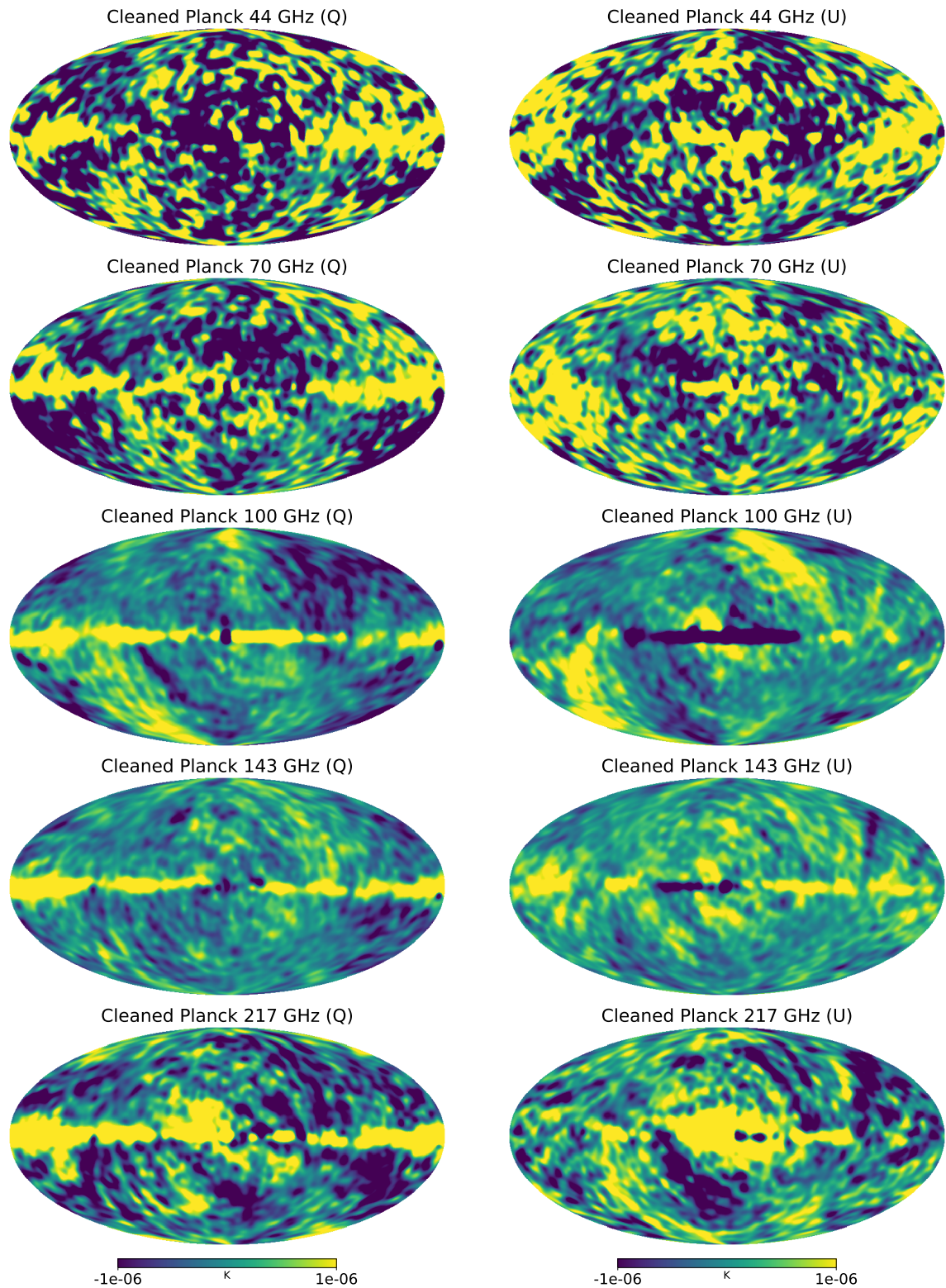


Figure 4.16: Public *Planck* polarisation maps cleaned from foreground contaminations using one global coefficient estimated with the MLE estimator on 70% of the sky.

5 Polarisation power spectra

In this section, we compute the power spectra from the cleaned public *Planck* polarised maps derived in the previous section. The resulting CMB estimates are then fed to the **xQML** estimator described in Sec. 5 of chapter 3.

Using the full missions intermediate channels allows us to compute $n_{\text{cross}} = n_{\text{freq}}(n_{\text{freq}} - 1)/2 = 10$ cross-spectra, with $n_{\text{freq}} = 5$ the number of intermediate channels. Using the half-missions datasets would provide $n_{\text{cross}} = (2n_{\text{freq}})(2n_{\text{freq}} - 1)/2 = 45$ distinct estimates. In the rest of the analysis, we focus on the full-missions results only.

5.1 Pixel covariance matrices

The **xQML** spectrum estimator takes the following datasets pixel covariance matrices as input :

- $\mathbf{S}(\tilde{C}_\ell)$, the CMB pixel covariance matrix.
- $\mathbf{C}^{AA} = \mathbf{S} + \mathbf{N}^A$, the pixel covariance matrix of the dataset A , with \mathbf{N}^A its noise covariance matrix.
- $\mathbf{C}^{BB} = \mathbf{S} + \mathbf{N}^B$, similarly for the dataset B .

To estimate $\mathbf{S}(\tilde{C}_\ell)$, we use a fiducial spectrum \tilde{C}_ℓ generated with CAMB with *Planck* best-fit parameters, a reionization depth $\tau = 0.06$, and no tensor-to-scalar ratio, $r = 0$.

We use the FFP10 noise simulations to build the matrices \mathbf{N}^A and \mathbf{N}^B when estimating *Planck* power spectra. Because the number of simulations (300) is relatively low compared to the size of the matrix ($N_{\text{pix}} \sim 4000$), we cannot estimate the full pixel-pixel correlation. Therefore, we only estimate the diagonal entries of \mathbf{N} , computed from the variance of the FFP10 noise simulations. This is a valid approximation since we showed in chapter 3 that the estimator is not biased regardless of the construction of the pixel covariance matrix. Moreover, any deviation of the fiducial noise from its true value used to build the matrices \mathbf{N} is shown to impact the variance of the spectrum estimation only at second order. We verified that using the white-noise levels to build \mathbf{N}^A and \mathbf{N}^B does not significantly change the results.

5.2 Full mission simulations

We first test our full pipeline on simulations. We start from 300 white or FFP10 noise simulations combined with the PySM foreground sky, to which we apply the cleaning method using the MLE method, and finally the **xQML** spectrum estimator.

We compute the resulting mean spectrum estimates and residuals. For each noise type we also estimate the spectra on simulations for which we do not include the foreground signal while still performing the cleaning process. Those foreground-less simulations allows us to identify if the source of any bias is due to the foreground residuals or the noise systematics.

The residual spectrum is defined as

$$R_\ell[\hat{C}_\ell] \equiv \frac{C_\ell - \langle \hat{C}_\ell \rangle}{\sqrt{\sigma^2(\hat{C}_\ell^{\text{MC}})/n_{\text{MC}}}}, \quad (4.10)$$

with C_ℓ the spectrum model, and n_{MC} the number of Monte-Carlo simulations. If no bias is present in the estimated spectrum \hat{C}_ℓ , the residuals are expected to be Gaussian distributed, with unit width and mean zero. In the following plots, this 3σ limit is indicated by a grey band.

White noise

The results for the full white noise missions are shown in Fig. 4.17. For a sky fraction $f_{sky} = 0.5$, the residual spectra R_ℓ indicate some bias for the 143x217. Those are produced by the foregrounds residuals as they disappear as soon as we remove the foreground signal from the simulations, as shown in Fig. 4.18 for the foreground-less simulations. Additional residuals show up for the 100x217, and 100x143 cross-spectra when considering larger sky fractions. The residuals on the EE spectrum are mainly present where the CMB signal is the lowest ($5 \lesssim \ell \lesssim 25$). The BB residuals are seen almost on the whole range of multipoles for the 143x217 spectra, and they are particularly high on the largest scales ($\ell \lesssim 5$). As expected, the level of the residuals increases as a larger sky coverage is considered. We remark that all those residuals produce upward bias on the spectrum estimation.

FFP10 noise

The results for the full FFP10 noise missions are shown in Fig. 4.19. On Fig. 4.20 we show the results for the foreground-less case only. When no foreground signal is include, we still observe some residuals for the 143x217, 100x217, and 100x143 cross-spectra. The large scales are the most contaminated, at $\ell \lesssim 15$ for the EE spectrum, and $\ell \lesssim 5$ for the BB spectrum. Those source of bias are therefore a consequence of the systematic errors present in the FFP10 simulations. When including the foreground signal, additional residuals caused by the foreground contaminations are observed. Those are similar to the white-noise case, and they add to the systematic errors observed on foreground-less simulations.

For the foreground-less simulations, we remark that some systematic residuals do not evolves with the change of the sky fraction considered. For example, this is visible on the BB residual spectrum which are systematically present on the $\ell = 2$ multipole for the 143x217 and 100x143. A similar observation is made on the $\ell = 4$ BB multipole for the 143x217, 100x143 and 100x217 spectra. We note that the systematic residuals can produce both upward and downward bias on the spectrum estimations.

Spectrum variance

In addition, we display the uncertainty for each cross-spectra in Fig. 4.21. As expected, the spectra estimation involving the 44 GHz channel are the noisiest. The 100x143 is the estimation with the less uncertainty, followed by 143x217 and 100x217, then by 70x143 and 70x100.

5.3 Planck data

The spectra estimations on *Planck* data for the full missions are displayed in Fig. 4.22 for $f_{fsky} = 0.5$ and $f_{fsky} = 0.8$. We removed the 44 GHz to improve the clarity of the plot, as the related power spectra have much more variance than the others. The spectra residuals are shown in Fig. 4.23. We also display the cosmic variance in shaded using a fiducial cosmology with $\tau = 0.06$ and $r = 0$. The residuals are computed using the same fiducial spectrum as for our simulations. We observe no significant departure of the residuals.

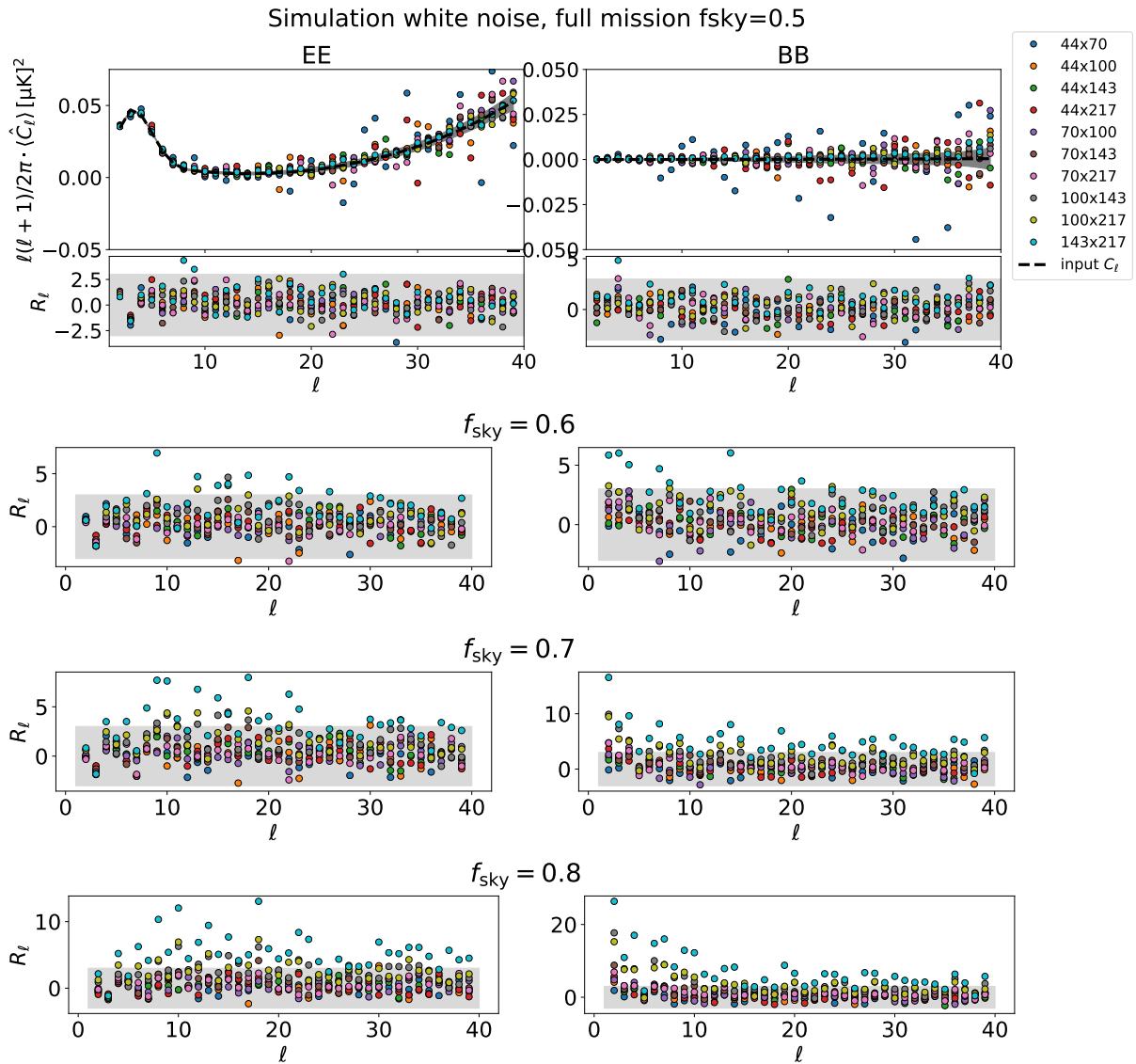


Figure 4.17: Spectrum estimation and residual from white noise full mission simulations.

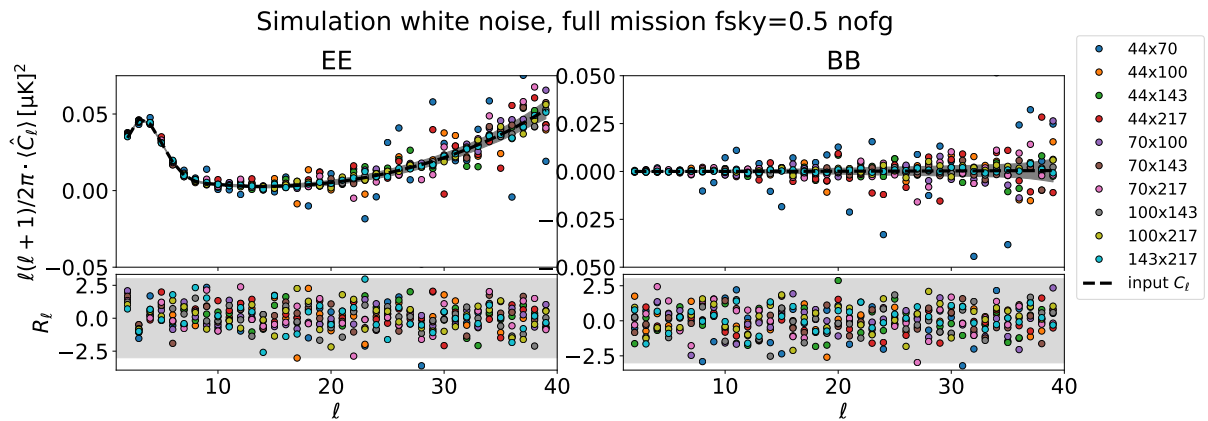


Figure 4.18: Spectrum estimation and residual from white noise full mission simulations with no foreground contamination.

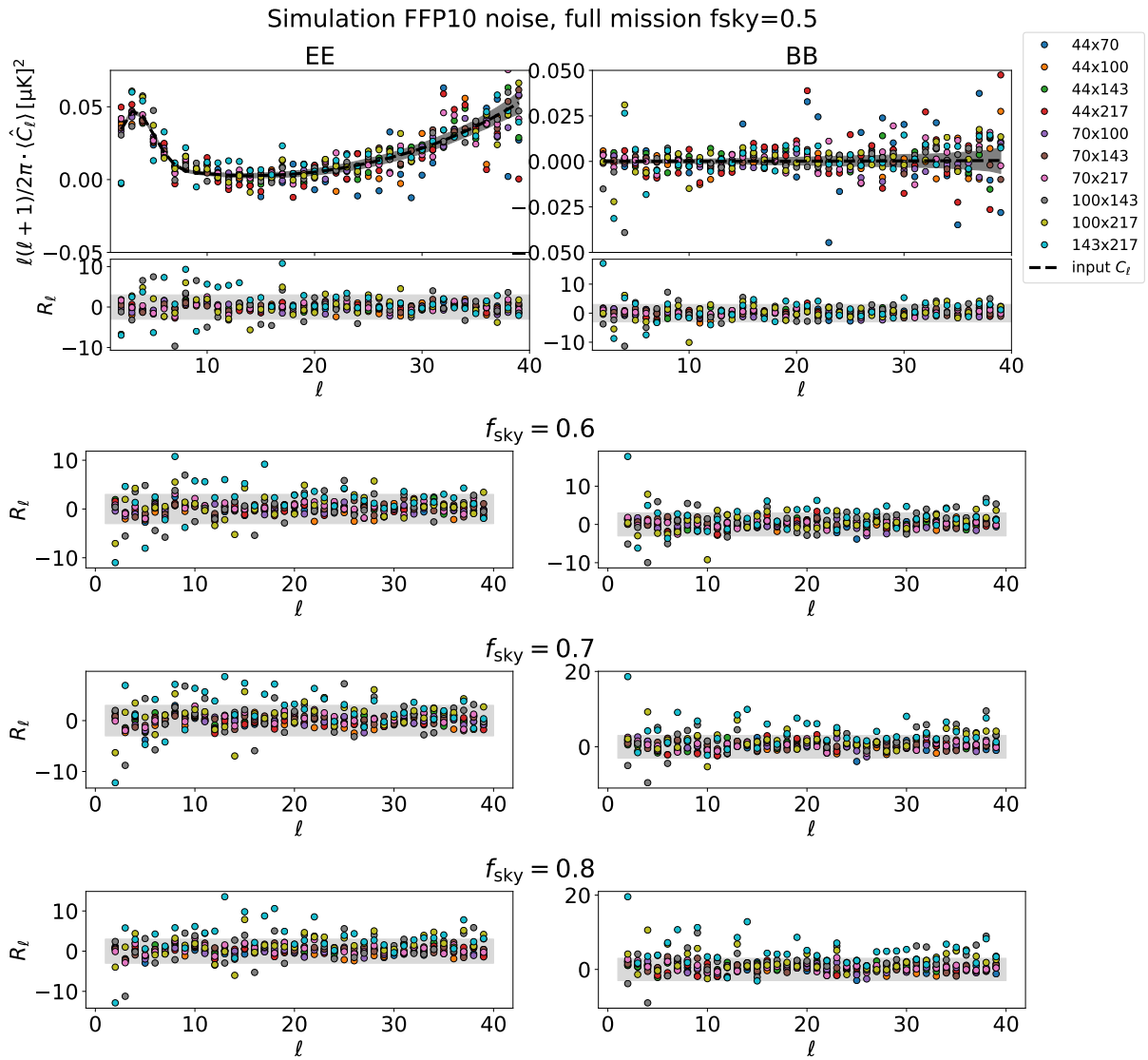


Figure 4.19: Spectrum estimation and residual from FFP10 noise full mission simulations.

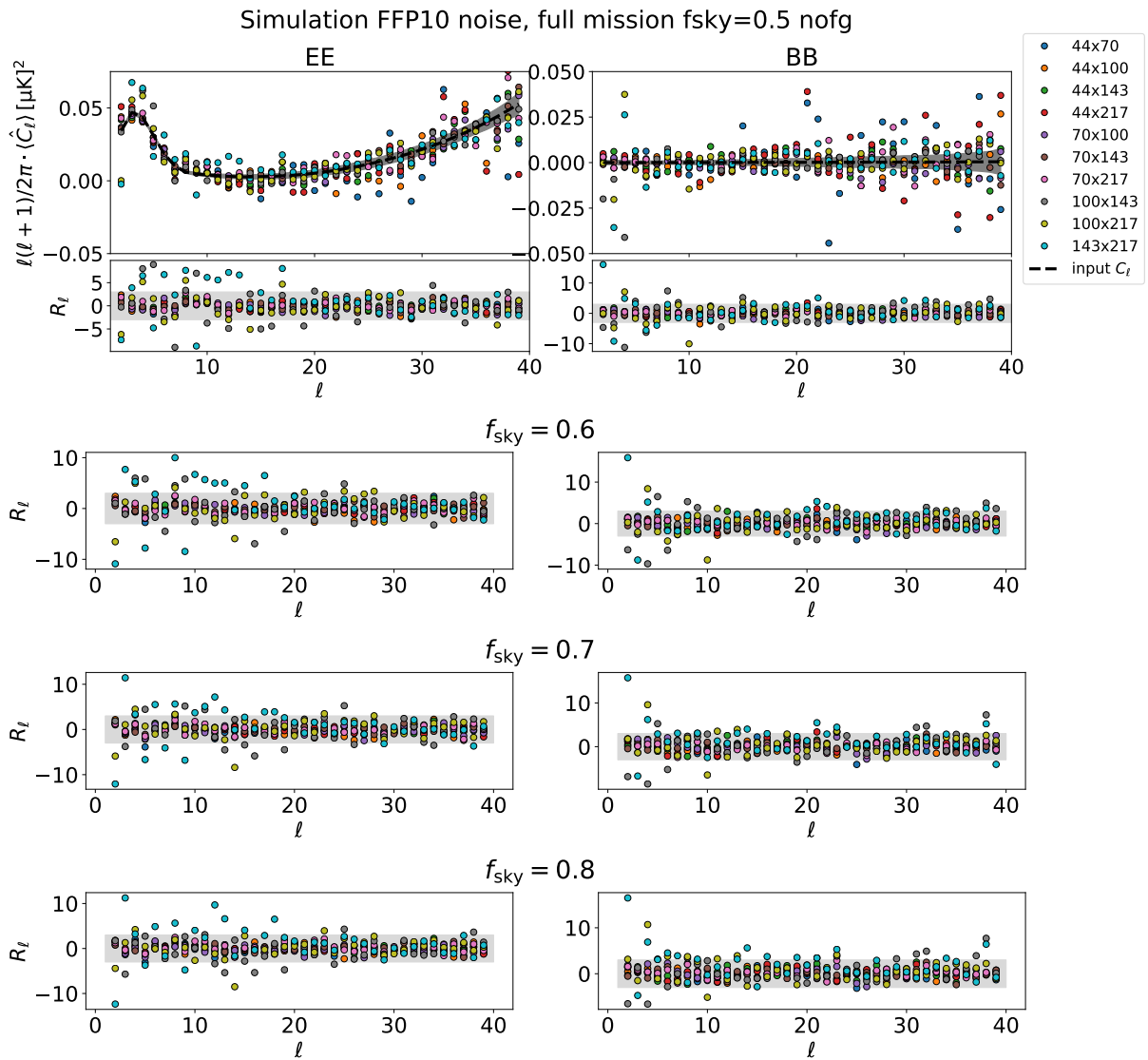


Figure 4.20: Spectra estimation from FFP10 full mission simulations with no foreground signal. We also show the residuals for each sky fraction.

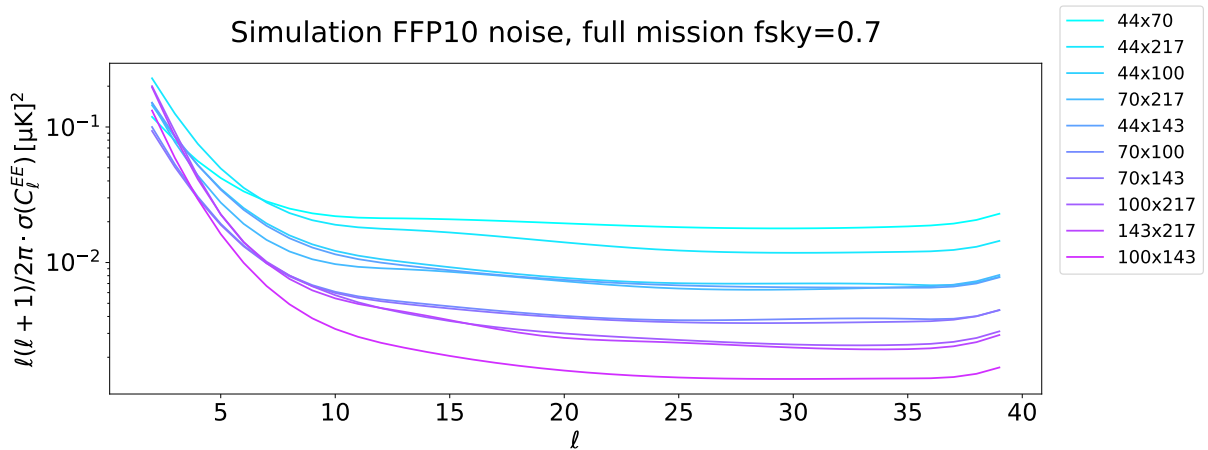


Figure 4.21: Spectrum MC uncertainties for the full mission simulations, on 70% of the sky.

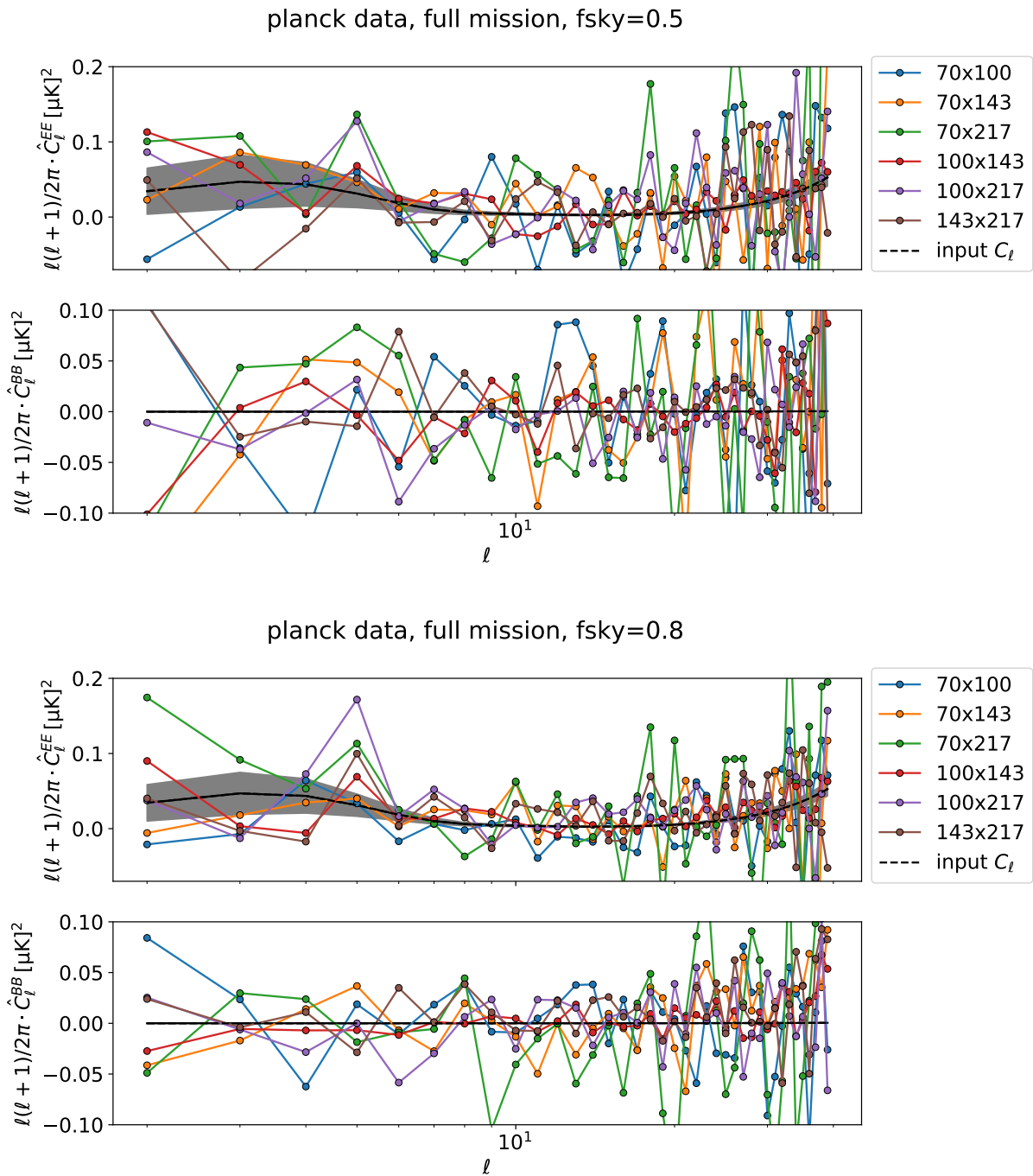


Figure 4.22: Spectrum estimation on *Planck* full mission datasets. The ‘input’ model correspond to the best fit, and the model used for the MC simulations validation tests.

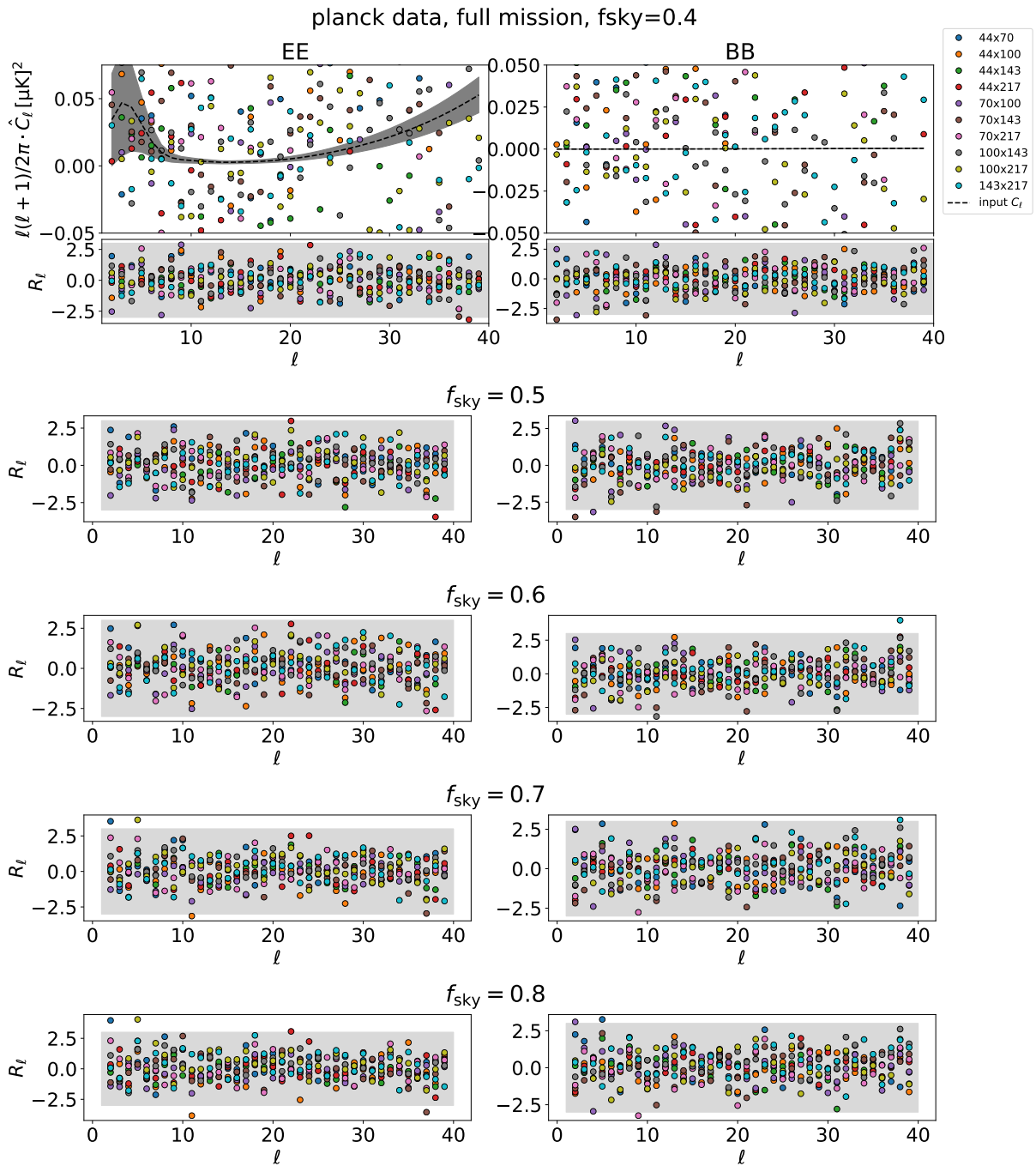


Figure 4.23: Spectrum estimation on *Planck* full mission datasets. The ‘input’ model correspond to the best fit, and the model used for the MC simulations validation tests.

6 Cosmological parameters likelihood

6.1 Large angular scale Likelihood

The Low- ℓ Likelihood on Polarized Power-spectra, **Lollipop**, is a cross power spectrum analysis approach for large angular scales (Mangilli et al. 2015). The methodology is based on a modification of the Hamimeche&Lewis (H&L) Likelihood developed in the context of large-angular scale measurement with auto power spectra (Hamimeche et al. 2008).

Generally, the estimation of the cosmological parameters on large scales data can either follow a pixels based or a harmonic approach. Since the CMB anisotropies are expected to be Gaussian, the likelihood function can be computed exactly in the pixel domain (K M Gorski et al. 1994; Page et al. 2007; Slosar et al. 2004; Bennett et al. 2013). As they work in pixel-space, those methods show two inconveniences: they can be computationally costly, and they do not allow for cross-correlations between datasets. The latter limitation therefore requires a precise estimate of the dataset noise in order to avoid any spurious bias when estimating the cosmological parameters. The harmonic approach do not suffers from any of those two limitations. However, the distribution of the power spectrum coefficients C_ℓ is non-Gaussian at low ℓ 's, and they are correlated between multipoles when accounting for reduced sky fractions. Studies such as Percival et al. 2006; Hamimeche et al. 2008 allow to model the non-Gaussianity of the C_ℓ at large angular scale for auto-spectra only, and they therefore share the same problem as the pixel-base approach for the noise bias. The **Lollipop** approach precisely fills this gap by extending the harmonic H&L likelihood to cross-spectra analysis.

Lollipop formalism

Following the notation in Mangilli et al. 2015, the log-likelihood function reads

$$-2\mathcal{L}(C_\ell|\hat{C}_\ell) = X_\ell^T [K^{-1}]_{\ell\ell'} X_{\ell'}, \quad (4.11)$$

where $C_\ell = C_\ell^{\text{model}}$ is the power spectrum model, and \hat{C}_ℓ its estimation from the data. The matrix $K_{\ell\ell'}$ encodes the covariance of the spectrum \hat{C}_ℓ . The vector

$$X_\ell \equiv \text{Vecp} \left[[\tilde{\mathbf{C}}^{1/2}]_\ell \mathbf{U}_\ell \mathbf{g}(\mathbf{D}_\ell) \mathbf{U}_\ell^T [\tilde{\mathbf{C}}^{1/2}]_\ell \right], \quad (4.12)$$

is a transformation of the spectrum estimation \hat{C}_ℓ such that X_ℓ follows a Gaussian distribution. The matrix

$$\tilde{\mathbf{C}}_\ell = \begin{pmatrix} \tilde{C}_\ell^{TT} & \tilde{C}_\ell^{TE} & \tilde{C}_\ell^{TB} \\ \tilde{C}_\ell^{TE} & \tilde{C}_\ell^{EE} & \tilde{C}_\ell^{EB} \\ \tilde{C}_\ell^{TB} & \tilde{C}_\ell^{EB} & \tilde{C}_\ell^{BB} \end{pmatrix}, \quad (4.13)$$

is built from a fiducial spectrum \tilde{C}_ℓ . Similarly, the matrix \mathbf{C}_ℓ is built from the spectrum model C_ℓ . The matrix $\mathbf{Q}_\ell \equiv \mathbf{C}_\ell^{-1/2} \hat{\mathbf{C}}_\ell \mathbf{C}_\ell^{-1/2}$ include the data spectra \hat{C}_ℓ , and is decomposed as $\mathbf{Q}_\ell = \mathbf{U}_\ell \mathbf{D}_\ell \mathbf{U}_\ell^T$, for an orthogonal matrix \mathbf{U}_ℓ and a diagonal matrix \mathbf{D}_ℓ whose entries are the eigenvalues of \mathbf{Q}_ℓ . In Eq. (4.12), the transformation

$$\mathbf{g}(\mathbf{D}_\ell) = \text{sign}(\mathbf{D}_\ell - \mathbf{1}) \sqrt{2(\mathbf{D}_\ell - \ln(\mathbf{D}_\ell) - \mathbf{1})}, \quad (4.14)$$

is applied to the eigenvalues of the matrix $\mathbf{Q}_\ell(\hat{C}_\ell)$. Finally, the operator $\text{Vecp}[\mathbf{Y}]$ vectorizes the distinct elements of any symmetric matrix \mathbf{Y} .

For example, $\text{Vecp}[\tilde{\mathbf{C}}_\ell] = (\tilde{C}_\ell^{TT}, \tilde{C}_\ell^{EE}, \tilde{C}_\ell^{BB}, \tilde{C}_\ell^{TE}, \tilde{C}_\ell^{TB}, \tilde{C}_\ell^{EB})$.

Offset

In the context of auto-spectra, the estimated spectrum has two contributions: the CMB signal and the noise, $\langle \hat{C}_\ell \rangle = C_\ell + N_\ell$. For cross-spectra the second term vanishes on average, and $\langle \hat{C}_\ell^{AB} \rangle = C_\ell$ for two datasets A and B . In that case, the estimated spectrum can show negative values. The matrix \mathbf{Q}_ℓ is therefore not guaranteed to be positive definite. Mangilli et al. 2015 propose to modify the matrices \mathbf{C}_ℓ , $\tilde{\mathbf{C}}_\ell$, and $\hat{\mathbf{C}}_\ell$, by adding an offset diagonal matrix $\mathbf{o}_\ell \equiv \text{diag}(o_\ell^{TT}, o_\ell^{EE}, o_\ell^{BB})$. The function defined in Eq. (4.14) must also be modified to regularise the likelihood function around zero, with $\mathbf{g}(\mathbf{D}_\ell) \rightarrow \text{sign}(\mathbf{D}_\ell) \mathbf{g}(\text{abs}(\mathbf{D}_\ell))$.

The offset can be chosen in order to mimic the noise bias present in auto-spectrum statistics. Writing the spectrum variance as

$$V_{\ell\ell}^{AB}(C_\ell, N_\ell^A, N_\ell^B) = \frac{1}{2\ell + 1} [2C_\ell^2 + C_\ell(N_\ell^A + N_\ell^B) + N_\ell^A N_\ell^B], \quad (4.15)$$

the effective noise offset is derived as

$$o_\ell = \sqrt{(2\ell + 1)V_{\ell\ell}^{AB}(C_\ell = 0)} \quad (4.16)$$

$$= \sqrt{N_\ell^A N_\ell^B}. \quad (4.17)$$

The offset can be computed using analytical estimate of the spectrum uncertainty, or Monte-Carlo simulations.

Polarisation leakage

We have found that in the case of likelihood analysis on polarisation spectra, the variance leakage also plays an important role in the offset construction. Indeed, the variance leakage is an additional source of uncertainty for the spectrum estimation. This observation especially concerns the B-modes analysis, for which the E-to-B leakage can significantly impact the large-scale variance, even if it is minimized by the use of the xQML estimator.

In the context of B-modes spectrum estimations using the xQML method, the offset can be derived analytically computing Eq. (4.16) from Eq. (3.58) and using a fiducial CMB spectrum C_ℓ with non-zero E-modes and vanishing B-modes. With that choice, we assure that the spectrum variance calculated includes the contribution from both the noise and the E-to-B variance leakage.

An other approach is to use Monte-Carlo simulations where the CMB signal is generated with a fiducial CMB spectrum with null B-modes signal. This solution allows us to propagate the additional uncertainties, coming for example from the foreground cleaning, and impacting the variance of the spectrum estimation.

We follow this latter approach for *Planck* data analysis. In this context, the variance leakage is completely overwhelmed by the instrumental noise and the foreground cleaning uncertainty. In order to fully propagate those errors and compute the offset, we therefore compute the spectra variance on our set of simulations from which we removed the totality of the CMB signal.

6.2 Results on individual cross-spectrum

We first discuss the results when applying the Lollipop approach on each cross-spectrum. This step of the analysis allows us to characterise the behaviour of the posteriors depending on which type of noise is included in the simulations. Firstly, we sample the likelihood by varying the reionization parameter τ and using the EE spectra data. In a second time, we sample for the tensor-to-scalar ratio r , using the B-modes signal. All results are provided with a 68% confidence level (C.L.). All other Λ CDM parameters are fixed to *Planck* best fit value (Planck Collaboration et al. 2018d).

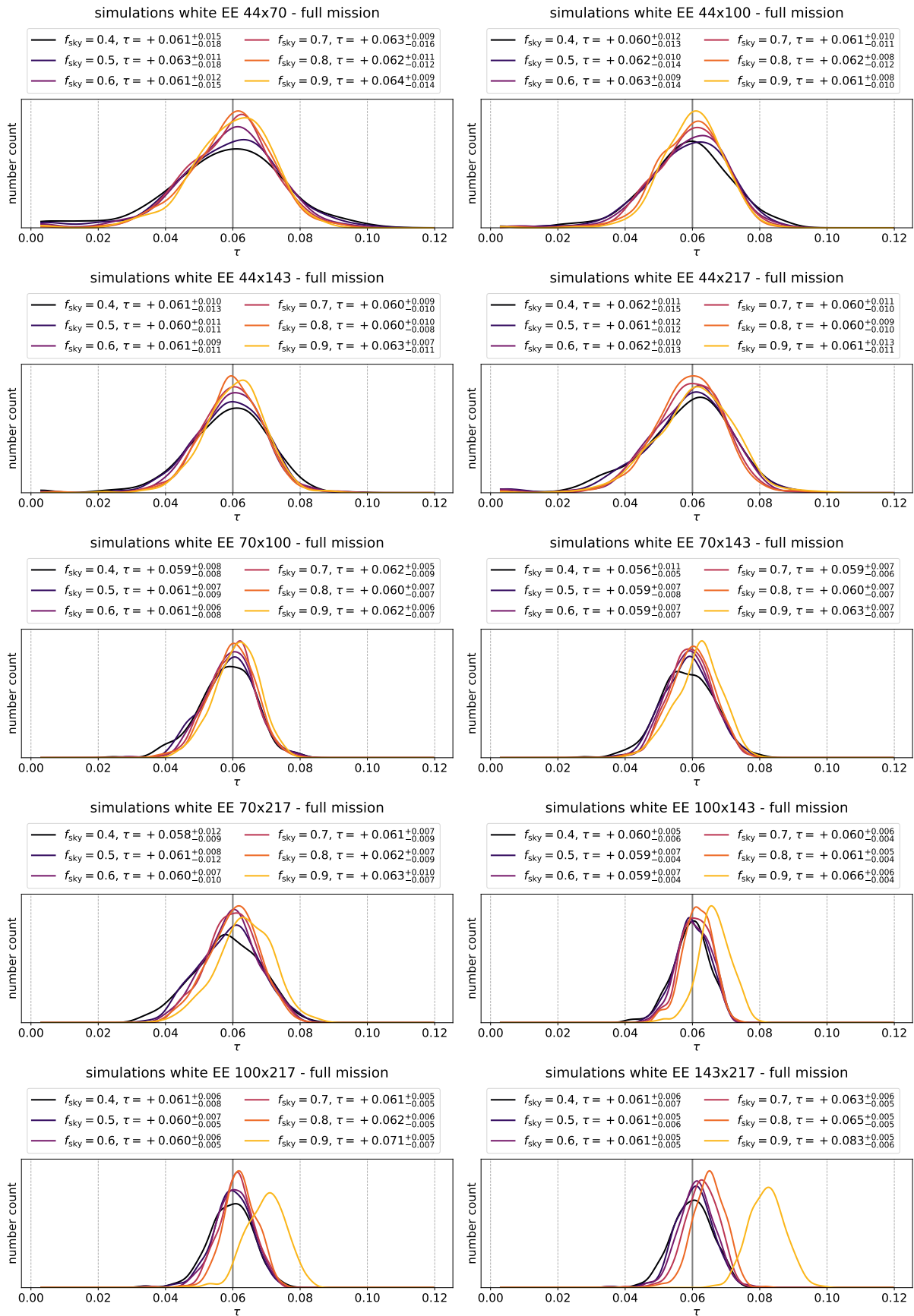
Reionization parameter from E-modes

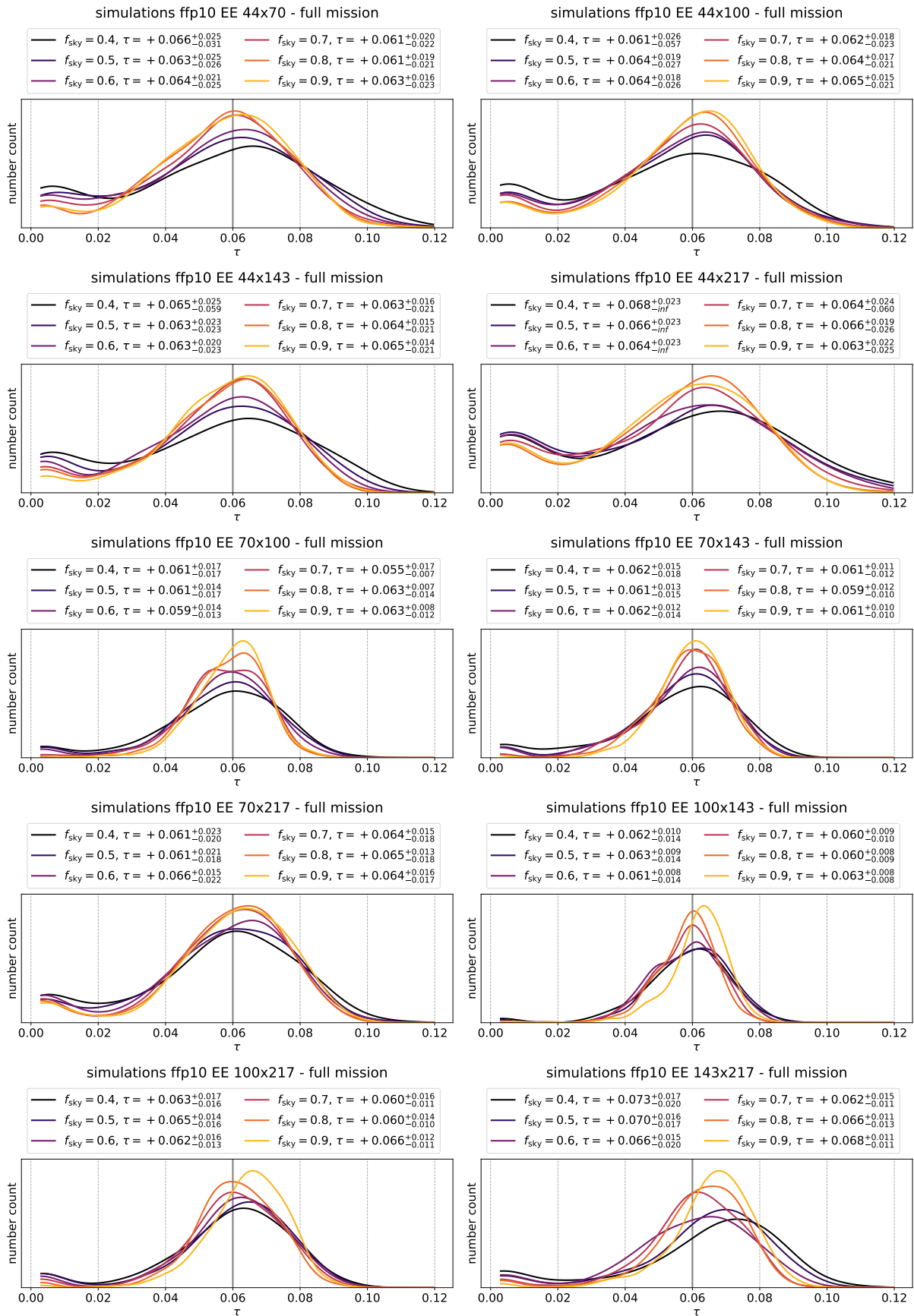
We first present the results of the analysis using the E-modes signal from the full missions to constrain the reionization parameter τ . We sample the likelihood function by varying the parameter τ used to build the theoretical power spectrum C_ℓ^{EE} , and fixing the tensor-to-scalar ratio to $r = 0$. We consider the signal over the multipole range $2 \leq \ell < 20$.

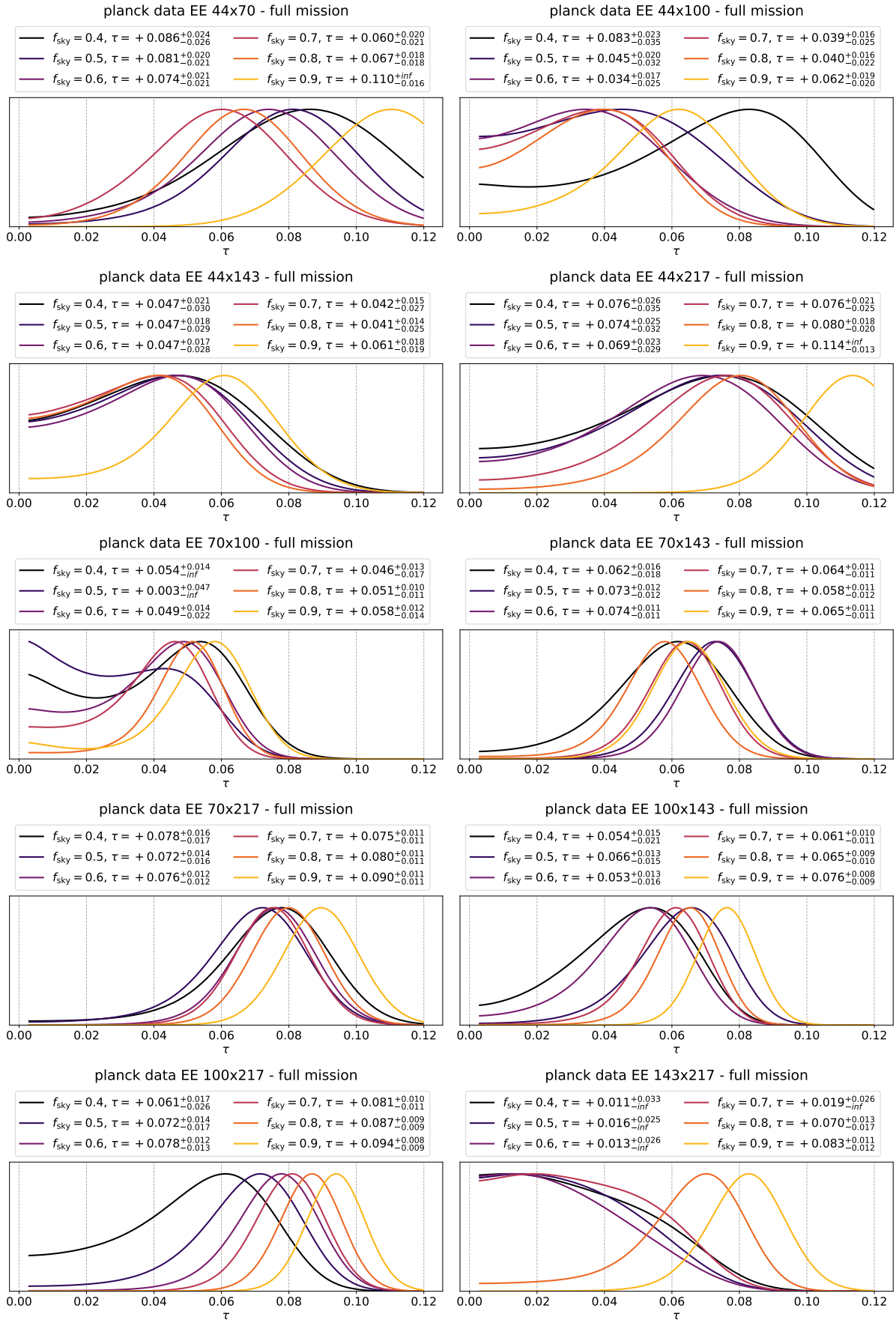
The distribution of the posterior maximum for the white noise simulations are shown in Fig. 4.24 for each cross-spectra. There is a clear bias for the 100x143, 100x217 and 143x217 when increasing the observed sky fraction ($f_{sky} \geq 0.7$). Those are in accordance with the residual foreground contaminations observed for those three cross-spectra and discussed in the previous section. Those were observed to drive the EE spectra upward, as a consequence favouring high values of τ in the likelihood. The most important bias occurs for the 143x217 distribution, with a mean estimation of $\tau = 0.065 \pm 0.005$.

Similarly, the distribution of the posterior maximum for the FFP10 noise simulations are shown in Fig. 4.25. As expected, the dispersion are larger than for the white-noise case, as those simulations account for additional systematic instrumental effects. Compared to the white noise case, we observe a deformation of the maximums distributions that drives the estimation of τ toward zero for some simulations. Those are particularly visible on the 44x70, 44x100, 44x143, 44x217, and 70x217. Those ‘low- τ bumps’ tend to decrease when sensitivity increase, when accounting for larger sky fraction for example.

Finally, we evaluate the posteriors on the *Planck* data. Those are shown in Fig. 4.26. We notice that the 70x100 and 143x217 posteriors are driving the τ parameter toward zero when small sky fractions are considered, $f_{sky} \leq 0.5$ for the 70x100, and $f_{sky} \leq 0.7$ for the 143x217. The position of the 44x143 posterior favours relatively low values of τ compared to the others, but remains stable with the change of sky coverage. This is not the case for the 44x100, for which the posterior at $f_{sky} = 0.4$ is shifted toward higher value of τ than for the remaining sky fractions. For the other cross-spectra, we observe a general behaviour where the posteriors systematically shift toward higher value of τ as larger sky fractions are considered. For example, we observe that the posterior for the 100x217 cross-spectra moves toward high values of τ as we decrease the surface of the masked regions. This behaviour can typically be induced by the presence of additional foreground residuals as we change the pixel masking.

Figure 4.24: White noise distribution of the posterior maximums for τ .



Figure 4.26: Planck data posteriors for the reionization parameter τ .

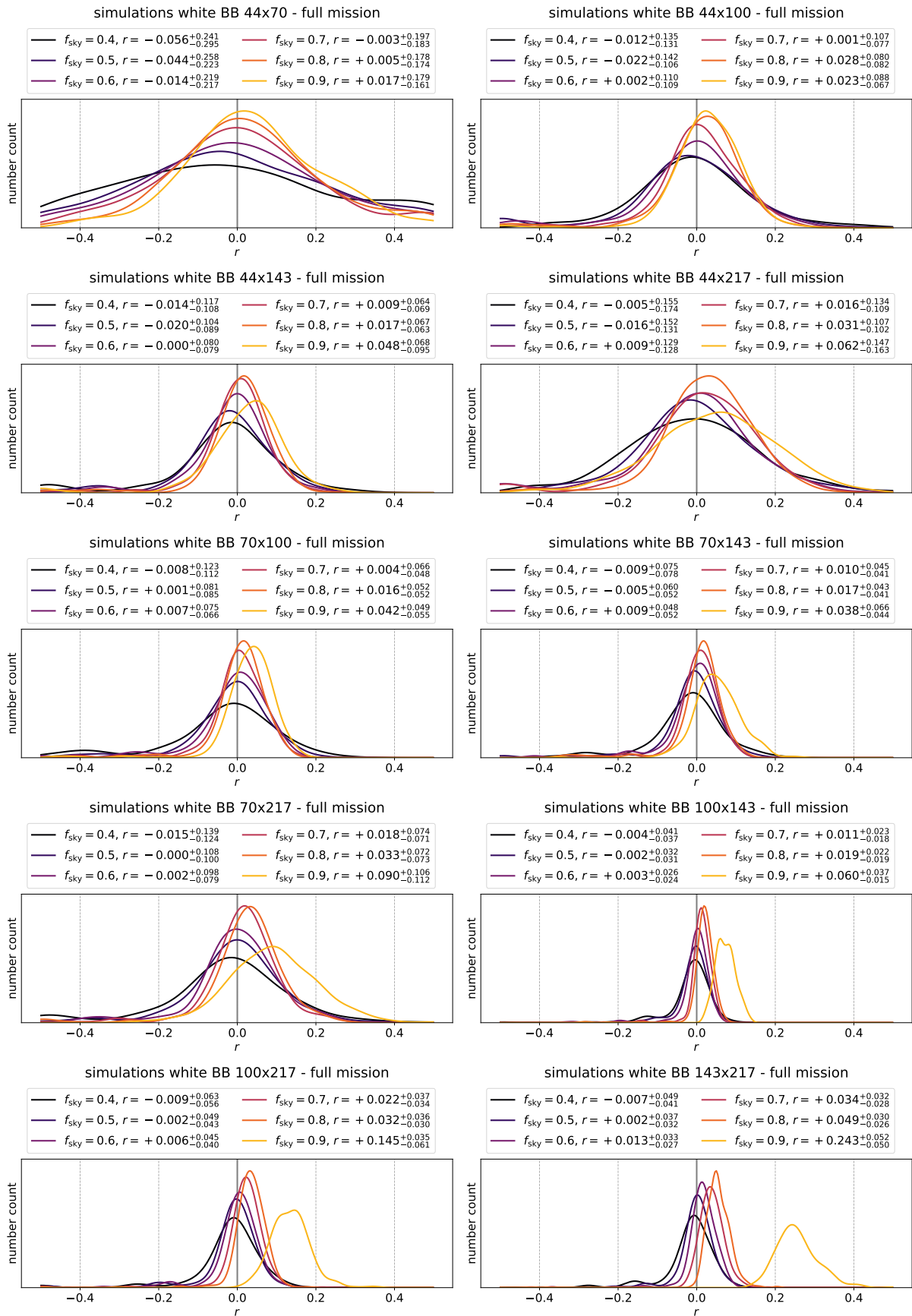
Tensor-to-scalar ratio from B-modes

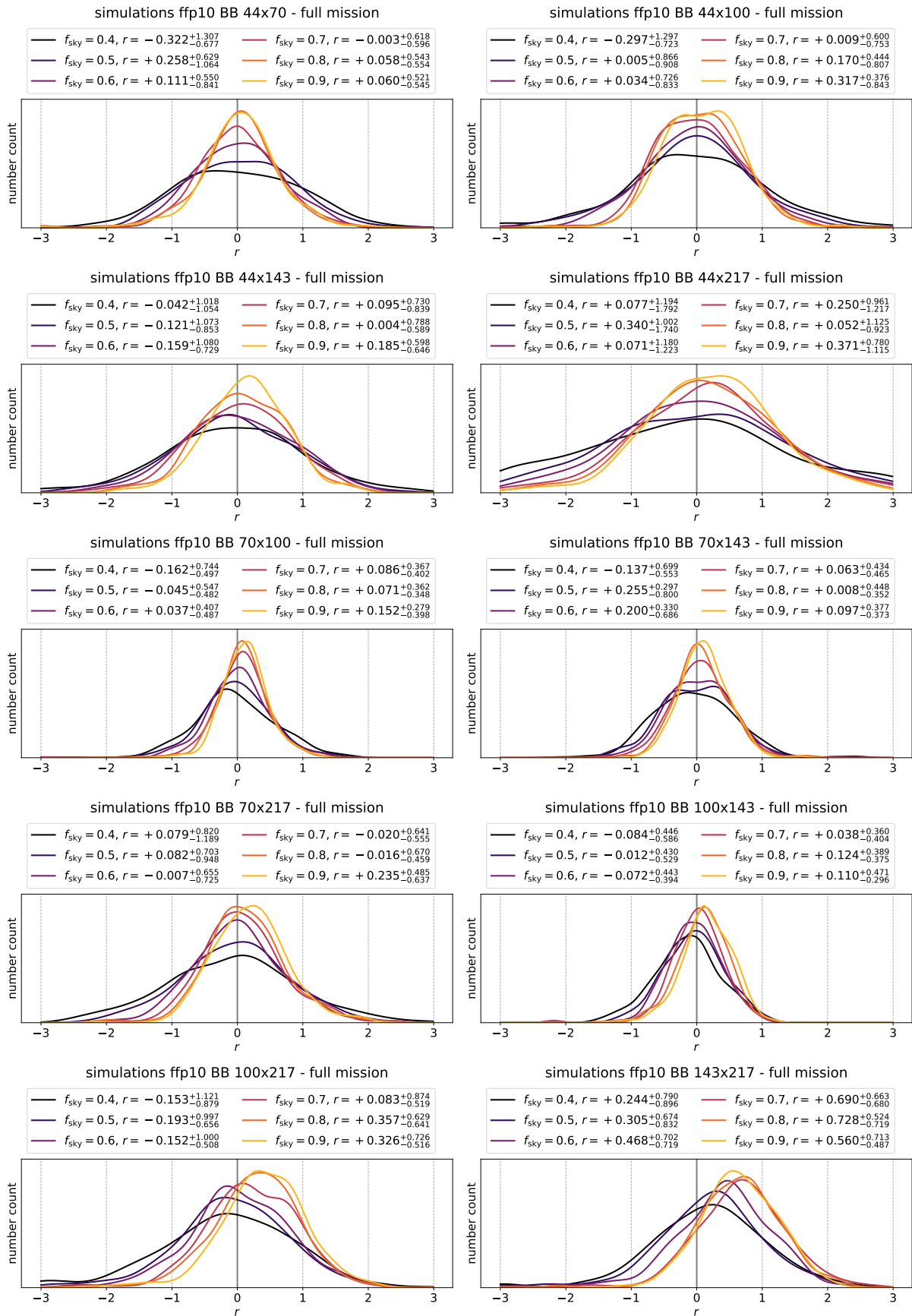
We estimate the parameter r from the B-modes cross-spectra. We fix the reionization parameter to $\tau = 0.06$ in our spectrum model, and consider the signal over the multipoles range $2 \leq \ell < 20$.

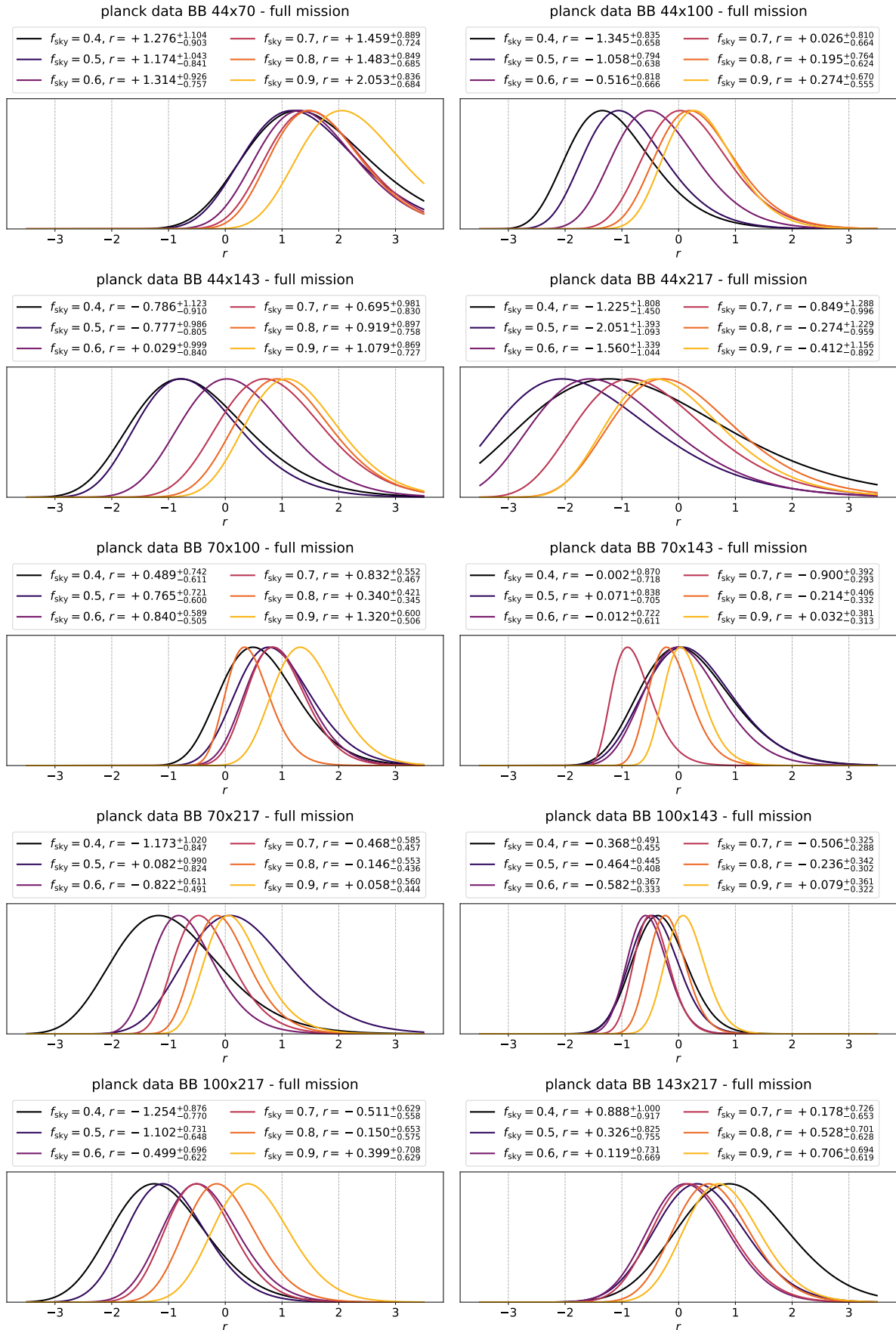
The distribution of the posterior maximums for the white noise simulations are shown in Fig. 4.27. They are relatively stable with the change of the sky coverage. We observe a small but systematic shift of the distributions as a larger sky fraction is included, which is induced by the foreground residuals.

Compared to the white noise case, we sample the likelihood over a wider range of r for the FFP10 simulations. The results, shown in Fig. 4.28, are similar to the white noise case, apart for the uncertainties which are globally larger. The error-bars of the 100x143 at $f_{\text{sky}} = 0.5$ are of the order of $\sigma_r \approx 0.032$ for the white-noise simulations, while they reach $\sigma_r \approx 0.45$ when including the FFP10 simulations.

The posteriors for the *Planck* data are shown in Fig. 4.29. As the sky coverage is increased, the posterior are systematically shifted toward high values of r for almost all crosses, which could be an indication that some foreground residuals are present when the masked regions is too small. The most stable results against the change of sky coverage under $f_{\text{sky}} \leq 0.6$ are provided by the 44x70, 100x143, and the 70x143.

Figure 4.27: White noise distribution of the posterior maximums for r .

Figure 4.28: FFP10 noise distribution of the posterior maximums for r .

Figure 4.29: Planck data posteriors for r using B-modes cross-spectra.

6.3 Combined cross-spectra

Cross-spectra correlation

In order to further constrain the cosmological parameters, we combine the different cross-spectra into the likelihood. The spectrum vector \hat{C}_ℓ used in the likelihood function defined in Eq. (4.11) is therefore a joint combination of all the cross-spectra that we have estimated. In that case, the cross-spectra covariance matrix $K_{\ell\ell'}$ is of size $n_{\text{cross}}n_{\text{bin}} \times n_{\text{cross}}n_{\text{bin}}$, with n_{bin} the number of multipoles considered. For the rest of our analysis, we consider two combination of datasets: either we include all available channels from 44 to 217 GHz ($n_{\text{cross}} = 10$), or we select the 70, 100, and 143GHz channels only ($n_{\text{cross}} = 3$). The former configuration is labelled **a11**, while the latter configuration, labelled **no44+217**, is motivated by the high level of noise and possibly high level of contamination residuals from the foreground signals for those two extreme channels. For our baseline analysis, we consider the multipole range $\ell \in [2, 20]$.

The correlation matrices $\text{Corr}[K_{\ell\ell'}]$ estimated from the FFP10 simulations are displayed in Fig. 4.30 for the E and B modes. We observe a correlation between the multipoles across the different EE spectra, and relatively low correlations between neighbouring ℓ 's. In contrast, the correlation between neighbouring multipoles is more pronounced for the BB spectra, particularly at low ℓ 's and for the spectra involving high frequency channels. We refer for example to the 100x217.

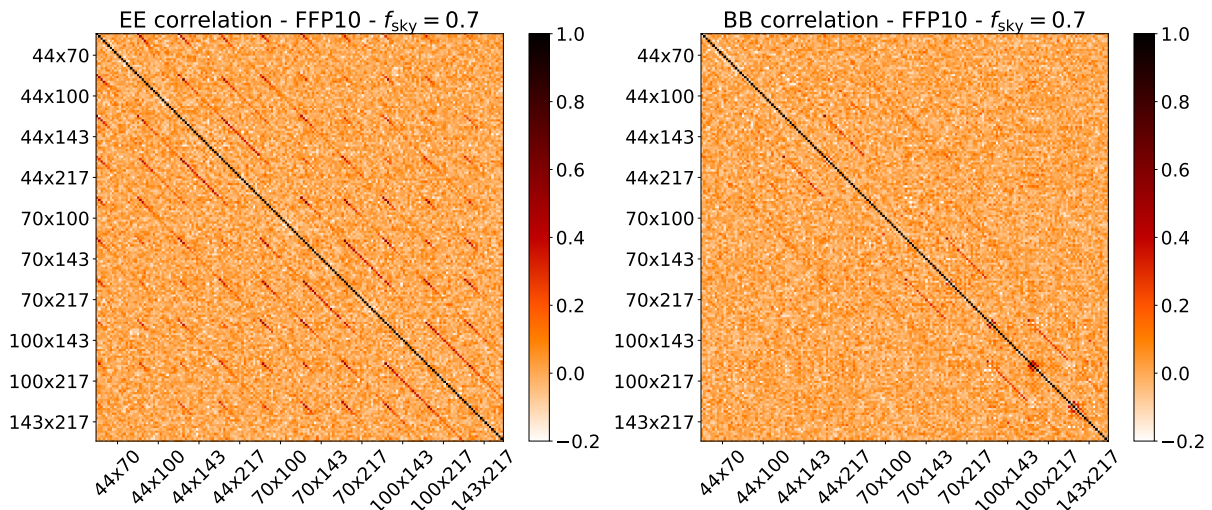


Figure 4.30: EE and BB cross-spectra correlation matrices $\text{Corr}[K_{\ell\ell'}]$ based on FFP10 MC simulations for $f_{\text{sky}} = 0.7$ and $\ell \in [2, 20]$.

Results for reionization parameter

We first present the combined likelihood results for the estimation of τ using the E-mode spectra. Those obtained on simulations and on *Planck* data are displayed in Fig. 4.31. For the simulations, we show the mean and error-bars derived from the distribution of the posterior maximums. For *Planck* data, the data-point correspond to the maximum of the likelihood posteriors, and the error-bars to the 68% C.L. We select a range of sky coverages $0.5 \leq f_{\text{sky}} \leq 0.9$. We do not include the case for $f_{\text{sky}} = 0.4$, since the posterior from the 70x100 cross-spectra produce ill results for this mask.

We observe a systematic bias for the white noise simulations, which is however reduced when removing the spectra including the 44 and 217 GHz channels (**no44+217**). In that case,

for $f_{\text{sky}} = 0.6$, we obtain $\tau = 0.061_{-0.004}^{+0.004}$. The estimated value of τ increases as larger sky fractions are considered, which reveals the presence of foreground residuals.

A similar behaviour is observed on the FFP10 simulations. We notice that the dispersion of the posterior maximums is wider for the `all` configuration than for the `no44+217`. The related error-bars are about twice larger for the FFP10 than for the white-noise sets.

The results from *Planck* data are relatively stable for $f_{\text{sky}} \leq 0.7$ and considering the `no44+217` combination. For $f_{\text{sky}} = 0.6$, we obtain $\tau = 0.0595_{-0.0083}^{+0.0075}$ (68% C.L.). For larger sky coverage, $f_{\text{sky}} \geq 0.8$, the presence of foreground residuals clearly impacts the estimation of τ . Combining only the 70x100, 70x143 and 100x143 cross-spectra in the likelihood provides the most stable results, which is consistent with the observations made on the simulations.

In addition, we show in Fig. 4.33 the results for the `no44+217` combination of *Planck* data when increasing the multipole range, from $\ell \in [2, 20]$ to $\ell \in [2, 35]$. We see that the estimations on τ remain stable, and that the error-bars are improved. For $\ell \in [2, 35]$, we obtain $\tau = 0.0599_{-0.0071}^{+0.0064}$ for $f_{\text{sky}} = 0.6$, and $\tau = 0.0604_{-0.0062}^{+0.0058}$ for $f_{\text{sky}} = 0.7$.

Results for tensor-to-scalar ratio

Following the same approach as for the reionization parameter, we discuss the results displayed in Fig. 4.32 when estimating r from the B-modes signal.

For both simulation sets, the choice of the cross-spectra combination (`all` and `no44+217`) has almost no effect on the bias. We notice that the error-bars derived from posterior maximums distributions are about one order of magnitude higher for the FFP10 compared to the white noise set.

The results on *Planck* data show globally more variation depending on the sky coverage considered. The `no44+217` provides relatively more stable results. In addition, because this choice of cross-spectra combination provides more robust constraints on τ , we choose to quote the value of r evaluated from this combinations only (70x100, 70x143 and 100x143). In that case, when considering the multipole range $\ell \in [2, 20]$, we measure $r = -0.0333_{-0.3041}^{+0.3307}$ (95% C.L.) for $f_{\text{sky}} = 0.4$, and $r = 0.2040_{-0.3057}^{+0.3316}$ for $f_{\text{sky}} = 0.5$. Using the Feldman&Cousins method, we deduce an upper-limit on the tensor-to-scalar ratio, $r \leq 0.6150$ (95% C.L.) for $f_{\text{sky}} = 0.4$, and $r \leq 0.8540$ for $f_{\text{sky}} = 0.5$.

On Fig. 4.34, we show the results for the `no44+217` combination of *Planck* data when increasing the multipole range, from $\ell \in [2, 20]$ to $\ell \in [2, 35]$. We see that the uncertainties on the estimation are almost improved by a factor of two, and that the results are more stable over the sky fractions considered. However, we still observe a systematic shift of r for $f_{\text{sky}} = 0.7$. We measure $r = 0.0198_{-0.1743}^{+0.1794}$ for $f_{\text{sky}} = 0.4$, and $r = 0.0996_{-0.1585}^{+0.1633}$ for $f_{\text{sky}} = 0.5$. From those measurements, we deduce the upper-limit on the tensor-to-scalar value, $r \leq 0.3714$ (95% C.L.) for $f_{\text{sky}} = 0.4$, and $r \leq 0.4196$ for $f_{\text{sky}} = 0.5$.

6.4 Conclusion

In this section, we constrained the two cosmological parameters τ and r from the *Planck* CMB polarisation data. The combination of the 70x100, 70x143 and 100x143 cross-spectra into the Lollipop method provides the most stable results on simulations and on the *Planck* data. This choice of combination is motivated by the high level of noise and possibly foreground residuals in the 44 and 217 GHz channels. We measure $\tau = 0.0604_{-0.0062}^{+0.0058}$ (68% C.L.) for the reionization depth when considering 70% of the sky.

Similarly, we derived an upper limit for the tensor-to-scalar ratio of $r \leq 0.37$ (95% C.L.) when considering 40% of the sky, and $r \leq 0.42$ when considering 50% of the sky

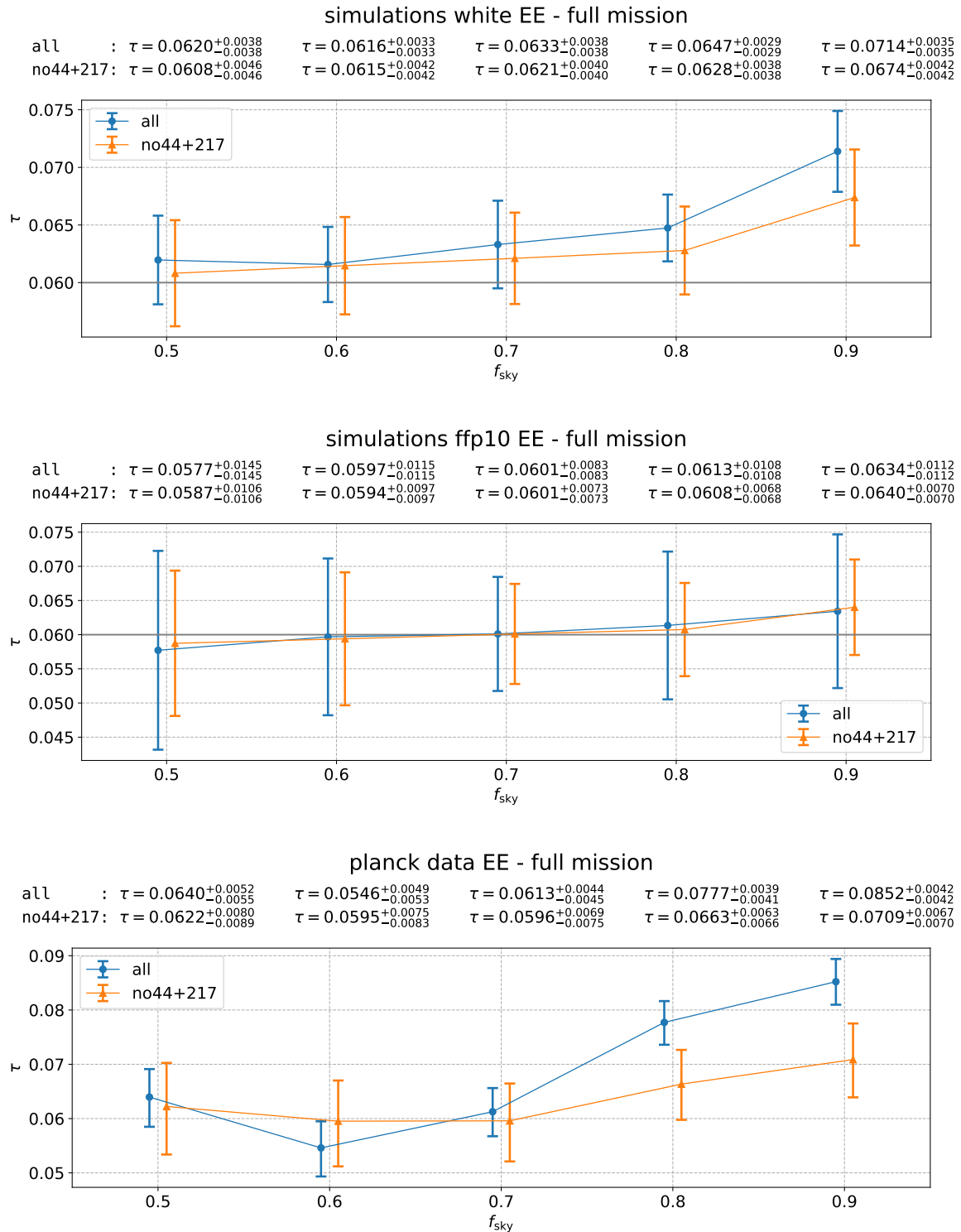


Figure 4.31: Simulations and *Planck* data results for the reionization parameter τ from E-modes using combined cross-spectra, on the multipole range $\ell \in [2, 20]$.

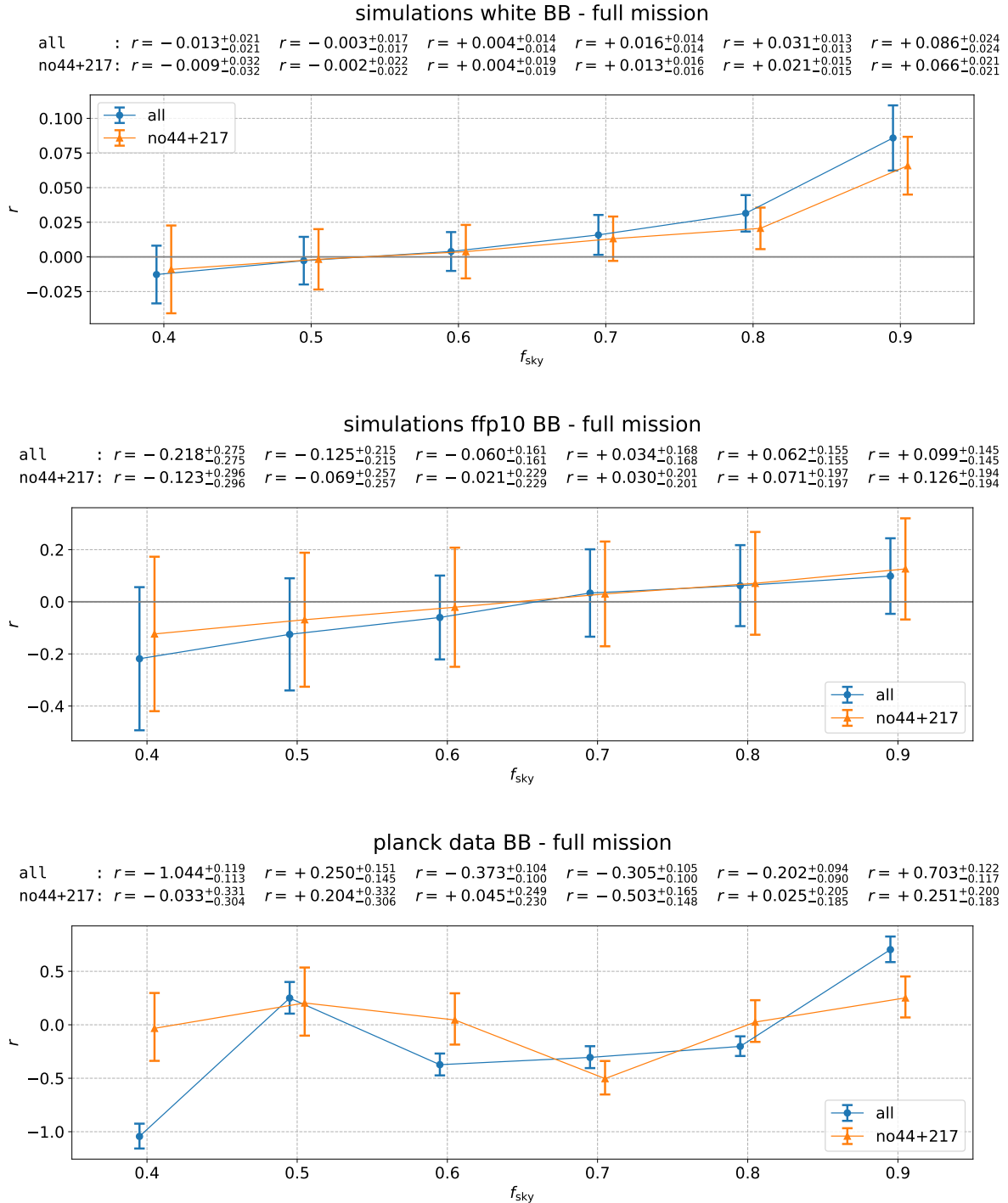


Figure 4.32: Simulations and *Planck* data results for the tensor-to-scalar ratio parameter r from B-modes using combined cross-spectra on the multipole range $\ell \in [2, 20]$.

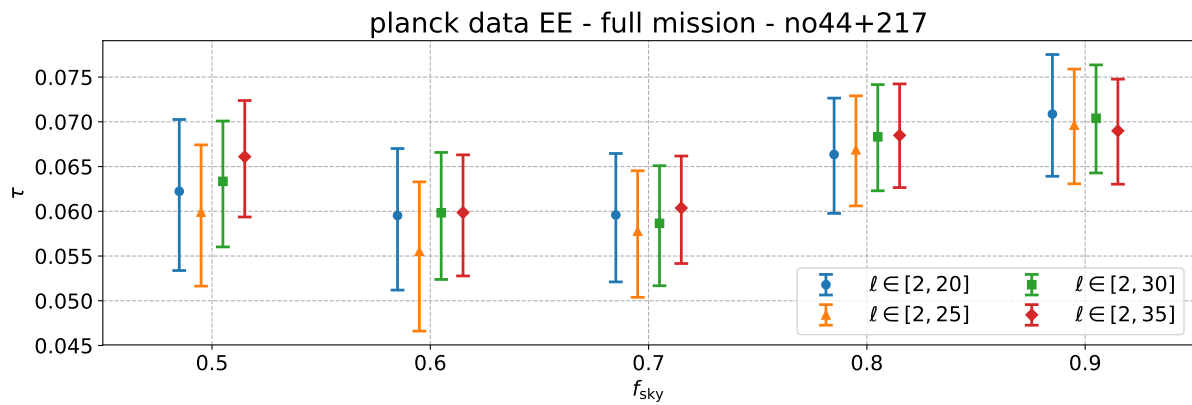


Figure 4.33: *Planck* data results for the reionization parameter τ from E-modes using combined cross-spectra 70x100, 70x143, 100x143, and varying the multipole range.

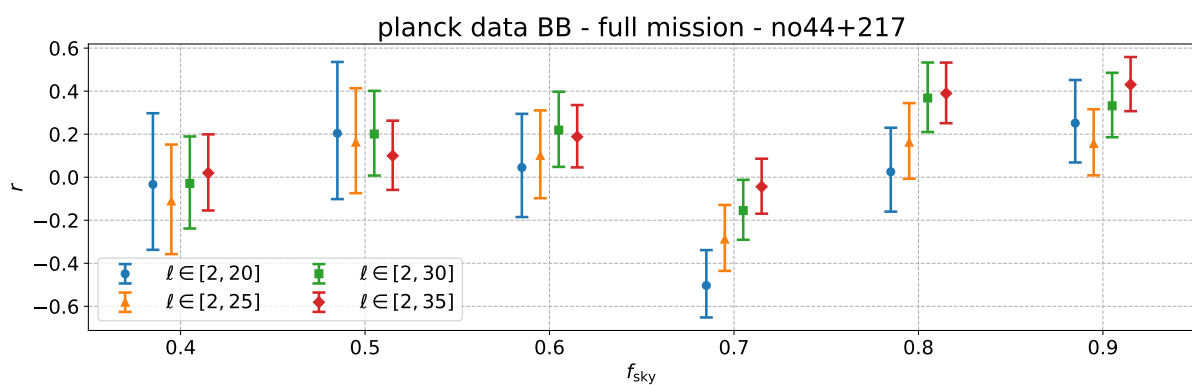


Figure 4.34: *Planck* data results for the tensor-to-scalar ratio r from B-modes using combined cross-spectra 70x100, 70x143, 100x143, and varying the multipole range.

7 Summary

In this chapter we provided a complete procedure to analyse the *Planck* polarisation data, from the map cleaning up to the estimation of the cross-spectra and the constraints on the cosmological parameters.

The foreground cleaning allowed us to test the robustness of the different template cleaning approaches that we proposed in chapter 2 against more complex noise realisations that include systematics. From our results on *Planck* data, we derived constraints on the foreground spectral parameters, for which the estimated values are in accordance with similar studies. Further work would allow us to highlight the foreground signal variations across the sky, or to include other datasets such as those provided by WMAP.

The application of our implementation of the pixel-based cross power spectrum estimator, `xQML`, allowed us to highlight the bias caused either by the foregrounds, or by the *Planck* systematics residuals present in the simulations. Further study could be made in order to quantify the improvement of using the `xQML` on *Planck* data compared using the pure pseudo-spectrum approach.

The estimation of the cross-spectra covariance matrix from MC simulations is a crucial step in order to ultimately derive the cosmological parameters using likelihood analysis. We presented the `Lollipop` approach which allows us to compute the parameter posteriors in the harmonic domain and using cross-spectra. We observed a significant enlargement of the uncertainty when considering the FFP10 simulations instead of pure white noise. We also highlighted the presence of bias when increasing the sky coverage, which is an indication of foreground residuals impeding the CMB signal.

Finally, we combined the different cross-spectra in order to derive a final constraint on τ and r . Considering 70% of the sky, for reionization depth we measure

$$\tau = 0.0604^{+0.0058}_{-0.0062} \quad (68\% \text{ C.L.}) \quad (4.18)$$

This result is 1.5σ away from the *Planck* result, $\tau_{\text{P1}} = 0.0506 \pm 0.0086$ (68% C.L.) ([Planck 2018 Results. VI](#)). For their baseline, they only use the 100x143 cross-spectra, over the multipole range $\ell \in [2, 29]$, and keep 50% of the sky. If we consider a similar set-up than *Planck*, we find $0.0641^{+0.0133}_{-0.0160}$ (68% C.L.). Further investigations are needed in order to understand the 150% difference between our error-bars and those of *Planck*.

Following the same approach, we derived an upper limit on the tensor-to-scalar ratio. Considering 40% of the sky, we measure

$$r \leq 0.3714 \quad (95\% \text{ C.L.}) \quad (4.19)$$

This result is compatible with the current *Planck* constraint based on tensor analysis, $r_{\text{P1}} \leq 0.41$ ([Planck 2018 Results. X](#)). Considering the same set-up of for *Planck*, using the 100x143 only, $\ell \in [2, 29]$, and 50% of the sky, we find $r \leq 0.3848$.

Further work is needed in order to better constrain those two parameters. The impact of the range of low- ℓ multipoles considered in the likelihood should be investigated, and other combinations of cross-spectra could be examined in order to better characterise the impact of each frequency channel on the posteriors. The correlation between r and τ also needs to be estimated by combining the E and B modes in the likelihood analysis.

More generally, other strategies for the mask constructions could also be explored, for example based on the mean foreground and systematic residuals instead of the dust amplitude only. Other approaches would be to adapt the masks for each frequency channel, based on the level of synchrotron and dust signals, or the level of residuals. The impact of the choice of the

foreground coefficient used to clean the data should also be quantified. We note that we only provided the analysis for the full mission dataset. The same pipeline could be applied on the half-mission maps. Thus providing 45 cross-spectra instead of 10 (but with roughly twice as much noise), and allowing more different combinations among the frequency channels to build the cosmological likelihood.

In a more distant future, the analysis that we proposed in this chapter could be applied to other large-scale missions, such as LiteBIRD.

Conclusion

In this thesis, we characterised and developed analysis tools allowing to study the large-scale CMB polarisation signal. We especially focused on the B-modes detection to constrain the tensor-to-scalar ratio, and on the E-modes to measure the reionization parameter τ .

We first assessed the problem of removing the foreground contaminations from experimental datasets full sky measurements. We developed several methods based on the template fitting that require minimum assumptions about the spectral behaviour of the contamination signals. We investigated different noise level ranging from *Planck* to the next CMB satellite mission LiteBIRD. We showed how the experimental noise and the CMB can induce a bias on the cleaning process, for which we proposed several solutions. In order to further reduce the level of the foreground residuals, the application of our cleaning methods on patches were also investigated. It revealed to be seriously impeded by the CMB variance when the level of contamination is low. This feature will have to be taken into account for future low-noise CMB measurements.

In the second part of this thesis, we fully characterised and developed a pixel-based CMB power spectrum estimator algorithm, the **xQML**, which implementation is made publicly available. Compared to other pixel-based estimators, the **xQML** offers the unique advantage to cross-correlate two different datasets, thus removing the noise bias from the spectrum estimate, and allowing to mitigate systematic effects. We showed that the estimator uncertainty is near-optimal, and that it is impacted only to second order by the error in the choice of the fiducial model. We showed that the method significantly improves the reduction of the E-to-B leakage on large-scales compared to the pure pseudo-spectrum approaches which require laborious weighting optimisations. The **xQML** method will be particularly suited for both E and B modes measurements in future large-scale CMB polarisation experiments.

Finally, we applied our algorithms to the public *Planck* polarisation maps. We showed that our foreground cleaning method allowed us to estimate the dust and synchrotron spectral parameters, and provides consistent results with published analysis. Using the **xQML** and the cross-spectra based likelihood for large angular scales, the **Lollipop** approaches, we successfully constrained the reionization and tensor-to-scalar ratio parameters. We found $\tau = 0.0604_{-0.0062}^{+0.0058}$ (68% C.L.), and $r \leq 0.37$ (95% C.L.). Those results are in agreements with current limits. The analysis pipeline that we propose is robust, and could be applied to future large-scale missions such as the LiteBIRD satellite.

Pixel signal covariance matrix

Stokes parameters

For E_x and E_y the components of the wave electric field of a monochromatic electromagnetic wave propagating in the z direction, the Stokes parameters are defined as (Zaldarriaga 1998; Kosowsky 1995; Kamionkowski et al. 1997; Ng et al. 1999)

$$I = |E_x|^2 + |E_y|^2 \quad (\text{A.1a})$$

$$Q = |E_x|^2 - |E_y|^2 \quad (\text{A.1b})$$

$$U = E_x^* E_y + E_x E_y^* = 2\Re(E_x^* E_y) \quad (\text{A.1c})$$

$$V = 2\Im(E_x^* E_y). \quad (\text{A.1d})$$

Under the x - y plane rotation of an angle α ,

$$\begin{pmatrix} x' \\ y' \end{pmatrix} = \begin{pmatrix} \cos(\alpha) & \sin(\alpha) \\ -\sin(\alpha) & \cos(\alpha) \end{pmatrix} \begin{pmatrix} x \\ y \end{pmatrix}, \quad (\text{A.2})$$

one can show from Eq. (A.1) that the Stokes parameters Q and U transform as

$$\begin{pmatrix} Q' \\ U' \end{pmatrix} = \begin{pmatrix} \cos(2\alpha) & \sin(2\alpha) \\ -\sin(2\alpha) & \cos(2\alpha) \end{pmatrix} \begin{pmatrix} Q \\ U \end{pmatrix}. \quad (\text{A.3})$$

A function ${}_s f(\theta, \varphi)$ defined on the sphere is said to have spin- s if under a right-handed rotation of (e_x, e_y) by an angle α it transforms as ${}_s f'(\theta, \varphi) = e^{-is\phi} {}_s f(\theta, \varphi)$. It is thus straightforward to show that the quantity $P = Q \pm iU$ is a spin ± 2 quantity.

Fields covariance

Expressing the temperature and polarization fields in terms of weighted spherical harmonics,

$$T = \sum_{\ell m} a_{\ell m} Y_{\ell m}, \quad (\text{A.4})$$

$$Q \pm iU = \sum_{\ell m} \pm 2a_{\ell m} \pm 2Y_{\ell m}, \quad (\text{A.5})$$

$$(\text{A.6})$$

the polarized Stokes parameters can be written

$$\begin{aligned} Q &= \frac{1}{2} \sum +2a_{\ell m} +2Y_{\ell m} + -2a_{\ell m} -2Y_{\ell m} \\ &= -\frac{1}{2} \sum (a_{\ell m}^E + ia_{\ell m}^B) +2Y_{\ell m} + (a_{\ell m}^E - ia_{\ell m}^B) -2Y_{\ell m}. \end{aligned} \quad (\text{A.7})$$

$$\begin{aligned} U &= \frac{1}{2} \sum +2a_{\ell m} +2Y_{\ell m} - -2a_{\ell m} -2Y_{\ell m} \\ &= \frac{i}{2} \sum (a_{\ell m}^E + ia_{\ell m}^B) +2Y_{\ell m} - (a_{\ell m}^E - ia_{\ell m}^B) -2Y_{\ell m}. \end{aligned} \quad (\text{A.8})$$

with the gradient E and curl B Fourier coefficients,

$$a_{\ell m}^E \equiv -\frac{1}{2} (+2a_{\ell m} + -2a_{\ell m}), \quad +2a_{\ell m} = -a_{\ell m}^E - ia_{\ell m}^B, \quad (\text{A.9})$$

$$a_{\ell m}^B \equiv \frac{i}{2} (+2a_{\ell m} - -2a_{\ell m}), \quad +2a_{\ell m} = -a_{\ell m}^E + ia_{\ell m}^B. \quad (\text{A.10})$$

The correlation functions between fields of spin s and s' can be expressed in term of the following function, which generalizes the Legendre polynomial,

$$P_{\ell}^{ss'}(\mathbf{x} \cdot \mathbf{x}') \equiv \sum_m {}_s Y_{\ell m}^*(\mathbf{x}) {}_{s'} Y_{\ell m}(\mathbf{x}'). \quad (\text{A.11})$$

The Wigner D-functions $d_{ss'}^{\ell}$ are related to the $P_{\ell}^{ss'}$ by

$$P_{\ell}^{ss'}(\cos \theta) = (-1)^s d_{ss'}^{\ell}(\theta). \quad (\text{A.12})$$

From the Wigner D-functions properties, it follows

$$d_{s's} = (-1)^{s-s'} d_{ss'} \Leftrightarrow P_{\ell}^{ss'} = P_{\ell}^{s's} \quad (\text{A.13})$$

$$d_{s's} = (-1)^{s-s'} d_{-s-s'} \Leftrightarrow P_{\ell}^{ss'} = P_{\ell}^{-s'-s}. \quad (\text{A.14})$$

Defining

$$Q_{\ell}^{ss'} = \frac{P_{\ell}^{ss'} + (-1)^{s'} P_{\ell}^{s-s'}}{2}, \quad R_{\ell}^{ss'} = \frac{P_{\ell}^{ss'} - (-1)^{s'} P_{\ell}^{s-s'}}{2}, \quad (\text{A.15})$$

the correlation functions between the Gaussian spin-0 and spin-2 fields can thus be computed as follow

$$\begin{aligned}\langle T^*T \rangle &= \sum_{\ell,m} |a_{\ell m}|^2 Y_{\ell m}^* Y_{\ell m} \\ &= \sum_{\ell} \frac{2\ell+1}{4\pi} P_{\ell}^{00} C_{\ell}^{TT},\end{aligned}\tag{A.16a}$$

$$\begin{aligned}\langle Q^*Q \rangle &= \frac{1}{2} \sum_{\ell} \frac{2\ell+1}{4\pi} \{P_{\ell}^{22} (C_{\ell}^{EE} + C_{\ell}^{BB}) + P_{\ell}^{2-2} (C_{\ell}^{EE} - C_{\ell}^{BB})\} \\ &= \sum_{\ell} \frac{2\ell+1}{4\pi} (C_{\ell}^{EE} Q_{\ell}^{22} + C_{\ell}^{BB} R_{\ell}^{22}),\end{aligned}\tag{A.16b}$$

$$\langle U^*U \rangle = \sum_{\ell} \frac{2\ell+1}{4\pi} (C_{\ell}^{EE} R_{\ell}^{22} + C_{\ell}^{BB} Q_{\ell}^{22}),\tag{A.16c}$$

$$\langle T^*Q \rangle = \langle Q^*T \rangle = -\frac{1}{2} \sum_{\ell} \frac{2\ell+1}{4\pi} P_{\ell}^{02} (C_{\ell}^{TE} + C_{\ell}^{ET}),\tag{A.16d}$$

$$\langle T^*U \rangle = \langle U^*T \rangle = -\frac{1}{2} \sum_{\ell} \frac{2\ell+1}{4\pi} (C_{\ell}^{TB} + C_{\ell}^{BT}) P_{\ell}^{02},\tag{A.16e}$$

$$\begin{aligned}\langle Q^*U \rangle = \langle U^*Q \rangle &= \frac{1}{2} \sum_{\ell} \frac{2\ell+1}{4\pi} (C_{\ell}^{EB} + C_{\ell}^{BE}) P_{\ell}^{2-2} \\ &= \frac{1}{2} \sum_{\ell} \frac{2\ell+1}{4\pi} (C_{\ell}^{EB} + C_{\ell}^{BE}) (Q_{\ell}^{22} - R_{\ell}^{22}).\end{aligned}\tag{A.16f}$$

Legendre polynomial generalisation

Defining $\rho_{\ell}^{ss'} = \sqrt{(\ell^2 + s^2)(\ell^2 - s'^2)}$, the following recursion may be used to evaluate the Wigner D-functions,

$$\rho_{\ell+1}^{ss'} d_{\ell+1}^{ss'}(z) = (2\ell+1) \left[z - \frac{ss'}{\ell(\ell+1)} \right] d_{\ell}^{ss'}(z) - \rho_{\ell}^{ss'} d_{\ell-1}^{ss'}(z),\tag{A.17}$$

with the initial conditions

$$d_s^{ss'}(z) = \frac{(-1)^{s-s'}}{2^s} \sqrt{\frac{(2s)!}{(s+s')!(s-s')!}} (z+1)^{(s+s')/2} (1-z)^{(s-s')/2},\tag{A.18}$$

$$\rho_{s+1}^{ss'} d_{s+1}^{ss'}(z) = (2s+1) \left(z - \frac{s'}{s+1} \right) d_s^{ss'}(z).\tag{A.19}$$

Other relations exist to compute the $P_{\ell}^{ss'}$ (Tegmark et al. 2001), but are generally computationally more costly than ours. Moreover, we found some instabilities when computing $P_{\ell}^{02}(z)$ for z close to 0, leading to bias in TE and TB spectra estimation, that does not show when using our algorithm.

Coordinate rotation

To compute the quantities of the pixel-pixel covariance matrix, we must correct for the difference of coordinate in which the Stokes parameters are measured. Following (Tegmark 1997), for two pixels i and j , see for example Fig. A.1, we define a new reference frame which local z direction is still pointing out of the celestial sphere, and the local x axis of both pixels is aligned with the great circle passing through pixels i and j . We define the angle α_{ij} between the meridian passing through i and the great i - j circle, and similarly with α_{ji} for the pixel j .

Denoting \mathbf{d}_i the measured dataset, with three measured parameters at pixel i ,

$$\mathbf{d}_i = \begin{pmatrix} T_i \\ Q_i \\ U_i \end{pmatrix}, \quad (\text{A.20})$$

the covariance matrix between the Stokes parameters measured for both pixels is the written

$$\langle \mathbf{d}_i^* \mathbf{d}_j^T \rangle = \mathbf{R}(\alpha_{ij}) \mathbf{M}(\hat{n}_i \cdot \hat{n}_j) \mathbf{R}(\alpha_{ji})^T, \quad (\text{A.21})$$

with

$$\mathbf{M}(\hat{n}_i \cdot \hat{n}_j) = \begin{pmatrix} \langle T_i^* T_j \rangle & \langle T_i^* Q_j \rangle & \langle T_i^* U_j \rangle \\ \langle Q_i^* T_j \rangle & \langle Q_i^* Q_j \rangle & \langle Q_i^* U_j \rangle \\ \langle U_i^* T_j \rangle & \langle U_i^* Q_j \rangle & \langle U_i^* U_j \rangle \end{pmatrix}, \quad (\text{A.22})$$

and the Stokes rotation matrix defined as

$$\mathbf{R}(\alpha) = \begin{pmatrix} 1 & 0 & 0 \\ 0 & \cos 2\alpha & \sin 2\alpha \\ 0 & -\sin 2\alpha & \cos 2\alpha \end{pmatrix}. \quad (\text{A.23})$$

Each meridian passing by the pixels has unit normal vector

$$\hat{r}_i^* = \frac{\hat{z} \times \hat{n}_i}{|\hat{z} \times \hat{n}_i|}, \quad \hat{r}_j^* = \frac{\hat{z} \times \hat{n}_j}{|\hat{z} \times \hat{n}_j|}, \quad (\text{A.24})$$

where \hat{z} is the unit vector at the centre of the sphere pointing to the zenith. The normal vector to the great circle is noted

$$\hat{r}_{ij} = \frac{\hat{n}_i \times \hat{n}_j}{|\hat{n}_i \times \hat{n}_j|}. \quad (\text{A.25})$$

Thus, the cosine and sine entries of the rotation matrix are computed from

$$\cos \alpha_{ij} = \hat{r}_{ij} \cdot \hat{r}_i^*, \quad \cos \alpha_{ji} = \hat{r}_{ij} \cdot \hat{r}_j^*, \quad (\text{A.26})$$

$$\sin \alpha_{ij} = (\hat{r}_{ij} \times \hat{r}_i^*) \cdot \hat{r}_i, \quad \sin \alpha_{ji} = (\hat{r}_{ij} \times \hat{r}_j^*) \cdot \hat{r}_j, \quad (\text{A.27})$$

and

$$\cos 2\alpha_{ij} = 2 \cos^2 \alpha_{ij} - 1, \quad \cos 2\alpha_{ji} = 2 \cos^2 \alpha_{ji} - 1, \quad (\text{A.28})$$

$$\sin 2\alpha_{ij} = 2 \cos^2 \alpha_{ij} \sin \alpha_{ij}, \quad \sin 2\alpha_{ji} = 2 \cos^2 \alpha_{ji} \sin \alpha_{ji}. \quad (\text{A.29})$$

The above relation breaks down for the two special cases. Firstly, both pixels can be identical or at diametrically opposed sides on the sphere, in which case we can define a great circle, parallel to their respective meridian, along which their local coordinate are already aligned. There is no need for rotation correction, and $\alpha_{ij} = \alpha_{ji} = 0$. The second case occurs when one of the pixel is at the north pole. In that case, the (Q,U) -convention is undefined, and we choose again $\alpha_{ij} = \alpha_{ji} = 0$.

Assuming vanishing C_ℓ^{EB} and C_ℓ^{TB} spectra, one gets

$$\langle \mathbf{d}_i^* \mathbf{d}_j^T \rangle = \begin{pmatrix} \langle T_i^* T_j \rangle & c_{ji} \langle T_i^* Q_j \rangle & -s_{ji} \langle T_i^* Q_j \rangle \\ c_{ij} \langle Q_i^* T_j \rangle & c_{ij} c_{ji} \langle Q_i^* Q_j \rangle + s_{ij} s_{ji} \langle U_i^* U_j \rangle & -c_{ij} s_{ji} \langle Q_i^* Q_j \rangle + s_{ij} c_{ji} \langle U_i^* U_j \rangle \\ -s_{ij} \langle Q_i^* T_j \rangle & -s_{ij} c_{ji} \langle Q_i^* Q_j \rangle + c_{ij} s_{ji} \langle U_i^* U_j \rangle & s_{ij} s_{ji} \langle Q_i^* Q_j \rangle + c_{ij} c_{ji} \langle U_i^* U_j \rangle \end{pmatrix}, \quad (\text{A.30})$$

with $c_{ij} = \cos 2\alpha_{ij}$ and $s_{ij} = \sin 2\alpha_{ij}$. The matrix assuming only C_ℓ^{EB} and C_ℓ^{TB} to be non-null, leads to

$$\langle \mathbf{d}_i^* \mathbf{d}_j^T \rangle = \begin{pmatrix} 0 & s_{ji} \langle T_i^* U_j \rangle & c_{ji} \langle T_i^* U_j \rangle \\ s_{ij} \langle U_i^* T_j \rangle & s_{ij} c_{ji} \langle U_i^* Q_j \rangle + c_{ij} s_{ji} \langle Q_i^* U_j \rangle & -s_{ij} s_{ji} \langle U_i^* Q_j \rangle + c_{ij} c_{ji} \langle Q_i^* U_j \rangle \\ c_{ij} \langle U_i^* T_j \rangle & c_{ij} c_{ji} \langle U_i^* Q_j \rangle - s_{ij} s_{ji} \langle Q_i^* U_j \rangle & -c_{ij} s_{ji} \langle U_i^* Q_j \rangle - s_{ij} c_{ji} \langle Q_i^* U_j \rangle \end{pmatrix}. \quad (\text{A.31})$$

The full $3n_{\text{pix}} \times 3n_{\text{pix}}$ signal correlation matrix

$$\mathbf{S} = \begin{pmatrix} S^{TT} & S^{TQ} & S^{TU} \\ S^{QT} & S^{QQ} & S^{QU} \\ S^{UT} & S^{UQ} & S^{UU} \end{pmatrix}, \quad (\text{A.32})$$

is then obtained by gathering the elements of the 3×3 matrix $\langle \mathbf{d}_i^* \mathbf{d}_j^T \rangle$ for each pixel pair i - j . We also define the \mathbf{P}_ℓ matrix as

$$\mathbf{P}_\ell = \frac{\partial \mathbf{S}}{\partial C_\ell}, \quad (\text{A.33})$$

where the index ℓ goes along the multipoles and the spectra. In other words, the vector C_ℓ encodes all six power spectra TT, EE, BB, TE, TB , and EB , see (Tegmark et al. 2001). For the computation of \mathbf{P}_ℓ at each multipole ℓ , this matrix can be computed by putting all $C_{\ell' \neq \ell}$ in Eqs.(A.16) at zero, except $C_{\ell' = \ell}$ at one.

For E and B polarizations, the Stokes blocks of the matrices have the following properties :

$$\mathbf{P}_\ell^{B,QQ} = \mathbf{P}_\ell^{B,UU} \quad (\text{A.34})$$

$$\mathbf{P}_\ell^{B,QU} = -\mathbf{P}_\ell^{B,UQ} \quad (\text{A.35})$$

$$\mathbf{P}_\ell^{B,UQ} = -\mathbf{P}_\ell^{B,QU} \quad (\text{A.36})$$

$$\mathbf{P}_\ell^{B,UU} = \mathbf{P}_\ell^{B,QQ} \quad (\text{A.37})$$

1 Introduction

L'évolution du monde peut être comparée à un feu d'artifice qui vient de se terminer. Quelques mèches rouges, cendres et fumées. Debout sur une escarville mieux refroidie, nous voyons s'éteindre doucement les soleils et cherchons à reconstituer l'éclat disparu de la formation des mondes.

(Georges Lemaître, 1931)

À l'aube du 20^{ème} siècle, la révolution en physique apportée par la mécanique quantique et la relativité générale a permis d'approfondir l'étude de l'Univers dans son ensemble. Alors que les travaux d'Albert Einstein, Willem de Sitter et Alexandre Friedmann jetaient les bases des solutions cosmologiques des équations générales de relativité, l'origine et l'évolution de l'Univers sont devenues des sujets de recherche, et la cosmologie contemporaine était née.

Avec l'amélioration des techniques d'observation astrophysique sont venus les premières preuves, d'Edwin Hubble, que de nombreuses nébuleuses observées étaient en fait des objets extragalactiques, connus sous le nom de galaxies (E. P. Hubble 1926). Leur vitesse radiale mesurée par Vesto Slipher indiquait une récession apparente de notre galaxie, et qui se manifeste comme un redshift du spectre observé. La relation linéaire entre la distance et la vitesse apparente des galaxies a d'abord été déduite par Georges Lemaître en 1927 (G. Lemaître 1927), puis par Edwin Hubble en 1929 (E. Hubble 1929). Lemaître a fourni la première interprétation du redshift cosmologique causé par l'expansion de l'Univers provenant d'une constante cosmologique, et non par le mouvement des galaxies (voir Luminet 2013). Il a également présenté pour la première fois une description de l'Univers primordial comme étant beaucoup plus dense et plus chaud, émergeant de 'l'atome primordial' (Georges Lemaître 1950). Cette idée, d'abord railleusement dénommée 'Big-Bang', s'est ensuite révélée révolutionnaire. La découverte du fond diffus cosmologique (CMB pour *Cosmic Microwave Background*) et les preuves observationnelles confirmant la théorie de la nucléosynthèse du Big-Bang développée par Gamow et ses collaborateurs (Gamow 1948), ont ouvert la voie vers le modèle standard cosmologique.

Le concept d'un écho radiatif résiduel du Big-Bang émanant des premiers instants d'un Univers chaud a d'abord été étudié par Alpher et Hermann (Ralph A. Alpher et al. 1948). Ils ont prédit que le CMB devrait suivre une loi de rayonnement de corps noir, caractérisé par une température qui a aujourd'hui chuté à seulement quelques Kelvin depuis son émission. Les photons du CMB portent à la fois l'information sur leur voyage cosmique et l'empreinte de la physique de l'Univers primordial, qui implique des échelles d'énergie bien au delà de la portée actuelle des accélérateurs de particules. Par conséquent, l'étude du CMB fournit un bras de levier cosmologique unique pour comprendre l'histoire de l'Univers, pour tester la relativité

générale, pour contraindre la physique des particules, et pour contraindre la nature de l'énergie noire ainsi que de la matière noire.

La première évidence de l'existence du CMB a été fournie en 1964 par Penzias et Wilson. Depuis lors, de nombreux télescopes au sol, satellites, et ballons, ont permis d'améliorer considérablement les mesures. La première validation de la nature du spectre du corps noir du CMB a été réalisée par le satellite COBE. Suivi des cartographies détaillées des anisotropies CMB sur le ciel par les satellites WMAP et *Planck* au 21^{ème} siècle, réalisant des contraintes sur les paramètres du modèle cosmologique standard au niveau du pour-cent, et marquant le début de l'ère de la cosmologie de précision.

Cependant, plusieurs pièces du puzzle cosmologique sont encore manquantes. La nature de l'énergie sombre et de la matière noire est encore inconnue. L'absence d'anti-matière dans l'Univers observable est inexplicée. Pourquoi notre Univers apparaît-il géométriquement plat? Et comment est-il devenu homogène sur des échelles *a priori* causalement déconnectées? Quelles sont les sources des fluctuations primordiales qui ont donné naissance aux anisotropies du CMB et aux structures cosmologiques à grande échelle observées aujourd'hui?

Correspondant à une période courte et précoce pendant laquelle l'Univers aurait connu une croissance exponentielle, l'inflation est le principal et probablement le plus élégant paradigme qui fournit une solution à trois des énigmes cosmologiques : la platitude et le problème de l'horizon, ainsi que l'origine des fluctuations primordiales.

L'expansion rapide de l'Univers à l'époque de l'inflation aurait dû élargir les fluctuations quantiques à des échelles macroscopiques, produisant un fond stochastique d'ondes gravitationnelles primordiales. Celles-ci auraient ensuite laissé une empreinte sur la polarisation des photons du CMB, les motifs dits *modes B*. La mesure précise des modes B, encore non détectés à ce jour, représente la sonde la plus prometteuse pour la physique inflationnaire, et permettrait un premier aperçu de la nature quantique de la gravité. Cependant, l'amplitude attendue du signal est au moins mille fois plus petite que celle de la température du CMB, et peut être sérieusement entravée par les contaminations d'avant-plan des émissions galactiques. Les futures détections des modes B nécessitent donc à la fois une expertise en sciences instrumentales, physiques et informatiques.

Cette thèse se concentre sur le développement d'outils d'analyse pour étudier les modes B primordiaux du fond diffus cosmologique. Notre but est d'extraire l'amplitude des ondes gravitationnelles primordiales produites pendant la période inflationnaire.

Plus précisément, nous nous intéressons aux grandes échelles angulaires, pour lesquelles le signal des mode B primordiaux devrait être dominant. Comme ces échelles sont particulièrement contaminées par des émissions galactiques polarisées, nous avons étudié et développé des approches pour réduire ces contaminations et caractériser leurs résidus. Ces méthodes sont applicables aux données issues de missions satellites telles que *Planck* ou LiteBIRD.

Afin d'estimer l'amplitude des modes B, nous avons développé et caractérisé un estimateur du spectre de puissance des anisotropies du CMB. L'algorithme travaille dans l'espace des pixels et permet de cross-corréler les cartes mesurées par différents détecteurs. La méthode est optimale et minimise les fuites de variance des modes E vers les modes B.

Nous avons appliqué les approches de nettoyage et d'estimation du spectre aux données de polarisation et aux cartes de simulation fournies publiquement par *Planck*. Les contraintes que nous en déduisons concordent avec les résultats actuelles. En fin de compte, nous calculons une limite supérieure sur l'amplitude des ondes gravitationnelles primordiales ainsi que sur le paramètre de réionisation.

2 Introduction à la Cosmologie moderne

2.1 Modèle du Big-bang

La cosmologie moderne est basée sur le modèle Big-Bang dont les étapes clés sont mises en évidence sur la Fig. A.2. Les trois piliers du modèle du Big-Bang peuvent être résumés comme suit :

- L'Univers est en expansion, et son expansion est caractérisée par un facteur d'échelle, $a(t)$, qui croît avec le temps, et égal à l'unité aujourd'hui, $a_0 = 1$.
- La matière baryonique, y compris les électrons, s'est formée au début de l'Univers, alors qu'il était beaucoup plus dense et plus chaude qu'aujourd'hui. L'Univers était rempli d'un plasma de particules élémentaires en équilibre thermique, comme des quarks, des électrons, des neutrino et des photons. Les premiers noyaux (protons et neutrons) se sont formés au cours d'une phase connue sous le nom de Nucléosynthèse primordiale (BBN pour Big-Bang Nucleosynthesis). Comme la température était encore élevée, les électrons et les photons étaient étroitement couplés par la diffusion de Coulomb, et aucun état lié aux atomes n'était autorisé à se former.
- Au fur et à mesure de l'expansion de l'Univers, sa température a chuté suffisamment bas pour que les électrons commencent à se combiner efficacement avec les noyaux pour former les premiers atomes, principalement l'hydrogène et l'hélium. Par conséquent, les photons se sont dissociés du plasma primordial et ont été autorisés à se propager librement dans l'espace. Ils forment alors un fond de rayonnement, connu sous le nom de 'fond diffus cosmologique' (CMB pour Cosmic Microwave Background), qui imprègne encore l'Univers aujourd'hui.

2.2 Inflation et Univers inhomogène

Les perturbations primordiales permettant d'expliquer notre Univers inhomogène sont commodément décomposées en trois types : scalaire, vectorielles, et tenseurs. Les modes vectoriels décroissent rapidement, et sont donc négligeables comparés aux deux autres.

À la fin de la période inflationnaire, les longueurs d'onde des perturbations quantiques du champs de l'inflation sont étirées jusqu'à des longueurs macroscopiques. Étant donné que la plupart des modes sont au delà de l'horizon cosmique, les spectre en puissance des perturbations sont quasiment invariant d'échelle, notés

$$P_k^{\mathcal{S}} = A_S k^{n_s - 1}, \quad \text{et} \quad P_k^{\mathcal{T}} = A_T k^{n_t}, \quad (\text{A.38})$$

respectivement pour les perturbations scalaires et tensorielles. Les paramètres A_S et A_T sont leur respectives amplitudes, alors que n_s et n_t sont leur indices spectraux.

Nous définissons enfin le ratio tenseur-sur-scalaire

$$r_{k_*} \equiv \frac{P_{k_*}^{\mathcal{T}}}{P_{k_*}^{\mathcal{S}}} \sim \epsilon_V \quad (\text{A.39})$$

avec k_* l'échelle pivot (in $[\text{Mpc}^{-1}]$). La valeur de r dépend du paramètre d'inflation de roulement lent, ϵ_V , et est lié à l'échelle d'énergie à laquelle l'inflation a eue lieu, $V^{1/4} \sim (r/0.01)^{1/4} \times 10^{16} \text{GeV}$.

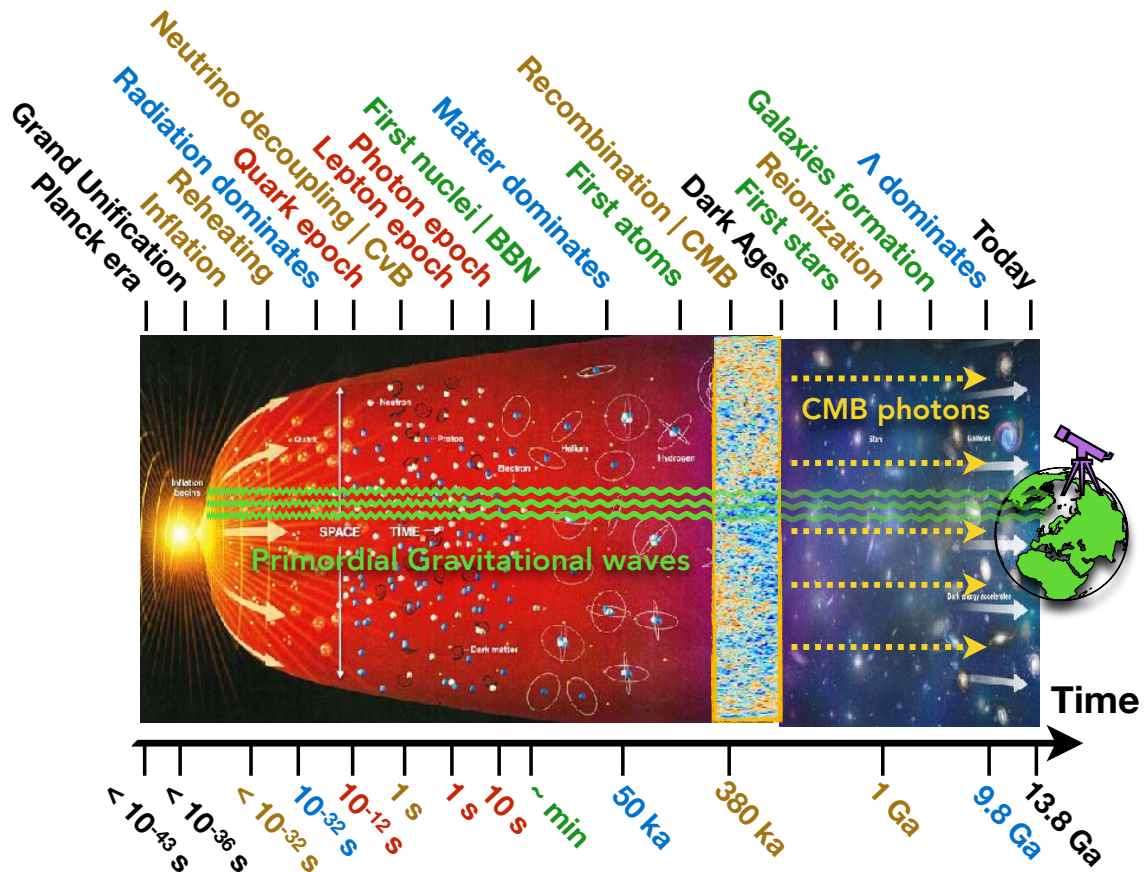


Figure A.2: Chronologie de l'Univers. Les axes vertical et horizontal représentent respectivement la dimension spatiale et temporelle. Au cours de son évolution, le taux d'expansion de l'Univers est entraîné par différents constituants : d'abord le rayonnement, puis la matière, et jusqu'à tout récemment, une forme d'énergie 'sombre' sous la forme d'une constante cosmologique Λ . Les premiers noyaux légers se sont formés pendant les 3 premières minutes et sont restés ionisés pendant 300 000 ans, jusqu'à ce qu'ils capturent des électrons, formant des atomes neutres. Le CMB a été émis il y a environ 13 milliards d'années. Adapté de National Geographic Society, avril 2014.

2.3 CMB et modes B

Le modèle cosmologique standard actuel fait de puissantes prédictions sur l'Univers primitif et son évolution. Une sonde comme le CMB nous permet de contraindre les paramètres du modèle standard avec une grande précision et compréhension. Une partie fondamentale du modèle, l'ère de l'inflation, résout élégamment à la fois plusieurs problèmes fondamentaux du modèle Big-Bang : le problème de l'horizon, le problème de platitude, et elle offre un mécanisme à l'origine des inhomogénéités primordiales. Cependant, aujourd'hui, la physique inflationnaire est faiblement contrainte. Une sonde la plus prometteuse réside dans la détection et l'observation de modes B primordiaux dans le CMB.

2.4 Plan

Dans la suite, nous nous concentrons sur le développement d'outils d'analyse des modes B primordiaux. Cette tâche s'avère complexe, car le signal attendu est faible par rapport aux autres

signaux de polarisation du CMB. De plus, en pratique, les mesures précises de la polarisation du CMB sont entravées par la présence de contaminations d'avant-plan et de bruit instrumental.

Les contaminations de premier plan se présentent sous diverses formes : terrestre, galactique ou extra-galactique. Nous avons exploré et adapté des méthodes permettant de nettoyer le signal polarisé du CMB des contamination d'avant-plans galactiques .

Le bruit instrumental peut produire un biais lors de l'estimation des spectres de puissance du CMB. La contribution du bruit peut soit être évaluée et supprimée, soit évitée en cross-corrélant des données ayant des bruits non-corrélés. Cette dernière technique sera décrite dans le contexte des estimateurs de spectres de puissance ciblant des mesures de polarisation précises.

Enfin, nous appliquons les approches de nettoyage et d'estimation du spectre aux données de polarisation et aux cartes de simulation fournies publiquement par *Planck*.

3 Nettoyage des contaminations d'avants-plan

Le CMB n'est pas la seule source d'émission micro-onde que nous observons dans le ciel. Plusieurs objets astrophysiques émettent dans la bande de micro-ondes, et contaminent ainsi toute mesure du CMB. Ces contaminations d'avant-plan peuvent avoir de nombreuses origines : des activités humaines ou des émissions atmosphériques, aux sources galactiques et extra-galactiques. Chaque source de contamination possède une intensité variable en fonction de l'échelle angulaire, de la longueur d'onde d'observation, ainsi que de la direction d'observation.

Les expériences en ballons et dans l'espace nous permettent d'être exempts de contaminations provenant de l'atmosphère, des émissions au sol, et des interférences radio-fréquence. Les composants restants proviennent de sources astrophysiques, comme les objets du système solaire, les galaxies et les amas de galaxies, ainsi que la lumière zodiacale, la Voie lactée et le fond diffus infrarouge (CIB). Dans le cas de la polarisation, deux sources sont dominantes : la poussière galactique, et le rayonnement synchrotron d'électrons spiralant autour du champ magnétique de la voie lactée.

3.1 Modélisation du signal

Le signal des avant-plans $f^\nu(\hat{n})$ pour une certaine direction \hat{n} et fréquence ν est généralement modélisé comme le produit entre la distribution spectral d'énergie (SED), $g_f(\nu, \hat{n})$, et l'amplitude du signal $F_f(\hat{n})$,

$$f^\nu(\hat{n}) = g_f(\nu, \hat{n})F_f(\hat{n}). \quad (\text{A.40})$$

Dans le cas d'une analyse des donnée de *Planck*, les traceurs d'avants plan $F_D(\hat{n})$ and $F_S(\hat{n})$ dans l'Eq. (A.40) sont respectivement basés sur les cartes à 353 GHz et 30 GHz.

Nous introduisons le coefficients d'avant-plan $\alpha(\hat{n})$, utilisant l'Eq. (A.40),

$$\alpha_f^\nu(\hat{n}) \equiv \frac{f^\nu(\hat{n})}{f^\mu(\hat{n})} \quad (\text{A.41})$$

$$= \frac{g_f(\nu, \hat{n})}{g_f(\mu, \hat{n})}, \quad (\text{A.42})$$

avec $f^\nu \in \{D, S\}$ le signal de la poussière où du synchrotron à la fréquence ν . Nous choisissons une fréquence de référence à $\mu = 353$ GHz pour la poussière, et $\mu = 30$ GHz pour le synchrotron.

Méthode template-fitting

Une solution simple et puissante pour obtenir une estimation du CMB nettoyée des contaminations d'avant-plan est de soustraire d'un set de données $d(\hat{n})$ un modèle de contamination d'avant-plan $t(\hat{n})$ pondéré par α_i .

$$\hat{s}(\hat{n}) = d(\hat{n}) - \sum_i^n \alpha_i(\hat{n}) \cdot t_i(\hat{n}). \quad (\text{A.43})$$

Résultat

Nous avons étudié le nettoyage des contaminants de premier plan à l'aide d'ensembles de simulations du signal polarisé. Celles-ci contiennent le signal du CMB, du bruit instrumental, et le signal des contaminants de premier plan contenant seulement la poussière et le rayonnement synchrotron.

Les incertitudes sur l'estimation des coefficients des avant-plans, α , sont comparées sur la Fig. A.3, à l'aide des simulations du module Python Sky Model (PySM) (Thorne et al. 2017). Nous considérons quatre catégories de méthodes que nous avons développé :

- les régression linéaire normalisée, **xnLR**,
- la régression linéaire ordinaire appliquée sur des cartes lissées à l'aide d'une fonction Gaussienne de 3° , **s₃oLR**,
- la régression ordinaire dont les variances sont soustraites, **v_{cn}oLR**,
- un algorithme de Newton-Raphson permettant de maximiser la fonction de vraisemblance, **MLE**.

Les estimateurs **xnLR** et **MLE** fournissent les incertitudes les plus faibles. La **xnLR** est la plus facile et rapide à implémenter. La méthode **v_{cn}oLR** est la méthode la moins sûre, car elle repose sur une estimation précise du bruit de l'ensemble de données et des variances du CMB pour soustraire le biais de l'estimateur.

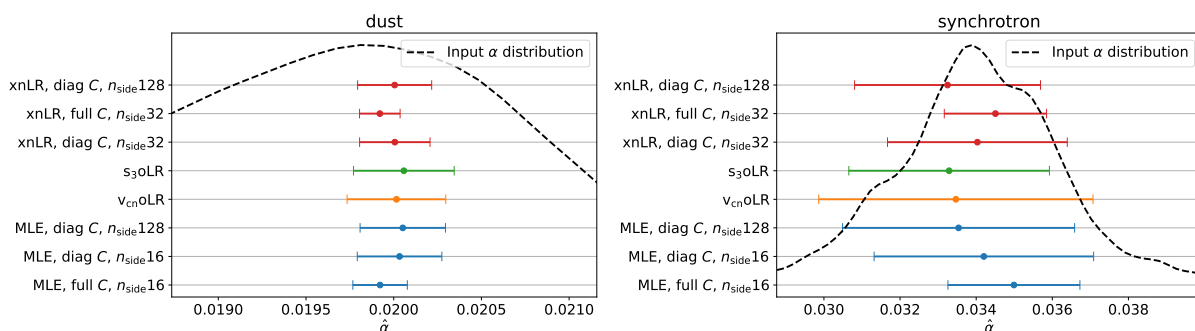


Figure A.3: Comparaison des incertitudes sur l'estimation de $\hat{\alpha}$ pour la poussière (gauche) et le synchrotron (droite) à 100 GHz. La distribution du signal sur le ciel est indiquée par les lignes pointillées.

4 Estimateur de spectres

Afin de contraindre le modèle cosmologique, les anisotropies du CMB sont projetés dans l'espace harmonique, avec leurs statistiques encodées dans les spectres de puissance angulaire C_ℓ^{XY} , où ℓ est le multipole, et $X, Y \in \{T, E, B\}$. Comme les anisotropies du CMB ont une statistique Gaussienne, toutes l'information cosmologiques est contenue dans la fonction C_ℓ . Les spectres de puissance estimés à partir des mesures du CMB, \hat{C}_ℓ , peuvent être comparés au modèle cosmologique $C_\ell(\theta)$ en utilisant une fonction de vraisemblance, afin d'estimer les paramètres du modèle cosmologique θ . L'utilisation de la technique des pseudo-spectres de puissance permet de calculer la fonction de vraisemblance jusqu'à de petites échelles angulaires sur le ciel dans une quantité raisonnable de puissance de calcul, tandis qu'une fonction de vraisemblance travaillant dans l'espace des pixels est limitée aux données CMB à faible résolution en raison de son coût de calcul. Dans cette partie, nous nous concentrerons sur l'estimation des spectres de puissance de polarisation E et B à grande échelle à partir des cartes de polarisation Q et U .

4.1 Estimateur maximum de vraisemblance quadratique

Pour cette partie, nous avons dérivé un estimateur de spectre travaillant dans l'espace des pixels et qui nous permet de cross-corréler différents set de données du CMB. La méthode est très similaire à l'estimateur maximum de vraisemblance quadratique (QML). Elle n'exige donc pas une connaissance précise des matrices de covariance de bruit des données pour soustraire le biais due au bruit instrumental. L'estimateur, par construction, fournit des barres d'erreur quasi minimales. La variance de l'estimateur n'est sensible qu'aux perturbations de second ordre de la matrice de covariance des pixels. De plus, en n'utilisant aucune corrélation TQ et TU pour la construction de cette matrice, l'analyse de la température et de la polarisation peut être faite complètement séparément. Nous fournissons une mise en œuvre publique de la méthode `xQML`, disponible sur Gitlab : <https://gitlab.in2p3.fr/xQML>.

4.2 Comparaison avec d'autres méthodes

Nous avons montré que l'estimateur `xQML` est non-biaisé, et que les barres d'erreur sur le spectre estimé, obtenues à partir des simulations de Monte-Carlo, correspondent à la variance analytique dérivée. La source des fuites de polarisation E-vers-B peut être identifiée dans la matrice de mélange de mode $W_{\ell\ell'}$. L'incertitude des modes B sur les grandes échelles et pour de faibles niveaux de bruit est particulièrement affectée par le mélange de polarisation, avec un maximum de 80% d'augmentation pour les grandes échelles angulaires à 0.1 - 1, $\mu\text{K.arcmin}$. Puisque la méthode `xQML` minimise les corrélations entre les bins ainsi que le mélange de polarisation, les barres d'erreur résultantes correspondent donc à l'incertitude minimale réalisable lors de la réduction des fuites de variance de polarisation. Une comparaison avec le formalisme des pseudo-spectres pures est effectuée ci-après.

Pour les méthodes pure pCl, l'apodisation du masque est une tâche non négligeable pour les formes de masque complexes. L'apodisation isotrope naïve peut produire des fonctions de fenêtre qui ne sont pas dérivables. Ceci induit un biais sur l'estimation des spectres qui en résulte, principalement visible aux grandes échelles angulaires. L'autre processus d'apodisation, basé sur un solveur PCG, fournit des fonctions de fenêtre beaucoup plus lisses. Cependant, un inconvénient est que, pour que le solveur converge, les fenêtres doivent être optimisées sur des bins de multipoles plutôt que sur chaque multipole. Le binning est arbitraire, et son choix optimal doit être défini sur la base de simulations Monte-Carlo. De plus, l'optimisation doit être réalisée dès que de nouvelles couvertures de ciel ou de nouveaux niveaux de bruit sont envisagés. Nous avons également observé que le solveur perd la convergence lorsqu'on considère

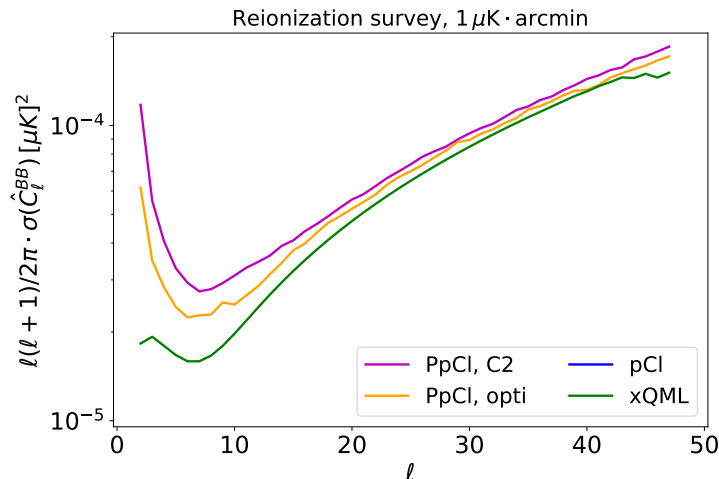


Figure A.4: Erreur sur l’estimation du spectre BB utilisant les méthodes \mathbf{xQML} , standard pseudo-spectre (pCl), et pure pseudo-spectre PpCl (pure pCl). Le niveau de bruit est $\sigma_n = 1 \mu\text{K}\cdot\text{arcmin}$, avec $r = 10^{-3}$.

les grandes échelles et de faibles niveaux de bruit. Enfin, en général, les méthodes de pseudo-spectres montrent une variance beaucoup plus élevée à bas ℓ ($\lesssim 10$) que la famille \mathbf{xQML} . Cet effet est d’autant plus visible que le ratio tenseur-scalaire bas r est pris en compte.

Par rapport au formalisme du pseudo-spectre, la \mathbf{xQML} montre des améliorations significatives sur les barres d’erreur et les corrélations pour BB et EB . L’avantage particulier par rapport aux méthodes pures est qu’il ne nécessite aucun traitement de masque spécial. En raison du coût de calcul plus élevé de ce dernier ($\mathcal{O}(N_d^3)$ opérations) par rapport aux pseudo-spectres ($\mathcal{O}(N_d^3/2)$ opérations), la méthode \mathbf{xQML} ne peut pas être exécutée sur autant de multipoles que pour les pseudo-spectres. Pour toutes ces raisons, nous concluons que l’estimateur \mathbf{xQML} convient particulièrement à l’analyse des grandes échelles angulaires.

5 Analyse des données de *Planck*

5.1 Les données *Planck*

La mission *Planck* fournit publiquement des mesures de polarisation du ciel en longueur d’onde millimétrique. Ce chapitre se concentre sur l’extraction de deux paramètres cosmologiques : le rapport tenseur-scalaire r par les mesures en modes B, et le paramètre de réionisation τ par les mesures en modes E. En plus des données de *Planck*, nous appliquons également notre pipeline d’analyse aux simulations de bruit *end-to-end* (E2E) qui comprennent des erreurs systématiques réalistes. La validation sur des simulations réalistes incluant des systématiques est une étape cruciale pour évaluer la robustesse de notre analyse et propager l’incertitude à travers toutes les étapes jusqu’à l’estimation des paramètres cosmologiques. Elle nous permet également d’estimer la matrice de covariance spectrale croisée qui sera utilisée pour contraindre et estimer les postérieurs sur les paramètres cosmologiques via une analyse de maximum de vraisemblance.

5.2 Résultats

Nous avons fourni une procédure complète pour analyser les données de polarisation fournies par *Planck*, depuis le nettoyage des cartes jusqu’à l’estimation des spectres croisés et des contraintes

sur les paramètres cosmologiques.

Le nettoyage des avant-plans nous a permis de tester la robustesse des différentes approches de nettoyage que nous avons proposées précédemment en considérant ici des réalisations de bruit plus complexes qui incluent des erreurs systématiques. A partir de nos résultats sur les données *Planck*, nous avons dérivé des contraintes sur les paramètres spectraux des avant-plans, pour lesquels les valeurs estimées sont conformes à des études similaires. D'autres travaux nous permettraient de mettre en évidence les variations des signaux d'avant-plans dans le ciel ou d'inclure d'autres ensembles de données comme celles fournies par WMAP.

L'application de notre implémentation de l'estimateur de spectre de puissance croisée travaillant dans l'espace des pixels, la méthode `xQML`, nous a permis de mettre en évidence le biais causé soit par les avant-plans, soit par les résidus systématiques de *Planck* présents dans les simulations. D'autres études pourraient être effectuées afin de quantifier l'amélioration de l'utilisation de la méthode `xQML` sur les données *Planck* comparées à l'aide de l'approche des pseudo-spectres purs.

L'estimation de la matrice de covariance des spectres croisés à partir de simulations MC est une étape cruciale afin de déterminer les paramètres cosmologiques à l'aide d'une analyse de maximum de vraisemblance. Nous avons utilisé l'approche `Lollipop` qui nous permet de calculer les postérieurs des paramètres dans le domaine harmonique et en utilisant des spectres croisés. Nous avons observé un élargissement significatif de l'incertitude lors de l'examen des simulations FFP10 au lieu de simulations avec purement du bruit blanc. Nous avons également remarqué la présence de biais lors de l'augmentation de la couverture du ciel, ce qui indique la présence de résidus en avant-plan.

Enfin, nous avons combiné les différents spectres croisés afin de dériver une contrainte finale sur τ et r . Considérant 70% du ciel, pour la profondeur de réionisation nous mesurons

$$\tau = 0.0604_{-0.0062}^{+0.0058} \quad (68 \% \text{ C.L.}) \quad (\text{A.44})$$

Ce résultat est à 1.5σ du résultat fourni par *Planck*, $\tau_{\text{PI}} = 0.0506 \pm 0.0086$ (68 % C.L.) ([Planck 2018 Results. VI.](#)). Pour baseline, ils n'utilisent que le spectre croisé 100x143, sur la plage multipoles $\ell \in [2, 29]$, et conservent 50% du ciel. Si nous considérons une configuration similaire à *Planck*, nous trouvons $0.0641_{-0.0160}^{+0.0133}$ (68 % C.L.). D'autres recherches sont nécessaires pour comprendre la différence de 150% entre nos barres d'erreur et celles de *Planck*.

Suivant la même approche, nous avons dérivé une limite supérieure sur le rapport tenseur-scalaire. Considérant 40% du ciel, nous mesurons

$$r \leq 0.3714 \quad (95 \% \text{ C.L.}) \quad (\text{A.45})$$

Ce résultat est compatible avec la contrainte *Planck* actuelle basée sur l'analyse du tenseur, $r_{\text{PI}} \leq 0.41$ ([Planck 2018 Results. X.](#)). Considérant la même configuration de pour *Planck*, utilisant seulement le spectre 100x143, $\ell \in [2, 29]$, et 50% du ciel, nous trouvons $r \leq 0.38$.

D'autres travaux sont nécessaires afin de mieux comprendre ces différences. Il convient d'étudier l'impact des choix des multipoles à faible concentration considérée dans la vraisemblance et d'examiner d'autres combinaisons de spectres croisés afin de mieux caractériser l'impact de chaque canal de fréquence sur les postérieurs. La corrélation entre r et τ doit également être estimée en combinant les modes E et B dans l'analyse de vraisemblance.

D'une manière plus générale, d'autres stratégies pour la construction des masques pourraient également être explorées, par exemple sur la base des résidus moyens au premier plan et systématiques au lieu de l'amplitude des poussières uniquement. D'autres approches consisteraient à adapter les masques de chaque canal de fréquence en fonction du niveau des signaux de synchrotron et de poussière ou du niveau des résidus. L'impact du choix du coefficient de

premier plan utilisé pour nettoyer les données devrait également être quantifié. Nous notons que nous n'avons fourni l'analyse que pour l'ensemble complet de données de mission. Le même pipeline pourrait être appliqué sur les cartes de demi-mission. Fournissant ainsi 45 spectres croisés au lieu de 10 (mais avec environ deux fois plus de bruit), et permettant des combinaisons plus différentes entre les canaux de fréquence pour construire la vraisemblance cosmologique.

Dans un avenir plus lointain, l'analyse que nous proposons dans ce chapitre pourrait être appliquée à d'autres missions de grande envergure, comme Litebird.

Bibliography

- Abazajian, Kevork N. et al. (Oct. 9, 2016). CMB-S4 Science Book, First Edition. arXiv: [1610.02743](#) [[astro-ph](#), [physics:gr-qc](#), [physics:hep-ph](#), [physics:hep-th](#)].
- Abitbol, Maximilian H. et al. (June 8, 2017). CMB-S4 Technology Book, First Edition. arXiv: [1706.02464](#) [[astro-ph](#)].
- Albrecht, Andreas and Paul J. Steinhardt (Apr. 26, 1982). Cosmology for Grand Unified Theories with Radiatively Induced Symmetry Breaking. *Physical Review Letters* 48.17. DOI: [10.1103/PhysRevLett.48.1220](#).
- Alonso, David, Javier Sanchez, and Anže Slosar (Jan. 16, 2019). A Unified Pseudo-Cl Framework. *Monthly Notices of the Royal Astronomical Society*. DOI: [10.1093/mnras/stz093](#). arXiv: [1809.09603](#).
- Alpher, R. A., H. Bethe, and G. Gamow (Apr. 1, 1948). The Origin of Chemical Elements. *Physical Review* 73.7. DOI: [10.1103/PhysRev.73.803](#).
- Alpher, Ralph A. and Robert Herman (Nov. 1948). Evolution of the Universe. *Nature* 162.4124. DOI: [10.1038/162774b0](#).
- Battye, R. A., I. W. A. Browne, M. W. Peel, N. J. Jackson, and C. Dickinson (May 1, 2011). Statistical Properties of Polarized Radio Sources at High Frequency and Their Impact on Cosmic Microwave Background Polarization Measurements: Properties of Polarized Radio Sources. *Monthly Notices of the Royal Astronomical Society* 413.1. DOI: [10.1111/j.1365-2966.2010.18115.x](#).
- Baumann, Daniel and Liam McAllister (Apr. 9, 2014). Inflation and String Theory. arXiv: [1404.2601](#) [[astro-ph](#), [physics:gr-qc](#), [physics:hep-ph](#), [physics:hep-th](#)].
- Benabed, K., J.-F. Cardoso, S. Prunet, and E. Hivon (Nov. 21, 2009). TEASING: A Fast and Accurate Approximation for the Low Multipole Likelihood of the Cosmic Microwave Background Temperature. *Monthly Notices of the Royal Astronomical Society* 400.1. DOI: [10.1111/j.1365-2966.2009.15202.x](#). arXiv: [0901.4537](#).
- Bennett, C. L. et al. (Sept. 20, 2013). Nine-Year Wilkinson Microwave Anisotropy Probe (WMAP) Observations: Final Maps and Results. *The Astrophysical Journal Supplement Series* 208.2. DOI: [10.1088/0067-0049/208/2/20](#). arXiv: [1212.5225](#).
- Bernstein, Jeremy, Lowell S. Brown, and Gerald Feinberg (Jan. 1, 1989). Cosmological Helium Production Simplified. *Reviews of Modern Physics* 61.1. DOI: [10.1103/RevModPhys.61.25](#).
- Béthermin, Matthieu et al. (Sept. 2013). The Redshift Evolution of the Distribution of Star Formation among Dark Matter Halos as Seen in the Infrared. *Astronomy & Astrophysics* 557. DOI: [10.1051/0004-6361/201321688](#).
- Blas, Diego, Julien Lesgourgues, and Thomas Tram (July 22, 2011). The Cosmic Linear Anisotropy Solving System (CLASS) II: Approximation Schemes. *Journal of Cosmology and Astroparticle Physics* 2011.07. DOI: [10.1088/1475-7516/2011/07/034](#). arXiv: [1104.2933](#).
- Bond, J. R., A. H. Jaffe, and L. Knox (Feb. 15, 1998). Estimating the Power Spectrum of the Cosmic Microwave Background. *Physical Review D* 57.4. DOI: [10.1103/PhysRevD.57.2117](#). arXiv: [astro-ph/9708203](#).
- Borrill, Julian (Nov. 19, 1999). MADCAP - The Microwave Anisotropy Dataset Computational Analysis Package. arXiv: [astro-ph/9911389](#).
- Brandt, W. N., C. R. Lawrence, A. C. S. Readhead, J. N. Pakianathan, and T. M. Fiola (Mar. 1994). Separation of Foreground Radiation from Cosmic Microwave Background Anisotropy Using Multifrequency Measurements. *The Astrophysical Journal* 424. DOI: [10.1086/173867](#).
- Bunn, Emory F. (Dec. 2003). Separating E from B. *New Astronomy Reviews* 47.11-12. DOI: [10.1016/j.newar.2003.09.021](#). arXiv: [astro-ph/0306003](#).
- Bunn, Emory F., Matias Zaldarriaga, Max Tegmark, and Angelica de Oliveira-Costa (Jan. 9, 2003). E/B Decomposition of Finite Pixelized CMB Maps. *Physical Review D* 67.2. DOI: [10.1103/PhysRevD.67.023501](#). arXiv: [astro-ph/0207338](#).
- Burles, Scott, Kenneth M. Nollett, and Michael S. Turner (Mar. 18, 1999). Big-Bang Nucleosynthesis: Linking Inner Space and Outer Space. arXiv: [astro-ph/9903300](#).
- Campanelli, L., A. D. Dolgov, M. Giannotti, and F. L. Villante (Nov. 20, 2004). Faraday Rotation of the Cosmic Microwave Background Polarization and Primordial Magnetic Field Properties. *The Astrophysical Journal* 616.1. DOI: [10.1086/424840](#). arXiv: [astro-ph/0405420](#).
- Caprini, Chiara, Ruth Durrer, and Tina Kahniashvili (Mar. 24, 2004). The Cosmic Microwave Background and Helical Magnetic Fields: The Tensor Mode. *Physical Review D* 69.6. DOI: [10.1103/PhysRevD.69.063006](#). arXiv: [astro-ph/0304556](#).
- Cardoso, Jean-François, Maude Le Jeune, Jacques Delabrouille, Marc Betoule, and Guillaume Patanchon (Oct. 2008). Component Separation With Flexible Models—Application to Multichannel Astrophysical Observations. *IEEE Journal of Selected Topics in Signal Processing* 2.5. DOI: [10.1109/JSTSP.2008.2005346](#).
- Carroll, Sean M. (Oct. 12, 1998). Quintessence and the Rest of the World. *Physical Review Letters* 81.15. DOI: [10.1103/PhysRevLett.81.3067](#). arXiv: [astro-ph/9806099](#).
- Challinor, Anthony and Hiranya Peiris (2009). Lecture Notes on the Physics of Cosmic Microwave Background Anisotropies. *AIP Conference Proceedings*. DOI: [10.1063/1.3151849](#). arXiv: [0903.5158](#).
- Choi, Steve K. and Lyman A. Page (Dec. 10, 2015). Polarized Galactic Synchrotron and Dust Emission and Their Correlation. *Journal of Cosmology and Astroparticle Physics* 2015.12. DOI: [10.1088/1475-7516/2015/12/020](#). arXiv: [1509.05934](#).
- Chon, Gayoung, Anthony Challinor, Simon Prunet, Eric Hivon, and István Szapudi (May 2004). Fast Estimation of Polarization Power Spectra Using Correlation Functions. *Monthly Notices of the Royal Astronomical Society* 350.3. DOI: [10.1111/j.1365-2966.2004.07737.x](#).
- Cline, James M. (Sept. 14, 2006). Baryogenesis. arXiv: [hep-ph/0609145](#).
- Coc, Alain and Elisabeth Vangioni (Aug. 2017). Primordial Nucleosynthesis. *International Journal of Modern Physics E* 26.08. DOI: [10.1142/S0218301317410026](#). arXiv: [1707.01004](#).

- De Terán, Fernando and Bruno Iannazzo (Mar. 2016). Uniqueness of Solution of a Generalized *-Sylvester Matrix Equation. *Linear Algebra and its Applications* 493. DOI: [10.1016/j.laa.2015.11.037](https://doi.org/10.1016/j.laa.2015.11.037).
- De Terán, Fernando, Bruno Iannazzo, Federico Poloni, and Leonardo Robol (Sept. 12, 2017). Nonsingular Systems of Generalized Sylvester Equations: An Algorithmic Approach. arXiv: [1709.03783 \[math\]](https://arxiv.org/abs/1709.03783).
- De Zotti, Gianfranco (Feb. 13, 2018). Prospects for next Generation Cosmic Microwave Background Experiments. arXiv: [1802.04753 \[astro-ph\]](https://arxiv.org/abs/1802.04753).
- Delabrouille, J., J.-F. Cardoso, and G. Patanchon (Dec. 2003). Multidetector Multicomponent Spectral Matching and Applications for Cosmic Microwave Background Data Analysis. *Monthly Notices of the Royal Astronomical Society* 346.4. DOI: [10.1111/j.1365-2966.2003.07069.x](https://doi.org/10.1111/j.1365-2966.2003.07069.x).
- Delabrouille, J. et al. (Jan. 2009). A Full Sky, Low Foreground, High Resolution CMB Map from WMAP. *Astronomy & Astrophysics* 493.3. DOI: [10.1051/0004-6361:200810514](https://doi.org/10.1051/0004-6361:200810514).
- Delabrouille, J. et al. (May 2013). The Pre-Launch *Planck* Sky Model: A Model of Sky Emission at Submillimetre to Centimetre Wavelengths. *Astronomy & Astrophysics* 553. DOI: [10.1051/0004-6361/201220019](https://doi.org/10.1051/0004-6361/201220019).
- Delabrouille, J. et al. (Apr. 5, 2018). Exploring Cosmic Origins with CORE: Survey Requirements and Mission Design. *Journal of Cosmology and Astroparticle Physics* 2018.04. DOI: [10.1088/1475-7516/2018/04/014](https://doi.org/10.1088/1475-7516/2018/04/014). arXiv: [1706.04516](https://arxiv.org/abs/1706.04516).
- Dickinson, Clive et al. (Feb. 2018). The State-of-Play of Anomalous Microwave Emission (AME) Research. *New Astronomy Reviews* 80. DOI: [10.1016/j.newar.2018.02.001](https://doi.org/10.1016/j.newar.2018.02.001). arXiv: [1802.08073](https://arxiv.org/abs/1802.08073).
- Ding, Feng and Tongwen Chen (Feb. 2005). Iterative Least-Squares Solutions of Coupled Sylvester Matrix Equations. *Systems & Control Letters* 54.2. DOI: [10.1016/j.sysconle.2004.06.008](https://doi.org/10.1016/j.sysconle.2004.06.008).
- Dodelson, Scott (Mar. 27, 2003). *Modern Cosmology*. Academic Press. 461 pp. Google Books: [3oPRxdXJexcC](https://books.google.com/books?id=3oPRxdXJexcC).
- Doré, Olivier et al. (Aug. 3, 2007). The Signature of Patchy Reionization in the Polarization Anisotropy of the CMB. *Physical Review D* 76.4. DOI: [10.1103/PhysRevD.76.043002](https://doi.org/10.1103/PhysRevD.76.043002). arXiv: [astro-ph/0701784](https://arxiv.org/abs/astro-ph/0701784).
- Efstathiou, G. (Apr. 2004). Myths and Truths Concerning Estimation of Power Spectra: The Case for a Hybrid Estimator. *Monthly Notices of the Royal Astronomical Society* 349.2. DOI: [10.1111/j.1365-2966.2004.07530.x](https://doi.org/10.1111/j.1365-2966.2004.07530.x).
- (July 21, 2006). Hybrid Estimation of CMB Polarization Power Spectra. *Monthly Notices of the Royal Astronomical Society* 370.1. DOI: [10.1111/j.1365-2966.2006.10486.x](https://doi.org/10.1111/j.1365-2966.2006.10486.x). arXiv: [astro-ph/0601107](https://arxiv.org/abs/astro-ph/0601107).
- Efstathiou, G., S. Gratton, and F. Paci (Aug. 11, 2009). Impact of Galactic Polarized Emission on B-Mode Detection at Low Multipoles. *Monthly Notices of the Royal Astronomical Society* 397.3. DOI: [10.1111/j.1365-2966.2009.14995.x](https://doi.org/10.1111/j.1365-2966.2009.14995.x).
- Eriksen, H. K., A. J. Banday, K. M. Gorski, and P. B. Lilje (Sept. 10, 2004). On Foreground Removal from the *Wilkinson Microwave Anisotropy Probe* Data by an Internal Linear Combination Method: Limitations and Implications. *The Astrophysical Journal* 612.2. DOI: [10.1086/422807](https://doi.org/10.1086/422807).
- Eriksen, H. K. et al. (Apr. 20, 2006a). CMB Component Separation by Parameter Estimation. *The Astrophysical Journal* 641.2. DOI: [10.1086/500499](https://doi.org/10.1086/500499). arXiv: [astro-ph/0508268](https://arxiv.org/abs/astro-ph/0508268).
- (Apr. 20, 2006b). Cosmic Microwave Background Component Separation by Parameter Estimation. *The Astrophysical Journal* 641.2. DOI: [10.1086/500499](https://doi.org/10.1086/500499).
- Eriksen, H. K. et al. (Mar. 20, 2008). Joint Bayesian Component Separation and CMB Power Spectrum Estimation. *The Astrophysical Journal* 676.1. DOI: [10.1086/525277](https://doi.org/10.1086/525277).
- Fernández-Cobos, R., A. Marcos-Caballero, P. Vielva, E. Martínez-González, and R. B. Barreiro (June 11, 2016). Exploring Two-Spin Internal Linear Combinations of the Recovery of the CMB Polarization. *Monthly Notices of the Royal Astronomical Society* 459.1. DOI: [10.1093/mnras/stw670](https://doi.org/10.1093/mnras/stw670). arXiv: [1601.01515](https://arxiv.org/abs/1601.01515).
- Ferte, A., J. Grain, M. Tristram, and R. Stompor (July 19, 2013). Efficiency of Pseudo-Spectrum Methods for Estimation of Cosmic Microwave Background B-Mode Power Spectrum. *Physical Review D* 88.2. DOI: [10.1103/PhysRevD.88.023524](https://doi.org/10.1103/PhysRevD.88.023524). arXiv: [1305.7441](https://arxiv.org/abs/1305.7441).
- Ferté, A., J. Peloton, J. Grain, and R. Stompor (Oct. 9, 2015). Detecting the Tensor-to-Scalar Ratio with the Pure Pseudo-spectrum Reconstruction of B-Mode. *Physical Review D* 92.8. DOI: [10.1103/PhysRevD.92.083510](https://doi.org/10.1103/PhysRevD.92.083510). arXiv: [1506.06409](https://arxiv.org/abs/1506.06409).
- Finkbeiner, Douglas P., Marc Davis, and David J. Schlegel (Oct. 20, 1999). Extrapolation of Galactic Dust Emission at 100 Microns to CMBR Frequencies Using FIRAS. *The Astrophysical Journal* 524.2. DOI: [10.1086/307852](https://doi.org/10.1086/307852). arXiv: [astro-ph/9905128](https://arxiv.org/abs/astro-ph/9905128).
- Fuskeland, U., I. K. Wehus, H. K. Eriksen, and S. K. Næss (July 10, 2014). Spatial Variations in the Spectral Index of Polarized Synchrotron Emission in the 9 Yr WMAP Sky Maps. *The Astrophysical Journal* 790.2. DOI: [10.1088/0004-637X/790/2/104](https://doi.org/10.1088/0004-637X/790/2/104). arXiv: [1404.5323](https://arxiv.org/abs/1404.5323).
- Galitzki, Nicholas (Oct. 4, 2018). The Simons Observatory: Project Overview. arXiv: [1810.02465 \[astro-ph\]](https://arxiv.org/abs/1810.02465).
- Gamow, G. (Oct. 1948). The Evolution of the Universe. *Nature* 162.4122. DOI: [10.1038/162680a0](https://doi.org/10.1038/162680a0).
- Génova-Santos, R. et al. (Feb. 1, 2017). QUIJOTE Scientific Results. II. Polarisation Measurements of the Microwave Emission in the Galactic Molecular Complexes W43 and W47 and Supernova Remnant W44. *Monthly Notices of the Royal Astronomical Society* 464.4. DOI: [10.1093/mnras/stw2503](https://doi.org/10.1093/mnras/stw2503). arXiv: [1605.04741](https://arxiv.org/abs/1605.04741).
- Gold, B. et al. (Feb. 1, 2011). SEVEN-YEAR WILKINSON MICROWAVE ANISOTROPY PROBE (WMAP) OBSERVATIONS: GALACTIC FOREGROUND EMISSION. *The Astrophysical Journal Supplement Series* 192.2. DOI: [10.1088/0067-0049/192/2/15](https://doi.org/10.1088/0067-0049/192/2/15).
- Goldreich, P. and N. D. Kylafis (Feb. 1982). Linear Polarization of Radio Frequency Lines in Molecular Clouds and Circumstellar Envelopes. *The Astrophysical Journal* 253. DOI: [10.1086/159663](https://doi.org/10.1086/159663).
- Gorski, K M et al. (Mar. 31, 1994). On Determining the Spectrum of Primordial Inhomogeneity from the COBE1 DMR Sky Maps: II. Results of Two Year Data Analysis.
- Gorski, K. M. et al. (Apr. 2005). HEALPix – a Framework for High Resolution Discretization, and Fast Analysis of Data Distributed on the Sphere. *The Astrophysical Journal* 622.2. DOI: [10.1086/427976](https://doi.org/10.1086/427976). arXiv: [astro-ph/0409513](https://arxiv.org/abs/astro-ph/0409513).
- Grain, Julien, Matthieu Tristram, and Radek Stompor (June 22, 2009). Polarized CMB Power Spectrum Estimation Using the Pure Pseudo-Cross-Spectrum Approach. *Physical Review D* 79.12. DOI: [10.1103/PhysRevD.79.123515](https://doi.org/10.1103/PhysRevD.79.123515). arXiv: [0903.2350](https://arxiv.org/abs/0903.2350).
- Grain, Julien, Matthieu Tristram, and Radek Stompor (Oct. 3, 2012). CMB EB and TB Cross-Spectrum Estimation via Pseudo-Spectrum Techniques. *Physical Review D* 86.7. DOI: [10.1103/PhysRevD.86.076005](https://doi.org/10.1103/PhysRevD.86.076005). arXiv: [1207.5344](https://arxiv.org/abs/1207.5344).
- Guth, Alan H. (Jan. 15, 1981). Inflationary Universe: A Possible Solution to the Horizon and Flatness Problems. *Physical Review D* 23.2. DOI: [10.1103/PhysRevD.23.347](https://doi.org/10.1103/PhysRevD.23.347).

- Hamimeche, Samira and Antony Lewis (May 28, 2008). Likelihood Analysis of CMB Temperature and Polarization Power Spectra. *Physical Review D* 77.10. DOI: [10.1103/PhysRevD.77.103013](https://doi.org/10.1103/PhysRevD.77.103013). arXiv: [0801.0554](https://arxiv.org/abs/0801.0554).
- Haslam, C. G. T., C. J. Salter, H. Stoffel, and W. E. Wilson (1982). A 408 MHz All-Sky Continuum Survey. II. The Atlas of Contour Maps. *Astron. Astrophys. Suppl. Ser.* 47.
- Hazumi, M. et al. (Mar. 2019). LiteBIRD: A Satellite for the Studies of B-Mode Polarization and Inflation from Cosmic Background Radiation Detection. *Journal of Low Temperature Physics* 194.5-6. DOI: [10.1007/s10909-019-02150-5](https://doi.org/10.1007/s10909-019-02150-5).
- Henning, J. W. et al. (Jan. 11, 2018). Measurements of the Temperature and E-Mode Polarization of the CMB from 500 Square Degrees of SPTpol Data. *The Astrophysical Journal* 852.2. DOI: [10.3847/1538-4357/aa9ff4](https://doi.org/10.3847/1538-4357/aa9ff4). arXiv: [1707.09353](https://arxiv.org/abs/1707.09353).
- Hivon, E. et al. (Mar. 2002). MASTER of the CMB Anisotropy Power Spectrum: A Fast Method for Statistical Analysis of Large and Complex CMB Data Sets. *The Astrophysical Journal* 567.1. DOI: [10.1086/338126](https://doi.org/10.1086/338126). arXiv: [astro-ph/0105302](https://arxiv.org/abs/astro-ph/0105302).
- Hoang, Thiem, A. Lazarian, and P. G. Martin (Dec. 3, 2013). Constraint on the Polarization of Electric Dipole Emission from Spinning Dust. *The Astrophysical Journal* 779.2. DOI: [10.1088/0004-637X/779/2/152](https://doi.org/10.1088/0004-637X/779/2/152). arXiv: [1305.0276](https://arxiv.org/abs/1305.0276).
- Horn, Roger A and Charles R Johnson (1991). Topics in Matrix Analysis. OCLC: 14212321. Cambridge; New York: Cambridge University Press.
- Hu, Wayne (Jan. 20, 2000). Reionization Revisited: Secondary CMB Anisotropies and Polarization. *The Astrophysical Journal* 529.1. DOI: [10.1086/308279](https://doi.org/10.1086/308279). arXiv: [astro-ph/9907103](https://arxiv.org/abs/astro-ph/9907103).
- Hu, Wayne, Matthew M. Hedman, and Matias Zaldarriaga (Feb. 28, 2003). Benchmark Parameters for CMB Polarization Experiments. *Physical Review D* 67.4. DOI: [10.1103/PhysRevD.67.043004](https://doi.org/10.1103/PhysRevD.67.043004). arXiv: [astro-ph/0210096](https://arxiv.org/abs/astro-ph/0210096).
- Hubble, E. P. (Dec. 1926). Extragalactic Nebulae. *The Astrophysical Journal* 64. DOI: [10.1086/143018](https://doi.org/10.1086/143018).
- Hubble, Edwin (Mar. 15, 1929). A Relation between Distance and Radial Velocity among Extra-Galactic Nebulae. *Proceedings of the National Academy of Sciences* 15.3. DOI: [10.1073/pnas.15.3.168](https://doi.org/10.1073/pnas.15.3.168). pmid: [16577160](https://pubmed.ncbi.nlm.nih.gov/16577160/).
- Hui, Howard et al. (July 9, 2018). BICEP Array: A Multi-Frequency Degree-Scale CMB Polarimeter. *Millimeter, Sub-millimeter, and Far-Infrared Detectors and Instrumentation for Astronomy IX*. DOI: [10.1117/12.2311725](https://doi.org/10.1117/12.2311725). arXiv: [1808.00568](https://arxiv.org/abs/1808.00568).
- Kahniashvili, Tina, Bharat Ratra, and ; (May 20, 2005). Effects of Cosmological Magnetic Helicity on the Cosmic Microwave Background. *Physical Review D* 71.10. DOI: [10.1103/PhysRevD.71.103006](https://doi.org/10.1103/PhysRevD.71.103006). arXiv: [astro-ph/0503709](https://arxiv.org/abs/astro-ph/0503709).
- Kamionkowski, Marc, Arthur Kosowsky, and Albert Stebbins (June 15, 1997). Statistics of Cosmic Microwave Background Polarization. *Physical Review D* 55.12. DOI: [10.1103/PhysRevD.55.7368](https://doi.org/10.1103/PhysRevD.55.7368). arXiv: [astro-ph/9611125](https://arxiv.org/abs/astro-ph/9611125).
- Kamionkowski, Marc and Ely D. Kovetz (Sept. 19, 2016). The Quest for B Modes from Inflationary Gravitational Waves. *Annual Review of Astronomy and Astrophysics* 54.1. DOI: [10.1146/annurev-astro-081915-023433](https://doi.org/10.1146/annurev-astro-081915-023433).
- Katayama, Nobuhiko and Eiichiro Komatsu (Aug. 20, 2011). SIMPLE FOREGROUND CLEANING ALGORITHM FOR DETECTING PRIMORDIAL B -MODE POLARIZATION OF THE COSMIC MICROWAVE BACKGROUND. *The Astrophysical Journal* 737.2. DOI: [10.1088/0004-637X/737/2/78](https://doi.org/10.1088/0004-637X/737/2/78).
- Keck Array/BICEP2 October 2015 Data Products (2018). URL: http://bicepkeck.org/bk14_2015_release.html (visited on 06/26/2018).
- Keskitalo, R. et al. (Nov. 2010). Residual Noise Covariance for Planck Low-Resolution Data Analysis. *Astronomy & Astrophysics* 522. DOI: [10.1051/0004-6361/200912606](https://doi.org/10.1051/0004-6361/200912606). arXiv: [0906.0175](https://arxiv.org/abs/0906.0175).
- Kim, Jaiseung, Pavel Naselsky, and Per Rex Christensen (Jan. 21, 2009). CMB Polarization Map Derived from the WMAP 5 Year Data through Harmonic Internal Linear Combination. *Physical Review D* 79.2. DOI: [10.1103/PhysRevD.79.023003](https://doi.org/10.1103/PhysRevD.79.023003). arXiv: [0810.4008](https://arxiv.org/abs/0810.4008).
- Kogut, A. et al. (June 10, 1996). Microwave Emission at High Galactic Latitudes. *The Astrophysical Journal* 464.1. DOI: [10.1086/310072](https://doi.org/10.1086/310072). arXiv: [astro-ph/9601060](https://arxiv.org/abs/astro-ph/9601060).
- Kogut, A. et al. (Sept. 2003). First-Year Wilkinson Microwave Anisotropy Probe (WMAP) Observations: Temperature-Polarization Correlation. *The Astrophysical Journal Supplement Series* 148.1. DOI: [10.1086/377219](https://doi.org/10.1086/377219).
- Kosowsky, Arthur (Feb. 1995). Cosmic Microwave Background Polarization.
- Krachmalnicoff, N. et al. (Oct. 2018). The S-PASS View of Polarized Galactic Synchrotron at 2.3 GHz as a Contaminant to CMB Observations. *Astronomy & Astrophysics* 618. DOI: [10.1051/0004-6361/201832768](https://doi.org/10.1051/0004-6361/201832768). arXiv: [1802.01145](https://arxiv.org/abs/1802.01145).
- Leitch, E. M., A. C. S. Readhead, T. J. Pearson, and S. T. Myers (Sept. 1, 1997). An Anomalous Component of Galactic Emission. *The Astrophysical Journal* 486.1. DOI: [10.1086/310823](https://doi.org/10.1086/310823).
- Lemaître, G. (1927). Un Univers Homogène de Masse Constante et de Rayon Croissant Rendant Compte de La Vitesse Radiale Des Nébuleuses Extra-Galactiques. *Annales de la Société Scientifique de Bruxelles* 47.
- Lemaître, Georges (1950). The Primeval Atom an Essay on Cosmogony. Van Nostrand.
- Lesgourgues, Julien and Sergio Pastor (July 2006). Massive Neutrinos and Cosmology. *Physics Reports* 429.6. DOI: [10.1016/j.physrep.2006.04.001](https://doi.org/10.1016/j.physrep.2006.04.001). arXiv: [astro-ph/0603494](https://arxiv.org/abs/astro-ph/0603494).
- Lewis, Antony (Oct. 22, 2003). Harmonic E/B Decomposition for CMB Polarization Maps. *Physical Review D* 68.8. DOI: [10.1103/PhysRevD.68.083509](https://doi.org/10.1103/PhysRevD.68.083509). arXiv: [astro-ph/0305545](https://arxiv.org/abs/astro-ph/0305545).
- Lewis, Antony and Anthony Challinor (June 2006). Weak Gravitational Lensing of the CMB. *Physics Reports* 429.1. DOI: [10.1016/j.physrep.2006.03.002](https://doi.org/10.1016/j.physrep.2006.03.002). arXiv: [astro-ph/0601594](https://arxiv.org/abs/astro-ph/0601594).
- Lewis, Antony, Anthony Challinor, and Anthony Lasenby (Aug. 2000). Efficient Computation of CMB Anisotropies in Closed FRW Models. *The Astrophysical Journal* 538.2. DOI: [10.1086/309179](https://doi.org/10.1086/309179). arXiv: [astro-ph/9911177](https://arxiv.org/abs/astro-ph/9911177).
- Lewis, Antony, Anthony Challinor, and Neil Turok (Dec. 19, 2001). Analysis of CMB Polarization on an Incomplete Sky. *Physical Review D* 65.2. DOI: [10.1103/PhysRevD.65.023505](https://doi.org/10.1103/PhysRevD.65.023505). arXiv: [astro-ph/0106536](https://arxiv.org/abs/astro-ph/0106536).
- Li, Hua-bai and Thomas Henning (Nov. 2011). The Alignment of Molecular Cloud Magnetic Fields with the Spiral Arms in M33. *Nature* 479.7374. DOI: [10.1038/nature10551](https://doi.org/10.1038/nature10551).
- Lin, Yiqin, Liang Bao, and Yimin Wei (Nov. 2010). Matrix Sign Function Methods for Solving Projected Generalized Continuous-Time Sylvester Equations. *IEEE Transactions on Automatic Control* 55.11. DOI: [10.1109/TAC.2010.2064590](https://doi.org/10.1109/TAC.2010.2064590).
- Linde, A D (1982). A NEW INFLATIONARY UNIVERSE SCENARIO: A POSSIBLE SOLUTION OF THE HORIZON, FLATNESS, HOMOGENEITY, ISOTROPY AND PRIMORDIAL MONOPOLE PROBLEMS. *PHYSICS LETTERS* 108.6.
- Loeb, Abraham and Arthur Kosowsky (Sept. 1996). Faraday Rotation of Microwave Background Polarization by a Primordial Magnetic Field. *The Astrophysical Journal* 469. DOI: [10.1086/177751](https://doi.org/10.1086/177751). arXiv: [astro-ph/9601055](https://arxiv.org/abs/astro-ph/9601055).

- Louis, Thibaut et al. (June 15, 2017). The Atacama Cosmology Telescope: Two-Season ACTPol Spectra and Parameters. *Journal of Cosmology and Astroparticle Physics* 2017.06. DOI: [10.1088/1475-7516/2017/06/031](https://doi.org/10.1088/1475-7516/2017/06/031). arXiv: [1610.02360](https://arxiv.org/abs/1610.02360).
- Lue, Arthur, Limin Wang, and Marc Kamionkowski (Aug. 23, 1999). Cosmological Signature of New Parity-Violating Interactions. *Physical Review Letters* 83.8. DOI: [10.1103/PhysRevLett.83.1506](https://doi.org/10.1103/PhysRevLett.83.1506). arXiv: [astro-ph/9812088](https://arxiv.org/abs/astro-ph/9812088).
- Luminet, Jean-Pierre (Aug. 2013). Editorial Note to "A Homogeneous Universe of Constant Mass and Increasing Radius Accounting for the Radial Velocity of Extra-Galactic Nebulae" by Georges Lemaître (1927). *General Relativity and Gravitation* 45.8. DOI: [10.1007/s10714-013-1547-4](https://doi.org/10.1007/s10714-013-1547-4). arXiv: [1305.6470](https://arxiv.org/abs/1305.6470).
- Macellari, N., E. Pierpaoli, C. Dickinson, and J. Vaillancourt (Dec. 1, 2011). Galactic Foreground Contributions to the WMAP5 Maps. *Monthly Notices of the Royal Astronomical Society* 418.2. DOI: [10.1111/j.1365-2966.2011.19542.x](https://doi.org/10.1111/j.1365-2966.2011.19542.x). arXiv: [1108.0205](https://arxiv.org/abs/1108.0205).
- Mangilli, A., S. Plaszczynski, and M. Tristram (Nov. 1, 2015). Large-Scale CMB Temperature and Polarization Cross-Spectra Likelihoods. *Monthly Notices of the Royal Astronomical Society* 453.3. DOI: [10.1093/mnras/stv1733](https://doi.org/10.1093/mnras/stv1733). arXiv: [1503.01347](https://arxiv.org/abs/1503.01347).
- Martin, Jerome, Christophe Ringeval, and Vincent Vennin (Mar. 15, 2013). Encyclopaedia Inflationaris. arXiv: [1303.3787](https://arxiv.org/abs/1303.3787) [[astro-ph](https://arxiv.org/abs/astro-ph), [physics:gr-qc](https://arxiv.org/abs/physics/gr-qc), [physics:hep-ph](https://arxiv.org/abs/physics/hep-ph), [physics:hep-th](https://arxiv.org/abs/physics/hep-th)].
- Mather, J. C. et al. (Jan. 1994). Measurement of the Cosmic Microwave Background Spectrum by the COBE FIRAS Instrument. *The Astrophysical Journal* 420. DOI: [10.1086/173574](https://doi.org/10.1086/173574).
- Matsumura, T. et al. (Sept. 2014). Mission Design of LiteBIRD. *Journal of Low Temperature Physics* 176.5-6. DOI: [10.1007/s10909-013-0996-1](https://doi.org/10.1007/s10909-013-0996-1). arXiv: [1311.2847](https://arxiv.org/abs/1311.2847).
- Matthews, Brenda C., Christie A. McPhee, Laura M. Fissel, and Rachel L. Curran (May 1, 2009). THE LEGACY OF SCUPOL: 850 Mum IMAGING POLARIMETRY FROM 1997 TO 2005. *The Astrophysical Journal Supplement Series* 182.1. DOI: [10.1088/0067-0049/182/1/143](https://doi.org/10.1088/0067-0049/182/1/143).
- Meisner, Aaron and Douglas Finkbeiner (Dec. 30, 2014). Modeling Thermal Dust Emission with Two Components: Application to the Planck HFI Maps. *The Astrophysical Journal* 798.2. DOI: [10.1088/0004-637X/798/2/88](https://doi.org/10.1088/0004-637X/798/2/88). arXiv: [1410.7523](https://arxiv.org/abs/1410.7523).
- Miville-Deschenes, M.-A. et al. (Nov. 2008). Separation of Anomalous and Synchrotron Emissions Using WMAP Polarization Data. *Astronomy & Astrophysics* 490.3. DOI: [10.1051/0004-6361/200809484](https://doi.org/10.1051/0004-6361/200809484). arXiv: [0802.3345](https://arxiv.org/abs/0802.3345).
- Molinari, D. et al. (May 11, 2014). A Comparison of CMB Angular Power Spectrum Estimators at Large Scales: The TT Case. *Monthly Notices of the Royal Astronomical Society* 440.2. DOI: [10.1093/mnras/stu386](https://doi.org/10.1093/mnras/stu386).
- Ned Wright's Cosmology Tutorial - Part 1 (2019). URL: http://www.astro.ucla.edu/~wright/cosmo_01.htm (visited on 06/05/2019).
- Ng, Kin-Wang and Guo-Chin Liu (Feb. 1999). Correlation Functions of CMB Anisotropy and Polarization. *International Journal of Modern Physics D* 08.01. DOI: [10.1142/S0218271899000079](https://doi.org/10.1142/S0218271899000079). arXiv: [astro-ph/9710012](https://arxiv.org/abs/astro-ph/9710012).
- Page, L. et al. (June 2007). Three Year Wilkinson Microwave Anisotropy Probe (WMAP) Observations: Polarization Analysis. *The Astrophysical Journal Supplement Series* 170.2. DOI: [10.1086/513699](https://doi.org/10.1086/513699). arXiv: [astro-ph/0603450](https://arxiv.org/abs/astro-ph/0603450).
- Patriota, A.G., H. Bolfarine, and M. de Castro (July 2009). A Heteroscedastic Structural Errors-in-Variables Model with Equation Error. *Statistical Methodology* 6.4. DOI: [10.1016/j.stamet.2009.02.003](https://doi.org/10.1016/j.stamet.2009.02.003).
- Penzias, A. A., P. M. Solomon, K. B. Jefferts, and R. W. Wilson (May 1972). Carbon Monoxide Observations of Dense Interstellar Clouds. *The Astrophysical Journal* 174. DOI: [10.1086/180945](https://doi.org/10.1086/180945).
- Percival, Will J. and Michael L. Brown (Nov. 1, 2006). Likelihood Methods for the Combined Analysis of CMB Temperature and Polarisation Power Spectra. *Monthly Notices of the Royal Astronomical Society* 372.3. DOI: [10.1111/j.1365-2966.2006.10910.x](https://doi.org/10.1111/j.1365-2966.2006.10910.x). arXiv: [astro-ph/0604547](https://arxiv.org/abs/astro-ph/0604547).
- Peter, Patrick and Jean-Philippe Uzan (2009). *Primordial Cosmology*. English ed. OCLC: ocn313665248. Oxford ; New York: Oxford University Press. 836 pp.
- Planck Collaboration et al. (Nov. 2014a). Planck 2013 Results. XIII. Galactic CO Emission. *Astronomy & Astrophysics* 571. DOI: [10.1051/0004-6361/201321553](https://doi.org/10.1051/0004-6361/201321553). arXiv: [1303.5073](https://arxiv.org/abs/1303.5073).
- Planck Collaboration et al. (Nov. 2014b). Planck 2013 Results. XXX. Cosmic Infrared Background Measurements and Implications for Star Formation. *Astronomy & Astrophysics* 571. DOI: [10.1051/0004-6361/201322093](https://doi.org/10.1051/0004-6361/201322093).
- Planck Collaboration et al. (Apr. 2015). Planck Intermediate Results. XXII. Frequency Dependence of Thermal Emission from Galactic Dust in Intensity and Polarization. *Astronomy & Astrophysics* 576. DOI: [10.1051/0004-6361/201424088](https://doi.org/10.1051/0004-6361/201424088). arXiv: [1405.0874](https://arxiv.org/abs/1405.0874).
- Planck Collaboration et al. (Oct. 2016a). Planck 2015 Results: VI. LFI Mapmaking. *Astronomy & Astrophysics* 594. DOI: [10.1051/0004-6361/201525813](https://doi.org/10.1051/0004-6361/201525813).
- Planck Collaboration et al. (Oct. 2016b). Planck 2015 Results. X. Diffuse Component Separation: Foreground Maps. *Astronomy & Astrophysics* 594. DOI: [10.1051/0004-6361/201525967](https://doi.org/10.1051/0004-6361/201525967). arXiv: [1502.01588](https://arxiv.org/abs/1502.01588).
- Planck Collaboration et al. (Oct. 2016c). Planck 2015 Results. XI. CMB Power Spectra, Likelihoods, and Robustness of Parameters. *Astronomy & Astrophysics* 594. DOI: [10.1051/0004-6361/201526926](https://doi.org/10.1051/0004-6361/201526926). arXiv: [1507.02704](https://arxiv.org/abs/1507.02704).
- Planck Collaboration et al. (Oct. 2016d). Planck 2015 Results. XIII. Cosmological Parameters. *Astronomy & Astrophysics* 594. DOI: [10.1051/0004-6361/201525830](https://doi.org/10.1051/0004-6361/201525830). arXiv: [1502.01589](https://arxiv.org/abs/1502.01589).
- Planck Collaboration et al. (Dec. 2016e). Planck Intermediate Results: XLVI. Reduction of Large-Scale Systematic Effects in HFI Polarization Maps and Estimation of the Reionization Optical Depth. *Astronomy & Astrophysics* 596. DOI: [10.1051/0004-6361/201628890](https://doi.org/10.1051/0004-6361/201628890).
- Planck Collaboration et al. (July 17, 2018a). Planck 2018 Results. II. Low Frequency Instrument Data Processing. arXiv: [1807.06206](https://arxiv.org/abs/1807.06206) [[astro-ph](https://arxiv.org/abs/astro-ph)].
- Planck Collaboration et al. (July 17, 2018b). Planck 2018 Results. III. High Frequency Instrument Data Processing and Frequency Maps. arXiv: [1807.06207](https://arxiv.org/abs/1807.06207) [[astro-ph](https://arxiv.org/abs/astro-ph)].
- Planck Collaboration et al. (July 17, 2018c). Planck 2018 Results. IV. Diffuse Component Separation. arXiv: [1807.06208](https://arxiv.org/abs/1807.06208) [[astro-ph](https://arxiv.org/abs/astro-ph)].
- Planck Collaboration et al. (July 17, 2018d). Planck 2018 Results. VI. Cosmological Parameters. arXiv: [1807.06209](https://arxiv.org/abs/1807.06209) [[astro-ph](https://arxiv.org/abs/astro-ph)].
- Planck Collaboration et al. (July 17, 2018e). Planck 2018 Results. X. Constraints on Inflation. arXiv: [1807.06211](https://arxiv.org/abs/1807.06211) [[astro-ph](https://arxiv.org/abs/astro-ph)].
- Planck Collaboration et al. (Jan. 15, 2018f). Planck 2018 Results. XI. Polarized Dust Foregrounds. arXiv: [1801.04945](https://arxiv.org/abs/1801.04945) [[astro-ph](https://arxiv.org/abs/astro-ph)].

- Planck Legacy Archive (2019). URL: <https://pla.esac.esa.int/#home> (visited on 06/04/2019).
- Pogosian, Levon, Tanmay Vachaspati, and Serge Winitzki (Mar. 21, 2002). Signatures of Kinetic and Magnetic Helicity in the CMBR. *Physical Review D* 65.8. DOI: [10.1103/PhysRevD.65.083502](https://doi.org/10.1103/PhysRevD.65.083502). arXiv: [astro-ph/0112536](https://arxiv.org/abs/astro-ph/0112536).
- POLARBEAR Collaboration, POLARBEAR Collaboration et al. (Oct. 7, 2014a). A Measurement of the Cosmic Microwave Background B-Mode Polarization Power Spectrum at Sub-Degree Scales with POLARBEAR. *The Astrophysical Journal* 794.2. DOI: [10.1088/0004-637X/794/2/171](https://doi.org/10.1088/0004-637X/794/2/171). arXiv: [1403.2369](https://arxiv.org/abs/1403.2369).
- POLARBEAR Collaboration, POLARBEAR Collaboration et al. (Apr. 2, 2014b). Evidence for Gravitational Lensing of the Cosmic Microwave Background Polarization from Cross-Correlation with the Cosmic Infrared Background. *Physical Review Letters* 112.13. DOI: [10.1103/PhysRevLett.112.131302](https://doi.org/10.1103/PhysRevLett.112.131302). arXiv: [1312.6645](https://arxiv.org/abs/1312.6645).
- POLARBEAR Collaboration, POLARBEAR Collaboration et al. (July 9, 2014c). Measurement of the Cosmic Microwave Background Polarization Lensing Power Spectrum with the POLARBEAR Experiment. *Physical Review Letters* 113.2. DOI: [10.1103/PhysRevLett.113.021301](https://doi.org/10.1103/PhysRevLett.113.021301). arXiv: [1312.6646](https://arxiv.org/abs/1312.6646).
- Ramadan, Mohamed A. and Talaat S. El-Danaf (Mar. 2015). Solving the Generalized Coupled Sylvester Matrix Equations over Generalized Bisymmetric Matrices. *Transactions of the Institute of Measurement and Control* 37.3. DOI: [10.1177/0142331213509398](https://doi.org/10.1177/0142331213509398).
- Remazeilles, M., C. Dickinson, A. J. Banday, M.-A. Bigot-Sazy, and T. Ghosh (Oct. 17, 2014). An Improved Source-Subtracted and Destriped 408 MHz All-Sky Map. arXiv: [1411.3628](https://arxiv.org/abs/1411.3628) [[astro-ph](https://arxiv.org/abs/astro-ph)].
- Rogers, Keir K., Hiranya V. Peiris, Boris Leistedt, Jason D. McEwen, and Andrew Pontzen (Dec. 11, 2016). Spin-SILC: CMB Polarisation Component Separation with Spin Wavelets. *Monthly Notices of the Royal Astronomical Society* 463.3. DOI: [10.1093/mnras/stw2128](https://doi.org/10.1093/mnras/stw2128). arXiv: [1605.01417](https://arxiv.org/abs/1605.01417).
- Seljak, Uros and Matias Zaldarriaga (Oct. 1996). A Line of Sight Approach to Cosmic Microwave Background Anisotropies. *The Astrophysical Journal* 469. DOI: [10.1086/177793](https://doi.org/10.1086/177793). arXiv: [astro-ph/9603033](https://arxiv.org/abs/astro-ph/9603033).
- Simoncini, V. (Jan. 2016). Computational Methods for Linear Matrix Equations. *SIAM Review* 58.3. DOI: [10.1137/130912839](https://doi.org/10.1137/130912839).
- Slosar, A., U. Seljak, and A. Makarov (June 18, 2004). Exact Likelihood Evaluations and Foreground Marginalization in Low Resolution WMAP Data. *Physical Review D* 69.12. DOI: [10.1103/PhysRevD.69.123003](https://doi.org/10.1103/PhysRevD.69.123003). arXiv: [astro-ph/0403073](https://arxiv.org/abs/astro-ph/0403073).
- Smith, Kendrick M. (Oct. 4, 2006). Pseudo- $\mathcal{C}_{\ell\ell}$ Estimators Which Do Not Mix E and B Modes. *Physical Review D* 74.8. DOI: [10.1103/PhysRevD.74.083002](https://doi.org/10.1103/PhysRevD.74.083002). arXiv: [astro-ph/0511629](https://arxiv.org/abs/astro-ph/0511629).
- Smith, Kendrick M. and Matias Zaldarriaga (Aug. 2, 2007). A General Solution to the E-B Mixing Problem. *Physical Review D* 76.4. DOI: [10.1103/PhysRevD.76.043001](https://doi.org/10.1103/PhysRevD.76.043001). arXiv: [astro-ph/0610059](https://arxiv.org/abs/astro-ph/0610059).
- Smoot, George F. (1999). Summary of Results from COBE. *Conference on 3K cosmology*. DOI: [10.1063/1.59326](https://doi.org/10.1063/1.59326). arXiv: [astro-ph/9902027](https://arxiv.org/abs/astro-ph/9902027).
- Sunyaev, R. A. and Ya. B. Zel'dovich (Sept. 1969). Small-Scale Fluctuations of Relic Radiation.
 — (Sept. 1980a). Microwave Background Radiation as a Probe of the Contemporary Structure and History of the Universe. *Annual Review of Astronomy and Astrophysics* 18.1. DOI: [10.1146/annurev.aa.18.090180.002541](https://doi.org/10.1146/annurev.aa.18.090180.002541).
- Sunyaev, R. A. and Ya. B. Zel'dovich (Mar. 1, 1980b). The Velocity of Clusters of Galaxies Relative to the Microwave Background. The Possibility of Its Measurement. *Monthly Notices of the Royal Astronomical Society* 190.3. DOI: [10.1093/mnras/190.3.413](https://doi.org/10.1093/mnras/190.3.413).
- Tegmark, Max (May 15, 1997). How to Measure CMB Power Spectra without Losing Information. *Physical Review D* 55.10. DOI: [10.1103/PhysRevD.55.5895](https://doi.org/10.1103/PhysRevD.55.5895). arXiv: [astro-ph/9611174](https://arxiv.org/abs/astro-ph/9611174).
- Tegmark, Max and Angelica de Oliveira-Costa (Aug. 16, 2001). How to Measure CMB Polarization Power Spectra without Losing Information. *Physical Review D* 64.6. DOI: [10.1103/PhysRevD.64.063001](https://doi.org/10.1103/PhysRevD.64.063001). arXiv: [astro-ph/0012120](https://arxiv.org/abs/astro-ph/0012120).
- Tegmark, Max, Angelica de Oliveira-Costa, and Andrew Hamilton (Dec. 29, 2003). A High Resolution Foreground Cleaned CMB Map from WMAP. *Physical Review D* 68.12. DOI: [10.1103/PhysRevD.68.123523](https://doi.org/10.1103/PhysRevD.68.123523). arXiv: [astro-ph/0302496](https://arxiv.org/abs/astro-ph/0302496).
- The Simons Observatory Collaboration et al. (Feb. 27, 2019). The Simons Observatory: Science Goals and Forecasts. *Journal of Cosmology and Astroparticle Physics* 2019.02. DOI: [10.1088/1475-7516/2019/02/056](https://doi.org/10.1088/1475-7516/2019/02/056). arXiv: [1808.07445](https://arxiv.org/abs/1808.07445).
- Thorne, Ben, Jo Dunkley, David Alonso, and Sigurd Naess (Aug. 2017). The Python Sky Model: Software for Simulating the Galactic Microwave Sky. *Monthly Notices of the Royal Astronomical Society* 469.3. DOI: [10.1093/mnras/stx949](https://doi.org/10.1093/mnras/stx949). arXiv: [1608.02841](https://arxiv.org/abs/1608.02841).
- Tristram, M., J. F. Macias-Perez, C. Renault, and D. Santos (Apr. 11, 2005). Xspect, Estimation of the Angular Power Spectrum by Computing Cross-Power Spectra with Analytical Error Bars. *Monthly Notices of the Royal Astronomical Society* 358.3. DOI: [10.1111/j.1365-2966.2005.08760.x](https://doi.org/10.1111/j.1365-2966.2005.08760.x). arXiv: [astro-ph/0405575](https://arxiv.org/abs/astro-ph/0405575).
- Trodden, Mark and Sean M. Carroll (Jan. 26, 2004). TASI Lectures: Introduction to Cosmology. arXiv: [astro-ph/0401547](https://arxiv.org/abs/astro-ph/0401547).
- Tucci, M. and L. Toffolatti (2012). The Impact of Polarized Extragalactic Radio Sources on the Detection of CMB Anisotropies in Polarization. *Advances in Astronomy* 2012. DOI: [10.1155/2012/624987](https://doi.org/10.1155/2012/624987). arXiv: [1204.0427](https://arxiv.org/abs/1204.0427).
- Vanneste, S., S. Henrot-Versillé, T. Louis, and M. Tristram (Nov. 26, 2018). Quadratic Estimator for CMB Cross-Correlation. *Physical Review D* 98.10. DOI: [10.1103/PhysRevD.98.103526](https://doi.org/10.1103/PhysRevD.98.103526). arXiv: [1807.02484](https://arxiv.org/abs/1807.02484).
- Vansyngel, F. et al. (July 2017). Statistical Simulations of the Dust Foreground to Cosmic Microwave Background Polarization. *Astronomy & Astrophysics* 603. DOI: [10.1051/0004-6361/201629992](https://doi.org/10.1051/0004-6361/201629992).
- Wilson, R. W., K. B. Jefferts, and A. A. Penzias (July 1970). Carbon Monoxide in the Orion Nebula. *The Astrophysical Journal* 161. DOI: [10.1086/180567](https://doi.org/10.1086/180567).
- Xpure (2019). URL: <https://gitlab.in2p3.fr/xpure/Xpure> (visited on 04/10/2019).
- Yadav, Amit P. S., Meng Su, and Matias Zaldarriaga (Mar. 11, 2010). Primordial B-Mode Diagnostics and Self Calibrating the CMB Polarization. *Physical Review D* 81.6. DOI: [10.1103/PhysRevD.81.063512](https://doi.org/10.1103/PhysRevD.81.063512). arXiv: [0912.3532](https://arxiv.org/abs/0912.3532).
- Zaldarriaga, Matias (Feb. 15, 1997). Polarization of the Microwave Background in Reionized Models. *Physical Review D* 55.4. DOI: [10.1103/PhysRevD.55.1822](https://doi.org/10.1103/PhysRevD.55.1822). arXiv: [astro-ph/9608050](https://arxiv.org/abs/astro-ph/9608050).
- (Aug. 10, 1998). CMB Polarization Experiments. *The Astrophysical Journal* 503.1. DOI: [10.1086/305987](https://doi.org/10.1086/305987). arXiv: [astro-ph/9709271](https://arxiv.org/abs/astro-ph/9709271).
- Zaldarriaga, Matias and Uros Seljak (Feb. 15, 1997). An All-Sky Analysis of Polarization in the Microwave Background. *Physical Review D* 55.4. DOI: [10.1103/PhysRevD.55.1830](https://doi.org/10.1103/PhysRevD.55.1830). arXiv: [astro-ph/9609170](https://arxiv.org/abs/astro-ph/9609170).

Titre: Contraintes sur les ondes gravitationnelles primordiales à partir de données CMB à grande échelle

Mots clés: Cosmologie, analyse de données, fond diffus cosmologique, inflation

Résumé:

Cette thèse s'articule autour du développement d'outils d'analyse des modes B du fond diffus cosmologique (CMB) dans le but d'estimer l'amplitude des ondes gravitationnelles primordiales produites durant la période inflationnaire.

Nous nous intéressons plus précisément aux grandes échelles angulaires, pour lesquelles le signal attendu des modes B primordiaux est dominant. Ces échelles étant particulièrement contaminées par des émissions polarisées galactiques, nous avons étudié et développé des méthodes permettant de réduire ces contaminations et de caractériser les résidus. Ces outils peuvent être utilisés pour analyser les données des satellites tels que Planck ou LiteBIRD.

Afin de quantifier l'amplitude des modes B, nous

avons développé et caractérisé un estimateur de spectre en puissance des anisotropies du CMB. Celui-ci s'exécute dans l'espace des pixels et permet de croiser des cartes mesurées par différents détecteurs. La méthode est optimale, et minimise les fuites de variance des modes E vers les modes B.

Nous avons appliqué les méthodes de nettoyage et d'estimation de spectre aux cartes de données et de simulations en polarisation fournies publiquement par Planck. Nos contraintes sur le comportement spectral de la poussière et du rayonnement synchrotron galactique sont en accord avec les analyses précédentes. Enfin, nous avons pu déduire une limite supérieure sur l'amplitude des ondes gravitationnelles primordiales.

Title: Constraints on primordial gravitational waves from large scales CMB data

Keywords: Cosmology, data analysis, cosmic microwave background, inflation

Abstract:

This thesis focuses on the development of analysis tools of the primordial B modes of the Cosmic Microwave Background (CMB). Our goal is to extract the amplitude of the primordial gravitational waves produced during the inflationary period.

Specifically, we are interested in the large angular scales, for which the primary B modes signal is expected to be dominant. Since these scales are particularly contaminated by polarised galactic emissions, we have studied and developed approaches to reduce those contaminations and to characterise their residuals. Those methods are applicable to satellite mis-

sions such as Planck or LiteBIRD.

In order to estimate the B modes amplitude, we developed and characterised a CMB anisotropies power spectrum estimator. The algorithm is pixels-based and allows to cross-correlate maps measured by different detectors. The method is optimal and minimises the E-to-B variance leakage.

We applied the cleaning and spectrum estimation approaches to the polarisation data and simulation maps publicly provided by Planck. The constraints that we deduce are in agreement with past analysis. Ultimately, we derive an upper limit on the primordial gravitational waves amplitude.

